UNIVERSITY OF
BIRMINGHAM

Low Dimensional Structures of some Mixed Metal Oxides Containing Antimony: Synthesis and Characterisation

by

Benjamin Paul de Laune

A thesis submitted to

The University of Birmingham

For the Degree of

Doctor of Philosophy

The School of Chemistry

College of Engineering and Physical Sciences

The University of Birmingham

B15 2TT, UK

November 2012

Abstract

This thesis describes the synthesis and characterisation of phases related to schafarzikite ($FeSb_2O_4$). A range of $Co_{1-x}Fe_xSb_{2-y}Pb_yO_4$ (where x = 0, 0.25, 0.50 and 0.75; y = 0-0.75) compounds have been synthesised and characterised by a variety of techniques e.g. neutron powder diffraction (NPD), and thermogravimetric analysis.

The refined lattice parameters for all compounds range between a = 8.4492(2) Å - 8.5728(2) Å and c = 5.9170(1) Å - 6.0546(2) Å (NPD, 300 K). The magnetic structures of $Co_{0.25}Fe_{0.75}Sb_2O_4$ and $Co_{0.50}Fe_{0.50}Sb_2O_4$ have been shown to possess dominant A- type ordering as a result of overriding direct exchange interactions between intrachain transition metal cations, whilst all other phases show dominant C- type ordering consistent with 90˚ superexchange. Unusual negative susceptibility is seen and explained in several samples including $CoSb_2O_4$. All phases are shown to display canted antiferromagnetic magnetic order.

Oxidised intermediates are formed and characterised for the first time. This has been critically linked to the presence of Fe^{2+} within these phases. There is evidence to suggest the excess oxygen is a peroxide and/or superoxide species.

The synthesis of $LiSbO_2$ is described and its structure determined: $P2_1/c$ symmetry with a = 4.8550(3) Å, b = 17.857(1) Å, c = 5.5771(4) Å, β = 90.061(6)˚. Its electrical and thermal properties are described.

Acknowledgements

Professor Colin Greaves, you have been a true inspiration to me over the past 4 years. You have given me an incredibly enjoyable and challenging subject area to study enabling me to grow and develop to my full potential. I always think a true sign of a man's metal is when despite being one of the busiest men on the planet you always had time to support, guide and give me a frequent thrashing at badminton. You are an understated true master of your subject and I am eternally grateful for the privilege of working with you.

Professor Frank Berry, I thought retirement was your chance to relax? Thank you for all your help with the Mössbauer data. I've really enjoyed your enthusiasm, support and our in depth discussions over the years, they really encouraged me.

Floor 5, you have been a brilliant place to work and an excellent place of learning; I have made lots of friends over the years. Thank you Evin for your legendary hotpot parties!

Greaves group: James, Maz, and Nicola, it's been a pleasure. Your company on our trips together and support has made the whole experience very fulfilling, thank you.

To my wife and parents. I wouldn't have been able to get to where I am today without your constant support and encouragement which has enabled to push myself to the maximum. Nicola, you have arguably had a harder job than I have and you have always stuck by me, cheered me up and supported me without question. I am forever grateful to you. Mum and Dad, well we all know the hours I've spent chewing your ears off and you're still listening, some people never learn! I can't thank you enough for everything.

I have been surrounded by brilliant people and everything I have achieved is as much testament to you as it is me. Thank you so much and here's to the future!

Table of Contents

Chapter 1 Introduction

Chapter 2 Experimental techniques

Abbreviations

ADP	Anisotropic displacement parameters
AFM	Antiferromagnetic
BSEI	Back scattered electron imaging
BU	Bulk
DTA	Differential thermal analysis
E	The physical representation of a lone pair of electrons
EDS	Energy dispersive X-ray spectrometry
ESDs	Estimated standard deviations
EXAFS	Extended X-ray absorption fine structure
F_{hkl}	Structure Factor
FM	Ferromagnetic
FOM	Figure of merit
FWHM	Full width at half maximum
GB	Grain boundary
HI	High intensity neutron powder diffraction data set
HR	High resolution neutron powder diffraction data set
Hrs	Hours
hkl	Miller indices
IDP	Isotropic displacement parameters
LP	Lone Pair
NPD	Neutron powder diffraction
MPMS	Materials properties measurement system
O_{ap}	Apical oxygen
O_B	Bridging oxygen
O_{eq}	Equatorial oxygen

O_T	Terminal oxygen
PO	Preferred orientation
PSD	Position sensitive detector
SEM	Scanning electron imaging
SEI	Secondary electron imaging
SQUID	Superconducting quantum interference device
TGA	Thermogravimetric analysis
TM	Transition metal
T_{abs}	Temperature at which O_2 absorption initiates
T_N	Néel temperature
T_V	Verwey transition
VT-XRPD	Variable temperature X-ray powder diffraction
XANES	X-ray absorption near edge structure
XRF	X-ray fluorescence
XRPD	X-Ray Powder Diffraction
ZPE	Zero Point Error

Chapter 1

Introduction

The search for new functional materials with features which could offer enhanced properties such as low dimensional magnetism and electrical conductivity is an area of increasing research [1-5]. This thesis is concerned with materials derived from the mineral schafarzikite, $FeSb_2O_4$, which is structurally related to minium, Pb_3O_4.

1.1 The Pb_3O_4 structure

The formula Pb_3O_4 is more accurately described as $Pb^{IV}Pb_2^{II}O_4$ in which heterovalent lead cations occupy two structurally distinct sites. Minium was first characterised in 1943 [6] by X-ray diffraction, and in 1965 by neutron diffraction [7] to locate more accurately the atomic positions of the lighter elements. The structure was characterised in accordance with the (*hkl*) values assigned to the obtained reflections and the symmetry shown to be consistent with the tetragonal space group $P4_2/mbc$ (a = 8.82 Å c = 6.59 Å, no errors given) [7]. The determined atomic positions (Table 1.1) demonstrated two crystallographically distinct sites where Pb^{4+} and Pb^{2+} have octahedral and trigonal pyramidal geometry respectively.

Table 1.1 Atom positions and Wyckoff positions used to refine the structure of Pb_3O_4 in the $P4_2/mbc$ setting [7].

Atom	Wyckoff position	Coordinates		
		x	*y*	*z*
A	4*d*	0	0.5	0.25
B	8*h*	0.143	0.161	0
O1 (O_{eq})	8*h*	0.114	0.614	0
O2 (O_{ap})	8*g*	0.672	0.172	0.25

For ease of comparison, all related phases shall be described using the notation AB_2O_4. The Pb^{4+}-containing octahedra propagate in a manner related to those of the rutile structure (TiO_2) to form infinite chains of edge sharing octahedra along [001] (Figure 1.1a). There are four parallel chains per unit cell (separated by a nearest neighbour Pb^{4+}-Pb^{4+} interchain distance of around 6.2 Å) which each run along a face of the unit cell. Trigonal pyramidal Pb^{2+} ions coordinate the discrete chains into their adopted orientation; consequently a channel (*ca* 3.79 Å diameter) is formed parallel to the chains which is occupied by the sterically demanding (6s) lone pair (LP) of electrons (Figure 1.1b). The geometry of the trigonal pyramidal B site is sometimes described, in related systems, as tetrahedral geometry where the lone pair forms the 4th ligand. The octahedral Pb^{4+}-O bond lengths calculated by Fayek *et al* [7] showed an almost symmetrical Pb^{4+} environment. The trigonal pyramidal Pb^{2+} which bind directly to the apical and equatorial oxygens of the octahedral environment showed that the Pb^{2+}-O_{ap} bonds were notably longer when compared with Pb^{2+}-O_{eq} bonds (2.18 Å and 2.13 Å respectively). Despite the virtually symmetric octahedral environment apical and equatorial bonds are distinguishable where the equatorial plane formed by the four equatorial bonds ($O_{eq} \equiv O1$) of the octahedron align roughly parallel to [001] whilst the apical oxygens ($O_{ap} \equiv O2$) align more closely in the *ab* plane (Figure 1.1a). Each Pb^{2+} forms one Pb-O_{eq} and two Pb-O_{ap} bonds and the chains of octahedra are orientated in an end on fashion where apical bonds of one chain bond through Pb^{2+} to the equatorial bonds of the next.

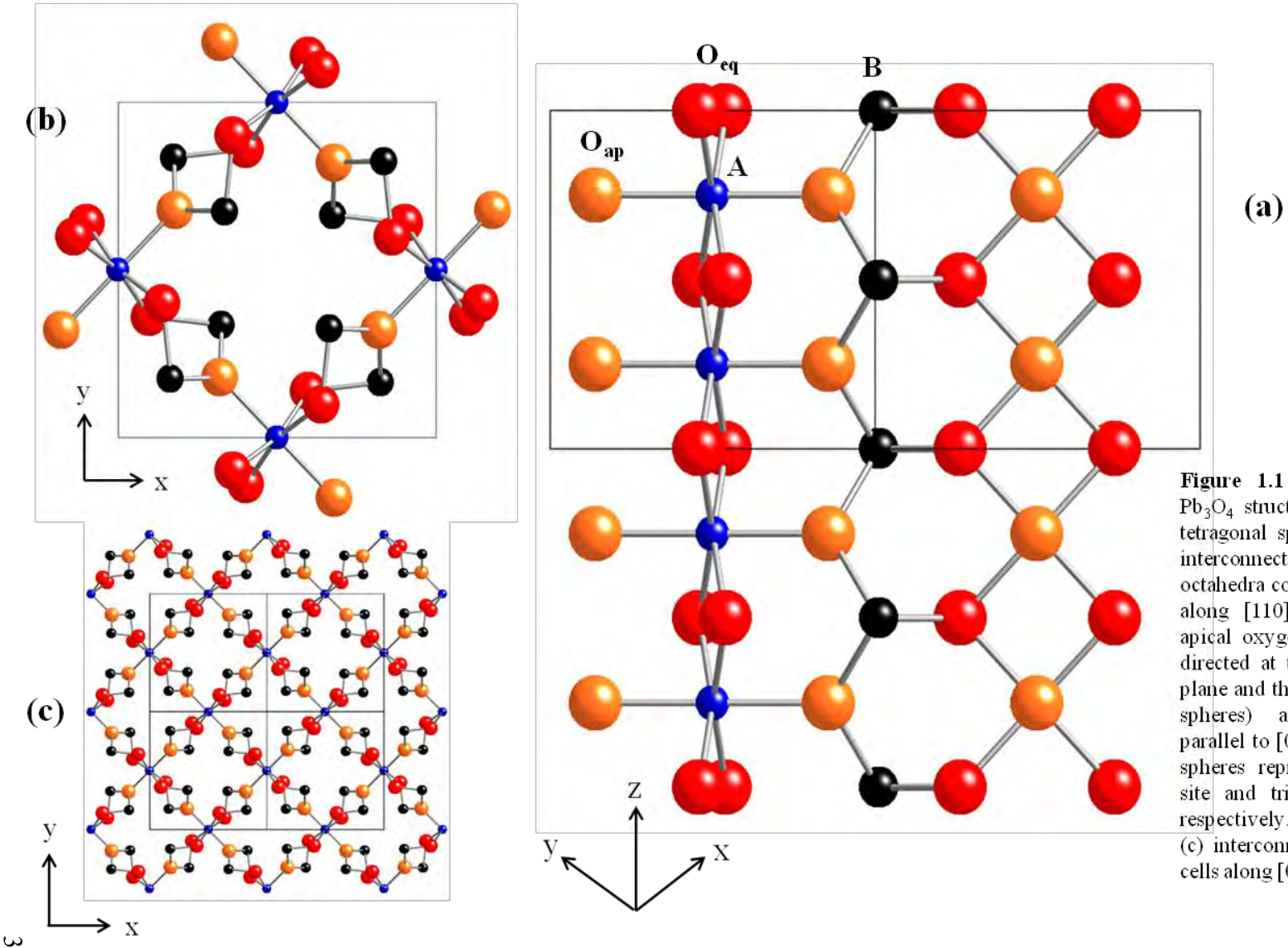

Figure 1.1 Representations of the Pb_3O_4 structure characterised by the tetragonal space group $P4_2/mbc$: the interconnectivity of the edge sharing octahedra containing the A site cation along [110] (a) showing how the apical oxygens (orange spheres) are directed at the next chain in the *ab* plane and the equatorial oxygens (red spheres) are orientated roughly parallel to [001]. The blue and black spheres represent the octahedral A site and trigonal pyramidal B site respectively. (b) A view along [001]; (c) interconnectivity of multiple unit cells along [001].

1.2 Lone pair interactions

The activity of a lone pair of electrons is well known and variable. The stereochemical preferences of a non bonding LP, also commonly referred to as an inert pair, of electrons is a strong driving force in the crystallographic outcome of many ns^2 containing compounds. Generalisations of the bonding preferences are possible which can be used to predict the coordination environment of an ns^2 cation although these can also be very complex. Andersson *et al* [8] proposed the volume of space occupied by a lone pair is approximately equal to that of an O^{2-} anion; subsequently it is often considered to form the fourth apex of a tetrahedron in Pb_3O_4 and can be denoted (E) so that Pb_3O_4 is equivalent to $Pb_3O_4E_2$ (showing two lone pairs per formula mass). This conveniently enables the steric effects of the lone pair to be visualised by a deviation of all bond angles away from 109.5˚ in accordance with VSEPR. The Pb_3O_4 structure whilst not unique with respect to containing a channel occupied by lone pairs, e.g. $Yb_4Sb_2S_{11.25}$ [9], $MnPb_2O_4$ [1], schafarzikite (*vide infra*) it is unusual with regard to many other systems which tend to direct a lone pair into an unoccupied region [10] generating layered compounds, e.g. $CaCo_2Te_3O_8Cl_2$ [11] and $KSbO_2$ [12] where the LP is effectively encapsulated by longer secondary bonds e.g. $SnBr_2$ [13]. A schematic representation of the Pb_3O_4 structure accounting for ionic radii (Shannon [14]) and the volume occupied by a LP (Figure 1.2) is shown. The possibility of LP interactions is yet to be fully explored and would be an area of fundamental interest. The effects on properties such as superconductivity and semiconductivity is still a question of origin, however the degree of interaction of a lone pair with coordination environment has been associated with a lowering of the band gap in some binary semiconducting compounds [15].

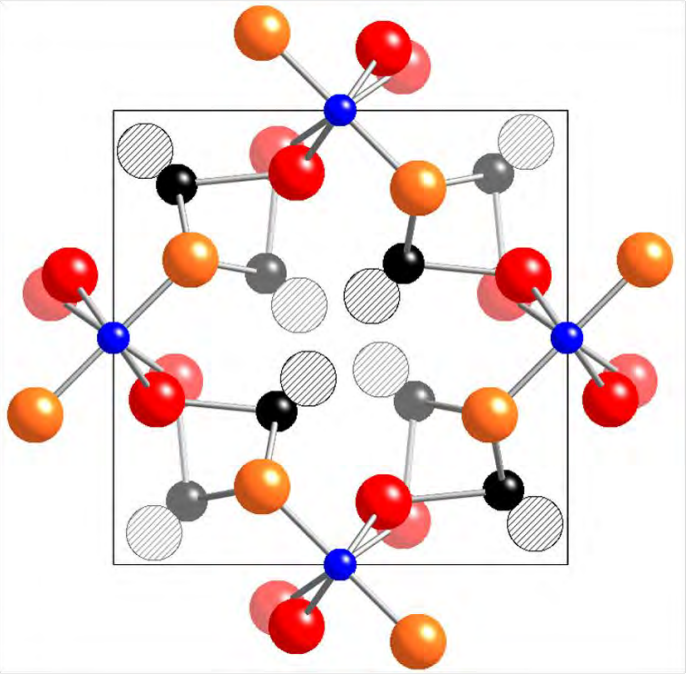

Figure 1.2 An illustration of the Pb_3O_4 structure viewed in the *ab* plane; the spheres represent Pb^{4+} (blue), O_{eq} (red) O_{ap} (orange) and Pb^{2+} (black), the striated circles schematically indicate the volume occupied by a lone pair of electrons on Pb^{2+}. Opposing pairs are formed at $z = 0$ and 0.5 (faded striated circles). The inter Pb^{2+} distance across [110] is 3.786 Å (*ca* 3.7 Å in $MnPb_2O_4$ [1]). Values used to generate the structure obtained from Gavarri *et al* [16].

1.3 Chemical considerations of the schafarzikite structure

The search for structural analogues of minium identified three materials of scientific interest; however, attention focused on the rare mineral schafarzikite ($FeSb_2O_4$). Isostructural to Pb_3O_4 the octahedral A site (4*d*) cation is substituted by a transition metal (TM) enabling functionalisation of the material. First discovered by Professor Ferenc Schafarzik this naturally occurring mineral has to date been identified only in a small number of locations around the globe e.g. Slovakia (Pernek) [17], the Apuan Alps (Buca della Vena mine) [18] and suspected in Bolivia (the Kharma antimony deposit) [19]. Found largely within antimony rich deposits, the mineral was first characterised in the centrosymmetric space group $P4_2/mbc$ with lattice parameters a = 8.592 Å, c = 5.905 Å (Z = 4) [20]. Largely but not exclusively isolated to the first row transition elements many isostructural synthetic variants have been created (MSb_2O_4; M = Mn, Fe, Ni, Co, Zn, and Mg) [21-27], see Table 1.2.

The (8*h*) B site of schafarzikite is solely occupied by Sb^{3+} where the lone pair of electrons is again directed into the channel [28-29]. It was noted that the occupancy of divalent cations on the B site with retention of $P4_2/mbc$ symmetry provided a theoretical route for oxidising the A site. Several systems exist which show the possibility of doping on both the A and B site exhibiting in some phases the possibility of oxidising A whilst in all cases retaining the $FeSb_2O_4$ structure: B = Sn^{2+}, A = Ti^{4+} [30]; B = As^{3+}, A = Cu^{2+} [31], Ni^{2+} [1] [32] and B = Pb^{2+}, A = Pb^{4+}, Pt^{4+} [2] (Table 1.2). Exceptions are seen in $ZnAs_2O_4$, leiteite [34] which is believed to possibly be a low temperature polymorph of the main phase. Constructed from sheets of corner linked Zn tetrahedra (Figure 1.3), reminiscent of a chess board, sandwiched between chains of corner linked $[AsO_3]^{3-}$ trigonal pyramids a layered structure is formed ($P2_1/c$, Z = 2; a = 4.542(1) Å, b = 5.022(1) Å, c = 17.597(5) Å) which more closely resembles the structure of the alkali metal arsenites $AAsO_2$ (A = Na, K and Rb [35-37]) and is especially similar to $LiSbO_2$ (*see Chapter 6*). Arsenic however does display the typical three short primary bonds (average bond length 1.79 Å) and 3 longer, weaker, secondary bonds (2.84-3.34 Å) [34] characteristic of cations containing a lone pair of electrons [10]. Synthesis of other phases have reportedly failed despite using the same conditions by which other variants have been formed e.g. $CuSb_2O_4$ [24-25].

Lattice parameters for the synthesised MSb_2O_4 compounds fall within the range a = 8.7023(7)-8.3719 Å: c = 5.9831(6)-5.9079 Å (Table 1.3), where it can be seen that more significant changes occur in a compared with c which remains relatively constant (Figure 1.4) upon substitution of the A site. This trend mirrors the changing ionic size of M remarkably well where the Ni and Mn posses the smallest and largest unit cells concordant with the ionic radii values calculated by Shannon [14] (based on all ions being high spin).

[1] No structural details given, previous attempts to synthesise the arsenites reportedly failed [20].
[2] Strictly of *Pbam* symmetry but contains similar structural features to schafarzikite [33].

Table 1.2 The known variants of the AB_2O_4 compounds with $P4_2/mbc$ symmetry where each site is occupied by a single element only. (?) This compound was reportedly not of the same structure but there is suggestion that there may be a related higher temperature polymorph.

A site elements	B site cations			
	Pb^{2+}	As^{3+}	Sb^{3+}	Sn^{2+}
Ti	-	-	-	Y
Mn	-	-	Y	-
Fe	-	-	Y	-
Co	-	-	Y	-
Ni	-	Y	Y	-
Zn	-	(?)	Y	-
Cu	-	Y	-	-
Pt	*Pbam*	-	-	-
Mg	-	-	Y	-

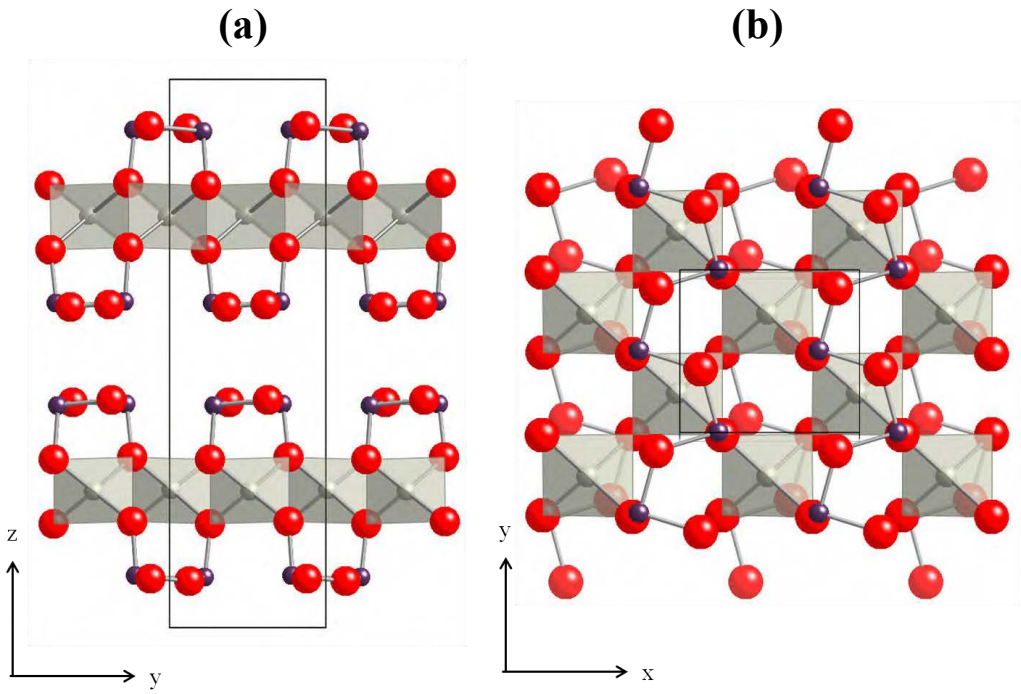

Figure 1.3 The structure of $ZnAs_2O_4$ refined in $P2_1/c$; (a) a view along [100] showing discrete chains of $[AsO_3]^{3-}$ parallel to [100] and tetrahedral Zn (grey spheres) sandwiched between layers of opposing apical oxygens. Red and dark purple spheres represent O^{2-} and As^{3+} respectively; (b) a view along [001] showing the corner linked arrangement of Zn tetrahedra and the zig-zag arrangement of the As-O backbone. Structural details obtained from Ghose *et al* [34].

Table 1.3 Refined lattice parameters of the schafarzikite-related phases at 300 K. Values given as reported. Ionic radii obtained from Shannon [14].

Compound	Lattice parameters (Å)		A site ionic radius (Å)
	a	*c*	
$MnSb_2O_4$ [22]	8.7023(7)	5.9831(6)	0.97
$FeSb_2O_4$ [21]	8.59	5.91	0.780
$FeSb_2O_4$ [38]	8.61574(9)	5.92069(8)	0.780
$CoSb_2O_4$ [24]	8.500(1)	5.931(1)	0.745
$NiSb_2O_4$ [27]	8.3719	5.9079	0.690
$ZnSb_2O_4$ [39]	8.527(2)	5.942(2)	0.740
$MgSb_2O_4$ [26]	8.476(2)	5.938(2)	0.720
$TiSn_2O_4$ [30]	8.490(2)	5.923(3)	0.605
$NiAs_2O_4$ [20]	8.22	5.62	0.690
$CuAs_2O_4$[31]	8.592(4)	5.573(4)	0.73
$SnPb_2O_4$ [40]	*a* = 8.7215 *b* = 8.7090	6.3054	0.69
Pb_3O_4 [7]	8.82	6.59	0.778
$PtPb_2O_4$ [33]	*a* = 9.115(4) *b* = 7.941(4)	6.306(4)	0.625

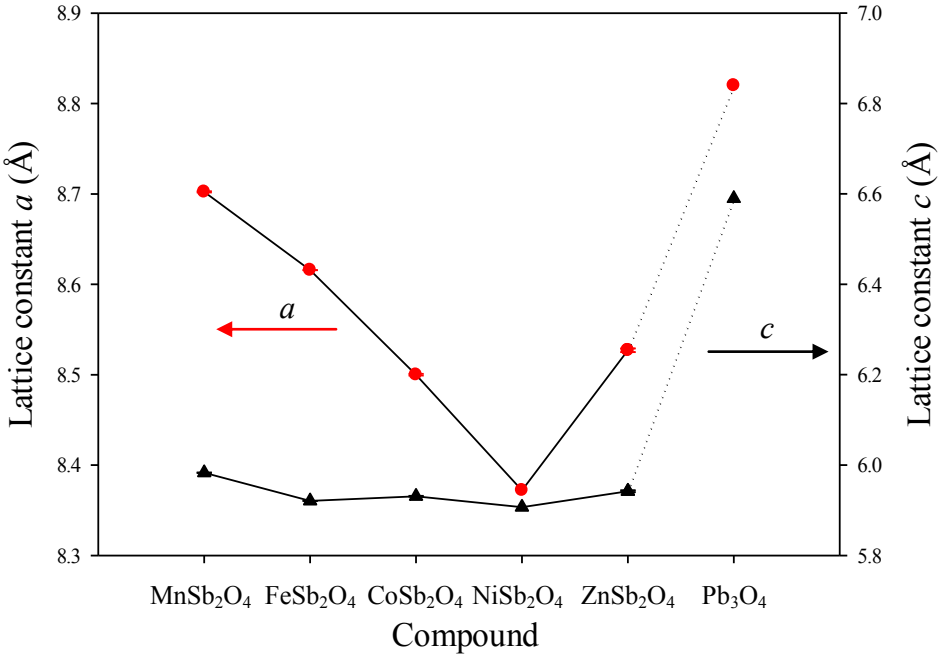

I ›orted
M

Col 1 vs Col 2

Ionic radii alone, however, do not fully explain this trend. In all cases, the octahedral environment has been shown to be distorted (Table 1.4) where all apical bonds are longer than

the equatorial bonds (except $ZnSb_2O_4$) representing a small elongation of the octahedral crystal field. Due to the "end on" nature of the octahedra a greater reduction in the TM-O_{ap} bonds with TM results in a larger contraction of *a* compared to *c*. A comprehensive study of the thermal expansion effects on the Fe, Ni, Mn, and Zn compounds [22-23, 27-29, 41-42] has linked temperature to changes in polyhedral environment, bond lengths, force constants and anisotropic Debye parameters. Attention was focused on the changes in bond lengths and two main points can be derived from the neutron powder diffraction (NPD) study by Gavarri *et al* [23] regarding the thermal expansion behaviour of the Mn, Ni, and Zn variants between 2-300 K: The findings reported:

- Greater changes in the thermal expansion of the *M*-O_{ap} bonds ($12.6 – 30 \times 10^{-6}$ K^{-1}) compared with the *M*-O_{eq} bonds (all below the value of uncertainty, 5×10^{-6} K^{-1}) upon heating and cooling.
- The Sb-O_{ap} bonds are longer but vary significantly less (below statistical significance) than the shorter Sb-O_{eq} bonds ($13.9 – 22 \times 10^{-6}$ K^{-1})

The overriding findings mirror the trend in Figure 1.4 showing that in all cases the thermal expansion of the unit cell between 2-300 K is an anisotropic process [22-23, 27-29, 41] where the expansion in *a* is largely greater than in *c* reflecting greater flexibility in the TM-O_{ap} bonds. The steric effects of the LP are clearly visible when considering the O-B-O bond angles all of which are less than 109.5˚ (for an ideal tetrahedron, including the lone pair) indicating the strong repulsive influence of the LP over the single bonds in accordance with VSEPR. It is noteworthy that a detailed investigation of $CoSb_2O_4$ had not been reported prior to this study.

Table 1.4 Refined bond lengths and angles obtained for the schafarzikite related compounds at 300 K. Values presented as reported (*) XRD data. [a] Values derived from [27]. [b] Values derived from [39].

	Compound ($M$$Sb_2O_4$)						
Bond lengths (Å)	Mg [26]	Mn [41]	Fe [38, 43]	Ni [29]	Zn [29]	Zn [39](*)	Pb_3O_4 [7]
A-O_{ap} (x2) (**8*g***)	2.131 (5)	2.2140(20)	2.187(2)	2.0830	2.1810	2.176(5)	2.13
A-O_{eq} (x4) (**8*h***)	2.058(4)	2.1322(20)	2.104(1)	2.051	2.073	2.075(4)	2.14
B-O1 (O_{eq})	1.910(5)	1.9534(20)	1.927(3)	1.930	1.935	1.937(5)	2.13
B-O2 (x2) (O_{ap})	1.995(5)	2.0136(20)	1.997(2)	1.999	2.002	1.993(5)	2.18
A-A	2.969	3.0005(1)	2.9603	2.9540[a]	2.974[b]	2.971	3.295
Bond angles (°)							
O_{eq}-A-O_{eq}	93.4		90.57(6)			88.6(1)	90
O_{eq}-A-O_{eq}	87.7		166.19(9)			165.4(2)	90
O_{eq}-A-O_{eq}		90.60(7)	91.08(6)			93.3(1)	90
A-O-A			89.43(6)				90
O_{eq}-B-O_{ap}	94.7	93.00(13)	94.49(7)			93.4(2)	
O_{ap}-B-O_{ap}	96.2		95.68(9)			96.4	

1.4 Mixed B site structures - Lead doped phases

The availability of a route to chemically oxidising the octahedral species is of considerable interest. Until recently only a single attempt had been made to substitute varying levels of Pb^{2+} for Sb^{3+} in $MnSb_2O_4$, this is despite there being a large number of unexplored possibilities (Table 1.2). The study by Abakumov *et al* [44] demonstrated a high degree of resistance in trying to synthesise pure $MnSb_{2-x}Pb_xO_4$ phases which theoretically would contain a mixture of octahedral Mn^{2+} (d^5) and Mn^{3+} (d^4). Their findings can be summarised as follows:

- All samples were multiphase; however, the main constituent was a phase similar to that of $MnSb_2O_4$ with varying lattice parameters as a function of lead content.
- As Pb increased the level of Mn-containing impurities increased and the formation of $(Mn_{1-x}Sb_x)(Sb_{2-y}Pb_y)O_4$ was proposed.

- $(Mn^{2+}_{1-x}Sb^{5+}_{x})(Sb^{3+}_{2-y}Pb^{2+}_{y})O_4$ phases were directly synthesised and characterised by refinement of X-ray powder diffraction (XRPD) data (charge balance maintained by the relationship $x = 3/2y$) whilst XANES experiments confirmed Mn^{2+} largely remained unoxidised but that a small amount of Mn oxidation could not be ruled out.
- Ordering effects and a slight orthorhombic distortion (b_0-a_0/b_0+a_0 = 5 x 10^{-4} at 20 K) were mentioned.

These findings were in stark contrast to a similar study by Whitaker *et al* [38] who used the lead substitution method to induce oxidation of Fe in the $FeSb_2O_4$ system. Here the systems were absent of deviation from $P4_2/mbc$ symmetry and significant amounts of iron-containing impurities up to Pb = 0.75. It was shown that Fe was oxidised preferentially over Sb (from Mössbauer data for $FeSb_{1.50}Pb_{0.50}O_4$).

In both systems opposing effects were seen to cause the changes in lattice parameters. Primarily related to a reduction of the bond lengths in the octahedral coordination sphere, the oxidised A site species resulted in a reduction in *a*, where differing ionic radii on the B site creates an elongation along *c*. There is an additional component of repulsion resultant from oxidation of the octahedral species.

1.5 Mixed A site species

Equally rare are reports of mixed A site MSb_2O_4 compounds [45-46]. A brief study by Abe *et al* [45] reported the formation of $(Mn_{1-x}V_x)Sb_2O_4$ (where x = 0-0.6) without any apparent change of lattice parameter (*a* = 6.00 Å, *c* = 8.71 Å) or deviation from $P4_2/mbc$ symmetry with composition and supposed high purity. It is unclear how these parameters were calculated and the findings are in contrast to those reported by Brach *et al* [46] where a rhombic distortion is mentioned in the $Mg_{1-x}Ni_xSb_2O_4$ phases ($0.01 \leq x \leq 0.20$), no further

structural details were given. The magnetic focus of the $Mn_{1-x}V_xSb_2O_4$ and $Mg_{1-x}Ni_xSb_2O_4$ studies are discussed later and the main magnetic focus of the present study is discussed below.

1.6 Magnetic properties

The low dimensional features of the structure and consequent magnetic effects are of interest. It is usual that the orbital contribution of a magnetic moment is perturbed by the crystalline environment for 3d metals and moments are given by the spin only formula. Exception is given to Co^{2+} where spin-orbit coupling is commonly seen but the orbital contribution is small [2, 47]. Schafarzikite is considered pseudo one dimensional (1D) when considering the interconnectivity of the chains of octahedra [5]; the inter-chain separation of TMs in the *ab* plane varies according to the 3*d* element, and is of the order of 6 Å in $FeSb_2O_4$. Compared with a TM-TM intrachain separation distance of around 3 Å along [001] stronger intrachain interactions would be expected to be observed. When all elements except the TMs are removed from the unit cell as shown in Figure 1.5, a cell of magnetic ions with identical lattice parameters to the nuclear structure remains which forms the basic unit for the long range ordered structure. Four symmetry-related TM positions remain: (0, 0.50, 0.25) S_1, (0, 0.50, 0.75) S_2, (0.50, 0, 0.25) S_3, and (0.50, 0, 0.75) S_4, where S_n indicates the spin vector of each site. Four theoretically possible collinear spin alignments can result within the magnetically ordered systems as shown in Figure 1.5, these are termed as A, C, G or F modes:

A mode- ferromagnetic ordering within a plane and antiferromagnetic ordering within the chain

$$A = S_1, -S_2, S_3, -S_4$$

C mode- ferromagnetic order within a chain and antiferromagnetic order between nearest neighbour chains

$$C = S_1, S_2, -S_3, -S_4$$

G mode- antiferromagnetic alignment between all nearest neighbours

$$G = S_1, -S_2, -S_3, S_4$$

F mode- all moments are align in a ferromagnetic arrangement

$$F = S_1, S_2, S_3, S_4$$

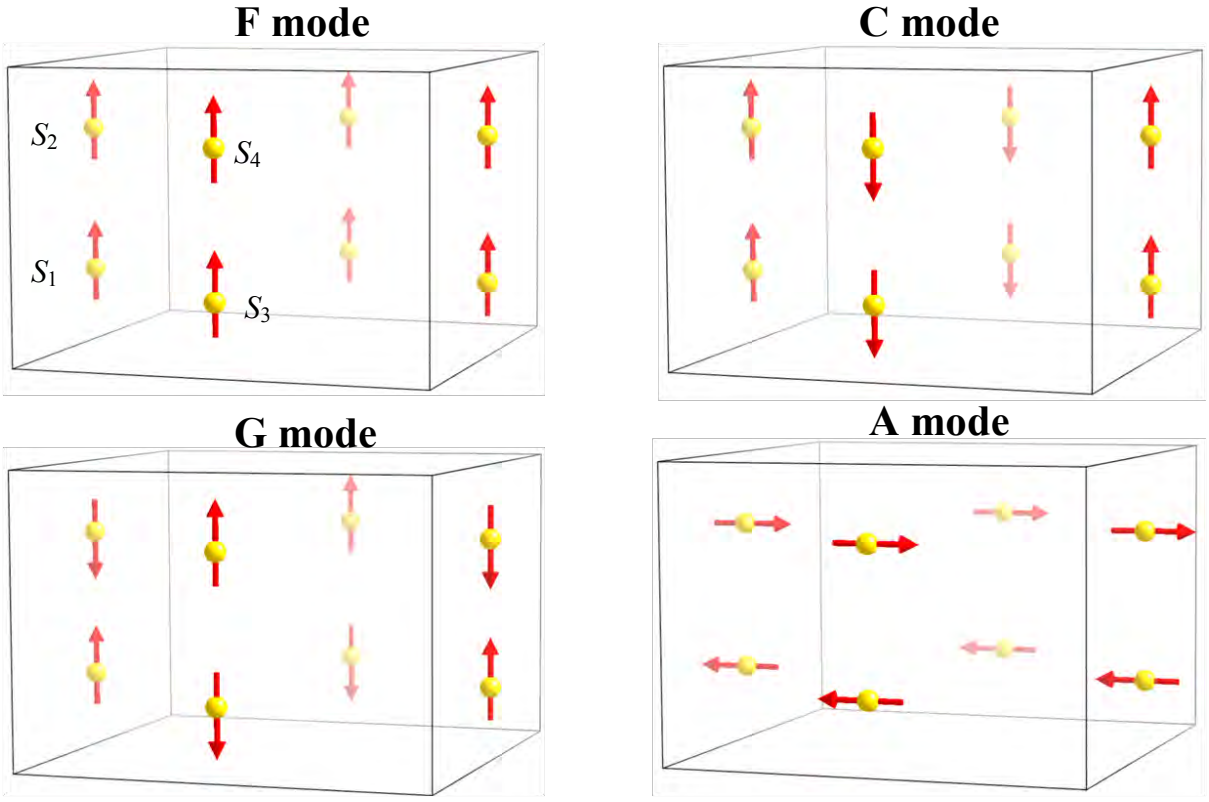

Figure 1.5 Representations of the different possible magnetic modes the schafarzikite structure can adopt. A and C modes also highlight the possible mode orientations between *x* and *z* common to $FeSb_2O_4$ and $NiSb_2O_4$ respectively.

All magnetically ordered compounds contain a degree of covalent character which is vital to the magnetic exchange of electrons within a crystalline solid. The underpinning science behind explaining the magnetic interactions which give rise to ordered systems were

reported by Kanamori and Goodenough [48-50]. Three main magnetic interactions are considered when generating long range order within the schafarzikite structure based upon these principles. The first is the direct exchange of electrons between adjacent TMs through interacting t_{2g} orbitals (Figure 1.6a) giving rise to antiferromagnetic order within the chain and is possible due to the rutile relationship of the structure. This is only applicable for TMs with vacancies within their degenerate t_{2g} orbitals (low spin $d^5\leq$, or $d^7\leq$ high spin complexes) and is strongly dependent on the degree of orbital overlap [47, 51]. The second, often considered the weaker interaction for these systems, is the 90° TM-O-TM super exchange pathway through the common edge O^{2-} (Figure 1.6b) responsible for generating ferromagnetic ordering within the chains. According to Witteveen [32] the third complex interaction of the type TM-O-Sb-O-TM is responsible for generating the interchain ordering (further discussed below).

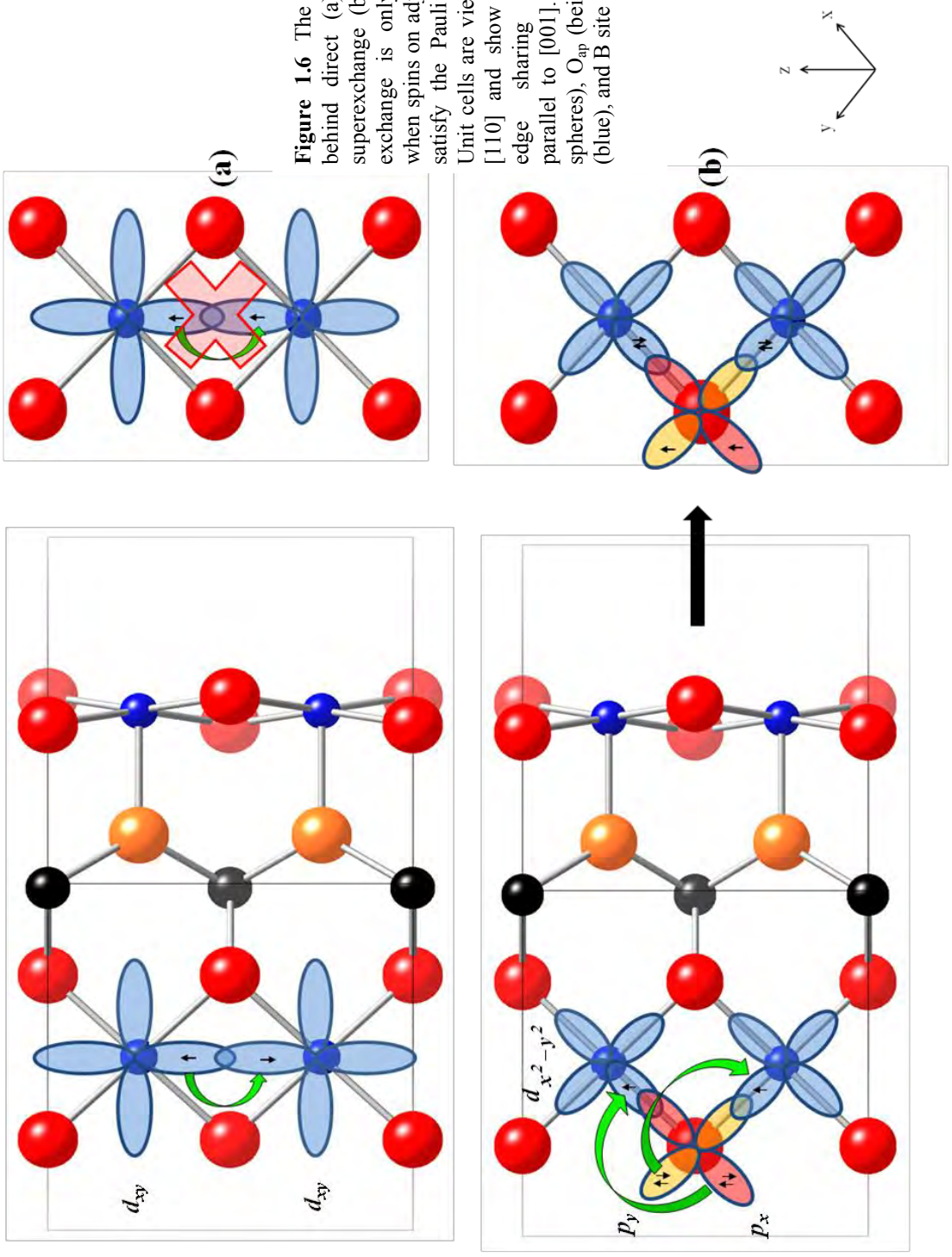

Figure 1.6 The principles behind direct (a) and 90° superexchange (b). Direct exchange is only possible when spins on adjacent ions satisfy the Pauli principle. Unit cells are viewed along [110] and show chains of edge sharing octahedra parallel to [001]. O_{eq} (red spheres), O_{ap} (beige), A site (blue), and B site (black).

All magnetic structure determinations by NPD pertaining to the schafarzikite variants Mn to Ni (until recently excluding $CoSb_2O_4$, *see Chapter 3*) have revealed magnetic structures consistent with A, C, and G components (Table 1.5) [22, 38, 41, 52-53]. There have been several attempts to determine the magnetic structure of many of the phases. Whilst there is broad agreement of the main ordering type for each phase there is a degree of variability between results. This has largely been attributed to impurities contained within samples during structural determinations [53]; particular difficulty was met when trying to synthesise pure $MnSb_2O_4$ reflecting the number of determinations.

Gonzalo *et al* [52] described one of the only attempts to assign magnetic symmetry to the system; this coincidently led to the identification of a possible distortion from tetragonal symmetry in $FeSb_2O_4$. The magnetic reflections could be indexed for a cell with lattice parameters consistent with the nuclear phase; however the indexed peaks corresponding to an A, C and G mode (001), (100) and (101) broke the symmetry restrictions of the $P4_2/mbc$ space-group ($h00$: h = 2n, and $00l$: l = 2n) but not only this, a combination of modes indicated further to the tetragonal arrangement being incompatible with the reflections. Gonzalo *et al* [52] suggested that of the possible space groups identified which would not restrict the moments to lie along an axis or plane only $Pmc2_1$ (Shubnikov and crystallographic) was deemed suitable. The orthorhombic space group was supported by limited evidence which suggested a minute orthorhombic distortion (≈ 0.2%) of the nuclear cell (broadening of the (h00), absent in the (hh0) or (hhl) peaks); however, the resolution at the time was insufficient to promote further comment. Subsequent NPD studies support evidence for a small orthorhombic distortion above T_N in $MnSb_2O_4$ [29] and $NiSb_2O_4$ [40] ($(a-b)/a_0 = 1x10^{-3}$ from [54]). Gavarri *et al* [53] suggested that the distortion could be related to magnetostriction ("a change of dimensions and shape of a sample due to a change of its

magnetic state" [55]) in $MnSb_2O_4$. Furthermore magnetostriction about T_N was reported in $FeSb_2O_4$ [28]. All of these findings are in contrast to later studies which do not report any orthorhombic distortion or magnetostrictive effects [22, 38].

Neglecting the minutiae, underlying similarities are observed between the characterised systems. From Mn to Ni there is a transition from a dominant A mode within the *ab* plane to a C mode parallel to *c*. The absence of data for $CoSb_2O_4$ seemed to imply the Co phase potentially lay on a magnetic transition boundary and required investigation. Furthermore of the MSb_2O_4 phases only the Ni system displayed purely C-type ordering. For the Mn and Fe systems, both high spin (see Table 1.6), it was possible for direct and 90˚ exchange to occur simultaneously. From the dependence of direct exchange on the degree of overlap between interacting d_{xy} orbitals it was clear from the refined magnetic structures that the overlap was sufficient to enable direct exchange as the dominant exchange process. Similar interactions and observations were made in $MnPb_2O_4$ (Mn-Mn distance 2.92 Å) [1].

The Ni system unlike its analogues was the first example of a divalent cation with a fully occupied set of t_{2g} orbitals, consequently direct exchange was impossible and only the 90˚ superexchange was observed giving rise to ferromagnetic ordering within a chain (an overall C mode). It was rationalised by Witteveen [32] based on the work of Frazer *et al* [56] that a third less obvious exchange was simultaneously occurring in order to provide the inter-chain antiparallel arrangement of ferromagnetic chains ($NiSb_2O_4$: T_N = 47.5(5) K and Curie temperature (θ) = -34 K indicating overall strong antiferromagnetic interactions). Frazer *et al* [56] studied the orthorhombic (*Cmcm*) ABO_4 systems (where A = Cr, B = V; and A = Fe, Ni, Co, B = S) which also consisted of chains of edge sharing octahedra parallel to *c* but with tetrahedral SO_4 linking units. They postulated that non magnetic linking units were involved in a complex and long range antiferromagnetic exchange linking octahedral sites through a

TM-O-O-TM, or TM-O-S-O-TM type interaction resulting in ferromagnetic ordering within all chains which were in turn arranged in an antiferromagnetic fashion. It was noted that this was dependent not only on the TM but also the interatomic distances and bond angles. Although weak compared with 90˚ superexchange this interaction could not be overlooked.

Table 1.5 Refined magnetic structures of the schafarzikite phases with associated mode (A, C, G) orientation (subscript *x*, *y*, *z*) and magnitude respectively. All modes were combined into a single phase. Temperature of data collection is indicated for assessment of magnitudes.

Compound	Magnitude (μ_B)	Temperature (K)
$MnSb_2O_4$ [54]	A_x, G_y, C_z $\mu_{total} = 3.8$ (3)	6
$MnSb_2O_4$ [53]	$A_x = 5.1$ (3)	4.5
$MnSb_2O_4$ [41]	$A_x = 4.3$ (2)	
$MnSb_2O_4$ [22]	$A_x = 4.37$ (6) $G_z = 1.25$ (25) $\mu_{total} = 4.52$(13)	10
$FeSb_2O_4$ [52]	$A_x = 3.5 \pm 0.2$ $C_z = 0.7 \pm 0.2$ $G_y = 0.9 \pm 0.2$	4.2
$FeSb_2O_4$ [28]	A_x dominant $C_z = 0.5$(3) $\mu_{total} = 3.8$(2)	2
$FeSb_2O_4$ [38]	$A_x = 3.62$(3) $G_z = 1.24$(7) $\mu_{total} = 3.83$(4)	4
$NiSb_2O_4$ [54]	$C_z = 1.8$ (3)	6
$NiSb_2O_4$ [53]	$C_x = -1.0$ $C_y = 1.0$ $C_z = 1.8$ $\mu_{total} = 2.1$ (3)	2.5
$FeSb_{1.70}Pb_{0.30}O_4$ [38]	$C_x = 2.91$(4); $C_x = 2.8$ (1) $C_z = 0.7$ (3) $\mu_{total} = 2.90$(3)	4
$FeSb_{1.50}Pb_{0.50}O_4$ [38]	$C_x = 3.10$ (9) $C_z = 1.3$ (1) $\mu_{total} = 3.36$(9)	4
$FeSb_{1.30}Pb_{0.70}O_4$ [38]	$C_x = 1.3$ (2) $C_z = 3.29$ (4) $\mu_{total} = 3.54$(8)	4
$Mn_{0.92}Pb_{0.44}Sb_{1.64}O_4$ [44]	$A_{xy} = 2.63$ (3)	20

A study by Motida *et al* [57] built upon the 90˚ interactions occurring between TMs in a range of compounds. Based upon empirical observations it aimed to differentiate further the

strength of competing direct exchange and 90° superexchange processes within a variety of TM containing compounds and the effect on Néel temperature (T_N) and paramagnetic θ. Predictions were made for the then unknown compounds $MnSb_2O_4$ and $NiSb_2O_4$. For $NiSb_2O_4$ their prediction (θ = +15 K) did not match the later reported empirically observed value (θ = -40±1 K) [32] but was in accord with $MnSb_2O_4$ (predicted θ = -210 K [57]; observed θ = -190±20 K [22]). The study had deliberately neglected the long range ordering to simplify the models; however this highlighted the significance of the extended TM-O-Sb-O-TM interactions within these systems.

In most cases there is a good agreement between 2*S* and the refined NPD moment suggesting little orbital contribution in the MSb_2O_4 phases. The presence of Fe_3O_4 in all samples of $FeSb_2O_4$ was problematic in susceptibility measurements primarily due to the Verwey transition (an ordering of the octahedral B site Fe^{2+} and Fe^{3+} cations at around 120 K [58]) which prevented the paramagnetic moment calculation. A re-examination of $FeSb_2O_4$ by Whitaker *et al* [38] however proposed an orbital contribution to the moment. When comparing with the novel $FeSb_{2-x}Pb_xO_4$ phases a large reduction in the 2*S* moment between $FeSb_2O_4$ and $FeSb_{1.70}Pb_{0.30}O_4$ (see Table 1.5) was found and attributed to a severe distortion of the octahedral environment, removing the triple degeneracy of the ground state. Whilst the interactions are highly complex a large increase in T_N with Pb_x (Table 1.6, $FeSb_2O_4 < T_N < FeSb_{1.40}Pb_{0.60}O_4$) implied strengthening of the magnetic interactions generating the mode of ordering. The magnetic structures of the $(Mn_{1-x}Sb_x)(Sb_{2-y}Pb_y)O_4$ phases [44] were not substantially investigated yet an A_x mode appeared consistent with the magnetic reflections at 20 K (Table 1.5) and a weakening of $|\theta|$ with increasing Pb_x (θ < -100 K for the entire range) implied weakening of the overall intrachain antiferromagnetic exchange interactions, likely due to octahedral Sb^{5+} disrupting long range order.

Table 1.6 The ordering temperatures of the magnetic systems. (-) missing or unable to calculate a value due to magnetite impurities. (●) value obtained from heat capacity measurements. (▼) value obtained from magnetic susceptibility measurements. Spin only values are calculated for high spin (HS) configurations only.

Compound	Magnetic moment (μ_B)	T_N (K)	θ (K)	Spin only value (μ_B)	Method of obtaining	d^n
$MnSb_2O_4$ [53]	-	60±5	-	5.92	NPD	d^5
$MnSb_2O_4$ [22]	6.02±0.10	55±2*	-190± 20		▼ and NPD*	
$MnSb_2O_4$ [45]		60.5			▼	
$FeSb_2O_4$ [38]	-	45	-	4.90	▼	d^6
$FeSb_2O_4$ [28]	-	45±6	-		NPD	
$FeSb_2O_4$ [59]	-	42	-		▼	
$CoSb_2O_4$	-	-	-	3.87	-	d^7
$NiSb_2O_4$ [60]	3.98±0.14	46±3* 45.0±0.1●	-98±5	2.83	NPD*,	d^8
$NiSb_2O_4$ [32]	3.30±0.03	47.0±0.5	-40±1		▼	
$NiSb_2O_4$ [53]		46±2			NPD	
$FeSb_{1.80}Pb_{0.20}O_4$ [38]	-	51	-		▼	$Fe^{2.2+}$; $d^{5.8}$
$FeSb_{1.70}Pb_{0.30}O_4$ [38]	-	56	-		▼	$Fe^{2.3+}$; $d^{5.7}$
$FeSb_{1.60}Pb_{0.40}O_4$ [38]	-	58	-		▼	$Fe^{2.4+}$; $d^{5.6}$
$FeSb_{1.50}Pb_{0.50}O_4$ [38]	-	69	-		▼	$Fe^{2.5+}$; $d^{5.5}$
$FeSb_{1.40}Pb_{0.60}O_4$ [38]	-	69	-		▼	$Fe^{2.6+}$; $d^{5.4}$
$(Mn_{1-x}V_x)Sb_2O_4$ x = 0.10, 0.20, 0.60 [45]	-	57	-		▼	

The magnetic susceptibility of the $(Mn_{1-x}V_x)Sb_2O_4$ phases displayed canted antiferromagnetic behaviour [45] consistent with that in the $FeSb_{2-x}Pb_xO_4$ phases. If the magnetic ordering temperature is to be taken as reported, T_c = 57 K is apparently independent of x (within error). It seemed apparent that a slight misinterpretation may have occurred. Despite this, the magnitude of magnetisation appears to increase with V content, indicating the systems were not V depleted posing further questions to the apparent independence of T_N with V content. The origin of the ferromagnetic component was most likely the result of a

ferrimagnetic arrangement of magnetic ions. In the brief report for the $Mg_{1-x}Ni_xSb_2O_4$ phases it was found that the strength of interaction between magnetic ions resulted in aggregation of the magnetic particles for the dilute systems indicating further that the magnetic interactions were strong.

1.7 Properties testing

In the search for new lithium storage devices a recent study by Jibin *et al* [61] investigated the schafarzikite related materials $CoSb_2O_4$ and $NiSb_2O_4$. Whilst the phases contained no readily reducible components which would maintain the structure the idea was to extend the lifetime of the electrode enhancing cycle life hence performance of the material. In light of the high carrier density of lithium based alloys e.g. Li_3Sb the material was of interest as it contained elements (i.e. Ni/Co) which upon cycling would theoretically act as a scaffolding to minimise volume changes and enhance electrochemical output by extending the life time of the electrode. They reported that two processes are important (shown in equations 1.1-1.3) where it is the alloying/de-alloying of Li_3Sb which is crucial for electrical conductivity and the formation of electrochemically inert elements (M) which provided enhanced cycle lifespan through reduced volume changes on cycling between 0.005-1.3 V. $CoSb_2O_4$ was found to have higher capacities after 35 cycles (348 mAh g^{-1}) when compared with $NiSb_2O_4$ (290 mAh g^{-1}) after 25 cycles due largely to $CoSb_2O_4$ having a smaller particle size enabling more efficient Li^+ migration.

$$M^{2+}Sb_2^{3+}O_4 + 8Li^+ + 8e^- \rightarrow M + 2Sb + 4Li_2O \quad (1.1)$$

$$Sb + 2Li \leftrightarrow Li_2Sb \quad (1.2)$$

$$Li_2Sb + Li \leftrightarrow Li_3Sb \quad (1.3)$$

1.8 Versiliaite and apuanite

Rarer still than naturally occurring schafarzikite, the minerals versiliaite and apuanite were discovered in the Buca della Vena mine and are named after the regions in which they were found (the Apuan Alps and the Versilia valley within the same region)[18, 62]. These derivatives of the $FeSb_2O_4$ compound share similar structural features with additional points of interest. Characterised in the orthorhombic space group *Pbam* (a maximal subgroup of $P4_2/mbc$) versiliaite adopts the formula $Fe_{12}Sb_{12}O_{32}S_2$. Deconvolution into its ionic components enables a clearer view of its chemical makeup: $(Fe_4^{2+}Fe_4^{3+})Fe_4^{3+}Sb_{12}^{3+}O_{32}S_2$. Three main differences exist compared with $FeSb_2O_4$ (Figure 1.7) which are intrinsically linked. Considering first the B site, a mixture of Sb^{3+} and Fe^{3+} are found to coexist where every 4th Sb^{3+} is replaced by Fe^{3+}. Antimony is in trigonal pyramidal coordination where the lone pair of electrons is directed into the channel as before; however, Fe^{3+}, also found on the B site, is in tetrahedral geometry where the 4th ligand of the tetrahedron is formed to a bridging S^{2-} anion located within the channel between a pair of opposite (in the *ab* plane) Fe^{3+} cations. Charge balance is maintained by oxidation of half of the octahedral Fe^{2+} to Fe^{3+} (see Table 1.7). Apuanite, the largest volume derivative of $FeSb_2O_4$, reverts back to tetragonal symmetry ($P4_2/mbc$) with the isotropic insertion of more sulphur within the *ab* plane (Figure 1.7c). Every third Sb^{3+} is now substituted for tetrahedral Fe^{3+} generating the formula $Fe_{20}Sb_{16}O_{48}S_4$: $(Fe_4^{2+}Fe_8^{3+})Fe_8^{3+}Sb_{16}^{3+}O_{48}S_4$. The same charge balance mechanism is seen where a higher proportion of oxidation is accommodated within the structure. Mössbauer spectroscopy

verified the Fe^{2+}:Fe^{3+} ratio [63]. These idealised chemical formulae differ slightly from the elemental composition first derived from the naturally occurring minerals where it was shown that minor components of zinc and arsenic coexisted on the A and B sites respectively [18, 64]. Versiliaite was shown to have a larger S^{2-} deficiency where closer structural analysis seemed to indicate an interleaving of schafarzikite and versiliaite (idealised composition) regions [64-65]. Furthermore, due to inconsistencies in bond lengths it was implied that small amounts of antimony had substituted tetrahedral Fe^{3+} to form bridging links of the form Sb^{3+}-S^{2-}-Fe^{3+} or Sb^{3+}-S^{2-}-Sb^{3+} [64].

Table 1.7 Structural details pertaining to the compounds versiliaite and apuanite [64].

	Versiliaite	Apuanite
Spacegroup	*Pbam*	$P4_2/mbc$
Lattice parameters:		
a	8.492(5)	8.372(5)
b	8.326(5)	
c	11.938(7)	17.97(1)
Bond length (Å)		
Fe^{2+}-O	2.07(1)	2.11(1) (x2)
	2.11(1)	2.11(1) (x4)
	2.14(1)	-
Fe^{3+}-O	1.96(1)	1.96(1)
	2.01(1)	2.02(1)
	2.05(1)	2.039(9)
	[64]	[64]

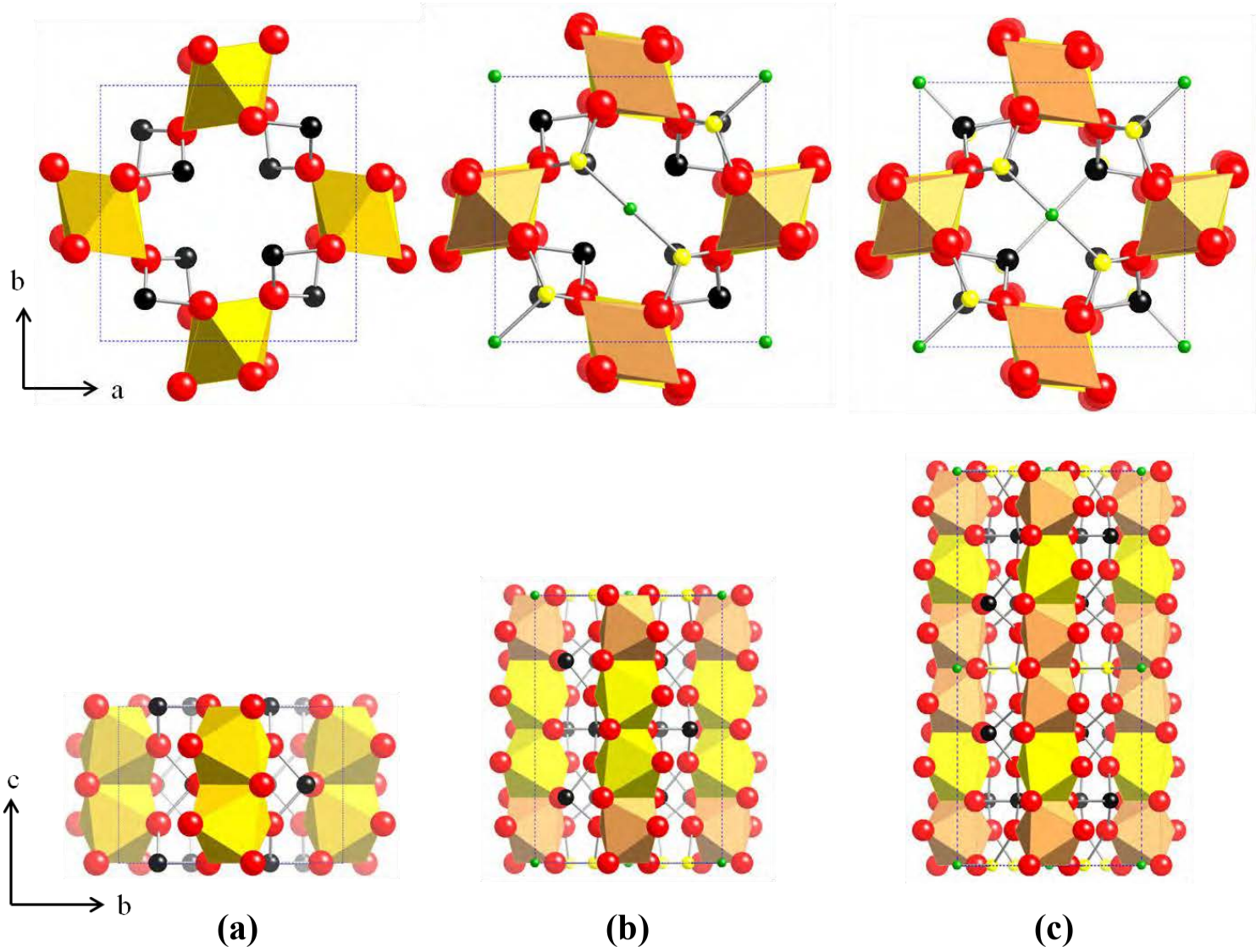

Figure 1.7 A schematic representation of the structures of: schafarzikite (a), orthorhombic versiliaite (b), and tetragonal apuanite (c). Oxygen (red spheres), Sb^{3+} (black spheres), B site Fe^{3+} (yellow spheres), and S^{2-} (green spheres) are indicated. The octahedra all contain iron; however, Fe^{2+} are found in the yellow octahedra and Fe^{3+} are located in the beige octahedra. Note the Fe^{3+} containing octahedra are directly connected to the B site Fe^{3+}.

1.9 Concluding Remarks

Schafarzikite related materials represent a relatively new area for scientific investigation of low dimensional properties. The existing details concerning the magnetic structures show a degree of variation and uncertainty, likely dependent on sample purity, whilst the main ordered components are concordant as are the highly sensitive underlying interactions.

1.10 Project aims

The aims of this thesis focus on the structural, magnetic and physical properties of new Co-related phases. Mixed $Co_{1-x}Fe_xSb_2O_4$ and $Co_{1-x}Fe_xSb_{2-y}Pb_yO_4$ phases are reported for the first time adding further to the knowledge of the limited mixed A site-containing species and demonstrating for the first time mixed A and B site schafarzikite-related compounds.

During this study attention was also given to the alkali metal MSbO$_2$ compounds (M = alkali metal) where it was of interest to investigate a possible structural link as seen in $MgSb_2O_4$ to $FeSb_2O_4$. Although details ware lacking for many variants (e.g. $LiSbO_2$) the reported structures are different from that of $FeSb_2O_4$. As a result this study has sought to structurally characterise and investigate the physical properties of $LiSbO_2$ relating it to the known MSbO$_2$ phases. More details of the alkali metal MSbO$_2$ phases are provided in Chapter 6.

1.11 References

[1] S. A. J. Kimber, J. P. Attfield, *J. Mater. Chem.* **17** (2007) 4885.
[2] P. Gambardella, M. Blanc, H. Brune, K. Kuhnke, K. Kern, *Phys. Rev.* **B 61** (2000) 2254.
[3] F. Y. Cheng, J. Chen, *J. Mater. Res.* **21** (2006) 2744.
[4] J. T. Hu, T. W. Odom, C. M. Lieber, *Accounts Chem. Res.* **32** (1999) 435.
[5] J. Rouxel, "*Crystal Chemistry and Properties of Materials with Quasi-One-Dimensional Structures*", D. Reidel Publishing Company, Dordrecht, Holland (1986).
[6] S. T. Gross, *J. Am. Chem. Soc.* **65** (1943) 1107.
[7] M. K. Fayek, J. Leciejewicz, *Z. Anorg. Allg. Chem.* **336** (1965) 104.
[8] S. Andersson, A. Åström, *National Bureau of standards special publication 364, Solid State Chemistry, proceedings of the 5th Materials Research Sympossium*, (1972).
[9] J. M. Babo, T. E. Albrecht-Schmitt, *J. Solid State Chem.* **187** (2012) 264.
[10] I. D. Brown, "*The Chemical Bonds in Inorganic Chemistry: The Bond Valence Method*", Oxford University Press, Oxford (2002).
[11] R. F. Takagi, D. T. Hjelmqvist, M. Johnsson, S. Lidin, *Solid State Sci.* **11** (2009) 13.
[12] C. Hirschle, C. Röhr, *Z. Anorg. Allg. Chem.* **626** (2000) 1305.
[13] I. Abrahams, D. Z. Demetriou, *J. Solid State Chem.* **149** (2000) 28.
[14] R. D. Shannon, *Acta Crystallogr.* **A 32** (1976) 751.
[15] A. Kyono, M. Kimata, M. Matsuhisa, Y. Miyashita, K. Okamoto, *Phys. Chem. Miner.* **29** (2002) 254.
[16] J. R. Gavarri, D. Weigel, *J. Solid State Chem.* **13** (1975) 252.
[17] S. Bahfenne, L. Rintoul, R. L. Frost, *Am. Miner.* **96** (2011) 888.
[18] M. Mellini, S. Merlino, P. Orlandi, *Am. Miner.* **64** (1979) 1230.
[19] H. G. Dill, T. Weiser, I. R. Bernhardt, C. R. Kilibarda, *Econ. Geol. Bull. Soc. Econ. Geol.* **90** (1995) 51.
[20] S. Ståhl, *Arkiv för Kemi, Min. och Geol.* **B 17** (1943) 1.
[21] R. Fischer, F. Pertlik, *Tschermaks Min. Petr. Mitt.* **22** (1975) 236.
[22] H. Fjellvåg, A. Kjekshus, *Acta Chem. Scand.* **A 39** (1985) 389.
[23] J. R. Gavarri, R. Chater, J. Ziolkowski, *J. Solid State Chem.* **73** (1988) 305.
[24] E. Koyama, I. Nakai, K. Nagashima, *Nippon Kagaku Kaishi* **6** (1979) 793.
[25] G. Tammann, *Z. Anorg. Allg. Chem.* **149** (1925) 21.
[26] C. Giroux-Maraine, G. Perez, *Rev. Chim. Minerale* **12** (1975) 427.
[27] J. R. Gavarri, *C. R. Acad. Sc. Serie II* **t. 292** (1981) 895.
[28] R. Chater, J. R. Gavarri, A. Hewat, *J. Solid State Chem.* **60** (1985) 78.
[29] J. R. Gavarri, *J. Solid State Chem.* **43** (1982) 12.
[30] N. Kumada, Y. Yonesaki, T. Takei, N. Kinomura, S. Wada, *Mater. Res. Bull.* **44** (2009) 1298.
[31] F. Pertlik, *Z. Anorg. Allg. Chem.* **436** (1977) 201.
[32] H. T. Witteveen, *Solid State Commun.* **9** (1971) 1313.
[33] N. Bettahar, P. Conflant, F. Abraham, D. Thomas, *J. Solid State Chem.* **67** (1987) 85.
[34] S. Ghose, P. K. Sengupta, E. O. Schlemper, *Am. Miner.* **72** (1987) 629.
[35] J. W. Menary, *Acta Crystallogr.* **11** (1958) 742.
[36] F. Emmerling, C. Röhr, *Z. Naturforsch.* **B 58** (2003) 620.
[37] C. Lee, W. T. A. Harrison, *Acta Crystallogr.* **C 60** (2004) m215.
[38] M. J. Whitaker, R. D. Bayliss, F. J. Berry, C. Greaves, *J. Mater. Chem.* **21** (2011) 14523.

[39] E. G. Puebla, E. G. Rios, A. Monge, I. Rasines, *Acta Crystallogr.* **B 38** (1982) 2020.
[40] J. R. Gavarri, J. P. Vigouroux, G. Calvarin, A. W. Hewat, *J. Solid State Chem.* **36** (1981) 81.
[41] R. Chater, J. R. Gavarri, *J. Solid State Chem.* **59** (1985) 123.
[42] R. Chater, J. R. Gavarri, F. Genet, *J. Solid State Chem.* **63** (1986) 295.
[43] M. J. Whitaker, *Personal Communication* (2012).
[44] A. M. Abakumov, M. G. Rozova, E. V. Antipov, J. Hadermann, G. Van Tendeloo, M. V. Lobanov, M. Greenblatt, M. Croft, E. V. Tsiper, A. Llobet, K. A. Lokshin, Y. S. Zhao, *Chem. Mater.* **17** (2005) 1123.
[45] H. Abe, K. Yoshii, H. Kitazawa, *Phys. Status Solidi* **A 189** (2002) 429.
[46] B. Y. Brach, N. V. Chezhina, Y. V. Shapoval, *Inorg. Mater.* **25** (1989) 601.
[47] D. J. Craik, "*Magnetic Oxides: Part 1*", John Wiley and Sons, London (1975).
[48] J. B. Goodenough, *Phys. Rev.* **100** (1955) 564.
[49] J. Kanamori, *J. Phys. Chem. Solids* **10** (1959) 87.
[50] J. B. Goodenough, *Phys. Rev.* **117** (1960) 1442.
[51] C. N. R. Rao, B. Raveau, "*Transition Metal Oxides*", VCH publishers Inc., New York (1995).
[52] J. A. Gonzalo, D. E. Cox, G. Shirane, *Phys. Rev.* **147** (1966) 415.
[53] J. R. Gavarri, A. W. Hewat, *J. Solid State Chem.* **49** (1983) 14.
[54] J. R. Gavarri, G. Calvarin, B. Chardon, *J. Solid State Chem.* **47** (1983) 132.
[55] K. H. J. Buschow, "*Handbook of Magnetic Materials*", Elsevier Science B. V., Amsterdam (1995).
[56] B. C. Frazer, P. J. Brown, *Phys. Rev.* **125** (1962) 1283.
[57] K. Motida, S. Miyahara, *J. Phys. Soc. Japan* **28** (1970) 1188.
[58] D. J. Dunlop, Ö. Özdemir, "*Rock Magnetism: Fundamentals and Frontiers*", Cambridge University Press, Cambridge (1997).
[59] G. Gorodetsky, M. Sayar, S. Shtrikman, *Mat. Res. Bull.* **5** (1970) 253.
[60] R. Chater, K. Chhor, J. R. Gavarri, C. Pommier, *Mat. Res. Bull.* **20** (1985) 1427.
[61] A. K. Jibin, M. V. Reddy, G. V. Subba Rao, U. V. Varadaraju, B. V. R. Chowdari, *Electrochim. Acta* **71** (2012) 227.
[62] M. Mellini, S. Merlino, C. S. Geologia, *Acta Crystallogr.* **A 34** (1978) S184.
[63] R. Bayliss, F. J. Berry, A. Bowden, C. Greaves, M. F. Thomas, *International Conference on the Applications of the Mossbauer Effect*, *Journal of Physics: Conference Series* **217** (2010) 012049.
[64] M. Mellini, S. Merlino, *Am. Miner.* **64** (1979) 1235.
[65] M. Mellini, M. Amouric, A. Baronnet, G. Mercuriot, *Am. Miner.* **66** (1981) 1073.

Chapter 2

Experimental techniques

2.1 Solid state synthesis

2.1.1 The ceramic method

The ceramic method is the most common and readily available synthesis technique accessible to the materials chemist. The principle involves heating reagent mixtures to form desired products at the interfaces of grain boundaries. Homogeneity along with particle size are imperative and several methods of achieving intimate mixing can be used, e.g. mortar and pestle or ball milling. The aim is to achieve an even distribution of reagents and particles by grinding the reactants together. In order to synthesise a new compound, elements must leave their host lattice and migrate to the grain boundary. This process usually requires substantial amounts of energy and so heat is applied to facilitate this migration, resulting in most solid state reactions taking place at high temperatures [1]. As the product crystallites form and increase in volume, diffusion of reagents across this region becomes increasingly inhibited and so it is usual to apply intermittent grinding to redistribute reagents evenly and achieve a purer product.

This work has used variations of the ceramic method. Reagents, where possible, were dried under dynamic vacuum ($x10^{-3}$ mbar) at 300˚C for a minimum of 1 hour prior to use. Intimately ground reaction mixtures were heated in evacuated (< $x10^{-6}$ mbar) fused silica tubes at temperatures between 400-1000˚C. The length and temperature of heat treatments

were determined from empirical observation. Intermittent grinding of all samples was used to improve sample homogeneity.

2.1.2 Hydrothermal synthesis

This technique, used infrequently throughout this study, involves placing a reaction mixture into an aqueous medium contained within a pressure vessel and heating the mixture at low temperatures (*ca* 200˚C) for extended periods of time generating autogenous pressure. This procedure was investigated for suitability in the synthesis of $CoSb_2O_4$ (*see Chapter 3*); a 0.75g reaction mixture of CoO and Sb_2O_3 was heated in a solution of 10 % NaOH for a period of 7 days at 250˚C in a Parr 4746 hydrothermal bomb.

2.2 Powder diffraction techniques

All samples were examined by a mixture of X-ray powder diffraction (XRPD) and neutron powder diffraction (NPD) techniques as a means of characterising the nuclear and magnetic structures of the products synthesised. When atoms arrange themselves within a crystalline solid, parallel layers, or planes, of atoms separated by a repeating set distance (*d*-space, d_{hkl}) result. The way in which the atoms arrange themselves gives rise to seven different crystal systems upon which all structures are based, these reflect geometrical differences between unit cells. When radiation of a comparable wavelength to the *d*-space is used to interrogate a crystalline material peaks, known as Bragg peaks, of varying intensity and position (in ˚2θ) result which creates a diffraction pattern. These can be characterised by a set of *hkl* values (Miller indices) which are related to the structure the compound adopts. Bragg peaks are produced by coherent scattering of the incident radiation and their observed position is linked to the wavelength of the investigative medium through the well known Bragg equation [2]. The background of a powder pattern is formed mainly from the

incoherent scattering of the compound although the atmosphere between radiation source and detector, sample container and fluorescence are other well known contributing factors.

The d_{hkl} values for a powder pattern can be used to gain information about the type of crystal system produced, sample purity and the lattice parameters of the phase. This was done through use of the indexing program DICVOL [3] and used in conjunction with the program DSPACE [4] which is able to generate all allowed reflections for a crystal system when the lattice parameters and space group are known.

2.2.1 X-ray powder diffraction

XRPD is one of the most commonly used techniques by the inorganic chemist to investigate sample purity and the structure a phase adopts. All samples reported in this thesis have been examined using a Bruker D8 auto-sampler in transmission (Debye-Scherrer) geometry at 300 K. When refinable data for structural analysis were obtained, an absorption correction was always simultaneously collected and applied. A D8 diffractometer in reflection (Bragg-Brentano) geometry with a fitted MRI heating stage was used for variable temperature X-ray powder diffraction (VT-XRPD) studies of all applicable Co containing phases. In both instances monochromatic X-rays (Cu $K_{\alpha1}$, λ = 1.5406 Å) were selected with a Ge-Crystal monochromator and scattered X-rays were detected with a one dimensional position sensitive detector (PSD), lynx-eye. A Siemens D5005 diffractometer, reflection geometry (Cu $K_{\alpha1}$ λ = 1.5418 Å, Braun PSD, with an Anton-Parr heating stage) was used in the variable temperature study of $LiSbO_2$ (*see Chapter 6*). These data were electronically stripped of the $K_{\alpha2}$ radiation.

X-rays are produced when high energy electrons, originating from a metal filament usually tungsten, are accelerated through a potential (typically 30-40 kV, to provide optimised

intensity) onto a metal anode (the target) ejecting electrons from an atomic nuclear shell, denoted K, L, M, N (n = 1, 2, 3, 4). The emitted photons give sharp intensities at discrete wavelengths superimposed onto a background of (white, Bremsstrahlung) radiation [2]. A Cu target was used throughout this work as it produces X-rays with a wavelength comparable to the inter-planar distance (*ca* 1 Å) of atoms within a crystalline solid; however, other targets are available which produce different wavelengths of radiation (e.g. K_α: Cr = 2.29 Å, Co = 1.79 Å [5], Mo = 0.71069 Å [1]). White radiation is produced when accelerated electrons collide with the target atoms resulting in a modification of the electrons energy (inelastic scattering) but does not result in the ejection of a core electron. When a collision results in the ejection of a core electron a vacancy is generated which is then filled by an electron from a higher energy level which undergoes a relaxation process. This results in the emission of an X-ray (Figure 2.1). The characteristic wavelength (λ) of the ejected X-ray (hence energy ($E = h\nu = hc/\lambda$ [6] where h is Planck's constant, ν the frequency and c is the speed of light) is determined by the shell and orbital from which the relaxing electron originated. Generally this occurs from the next highest shell (Figure 2.1) e.g. L→K [1].

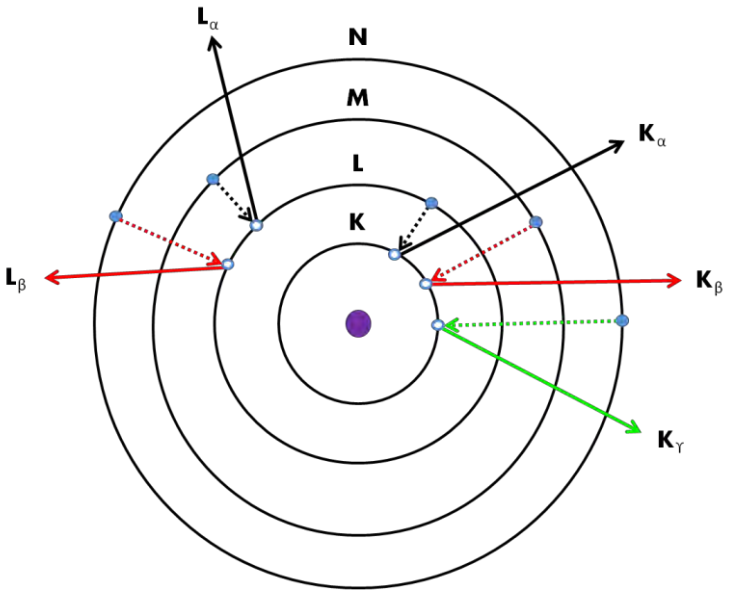

Figure 2.1 Some of the possible relaxation processes of an electron (solid circle) can undertake (dotted lines) into a hole (hollow circle) emitting a photon of light (solid lines).

X-rays are scattered by the electrons surrounding an atom where scattering increases with atomic number (Z); this, from a simplified atomistic point of view determines the observed peak intensities in a powder pattern. Due to the diffuse nature of the electron clouds it is difficult to locate lighter elements with a conventional laboratory X-ray source accurately, especially when a sample contains much heavier elements e.g. Pb. This has a tendency to result in a powder pattern dominated by the heavier elements providing less reliable information about the poor scattering species e.g. O. When considering the scattering provided by a crystalline solid however, the situation increases in complexity and peak intensities (I_{hkl}) are found to depend on other contributory factors (Equation 2.1) [1]:

$$I_{hkl} = sLpF_{hkl}^{2} \qquad (2.1)$$

where s is the scale factor, L the Lorentz correction and p the polarization correction. It is found that peak intensities drop off with increasing angle ($^{\circ}2\theta$), a process which is described by a scattering factor and is dependent on the relationship (sin θ)/λ where θ is the Bragg

angle. It is based on the drop off of electron density extending from the nucleus resulting in a loss of information at high angle [7]. Crucial to Equation 2.1 is the structure factor (F_{hkl}) which collates this information with the elemental composition and structure type (Equation 2.2) so that the intensity of any given peak within a powder pattern can be estimated to a good approximation using the relationship $I_{hkl} = |F_{hkl}|^2$:

$$F_{hkl} = \sum_j N_j f_j \exp[2\pi i(hx_j + ky_j + lz_j)] \exp\left[\frac{-8\pi^2 \overline{\mu_j^2}\left(\sin^2\theta\right)}{\lambda^2}\right] \text{[8]} \qquad (2.2)$$

where f_j is the scattering factor, N_j the site multiplicity, x_j, y_j, z_j are the fractional coordinates for atom j in a plane described by hkl, $\overline{u_j^2}$ is the mean-square thermal displacement of atom j, $i = \sqrt{-1}$ and λ is the wavelength of radiation. When the terms of the exponential factors are combined they describe the thermal motion of atoms in a crystal and the effect this has on coherent scattering. When combined for every reflection the total scattering for a given unit cell is obtained [8].

2.2.2 Neutron Powder diffraction

Neutron powder diffraction experiments were carried out on the high resolution powder diffractometer at the Institut Laue Langevin (ILL, D2B) and the Paul Scherrer Institute (PSI Zurich, SINQ - HRPT beam line). These distinctly different national facilities reflect the 2 commonly used methods of obtaining neutrons for constant wavelength diffraction. The ILL, uses the fission products from the decay of enriched ^{235}U, to produce a continuous stream of neutrons 1.5 x10^{15} neutrons/cm^2/s [9-10] (Equation 2.3) where $n_{thermal}$ (*ca* 1 meV) and n_{fast} (*ca* 1MeV) are distinguished by their relative energies. The D2B diffractometer has two modes of data analysis; the first is an electronic manipulation of the

full detected beam which enables a reduction in the Lorentzian character of low angle peaks (*ca.* 0 - 20 ˚2θ) this shall be termed high resolution (HR) data (*ca.* $\Delta d/d = 5x10^{-4}$) and leads to a reduction in the observed intensity for the whole powder pattern. The second mode uses the whole detected beam intensity which has a lower resolution (*ca.* $\Delta d/d \approx 2x10^{-3}$) but better counting statistics, and shall be discussed as high intensity (HI) data. Utilisation of both data extraction methods are discussed later (*see Chapters 3 and 4*).

$$n_{thermal} + {}^{235}U \rightarrow 2\text{fission fragments} + 2.5n_{fast} \quad [10] \qquad (2.3)$$

PSI is a spallation neutron source which produces the world's only constant wavelength neutrons from this type of generator and has a flux density of around 10^{14} neutrons/cm^2/s. An analogous data manipulation is possible with resolution in the order of $\Delta d/d = < 1\ x10^{-3}$ (HR), and $< 2\ x10^{-3}$ (HI) [11-12] however only the full intensity data sets were interpreted from this source. Spallation neutrons are produced when protons are accelerated to high velocity and focused onto a heavy metal target, in this case Pb, where they penetrate into the metal and collide with the Pb nuclei resulting in their excitation. As the nuclei relax they emit high energy neutrons, about 10 for every proton from this source [13]. As in the ILL, a flux of high energy neutrons results after generation and a moderator is used (either H_2O or D_2O) which reduces the energy of the neutrons modifying the λ to within a useful range. A monochromator is then used to select the desired λ of neutrons; planes (*hkl*) are generally selected to give the highest intensity [10]. The experimental set up used for data acquisition from each source is shown in Table 2.1.

Table 2.1 A comparison of details for the ILL D2B beam line [14] and SINQ HRPT beam line [11-12, 15]. The environments that measurements were taken in are listed.

	Neutron source	
	ILL - D2B	PSI - HRPT
Wavelength (Å)	1.594	1.886
Temperature of data acquisition (K)	300 and 4	300, 2 and 1.5
Detector type	PSD ^{3}He	PSD (^{3}He/CF_4)
Detector range/ step size	128, 300 mm long wires, move 25 steps of 0.05˚ through an arc of 5˚–165˚	1600 wires of angular separation 0.1˚ able to scan an arc between 0 –160˚
Monochromator	Ge (335)	Ge (511)
Cryogen used	He gas flow cryostat	He cryostat
Sample container	8mm V can	8mm V can
Geometry	Debye-Scherrer	Debye-Scherrer
Flux density with resolution mode (neutrons/cm^2/s)	10^6 at high resolution, 10^7 at high intensity.	$2.5x10^4$ at high resolution, $2.5x10^5$ at high intensity

2.2.2.1 Nuclear scattering of neutrons

Neutrons, unlike X-rays, can be diffracted by both the nucleus and unpaired electrons (giving rise to magnetic scattering from a neutrons spin +½; $\mu = -9.649x10^{-27}$ JT^{-1} [10]) of an atom giving rise to coherent and incoherent scattering. Scattering intensity for the nuclear component, the dominant contributor, is found to be largely independent of *Z* unlike X-rays which varies according to atomic number. Furthermore a drop off of scattering intensity as a function of ($\sin\theta/\lambda$) is not observed in NPD due to the small isotropic dimensions of the nucleus when compared with X-ray scattering which occurs from the electron cloud. This presents a distinct advantage when used in conjunction with X-ray diffraction in that the discrepancy between heavy and light scatterers can be reduced so that a powder pattern is not dominated by the heavier elements as seen in XRPD. Furthermore peak intensities do not drop off with 2θ. The measure of an atoms ability to diffract neutrons, in analogy to an X-ray scattering factor, is given by the scattering length (*b*) which is dependent on the isotope and nuclear spin value for a given element. Coherent scattering is seen for atoms with a positive

value of b which corresponds to a 180° phase change of the incident radiation upon diffraction. It is noted that all values assigned to b in data analysis herein used the average scattering length which takes into account isotopic abundance and nuclear spin [16]. Scattering length contributes to the observed peak intensity in a similar way to X-rays through a structure factor and a given reflection by the relationship [16]:

$$F_{hkl}^2 = \left| \sum_1^n b \exp[2\pi i(\frac{hx}{a} + \frac{ky}{b} + \frac{lz}{c})] \right|^2 \exp^{-2w} \tag{2.4}$$

where b is the scattering length, a, b, c are the lattice constants, hkl the Miller indices and x, y, z represent the fractional coordinates for a given atom n. The exponential term represents a loss of coherent scattering due to the thermal motion of atoms (w) within a crystalline solid in analogy to that used in the structure factor equation for X-rays, refer to Equation 2.2 [16].

2.2.2.2 Magnetic scattering of neutrons

Neutrons, as already mentioned, can be diffracted by the magnetic field generated by an unpaired electrons spin and where relevant orbital momentum. In magnetically ordered systems the scattering length b is replaced by the magnetic scattering amplitude (p, Equation 2.5), which varies with valence state, and has the form [16]:

$$p = \left(\frac{e^2 \gamma}{2mc^2} \right) 2Sf \tag{2.5}$$

$$|q| = \sin \alpha \tag{2.6}$$

where (e^2/mc^2) is the radius of an electron, S is the total spin of the atom, f the form factor for the magnetic ion and γ the magnetic moment of a neutron. The magnetic form factor has a

similar dependence on 2θ as X-ray scattering; however, the unpaired electrons used in magnetic diffraction are fewer and more diffuse so that magnetic peaks are seen to decrease in intensity over a shorter 2θ range. The value of q (Equation 2.6) the so called "magnetic interaction vector" relates the spin vector of an atoms unpaired electrons to the diffraction plane by the angle α and enables the determination of moments direction in the ordered systems. At temperatures above the magnetically ordered state magnetic diffraction still occurs however the random alignment of spins contribute to the background through incoherent scattering. The total scattering amplitude is given by the sum of the squares of the nuclear and magnetic scattering contributions in the following form [16]:

$$\left|F_{hkl}\right|^2 = \left|\sum_n b_n \exp\left\{2\pi i\left(\frac{hx_n}{a}+\frac{ky_n}{b}+\frac{lz_n}{c}\right)\right\}\right|^2 + \left|\sum_n \mathrm{q}_n p_n \exp\left\{2\pi i\left(\frac{hx_n}{a}+\frac{ky_n}{b}+\frac{lz_n}{c}\right)\right\}\right|^2 \quad (2.7)$$

Equation 2.7 has neglected the Debye-Waller factor (isotropic temperature displacement) associated with both the nuclear and magnetic structure factors, this can be seen more clearly in Equation 2.4 and has been excluded to demonstrate that coherent magnetic and nuclear scattering are independent [16].

2.3 Rietveld refinement

Rietveld refinement [17-18] is a highly valuable methodology for refining structures based on diffraction data. There are several programs which are commonly used to refine structures notably Topas and Fullprof. However, all refinements reported within this thesis are based upon using GSAS [19] with the aid of the EXPGUI [20] graphical user interface.

The method is based upon the minimisation of the difference, known as the residual (S_y, Equation 2.8), between a simulated powder pattern and an empirically observed data set made up of counts (y_i) for a given step (i) [21]:

$$S_y = \sum_i w_i \left(y_i(obs) - y_i(calc)\right)^2 \tag{2.8}$$

where $y_i(obs)$ is the observed intensity, $y_i(calc)$ is the calculated intensity and w_i is the weight for point i [8]. The empirically observed powder pattern can be broken into two components; the peak positions, which encompasses intensities, and secondly the peak shape or profile. Peak positions are dependent upon the unit cell size and symmetry of a given phase whilst the profile is contributed to by both instrumental effects e.g. radiation source, geometry and intrinsic sample features e.g. crystallite size/strain broadening. Consequently, the fundamental difference and set up between radiation sources can have a pronounced effect on the obtained profile shape of a powder pattern; equally differences in sample characteristics can play a more dominant role. Structural determinations throughout this work have accounted for these factors by altering the profile functions and parameters used which are able to model more accurately sample effects (e.g. Pseudo-Voigt) or instrumental effects (e.g. Finger-Cox-Jephcoat). To minimize the residual, parameters which influence both the structure and profile must be adequately modelled [21]. The calculated powder pattern which accounts for these major contributing factors is given by Equation 2.9 [8]:

$$y_{ci} = s\sum_{hkl} L_{hkl} |F_{hkl}|^2 \phi(2\theta_i - 2\theta_{hkl}) P_{hkl} A + y_{bi} \tag{2.9}$$

where s is the scale factor, (hkl) miller indices, F_{hkl} structure factor, ϕ reflection profile function, P_{hkl} preferred orientation function, A absorption factor and y_{bi} represents the back ground intensity at step i. L_{hkl} contains the Lorentz, polarization and multiplicity factors [8]

and it is imperative that a good starting model is first defined in order to prevent reaching a false minimum [21]. The Shifted Chebyschev profile function was largely used to model the background intensity (*ca* 15 terms).

Statistical indicators are used, in conjunction with the profile fit, as a guide to help determine if iterations made to the structural model result in convergence or divergence of y_{ci} from the raw data. Perhaps the most useful of these are the indicators R_{exp} (Equation 2.10) and R_{wp} (Equation 2.11) where N is the number of observables and P the number of parameters:

$$R_{exp} = \left(\frac{(N-P)}{\sum_{i}^{N} w_i y_i(obs)^2} \right)^{1/2} \tag{2.10}$$

$$R_{wp} = \left(\frac{\sum_{i}^{N} w_i [y_i(obs) - y_i(calc)]^2}{\sum_{i}^{N} w_i [y_i(obs)]^2} \right)^{1/2} \tag{2.11}$$

$$\chi^2 = \left(\frac{R_{wp}}{R_{exp}} \right)^2 \tag{2.12}$$

When combined (Equation 2.12) they can provide a measure of the applied models "goodness of fit" to the raw data indicated by the well known figure χ^2 which reflects attempts in the refinement procedure to match the calculated model to the observed data [8, 21].

There are many strategies available for the refinement of magnetic structures. The assignment of "colour" operators to a magnetic moment is vital in the determination of a

magnetic structure based on the crystal unit cell. The "black" operator is used to assign symmetry to a moment vector, whilst "red" operators apply the same symmetry but with a spin inversion [22]. The method used to determine the magnetic structures within this thesis has treated the magnetic and nuclear phases separately without the assignment of a magnetic spacegroup. The magnetic structures were refined in *P*1 which enabled the identification of magnetic modes and moment magnitudes without symmetry constraint. This is in contrast to another possible strategy which combines the nuclear and magnetic structures into a single phase enabling the assignment of a magnetic spacegroup to the structure. Whilst the basic structures have been accurately determined more detailed studies could be completed to determine the magnetic symmetry of the systems. However, for issues highlighted by Gonzalo *et al* [23] the current resolution of neutron powder diffractometers is such that they are unable to provide conclusive evidence required to support the suggestion of an orthorhombic magnetic spacegroup.

2.4 DC magnetic susceptibility measurements

DC magnetic susceptibility measurements were made on a Quantum Design, materials properties measurement system (MPMS) XL. The instrument uses a superconducting quantum interference device (SQUID) to monitor changes in the applied magnetic field. When a sample containing an intrinsic magnetic moment passes though the magnetic flux the applied field is modified and a change in the output voltage results which is then converted into a value (emu) used to calculate the magnetic moment of the sample [24].

All samples (≈ 50 mg each, powder) used in this technique were contained in nonmagnetic capsules and compressed with PTFE tape to suppress sample movement whilst measurements were taken upon heating. Samples were centred in fields (typically 100 Oe)

amenable to sample detection prior to measurement where subsequent zero field cooled (ZFC), field cooled (FC) (typically 100 Oe applied field) and hysteresis type measurements (-50 000 Oe to 50 000 Oe) were acquired. ZFC/FC measurements were generally made under temperature sweep conditions i.e. the temperature continuously increased at a rate of 5 K/min and measurements were taken at designated intervals, typically every 5 K. In certain instances it was necessary to acquire more accurate results e.g. in isolating the magnetic transition point, this was achieved using temperature settle conditions. This is where the temperature increases in incremental steps, typically 2 K, and measurements are made once the temperature is settled at a constant value. Details of the method used for data acquisition are given in the results chapters.

2.5 Raman spectroscopy

All Raman spectra reported were collected on a Renishaw inVia Raman microscope fitted with a 600 cm^{-1} filter, using a red RL633 HeNe laser. Samples were analysed in powder and sintered pellet form, where powder sample surfaces were flattened normal to the incident beam prior to measurement. Spectra were optimised through variation of the scan time and laser powers used.

Raman is a spectroscopic technique which uses the collision of a photon ($2.5 \leq \lambda \leq 1000$ μm) with a substrate to resulting in a change of the polarizability of the bonds; hence, modifying the energy of the detected photon [25]. Two types of process determine the energy of the emitted photon; the photon can be scattered elastically, also known as Rayleigh scattering, a process where a photons energy is conserved upon scattering. The second form which gives rise to Raman scattering more specifically Stokes and Anti-Stokes (Figure 2.2) lines, relies upon inelastic scattering. A photon-molecule collisions results in an excitation of

the molecule to a higher energy virtual state from the ground state $V = 0$ (where V is the potential energy). Stokes lines are the result of a scattered photon having less energy post collision and so a lower frequency. These form the more dominant signal in the Raman spectrum. Anti-Stokes lines are the result of scattered photons having more energy than the incident photon and so a higher frequency [25]. This information has been used to indicate the presence of and change to key structural components [25].

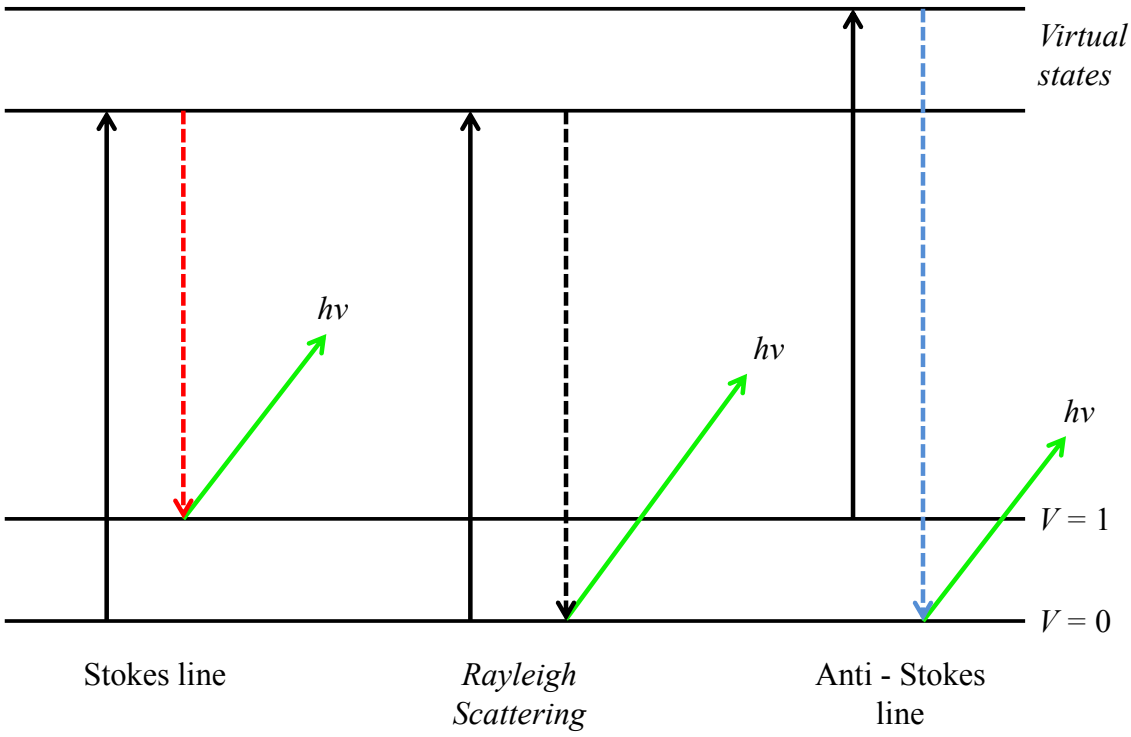

Figure 2.2 A diagram displaying the possible excitation processes observed in Raman spectroscopy. Solid black lines show the excitation of the molecular fragment from the ground state to an excited virtual state. The broken lines show the relaxation process resulting in the emission of a photon (green solid lines) with modified energy.

2.6 AC impedance spectroscopy

AC impedance measurements were made on a Solartron SI 1260 impedance/gain-phase analyser within the frequency range 1 Hz – 1 MHz. A portion of synthesised $LiSbO_2$ (investigated by NPD, *see Chapter 6*) was pressed into a pellet using an 8mm die with 1 tonne of applied force and sintered at 550˚C for 24 hrs. A dummy pellet (made from the same stock sample) was synthesised in parallel to the main pellet in order to validate that the main

structure was retained during preparation. The pressed pellets were sintered in a silver tube with the ends crimped shut within an evacuated fused silica tube. The large circular faces of the pellets were coated with Ag-electrodag (Agar Scientific) and allowed to dry in air over night before measurements were made using the spring tensioned set up shown in Figure 2.3. Thermal stability was ensured before measurement acquisition and variable temperature impedance measurements were taken within the thermally stable region of the main phase. Sample aliquots were taken post measurement for phase monitoring purposes.

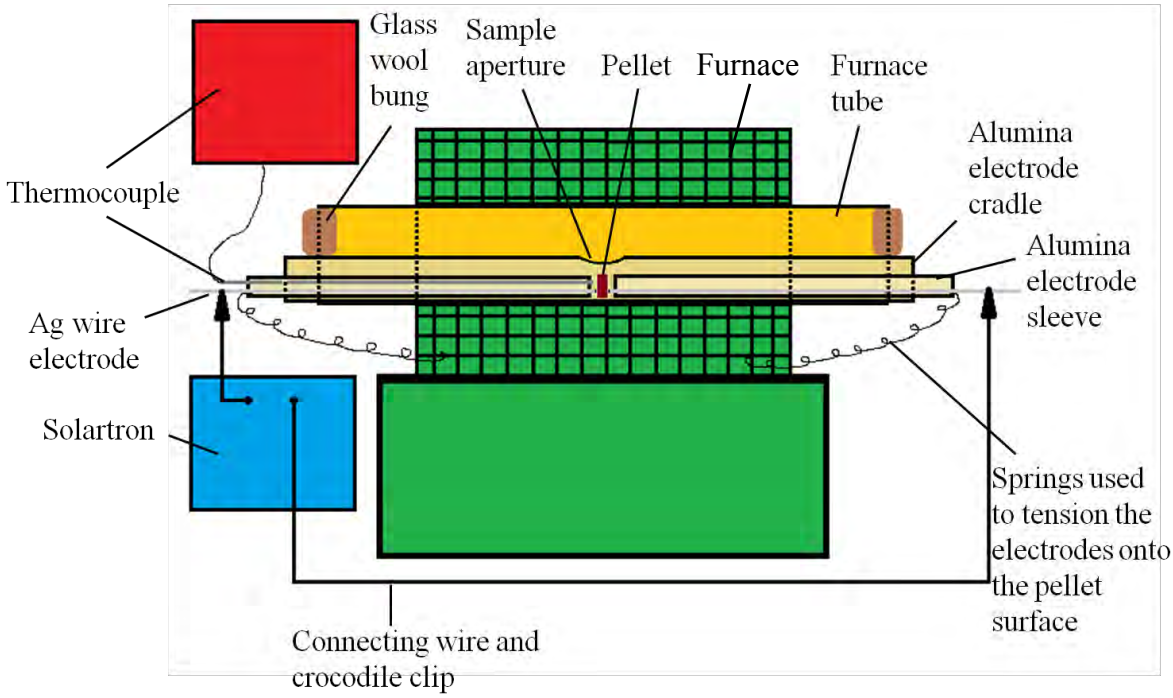

Figure 2.3 A schematic diagram of the spring tensioned set up used to acquire AC impedance measurements of $LiSbO_2$.

This technique is based upon the application of a time dependent potential, i.e. an AC voltage, across a sample resulting in the charge carrier species migrating towards its complimentary pole, generating a current. As the frequency is changed (sweep mode, applied frequency range of 1 MHz - 1 Hz) the charge carriers movement mirrors the frequencies sinusoidal form where there is a phase shift or lag between the voltage being applied and the current flowing. The phase shift is described by the phase angle (θ) if the sample does not

behave as a perfect resistor. The impedance (z) is defined as the ratio between the applied voltage and the current flowing:

$$z = \frac{\Delta E \sin \omega t}{\Delta i \sin(\omega t + \theta)} \text{ [26]} \qquad (2.13)$$

where ω is equal to $2\pi f$, f is the frequency in Hz, and t is the time. Impedance, a vector quantity, is defined as a complex number and the impedance is plotted as the real (z') against imaginary components (jz''). This enables both the capacitance and resistance values of the system to be calculated. The magnitude of these components relates the crystal morphology to the physical properties of the system by the so called "brick work model" [27] and can be used as a rough basis in identifying which component is being analysed e.g. capacitance values for a bulk component would be expected to be in the region of 10^{-12} F [27]. It is usual in the reported systems however that deconvolution of the bulk (Bu) and grain boundary (GB) components was not easily achieved and so values of the total conductivity are reported (i.e. GB + Bu). The resistive and capacitive components can be modelled using equivalent circuits and the typical response expected in the impedance plot for a resistor and capacitor in parallel is a semicircle [26, 28]. Extraction of the low frequency resistance values enabled the conversion to conductivity (σ). From this the activation energy (E_a) for ion migration could be calculated using the Arrhenius type formula:

$$\ln(\sigma) = \frac{-E_a}{R} \times \frac{1}{T} + \ln \sigma_0 \equiv \log(\sigma) = \frac{-E_a}{2.303R} \times \frac{1}{T} + \log \sigma_0 \qquad (2.14)$$

where σ_0 is a constant and R is the gas constant.

2.7 Thermogravimetric analysis (TGA)

Thermogravimetric and differential thermal analysis (DTA) has been used within this thesis to determine the thermal stability of the synthesised compounds and to identify any possible transient intermediate phases. All measurements were carried out on a Netzsch Sta 449 F1 analyser within the temperature region 30-1000˚C. Dynamic measurements were acquired from samples (*ca* 50 mg) under oxidising and reducing atmospheres (N_2, O_2, and N_2/10% H_2) at a heating and cooling rate 10˚C min^{-1}. A calibration for buoyancy effects (determined in an atmosphere of N_2, the protective gas) and sensitivity were applied for all measurements.

2.8 Scanning electron microscopy (SEM)

SEM has been used to identify crystal morphology of the compounds synthesised relating this to morphological phenomena e.g. preferred orientation effects in XRPD. All images were collected on a JEOL 6060 microscope fitted with an Oxford instruments Inca 300 EDS system. Thin layers of powdered sample and small sintered masses were bound to a conductive sample puck and coated with a conductive layer of carbon or gold subject to the analysis performed and conductivity of the sample. Secondary electron imaging (SEI) and back scattered electron imaging (BSEI) were used mainly to image the crystal morphology but were also used to investigate sample purity [29].

2.9 Mössbauer spectroscopy

The ^{57}Fe Mössbauer spectrum of $Co_{0.50}Fe_{0.50}Sb_{1.50}Pb_{0.50}O_4$ was recorded at 300 K in constant acceleration mode. A 25 mCi ^{57}Co/Rh source was used. All data were computer fitted and chemical isomer shifts were quoted relative to Fe at room temperature. All Mössbauer data were collected and interpreted by Professor Frank Berry.

2.10 References

[1] A. K. Cheetham, P. Day, "*Solid State Chemistry: Techniques* ", Oxford University Press, Bury St Edmunds (1995).

[2] E. W. Nuffield, "*X-Ray Diffracion Methods*", John Wiley and sons, INC, New York; London (1966).

[3] A. Boultif, D. Louer, *J. Appl. Crystallogr.* **37** (2004) 724.

[4] C. Greaves, *DSPACE*, University of Birmingham (1982).

[5] J. P. Eberhart, "*Structural and Chemical Analysis of Materials: X-ray, electron and neutron diffraction. X-ray, electron and ion spectroscopy. Electron microscopy.*", John Whiley and Sons, Chichester (1991).

[6] P. Atkins, J. de Paula, "*Elements of Physical Chemistry*", fourth ed, Oxford University Press, Oxford (2005).

[7] R. E. Dinnebier, J. L. Billinge, "*Powder Diffraction: Theory and Practice*", RSC Publishing, Cambridge (2009).

[8] R. A. Young, "*The Rietveld Method*", Oxford University Press, New York (2002).

[9] http://www.ill.eu.

[10] A. J. Dianoux, G. Lander, "*Neutron data Booklet*", Old City Publishing, Philadelphia (2003).

[11] http://sinq.web.psi.ch/sinq/instr/hrpt/index.html (2012); V. Pomjakushin.

[12] P. Fischer, G. Frey, M. Koch, M. Konnecke, V. Pomjakushin, J. Schefer, R. Thut, N. Schlumpf, R. Burge, U. Greuter, S. Bondt, E. Berruyer, *Physica* **B 276** (2000) 146.

[13] S. Janssen, B. Gerber, "*Neutrons for research: The Spallation Neutron Source SINQ at the Paul Scherrer Institute"* in: PSI, (Ed.), Paul Scherrer Institute, Villigen, 2009.

[14] G. Cicognani, "*The Yellow Book: Guide to Neutron Research Facilities*", Institut Laue-Langevin, Greonble (2008).

[15] http://sinq.web.psi.ch/sinq/instr/img/hrpt_essentials.pdf (2012); J. Schefer.

[16] G. E. Bacon, "*Neutron Diffraction*", 3rd ed, Clarendon Press, Oxford (1975).

[17] H. M. Rietveld, *J. Appl. Cryst.* **2** (1969) 65.

[18] H. M. Rietveld, *Acta Crystallogr.* **22** (1967) 151.

[19] A. C. Larson, R. B. V. Dreele, *General Structural Analysis System (GSAS)*, Los Alamos National Laboratory LAUR 86-748 (1994).

[20] B. H. Toby, *J. Appl. Crystallogr.* **34** (2001) 210.

[21] L. B. McCusker, R. B. Von Dreele, D. E. Cox, D. Louer, P. Scardi, *J. Appl. Crystallogr.* **32** (1999) 36.

[22] J. Cui, Q. Huang, B. H. Toby, *Powder Diffr.* **21** (2006) 71.

[23] J. A. Gonzalo, D. E. Cox, G. Shirane, *Phys. Rev.* **147** (1966) 415.

[24] J. Clarke, A. I. Braginski, "*Fundamentals and Technology of SQUIDs and SQUID systems* ", WILEY-VCH Verlag GmbH & Co, Weinheim (2004).

[25] S. K. Freeman, "*Applications of Laser Raman Spectrscopy*", Whiley-Interscience, London (1974).

[26] H. R. Thrisk, "*Electrochemistry: Volume 7*", RSC, London (1980).

[27] J. T. S. Irvine, D. C. Sinclair, A. R. West, *Adv. Mater.* **2** (1990) 132.

[28] E. Barsoukov, J. R. Macdonald, "*Impedance Spectroscopy: Theory, experiment, and Applications*", 2nd ed, Wiley-Interscience, Hoboken, N. J. (2004).

[29] V. S. Ramachandran, J. J. Beaudoin, "*Handbook of Analytical Techniques in Concrete Science and Technology*", William Andrew Publishing/Noyes, Park Ridge N. J. (2001).

Chapter 3

Characterisation of $CoSb_2O_4$ and lead doped variants

3.1 Introduction

$CoSb_2O_4$, a member of the MSb_2O_4 schafarzikite-related materials (where *M* is: Mn, Fe, Co, Ni, Zn) [1-5] remains as one of the least studied variants. This provided the opportunity to investigate the nuclear and magnetic structures of this compound as well as other physical properties. To date all MSb_2O_4 variants [1, 3, 5-7] have been synthetically produced and are characterised by the tetragonal spacegroup $P4_2/mbc$, and all except $CoSb_2O_4$ have received detailed analysis. The lattice parameters for the variants fall into the region: a = 8.712(1) Å, c = 6.001(2) Å for $MnSb_2O_4$ and a = 8.395(2) Å, c = 5.923(2) Å for $NiSb_2O_4$ [3] at room temperature and no change of symmetry is observed upon substitution of the transition metal (TM) species. It has been suggested [2] through analysis of peak half widths (in particular the (h00) and (hkl), which were visibly broadened) and magnetic symmetry that the $FeSb_2O_4$ system is more accurately described as an orthorhombic system where a rough estimate for the difference between a and b was given as 0.2%.

A means of introducing new functionality and enhanced magnetic properties whilst retaining the original structure was first investigated by Abakumov *et al* [8] on the $MnSb_2O_4$ system. It was proposed that the substitution of Pb^{2+} onto the Sb^{3+} (8h) site, as in Pb_3O_4, would oxidise the octahedrally coordinated transition metal atom. Empirically, this was found not to be the case and significant amounts of Sb^{3+} were oxidised to Sb^{5+} displacing Mn as MnO and Mn_2O_3 (when x > 0.25) and $Pb_2Sb_2O_7$ and $Pb_5Sb_2MnO_{11}$ (when x > 0.60)

impurities. Conversely, application of the same principle by Whitaker *et al* [9] to the $FeSb_2O_4$ system resulted solely in the oxidation of Fe^{2+} to Fe^{3+} and retention of the original symmetry. This was evidenced by an increase in the Néel temperature (from 45 K for $FeSb_2O_4$ to 69 K for $FeSb_{1.40}Pb_{0.60}O_4$), a change in the magnetic ordering mode from a dominant A mode to a dominant C mode and a significant elongation of *c*, with an associated contraction of *a*, due to increased repulsion between intrachain Fe^{2+} and Fe^{3+}. This chapter details the findings from XRPD, NPD, SEM, TGA and DC magnetic susceptibility measurements on $CoSb_2O_4$ and the lead substituted variants.

3.2 Experimental

Polycrystalline samples of $CoSb_2O_4$ were produced by the solid state reaction of CoO (325 mesh Aldrich) and Sb_2O_3 (99% Reagent Plus, 5 micron powder, Aldrich) in the stoichiometric ratio 1:1. Intimately ground mixtures were heated in alumina inserts within evacuated ($1x10^{-5}$ < mbar) sealed silica ampoules for two 6 hr periods with intermittent grinding. $CoSb_{1.50}Pb_{0.50}O_4$ was formed by heating a homogenous mixture of CoO, Co_3O_4 (<10 micron, Sigma-Aldrich), Sb_2O_3 and PbO (≥ 99%, Puriss) in an analogous containment vessel. Heating times and temperatures were adjusted to 6 hours at 800˚C followed by a further 4 hrs at 800˚C, with intermittent grinding, to limit impurity formation. All reagents were dried at 350˚C under dynamic vacuum prior to use.

3.3 Synthesis and characterisation of $CoSb_2O_4$

Two main routes for synthesising the schafarzikite-related structures have been previously reported. Koyama *et al* [3] utilised a hydrothermal synthesis process, whereas many others commonly used variations of the ceramic method [4, 10]. Given that the significant body of existing work utilised the ceramic method in sealed tubes this was chosen

as our starting point. Initially, reaction mixtures (*vide infra* Equation 3.1) were heated directly in evacuated fused silica tubes; however, this met with difficulty as heating at 600˚C resulted in reaction with the silica vessel (Figure 3.1) and mixed products ($CoSb_2O_6$ impurity). Heat treatments at 500˚C were found to result in little reaction even after heating for 192 hrs, whereas pure samples could be synthesised from pressed pellets at 550˚C for 192 hrs. Heating times and temperatures were revisited using alumina inserts to contain the reaction mixture within the evacuated fused silica tubes but extended periods of heating at elevated temperatures were found to result in $CoSb_2O_6$ impurities and a loss of antimony oxide. Shorter heat treatments at elevated temperatures provided a more efficient route to the desired product and eliminated the need for excess antimony oxide whilst alumina inserts offered significant improvement in purity. Alternative routes were tested (Equation 3.2) at a range of temperatures but were unsuccessful due to a resistance of Sb_2O_4 to react.

$$CoO + Sb_2O_3 \xrightarrow{550\text{–}700°C} CoSb_2O_4 \quad (3.1)$$

$$Co + Sb_2O_4 \xrightarrow{500\text{–}700°C} CoSb_2O_4 \quad (3.2)$$

Figure 3.1 The resultant silica tube where a reaction mixture was heated in direct contact with the silica. The smooth surface had been pitted.

A hydrothermal route of producing $CoSb_2O_4$ was tested in analogy to the early work of Koyama *et al* [3] by heating a stoichiometric mixture of CoO and Sb_2O_3 at 250˚C for 7 days in a 10 % NaOH solution within a hydrothermal bomb. The resulting sample, a pinkish powder with patches of a dark blue substance was verified by XRPD as containing $CoSb_2O_4$ but in poor purity (where Sb_2O_5, and CoO were the considerable impurities). This method was not pursued.

Highly crystalline samples (light pinkish/brown in colour) produced by heating at 700˚C for two 6 hr sessions were indexed as a pure single phase and the reflection conditions (*hkl: h+k*, *l* = 2*n* and *l* = 2*n*) [11] of the tetragonal spacegroup $P4_2/mbc$ were satisfied. The lattice parameters *a* = 8.4958(7) Å, *c* = 5.9255(7) Å, obtained with a high figure of merit (50 < FOM), compared favourably with those previously determined where *a* = 8.500(1) Å, *c* = 5.931(1) Å [3] and this value was within the range of lattice parameter for the MSb_2O_4 analogues. Rietveld refinement of the XRPD data with applied absorption correction proceeded using the lattice parameters obtained from indexing and the structure reported by Chater *et al* [12] as the initial model. The final fit (Figure 3.2, $\chi^2 = 1.924$, $R_{wp} = 0.0471$) was for independent variation of all atomic coordinates (excluding Co), isotropic displacement parameters (IDPs), lattice parameters, zero point error (ZPE), back ground (Shifted Chebyschev), phase fractions and profile parameters being refined independently for the main phase. Lattice parameters of *a* = 8.49285(7) Å and *c* = 5.92449(5) Å were obtained. This refinement accounted for a small CoO impurity identified in the early NPD work (*see Section 3.5.1*). Parameters for the impurity were initially refined and then fixed.

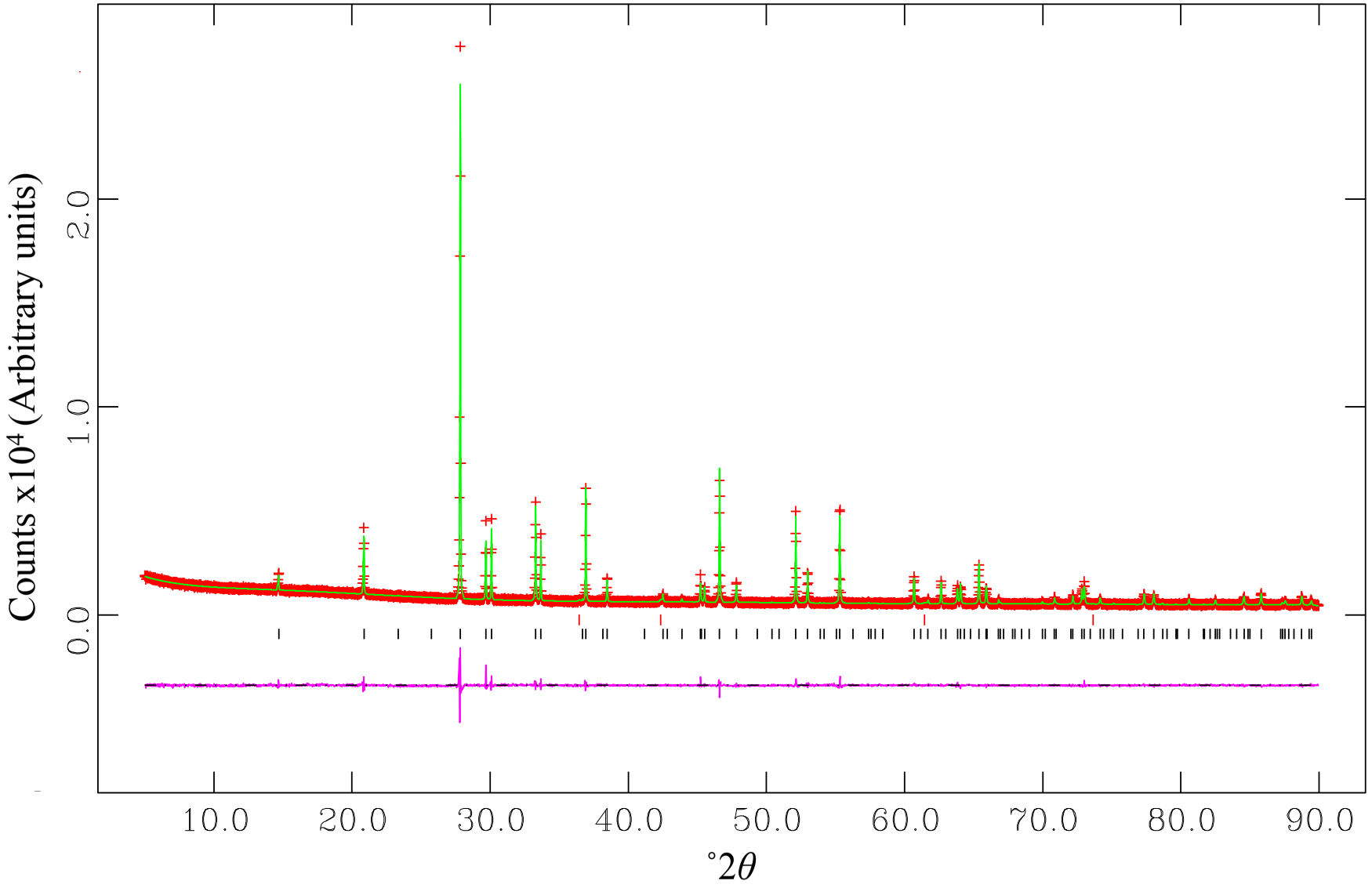

Figure 3.2 The final Rietveld refinement plot of $CoSb_2O_4$ based on XRPD data using $P4_2/mbc$: observed data (+), calculated and difference profiles (continuous lines) and, from the bottom, reflection positions of $CoSb_2O_4$ (|) and CoO (|) nuclear structures respectively.

3.4 Synthesis and characterisation of $CoSb_{1-x}Pb_xO_4$

Initial attempts to synthesise lead doped variants of $CoSb_{2-x}Pb_xO_4$ were unsuccessful (where x = 0.25, 0.40, 0.50, 0.60, 1.00 and 2.00). Consequently efforts were concentrated on developing a single lead doped system with the highest possible purity and only $CoSb_{1.50}Pb_{0.50}O_4$ was fully studied. Several strategies for forming $CoSb_{1.50}Pb_{0.50}O_4$, based upon the ceramic method, were first investigated centred around Equations 3.3 and 3.4:

$$0.25CoO + 0.25Co_3O_4 + 0.75Sb_2O_3 + 0.5PbO \rightarrow CoSb_{1.50}Pb_{0.50}O_4 \quad (3.3)$$

$$0.5CoSb_2O_4 + 0.125Co + 0.125Co_3O_4 + 0.25Sb_2O_4 + 0.5PbO \rightarrow CoSb_{1.50}Pb_{0.50}O_4 \quad (3.4)$$

A wide range of heating times ($4 \leq$ hrs ≤ 192) and temperatures (500, 550, 600, 700, 750 800˚C) were tested where length of heating varied inversely with temperature. Reaction mixtures were prone to antimony oxide loss when heating for extended periods of time. Whilst short heating times at elevated temperatures (700-800˚C) did not remove the common recurrent impurity (related to the spinel $Co(Co_{1.33}Sb_{0.66})O_4$) heating at 800˚C for 6 and 4 hrs with intermittent grinding significantly reduced it, indicating the main phase to be slightly cobalt- and antimony- deficient. This reflected the difficulty in oxidising certain transition metals by doping with aliovalent cations also observed by Abakumov *et al* [8]. The powder pattern was indexed to a tetragonal unit cell with lattice parameters a = 8.4752(8) Å, c = 6.0534(9) Å, showing a large increase in c and small decrease in a compared with $CoSb_2O_4$. This primarily reflected the accommodation of the larger Pb^{2+} cation (0.98 Å) on the Sb^{3+} (0.76 Å) [13], (8*h*) site causing a stretch along [001] through displacement. Furthermore partial oxidation of Co^{2+} to Co^{3+}, governed by the amount of Pb^{2+}, complemented the

elongation of *c* due to the increased coulombic repulsion between intrachain adjacent sites, much like the situation found in $FeSb_{2-x}Pb_xO_4$ [9].

3.5 $CoSb_2O_4$; nuclear and magnetic characterisation by NPD

3.5.1 NPD at 300 K

Initially, both HR and HI data sets (ILL, D2B) were investigated but the better profile fitting and easier identification of impurities in the HR data led to subsequent analysis using only this data form at the expense of intensity. The refinement proceeded by using the lattice parameters and atom positions obtained from the XRPD refinement. Independent variation of each atomic position and IDPs whilst the profile was refined using function 2 (Pseudo-Voigt) [14-15] resulted in a stable fit and showed excellent coincidence between the observed and calculated data. Different profile functions were investigated for completeness but profile function 2 was deemed the best and the background was refined using the shifted Chebyschev function. Comparison of the refined lattice parameters with those obtained from XRPD showed a larger than acceptable difference. The neutron wavelength was subsequently calibrated using the lattice parameters obtained from the XPRD refinement. The newly refined wavelength 1.591780(6) Å (λ_{old} = 1.59432 Å), was substituted for the old and all pre existing parameters were allowed to vary independently once more. The final fit Figure 3.3 (χ^2 = 2.606, R_{wp} = 0.0493, R_{F^2} = 0.0461) shows excellent agreement with $P4_2/mbc$ symmetry and a small CoO (*ca* 3 wt %) impurity.

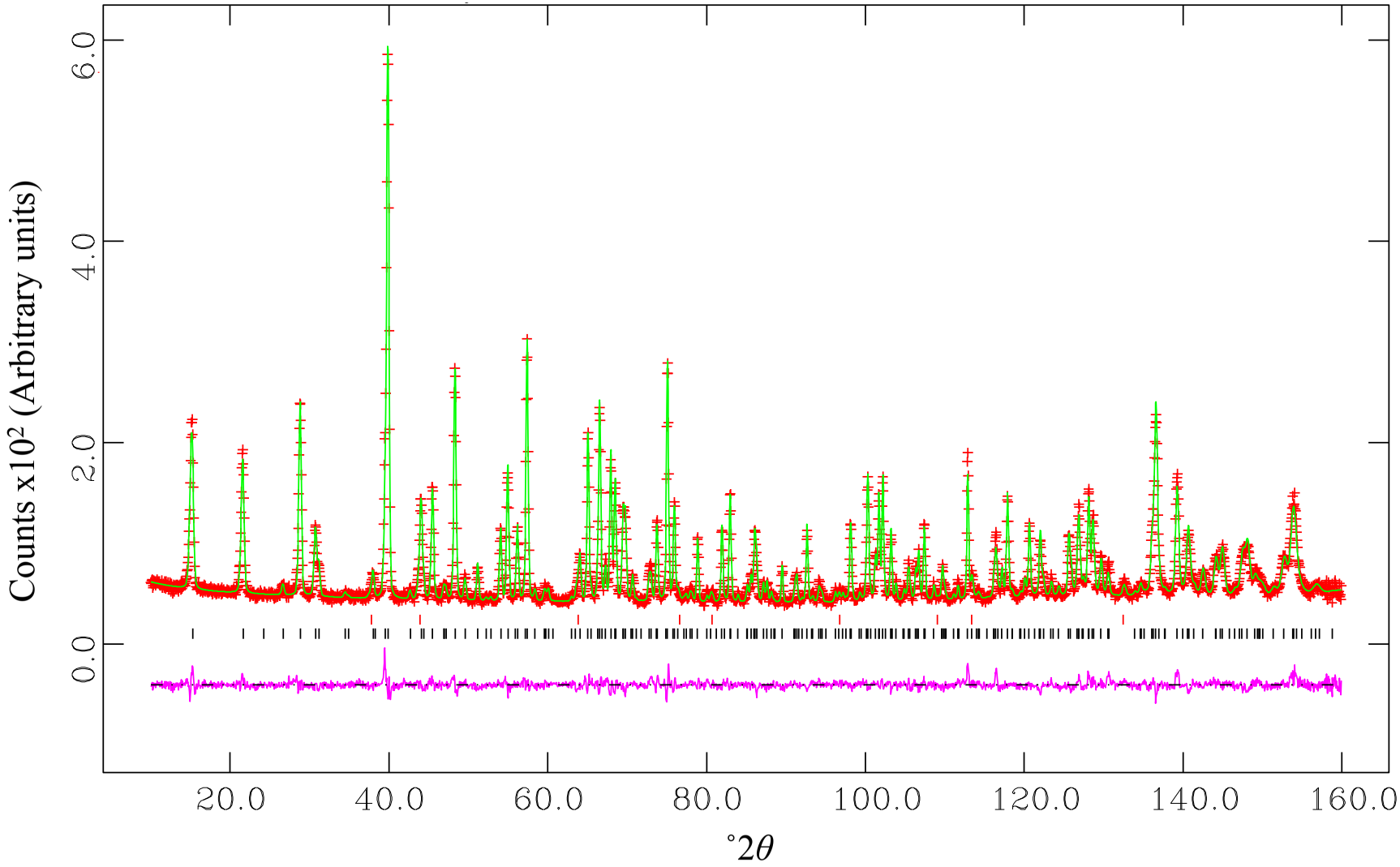

Figure 3.3 The final Rietveld refinement plot of $CoSb_2O_4$ based on 300 K NPD data using $P4_2/mbc$: observed data (+), calculated and difference profiles (continuous lines) and, from the bottom, reflection positions of $CoSb_2O_4$ (|) and CoO (|) nuclear structures respectively.

Figure 3 ...ıs lines) and, fro...

3.5.2 NPD at 4 K

On cooling to 4 K several new reflections at low angle emerged which were attributed to long range magnetic ordering of the system. An absence of any other significant reflections or peak broadening for the nuclear phase implied retention of the original symmetry. The nuclear phase was first considered by using the structure derived from the 300 K refinement. ZPE, lattice parameters, background, profile parameters, atomic positions and IDPs were refined independently to an acceptable standard. Nuclear and magnetic contributions from the impurity were coincidently refined and then fixed throughout allowing only the scale factor to vary. The more clearly defined magnetic peaks (10.828˚, 24.285˚, 32.762˚, and 39.613˚2θ) could be indexed ((100), (210), (300) and (320) respectively) suggesting a C-type ordering of the magnetic structure. A magnetic cell consisting of Co^{2+} ions was inserted with lattice parameters equal to the existing nuclear phase and defined by the space group *P*1 to allow unrestricted variation of each moment's direction. The form factor for the phase was set to be consistent with Co^{2+}. Moment orientations dictated by the four possible modes (A, C, G, and F) were methodically tested in both the *x* and *z* directions. Constraints were placed to maintain parallel spin alignment, a constant moment magnitude initially fixed to 3 μ_B (from 2*S*) for each magnetic ion, and to ensure that only the magnetic intensity along a specified direction was generated whilst the representative modes were identified. The findings supported the initial indexing and only a C mode, described by parallel intra-chain spin alignment and antiparallel interchain alignment, was found. The mode orientation was investigated between the *x* and *z* directions. The results of assigning the spin direction along [100], [001] and [101] (Table 3.1) and allowing the magnitude of the moments to vary implied that C_{xz} was the best fit on the basis of figure of merit alone. It was clear however, from the large errors obtained for the *x* component that the more accurate

model which described the magnetic structure was a C_z mode, but it is accepted that a small *x* component could exist.

Table 3.1 The Rietveld refinement results from varying the collinear spin alignment corresponding to a C mode along the *x*, *z*, and *xz* directions. *A model where the *x* and *z* components form a single phase but separate constraints are imposed upon the moment magnitude in the *x* and *z* which allows their independent variation.

Mode orientation	Moment magnitude (μ_B)	χ^2
C_z	3.72(2)	2.881
C_x	4.28(4)	8.306
C_{xz} *	$M_x = 0.1(6)$ $M_z = 3.70(3)$	2.868

The final fit (Figure 3.4, $\chi^2 = 2.881$, $R_{wp} = 0.0580$, $R_{F^2} = 0.0442$) shows excellent coincidence of original symmetry and collinear spin alignment of the magnetic cell, consistent with C_z- type magnetic ordering ($C_z = 3.72(2)\mu_B$) i.e. ferromagnetic spin alignment within a chain and antiferromagnetic alignment in the *ab* plane. The final results are shown in Table 3.2. The larger than spin only moment indicates a large orbital contribution to the overall moment. This has also been observed in other Co^{2+} containing rutile type compounds $CoTa_2O_6$ ($\mu = 3.25\pm0.02\ \mu_B$) [16] and α-$CoSO_4$ ($\mu = 3.3\pm0.2\ \mu_B$) [17].

Table 3.2 The details obtained from the final refinements of $CoSb_2O_4$ at 300 and 4 K.

		$CoSb_2O_4$	
		300 K	4 K
Co, ***4d***	$100*U_{iso}$ (Å^2)	0.76(7)	0.04(9)
Sb, ***8h***	(*x*, *y*, 0)	0.1750(2), 0.1644(1)	0.1749(2), 0.1639(2)
	$100*U_{iso}$ (Å^2)	0.84(3)	0.05(3)
O1, ***8h*** (O_{eq})	(*x*, *y*, 0)	0.0985(1), 0.6391(1)	0.0978(2), 0.6392(2)
	$100*U_{iso}$ (Å^2)	0.96(3)	0.10 (3)
O2, ***8g*** (O_{ap})	(*x*, *y*, 0.25)	0.6791(1), 0.1791(1)	0.6787(1), 0.1787(1)
	$100*U_{iso}$ (Å^2)	1.42(2)	0.18(3)
χ^2		2.606	2.881
R_{wp}		0.0493	0.0580
R_{F^2}		0.0461	0.0422
a (Å)		8.49340(9)	8.4809(1)
c (Å)		5.92387(8)	5.92093(9)
Magnetic moment (μ_B)			$C_z = 3.72(2)$

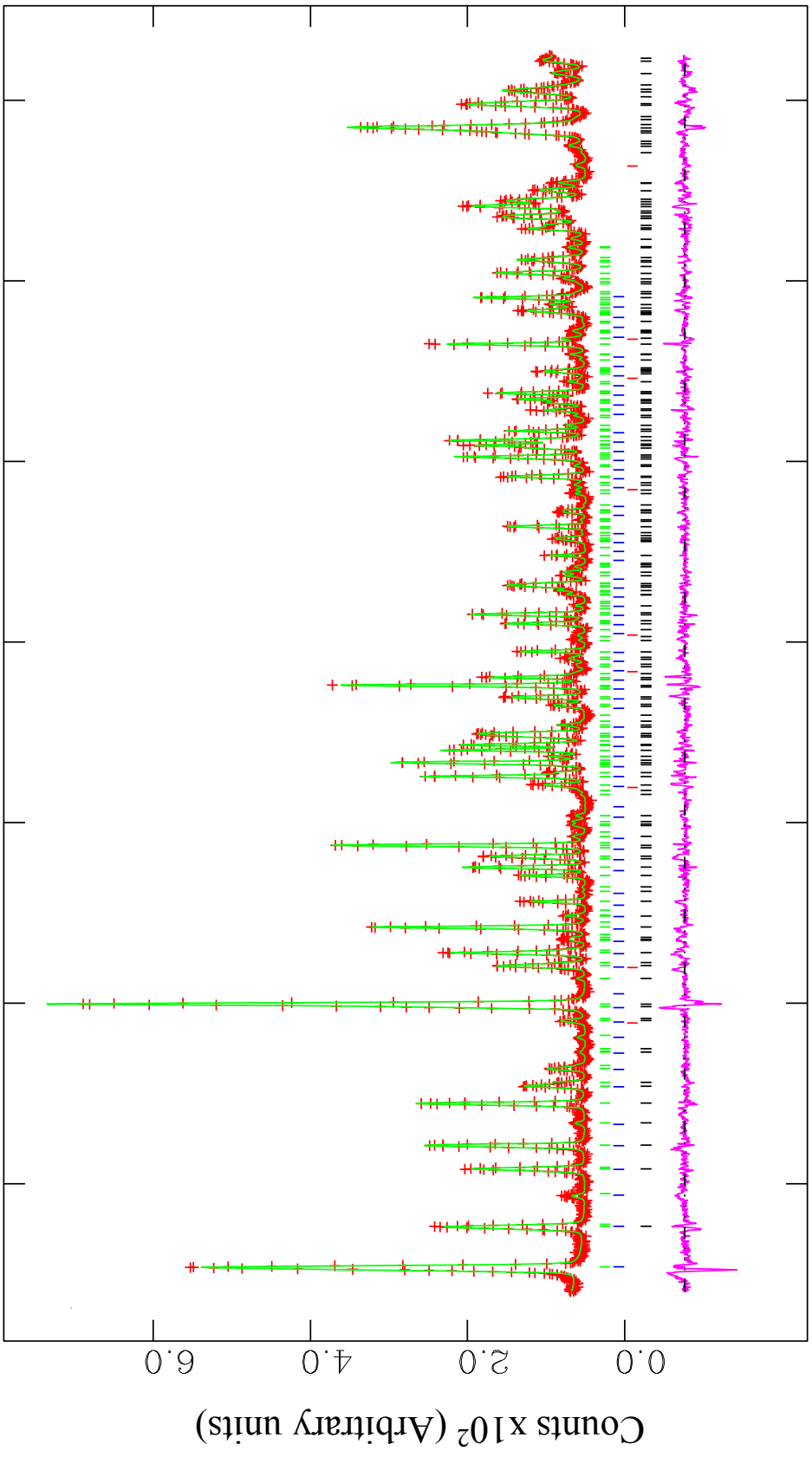

Figure 3.4 The final Rietveld refinement plot of $CoSb_2O_4$ based on 4 K NPD data using $P4_2/mbc$: observed data (+), calculated and difference profiles (continuous lines) and, from the bottom, reflection positions of $CoSb_2O_4$ (|) and CoO (|) nuclear structures, CoO (|) $CoSb_2O_4$ (|) magnetic structures reined in $P1$ respectively.

3.6 Nuclear and magnetic characterisation of $CoSb_{1.50}Pb_{0.50}O_4$ by NPD

3.6.1 NPD at 300 K

Refinement of the 300 K HR dataset was initially carried out as for $CoSb_2O_4$ where the lattice parameters obtained from indexing and atomic positions from the 300 K refinement of $CoSb_2O_4$ were used. Nuclear neutron scattering lengths were set to 0.249 (Co), 0.581 (O), 0.557 (Sb) and 0.940 (Pb; all $x10^{-14}$m). Occupancy of the Sb^{3+} and Pb^{2+} 8*h* site was set to be consistent with the ideal composition, and a constraint was used to ensure unified variation of both atomic coordinates and IDPs of the site. Nuclear contributions from the impurity phase were included throughout the refinement. The fit where only atomic coordinates, phase fractions, ZPE, background, cell and profile parameters were refined (Figure 3.5; $\chi^2 = 3.301$, $R_{wp} = 0.0518$, $a = 8.4826(2)$ Å, $c = 6.0543(3)$ Å) was satisfactory. This implied that the composition was close to stoichiometry and only Co was being oxidised. However, allowing the IDPs to vary, ($\chi^2 = 2.770$, $R_{wp} = 0.0474$, 31 variables) returned an anomalously small value for Co (U_{iso}*100 = 0.09(9) $Å^2$, compared with approximately 2.40 $Å^2$ for all other sites). This indicated that a more heavily scattering species may be present on the site and that Sb had possibly substituted some Co in the octahedral chains in analogy to the findings of Abakumov *et al* [8].

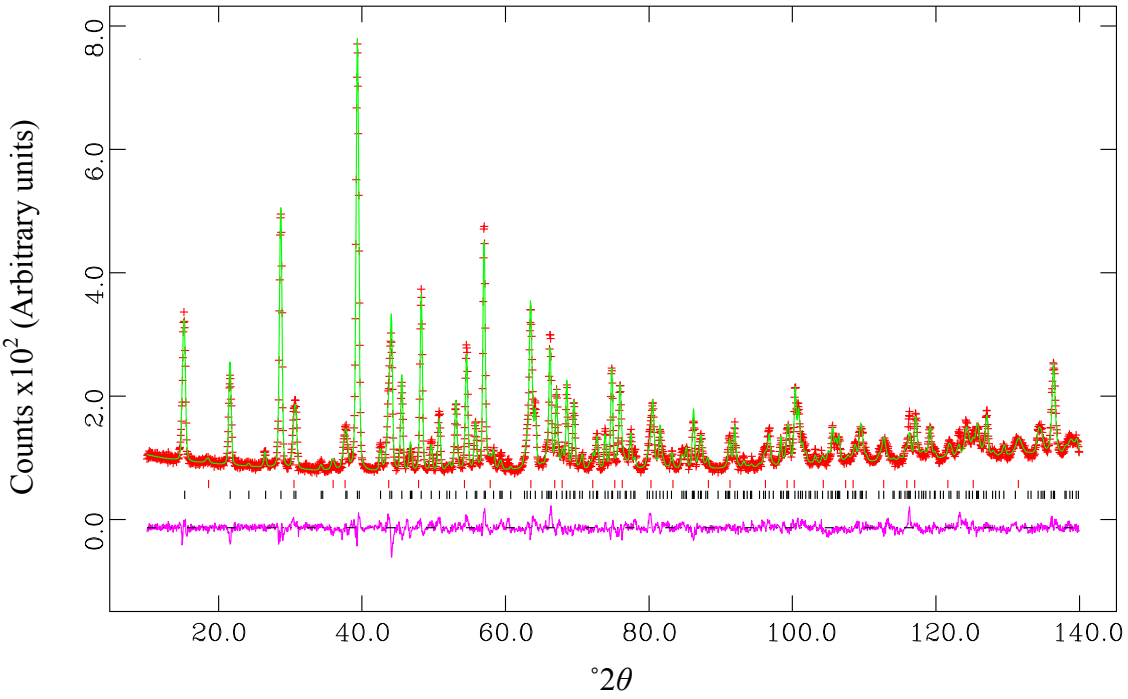

Figure 3.5 The initial Rietveld refinement plot of $CoSb_{1.50}Pb_{0.50}O_4$ based upon the oxidation of only Co. Only atomic coordinates, phase fractions, ZPE, back ground, cell and profile parameters have been refined in $P4_2/mbc$. Observed data (+), calculated and difference profiles (continuous lines) and, from the bottom, reflection positions (|) of $CoSb_{1.50}Pb_{0.50}O_4$ and (|) $Co(Co_{1.33}Sb_{0.66})O_4$ nuclear structures respectively.

It was unfortunate that the neutron scattering length of Sb is longer than Co, a trend which is reflected in the X-ray scattering ability of the two species, as this prevented any superior identification of the anomaly surrounding the 4*d* Co site with dual XRPD/NPD refinement. Consequently two extreme models were used as a means of probing the structure. A refinement was carried out based upon a model which explored the hypothetical opposite extreme where only antimony was oxidised to see how the 4*d* and 8*h* site fractional occupancy would accord with the cobalt oxidation model. This was initially done in the absence of any IDP variation to prevent correlation effects. The absence of any lead-containing impurity was used to set the initial occupancies to Co^{2+}/Sb^{5+} 4*d* = 0.833/0.167, Sb^{3+}/Pb^{2+} 8*h* = 0.75/0.25 where the 4*d* site occupancy was set to have a charge of +2.5 based solely on the oxidation of antimony and overall occupancy of 1. One constraint was enforced which maintained each site to have a total occupancy of 1 whilst allowing cross site i.e. the 4*d* Sb and 8*h* Sb, variation to be linked e.g. when the 4*d* site occupancy decreased the 8*h* Sb site

increased. IDPs were refined for all sites once occupancies had been suitably refined in order to ascertain the validity of the model through more realistic atomic displacement, no significant difference was made to the occupancies upon doing so. The results (Table 3.3) show little difference in χ^2 obtained when compared to the cobalt oxidation model; however, there is a significant difference in the occupancies of each site. It was decided that a third model was needed to compare the two previous results.

The premise of the "free model" was to allow simultaneous oxidation of antimony and cobalt. All sites were set to their ideal occupancy and the 4*d* Co site was split to have initial zero Sb occupancy. A constraint was placed on each Co/Sb and Sb/Pb site to allow independent occupancy variation whilst maintaining a total site occupancy of one, and unified IDPs. Once a stable fit was achieved IDPs were evaluated, with little change in the occupancy of each site. The final fit (Figure 3.6) shows a superior value of χ^2 and parameters which lie between those derived from the two extreme models, suggesting that both cobalt and antinomy oxidation had simultaneously occurred. Notably, the dominant species to be oxidised was Co giving an overall oxidation state of +2.30 (*cf* +2.50) and the impurity was calculated at around 11 wt %. This model was chosen to be the most representative of the main phase, where the larger than ideal IDPs of the Sb/Pb and O positions reflect cation variation on the 8*h* site. A direct comparison between models can be seen in Table 3.3.

Table 3.3 Showing the final results obtained from the Rietveld refinement of $CoSb_{1.50}Pb_{0.50}O_4$ based upon the 3 models: model 1, only Co is oxidised, model 2 is based upon antimony oxidising only and model 3 the free model where 4*d* and 8*h* site occupancies varied independently • hard constraint imposed so that the occupancy of the 8*h* site is always x1.5 greater than the 4*d* site.

		Model		
		Co oxidation	Sb oxidation•	Free model
Co/Sb, **4*d***	$100*U_{iso}$ (Å^2)	0.09(10)	1.4(1)	0.7(2)
	Occupancy	1/0	0.823(7)/ 0.177(7)	0.92(2)/0.08(2)
Sb/Pb, **8*h***	(*x*, *y*, 0)	0.1614(3), 0.1619(3)	0.1613(3), 0.1618(3)	0.1613(3), 0.1618(3)
	$100*U_{iso}$ (Å^2)	2.39(4)	2.36(5)	2.38(5)
	Occupancy	0.75/0.25	0.74(1)/0.27(1)	0.74(1)/0.26(1)
O1, **8*h*** (O_{eq})	(*x*, *y*, 0)	0.0959(2), 0.6347(2)	0.0965(2), 0.6356(2)	0.0962(3), 0.6351(3)
	$100*U_{iso}$ (Å^2)	2.08(6)	2.00(6)	2.04(6)
O2, **8*g*** (O_{ap})	(*x*, *y*, 0.25)	0.6745(2), 0.1745(2)	0.6749(2), 0.1749(2)	0.6746(2), 0.1746(2)
	$100*U_{iso}$ (Å^2)	2.73(5)	2.55(6)	2.65(6)
χ^2		2.770	2.788	2.743
R_{wp}		0.0474	0.0476	0.0472
R_{F^2}		0.0580	0.0565	0.0569
a (Å)		8.4826(2)	8.4827(2)	8.4826(2)
c (Å)		6.0545(2)	6.0547(2)	6.0546(2)

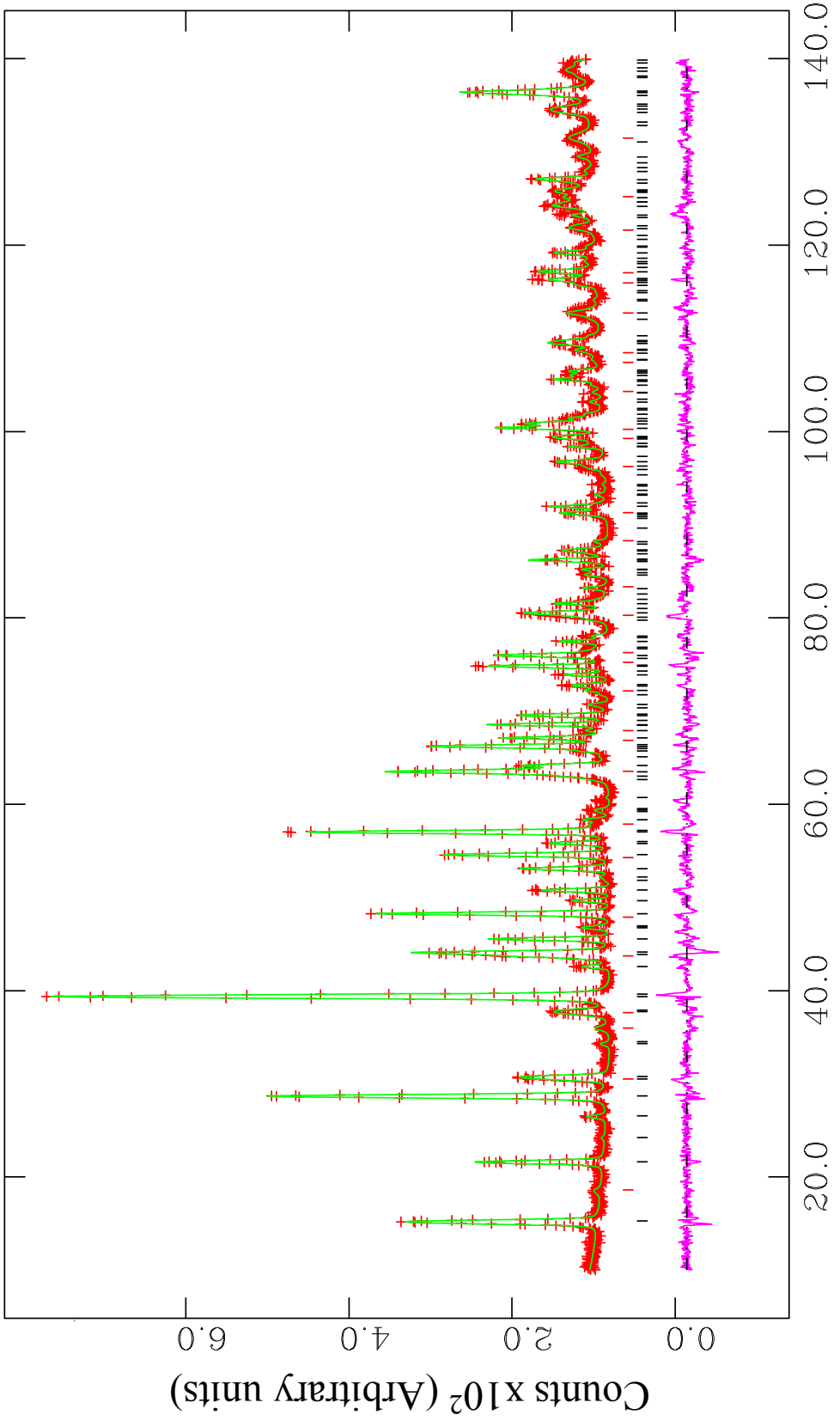

Figure 3.6 The final Rietveld refinement plot of $CoSb_{1.50}Pb_{0.50}O_4$ at 300 K based upon the occupancy of the Co/Sb and Sb/Pb sites varying independently, the "Free model". Data was refined in $P4_2/mbc$. Observed data (+), calculated and difference profiles (continuous lines) and, from the bottom, reflection positions (|) of $CoSb_{1.50}Pb_{0.50}O_4$ and (|) $Co_{2.33}Sb_{0.66}O_4$ nuclear structures respectively.

3.6.2 NPD at 4 K

The initial model was setup in accordance with the final 300 K refinement. Two new sets of reflections at discrete 2θ values were identified. The first peak of each set, the (100) at 10.9 ˚2θ and (101) 18.6 ˚2θ, differed greatly in intensity and were used as a primary guide to identify the presence of C- and G- modes for the magnetically ordered system. No changes to the nuclear profile were observed on cooling. The structural refinement was first addressed and carried out as in previous refinements where fractional occupancies were fixed to the 300 K values for simplicity. Variation of all IDPs returned a small negative value for the Co/Sb site ($100*U_{iso}$ = -0.1(1) Å^2) and was subsequently constrained at 0.2 Å^2. The magnetic structure was refined by inserting a magnetic cell with lattice parameters and cation occupancy consistent with the nuclear structure. A moment equal to *2S* was inserted on each cation site. The magnetic form factor was set to be consistent with the more abundant Co^{2+} species. Two different magnetic components were identified which described a C mode along [001] and a G mode along [100] supporting the initial indexing. Incorporation of both modes into a single phase (Table 3.4) was attempted (χ^2 = 2.517, R_{wp} = 0.0599; C_z = 2.87(3) μ_B, and G_x = 1.43(5) μ_B); however, a better fit was obtained (χ^2 = 2.480 R_{wp} = 0.0595; C_z = 2.86(2) μ_B, and G_x = 1.65(6) μ_B) by treating the G- type and C- type ordering as separate phases. Closer examination of the profile showed that (101) peak was visibly broader than the (100); this accounted for the less satisfactory fit when the models were combined into a single phase. The final fit (Figure 3.7, χ^2 = 2.480, R_{wp} = 0.0595) is for variation of the lattice parameters, atomic coordinates, phase fractions, ZPE, profile parameters, moment magnitude, and lattice parameters. Only the IDPs for O and constrained Sb/Pb positions were varied. The obtained moments for each component had a magnitude of C_z = 2.86(2) μ_B and G_x = 1.65(6) μ_B. Details of the final refinement can be seen in Table 3.5. It is proposed that the broadness of

the (101) peak is a reflection of the length scale relating to the G_x phase where the G-type order extends over a shorter distance. Whilst the final fit refined the G_x and C_z components independently to obtain more accurate moment magnitudes it is believed that combining both types of ordering into a single phase represents the true structure of the compound as shown in Figure 3.8, giving a total moment of $\mu_{Total} = 3.30(5)\ \mu_B$.

Table 3.4 Showing how two magnetic modes were combined into a single phase. M_x, M_y, M_z represent the moment contributions along each respective direction.

	M_x	M_y	M_z	Occupancy
Co1 (0.5, 0, 0.25)	1	0	2	0.92
Co 2 (0.5, 0, 0.75)	-1	0	2	0.92
Co 3 (0, 0.5, 0.25)	-1	0	-2	0.92
Co 4 (0, 0.5, 0.75)	1	0	-2	0.92

Table 3.5 The details obtained from the final nuclear refinements of $CoSb_{1.50}Pb_{0.50}O_4$ based upon 300 and 4 K data. * indicates a parameter which was fixed throughout refinement.

		$CoSb_{1.50}Pb_{0.50}O_4$	
		300 K	4 K
Co/Sb, ***4d***	$100*U_{iso}$ (Å^2)	0.7(2)	0.2*
	Occupancy	0.92(2)/0.08(2)	0.92/0.08*
Sb/Pb, ***8h***	(x, y, 0)	0.1613(3), 0.1618(3)	0.1616(3), 0.1618(3)
	$100*U_{iso}$ (Å^2)	2.38(5)	1.49(5)
	Occupancy	0.74(1)/0.26(1)	0.74/0.26*
O1, ***8h***	(x, y, 0)	0.0962(3), 0.6351(3)	0.0959(3), 0.6355(3)
	$100*U_{iso}$ (Å^2)	2.04(6)	1.04(7)
O2, ***8g***	(x, y, 0.25)	0.6746(2), 0.1746(2)	0.6742(2), 0.1742(2)
	$100*U_{iso}$ (Å^2)	2.65(6)	1.30(6)
χ^2		2.743	2.480
R_{wp}		0.0472	0.0595
R_{F^2}		0.0569	0.0645
a (Å)		8.4826(2)	8.4727(2)
c (Å)		6.0546(2)	6.0494(3)
Magnetic moment (μ_B)			$C_z = 2.86(2)$ $G_x = 1.65(6)$ $\mu_{Total} = 3.30(5)$

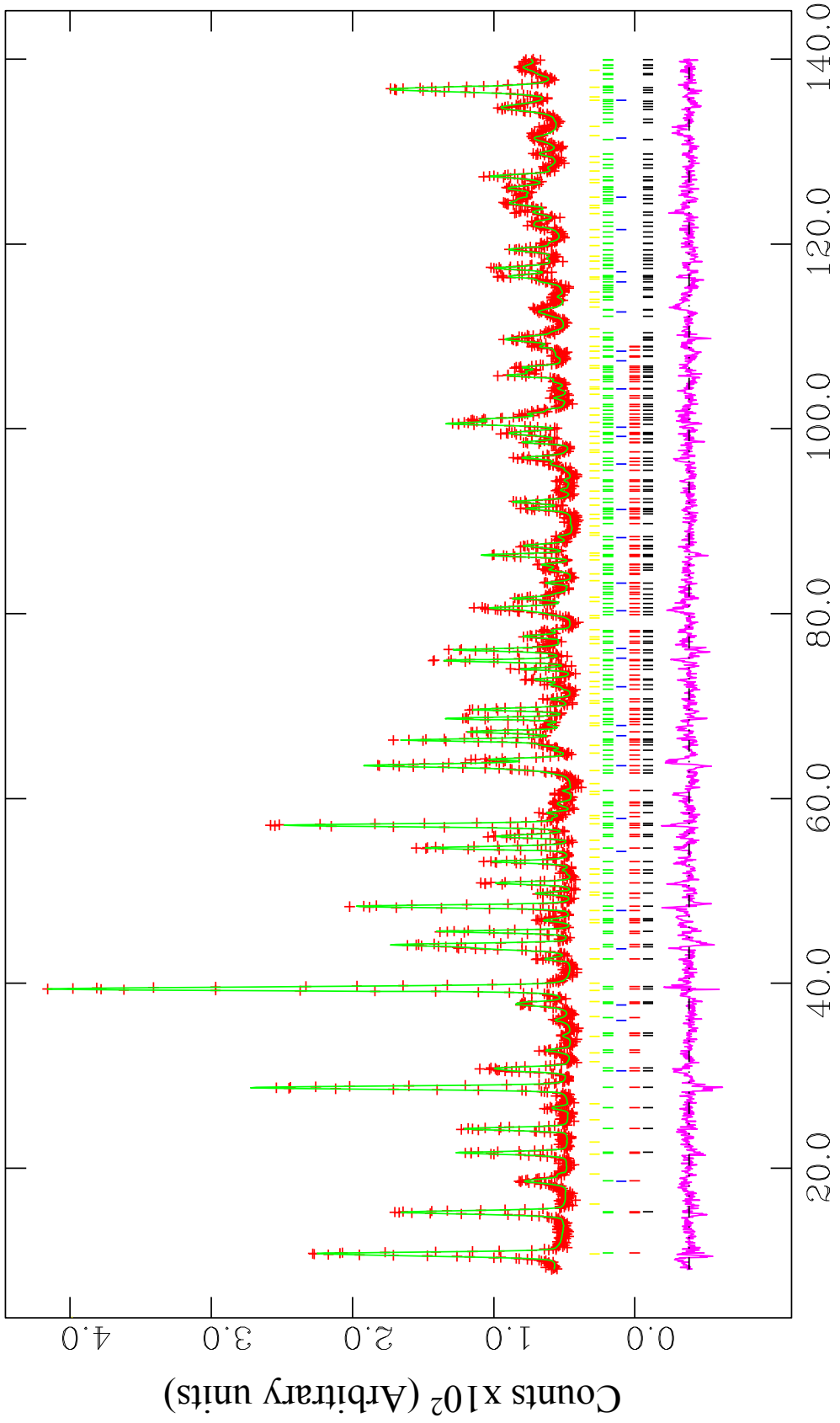

Figure 3.7 The final Rietveld refinement of $CoSb_{1.50}Pb_{0.50}O_4$ based on 4 K NPD data using $P4_2/mbc$: observed data (+), calculated and difference profiles (continuous lines) and, from the bottom, reflection positions (|) of $CoSb_{1.50}Pb_{0.50}O_4$ nuclear, C_z (|), $Co_{2.33}Sb_{0.66}O_4$ nuclear (|), G_x (|) and $Co_{2.33}Sb_{0.66}O_4$ magnetic (|) structures respectively.

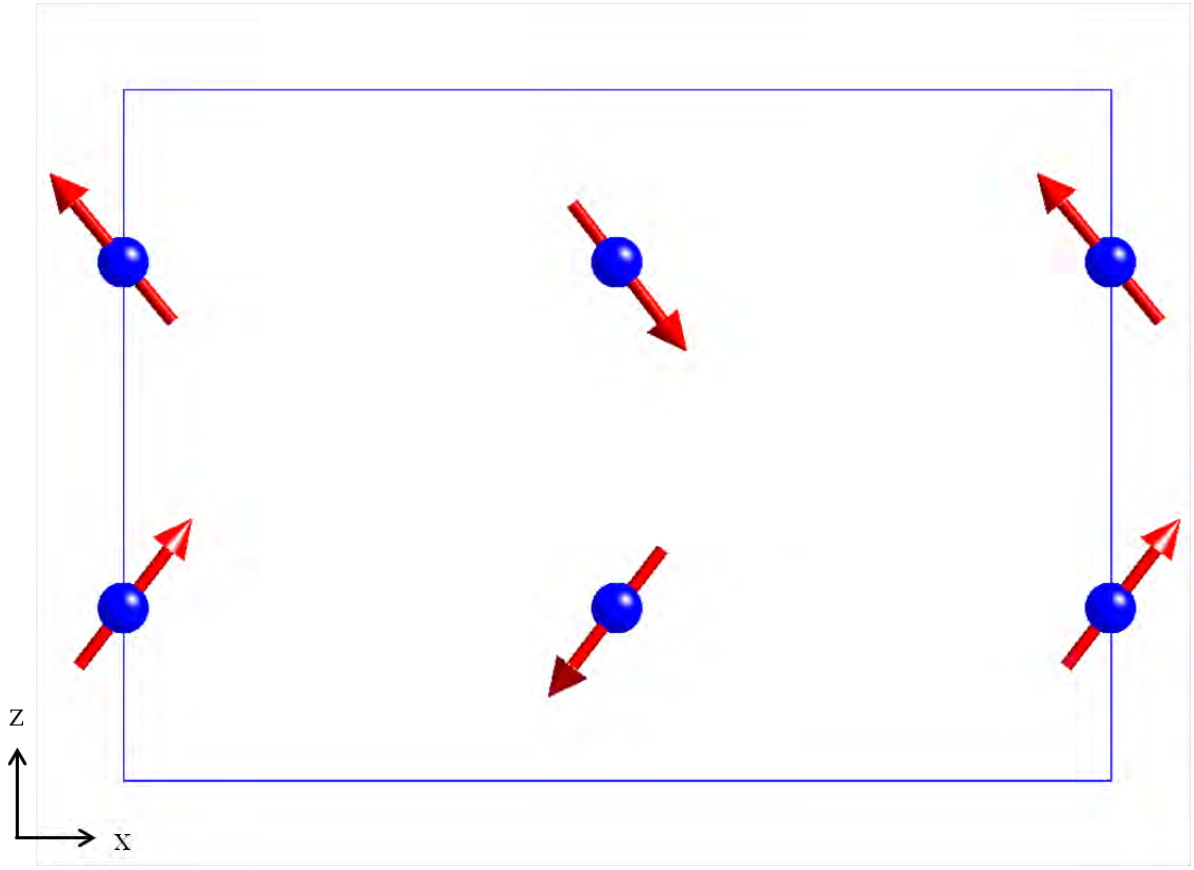

Figure 3.8 A representation of the magnetic structure of $CoSb_{1.50}Pb_{0.50}O_4$ determined from the refinement of NPD data obtained at 4 K.

3.7 Comparison of the $CoSb_2O_4$ and $CoSb_{1.50}Pb_{0.50}O_4$ structures

It can be seen from Table 3.6 that all systems have slightly elongated octahedra where the Co-O1 (equatorial bonds, O_{eq}) are shorter than the Co-O2 (apical bonds, O_{ap}). The elongation can be seen to have little effect on the degeneracy of the t_{2g} and e_g orbitals due to the large orbital contribution to the magnetic moment. It has been suggested that the nature of a pseudo one dimensional structure could reduce the quenching of any orbital contributions to a magnetic moment [18] but it is acknowledged that an orbital contribution is commonly seen in Co^{2+} containing compounds not of a low dimensional structure. The octahedral environment of Co^{2+} compares well with the values determined from $CoTa_2O_6$ (Co-O_{eq} = 2.082(2) Å, Co-O_{ap} = 2.101(3) Å) and to a lesser degree with $CoSb_2O_6$ (Co-O_{eq} = 2.026(3) Å, Co-O_{ap} = 2.068(3) Å [16] whist both also show a similar elongation.

Table 3.6 A table of selected bond lengths and angles for the $CoSb_2O_4$ and $CoSb_{1.50}Pb_{0.50}O_4$ systems at 300 and 4 K.

	$CoSb_2O_4$		$CoSb_{1.50}Pb_{0.50}O_4$	
	300 K	4 K	300 K	4 K
Bond length (Å)				
Co/Sb-O_{eq} x4	2.0710(9)	2.067(1)	2.067(2)	2.065(2)
Co/Sb-O_{ap} x2	2.151(1)	2.143(1)	2.095(2)	2.088(3)
Sb/Pb-O_{eq}	1.936(2)	1.939(3)	2.069(3)	2.067(4)
Sb/Pb-O_{ap} x2	1.990(1)	1.994(1)	2.056(2)	2.057(2)
Bond angle (˚)				
O_{eq}-Co-O_{eq}	88.70(5)	88.53(6)	85.81(9)	85.8(1)
O_{eq}-Co-O_{eq}	166.46(7)	166.23(8)	167.0(1)	166.8(1)
O_{eq}-Co-O_{eq}	92.89(5)	93.12(6)	95.66(9)	95.7(1)
Co-O_{eq}-Co	91.30(5)	91.47(6)	94.19(9)	94.2(1)
O_{eq}-Sb-O_{ap}	93.25(6)	93.24(7)	91.1(1)	91.2(1)
O_{ap}-Sb-O_{ap}	96.16(7)	95.88(8)	94.8(1)	94.7(1)

Substitution of antimony by lead results in a contraction of the octahedral environment reminiscent of the iron analogues [9] such that the tetragonal distortion is reduced (Table 3.6) further supporting the oxidation of the octahedral species. Despite this a distortion of the octahedral bond angles is seen, most noticeably in the large increase in the O_{eq}-Co-O_{eq} bond angle from 91.30(5)˚ to 94.19(9)˚, consistent with the iron variants. Shortening of the Co-O_{ap} bonds which are directed at the next chain are seen to result in a contraction of *a*. Two cooperative effects are seen to result in an elongation of *c*. Oxidation of the octahedral species results in increased repulsion between adjacent octahedra, originating from the rutile nature of the chains. Increasing the average cation size on the Pb/Sb 8*h* site also causes a stretch of *c*. To accommodate the simultaneous stretch and contraction the octahedral bond angles distort away from the ideal 90˚. Furthermore an extension of all Sb/Pb-O (x8 greater than the largest Co-O increase) bonds facilitates this motion. The overall effect is similar to that of a concertina and is modelled in Figure 3.9.

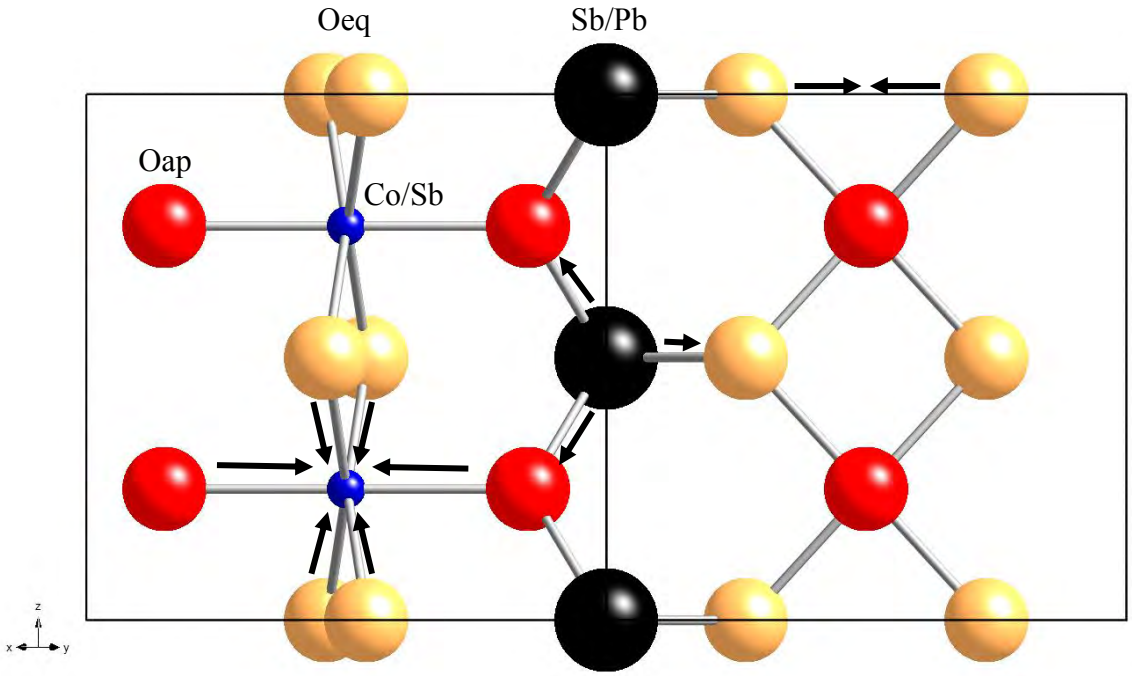

Figure 3.9 Influence of lead substitution in $CoSb_2O_4$ on bond lengths and angles. Arrows indicate the direction atom positions change. Beige and red spheres represent O_{eq} and O_{ap} bonds respectively.

Considering a hypothetical situation where Co^{3+} is in a high spin state and therefore has the same electronic configuration as Fe^{2+}, both d^6 cations, it would perhaps be expected that $CoSb_{1.50}Pb_{0.50}O_4$ would have a similar magnetic structure to that of $FeSb_2O_4$. Although the details of the magnetic ordering in $FeSb_2O_4$ differ slightly [2, 9] there is a general agreement with respect to the dominant mode of ordering being A-type along *x* (3.62(3) μ_B) with a lesser G-type component along *z* (1.24(7) μ_B) [9]. It is noteworthy that these components could be combined into a single structure if the broadening for the (101) peak is ignored. The two identified components (C_z and G_x) in $CoSb_{1.50}Pb_{0.50}O_4$ which were different from $FeSb_2O_4$, is indicative of different mechanisms for ordering existing between the two compounds. Consideration of the intrachain TM separation distance can offer a partial explanation as to the change in the dominant mode of ordering seen in $CoSb_2O_4$ and $CoSb_{1.50}Pb_{0.50}O_4$. The substantial elongation of *c* for $CoSb_{1.50}Pb_{0.50}O_4$ results in an intrachain Co-Co separation distance of 3.024 Å when compared to 2.952 Å in $FeSb_2O_4$ (at 4 K) [9], 2.9933Å in $MnSb_2O_4$ (at 2 K) [19], and 2.960 Å in $CoSb_2O_4$ at 4 K. It has already been seen

that a Δc = 0.008 Å between lead-free variants ($FeSb_2O_4$ and $CoSb_2O_4$) is sufficient to result in a dominant intrachain ferromagnetic exchange so it is of little surprise that the same is seen for $CoSb_{1.50}Pb_{0.50}O_4$ with an even larger Co-Co separation distance. It was inferred that the difference was large enough to reduce the direct exchange processes resulting in an increase in the dominance of the 90˚ superexchange through the common edge O^{2-} of the octahedra. It would appear that distortion away from the ideal 90˚ O_{eq}-Co-O_{eq} bond angle is of little consequence to the superexchange generating the dominant C mode; this is supported by Motida *et al* [20]. The small G_x component can be explained by octahedral Sb^{5+} disrupting the long range ordering where the corresponding small broad magnetic peaks suggests that this component only exists over a short range.

The TM-TM separation distance alone does not appear to provide a complete explanation for the change in dominant mode of ordering between $MnSb_2O_4$ (A-type) and $CoSb_2O_4$ (C-type). Consideration of ionic radii is likely a crucial component in explaining the magnetic ordering. The ionic radii reported by Shannon [13] show that Mn^{2+} (HS, 0.830 Å) is larger than that of Fe^{2+} (HS, 0.780 Å) and Co^{2+} (HS, 0.745 Å). The strength of direct exchange is well known to be heavily dependent on the degree of orbital overlap [21]. $MnSb_2O_4$ possess a larger *c* parameter than $CoSb_2O_4$ but the ionic radius of Mn^{2+} is also significantly larger than that of Co^{2+}. It therefore seems probable that in the Mn containing phase direct exchange is still the dominant process, as the larger orbitals are able to overlap despite a greater separation distance between TMs, and an A mode results. In $CoSb_2O_4$ however, a complex interplay between TM-TM separation distance and orbital contraction could result in a reduction in the strength of the direct exchange; this is despite the smaller TM-TM distance and results in dominant 90˚ interactions generating FM ordering within a chain.

3.8 SEM analysis

Scanning electron microscopy was used to identify crystal morphology. A SEI obtained from the surface of a sintered pellet of $CoSb_2O_4$ (Figure 3.10) shows a range of crystal morphologies extending from isotropic to semi needle like crystals. All crystallites are in the order of 5 μm in length or smaller.

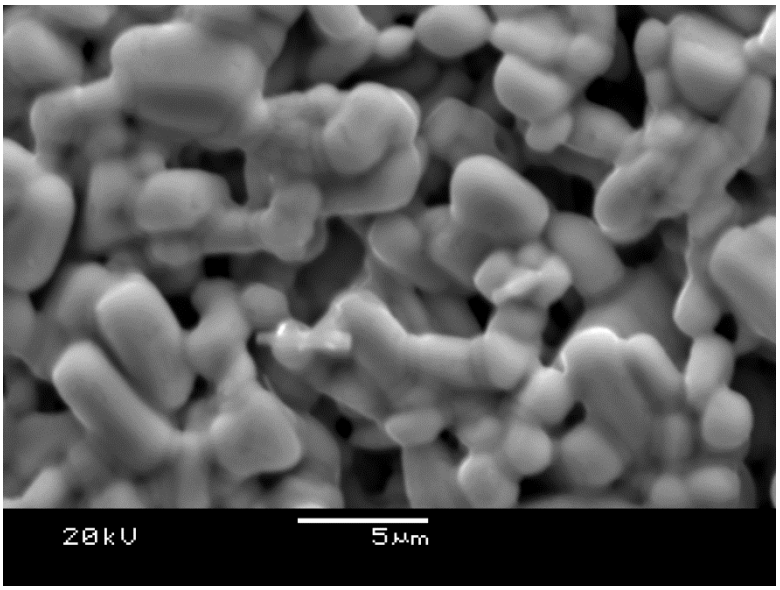

Figure 3.10 A SEM micrograph of $CoSb_2O_4$ in sintered pellet form.

A similar range of crystallite morphology, with comparable sizes, was observed in the SEI of powdered $CoSb_{1.50}Pb_{0.50}O_4$ (Figure 3.11).

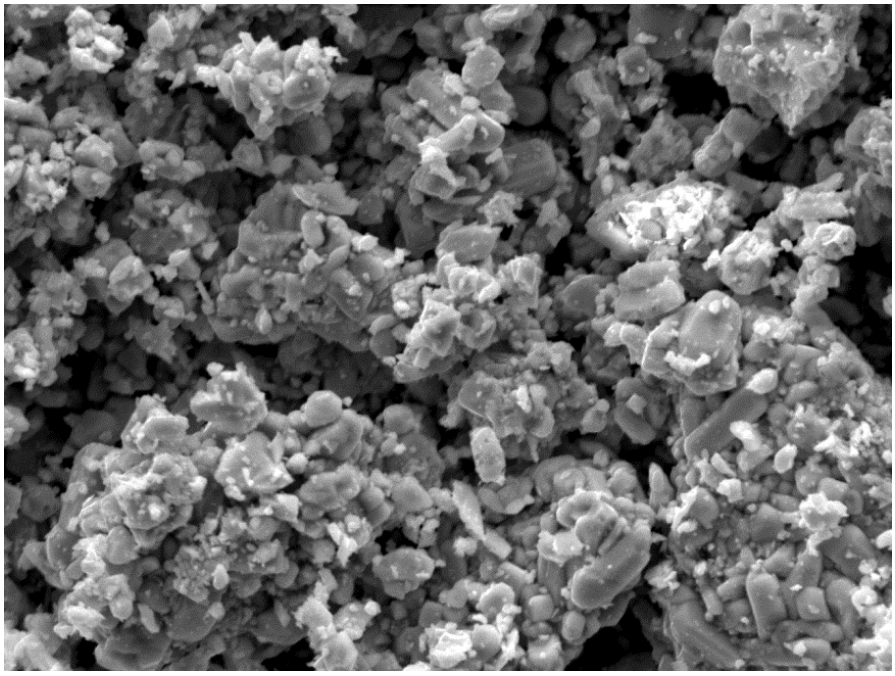

Figure 3.11 A SEM micrograph of $CoSb_{1.50}Pb_{0.50}O_4$; applied magnification x1800. At 20 kV.

3.9 Magnetic susceptibility of $CoSb_2O_4$

Early FC/ZFC measurements taken between 5 and 300 K with an applied field of 100 Oe showed highly unusual magnetic susceptibility behaviour (Figure 3.12). It should be noted that all measurements were made on the same sample as that used in the NPD study. The overall response characteristic of a canted antiferromagnetic system shows a decrease in ZFC susceptibility and increase in FC susceptibility coincident about the Néel temperature (T_N). The negative susceptibility shown in the ZFC measurements below 77 K was highly unusual. Initially believed to be an instrumental artefact the experiment was repeated several times at the same field but the result was consistent. It should be noted that attempts to introduce a ferromagnetic component to the refined magnetic structure were unsuccessful indicating the components small magnitude.

The inverse susceptibility plot (Figure 3.12 inset) clearly shows deviation from linearity. The high temperature paramagnetic region (140-300 K) was used to evaluate the effective moment for Co by application of the Curie-Weiss law, calculated as 5.06 μ_B per

mole with a Weiss constant, θ = 3.28±1 K. The moment consistent with a high spin configuration and large orbital contribution (spin only moment = 3.87 μ_B) supported the findings of the NPD study. The small positive Weiss constant shows net weak ferromagnetic exchange above 140 K possibly originating from the strong underlying ferromagnetic component of the system; However, a reduction to θ = -40±1 K ($87 \leq K \leq 140$) shows the expected dominance in antiferromagnetic interactions approaching T_N. The Néel temperature obtained from temperature settle measurements (*see Section 2.4*) was found to be 79 K, significantly greater than its structural analogues ($FeSb_2O_4$ = 45 K [9], $NiSb_2O_4$ = 47.0(5) K [4]) implying that the strength of magnetic interaction has been greatly increased.

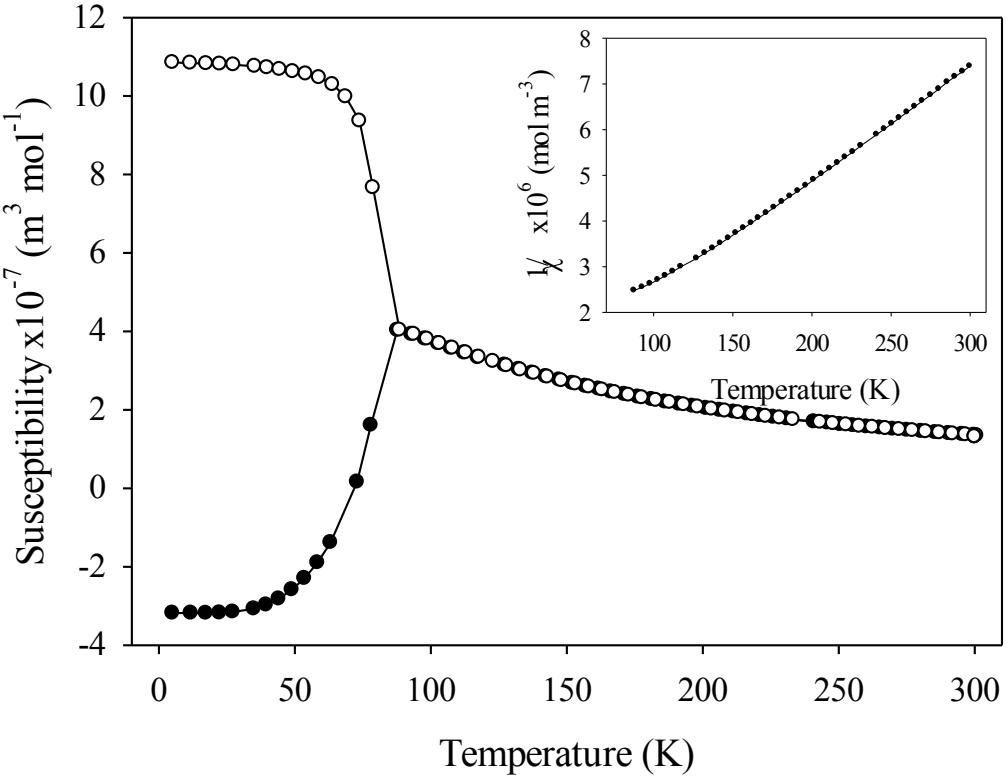

Figure 3.12 The magnetic susceptibility plot of $CoSb_2O_4$ taken in an applied field of 100 Oe showing ZFC measurements (●) and FC measurements (○) in an applied field of 100 Oe under sweep conditions. Inset shows the inverse susceptibility plot of the paramagnetic region, 87-300 K.

Unlikely to be related to superconducting behaviour the negative susceptibility was believed to be related to small trapped fields within the superconducting magnet when at zero

applied field as seen by Kumar *et al* [22] in $CoCr_2O_4$. His group found that upon setting the applied field to zero Oe a small trapped field resulted within the magnet the sign of which was in direct opposition to the previously applied field. Consequently ZFC samples were in fact cooled within a small applied field. Such an effect would usually be of little consequence however the apparent high coercivity of the ferromagnetic component rendered this effect clearly visible. A simple test was instigated where a field of 2T and -2T (both were tested) was applied for 60 seconds immediately after centring but before cooling to 5 K and measurements of the magnetic response were taken on warming in the absence of an applied field. The results (Figure 3.13) clearly showed that when a positive field was initially applied the resultant sample response was negative (-0.00736 emu/g at 5 K) and that when a negative field was applied a positive response was obtained (0.00797 emu/g at 5 K). This demonstrated that when the applied field was set to zero Oe a trapped field (flux) remained the sign of which opposed the previously applied field. ZFC-FC measurements acquired in applied fields of 10, 100 and 1000 Oe where the previously applied field was 100 Oe during centring showed that the negative susceptibility was only removed at 5 K when the applied field surpassed 100 Oe. This demonstrated the high coercivity of the small canted ferromagnetic component of the system.

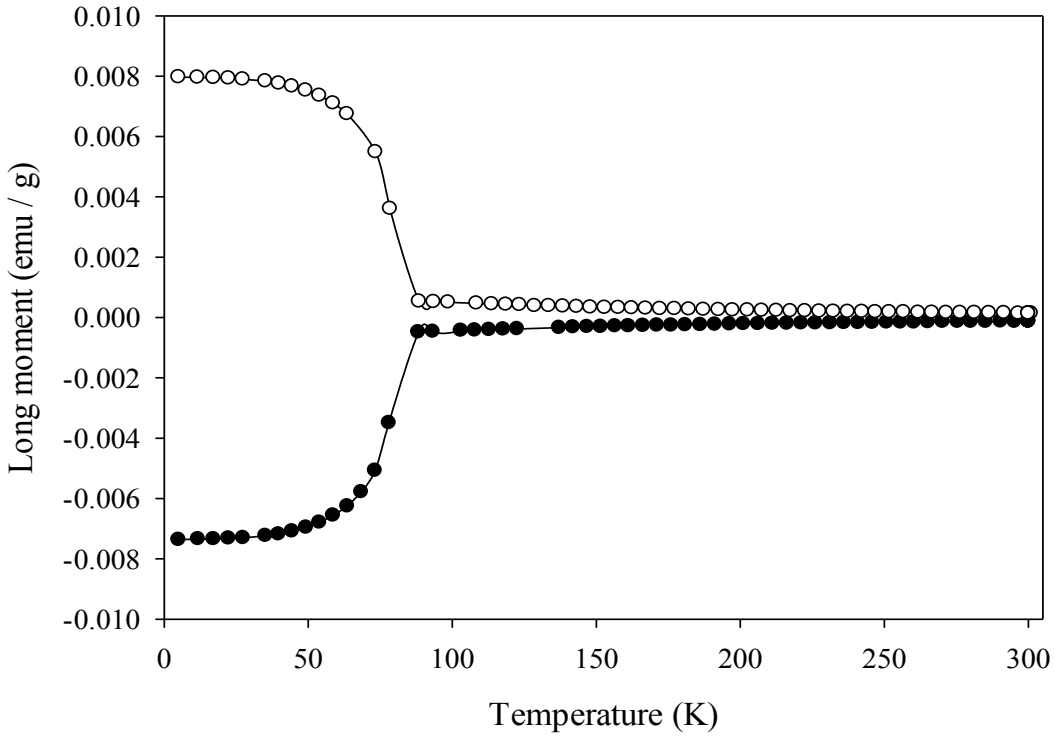

Figure 3.13 A plot demonstrating the effect that the previously applied field has on magnetisation. Measurements taken when the field applied, 2T (●), -2T (○) immediately before ZFC measurements were taken in the absence of any applied field.

Hysteresis measurements were acquired at 5, 70 and 75 K and showed no sign of saturation (Figure 3.14). Hysteresis type behaviour was most clearly seen for the sample held at 75 K where the hysteresis loop exists between 7000 and -7000 Oe. Remnant magnetisation values of 7.29×10^{-4} and -7.32×10^{-4} emu were achieved and the coercive field was found to be 136 Oe (Figure 3.14 inset).

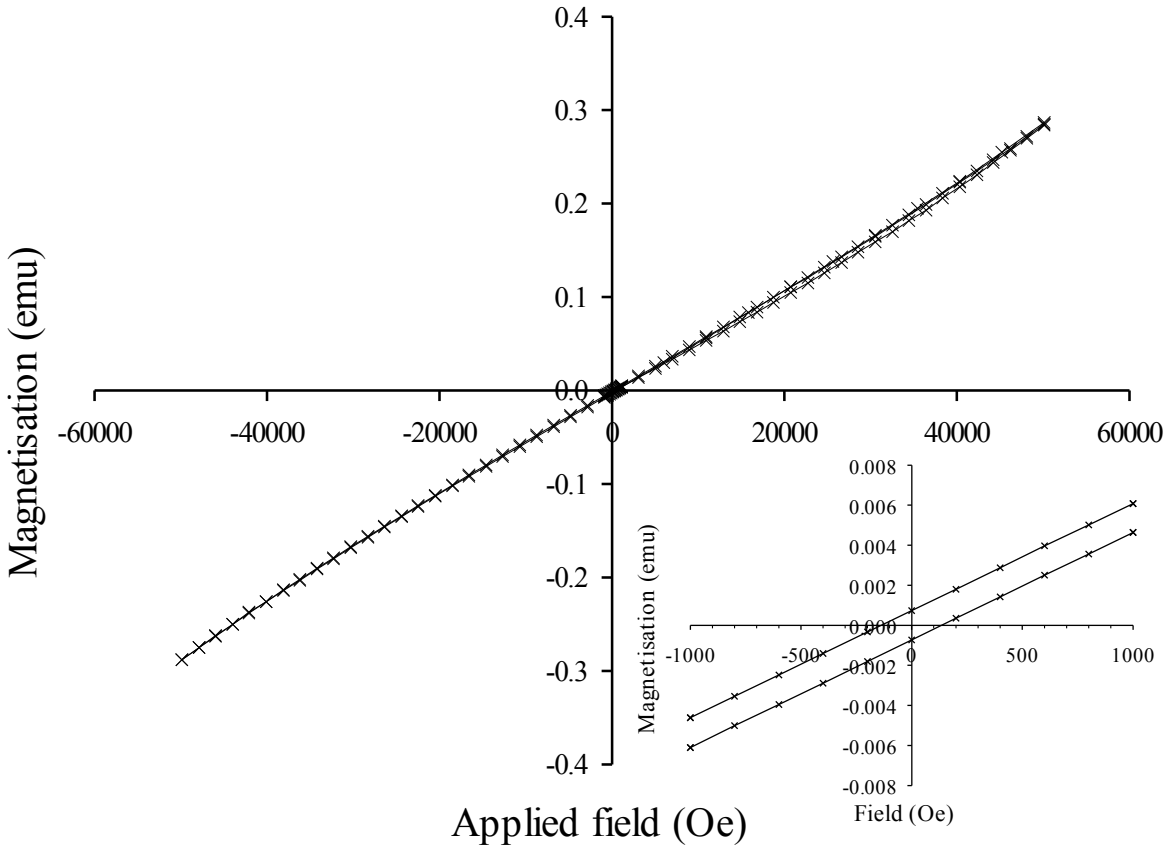

Figure 3.14 A hysteresis plot recorded from $CoSb_2O_4$. Measurements were conducted at 75 K between 50000 and -50000 Oe. The inset shows a magnified view of the hysteresis region.

3.10 Magnetic susceptibility of $CoSb_{1.50}Pb_{0.50}O_4$

The magnetic susceptibility of $CoSb_{1.50}Pb_{0.50}O_4$ also displayed a canted antiferromagnetic response similar to that of $CoSb_2O_4$ (Figure 3.15): however, the structure surrounding the Néel temperature (T_N = 64 K, $FeSb_{1.50}Pb_{0.50}O_4$ = 69 K) was found to be different to that of the lead free variant. An increase is seen in both the ZFC and FC susceptibilities before divergence at a lower temperature than T_N; upon further cooling the FC susceptibility increases until saturation and the ZFC susceptibility decreases ending in a negative value. This indicates further that Co has been oxidised and the superexchange processes have been weakened possibly due to the presence of diamagnetic Sb^{5+}. Deviation from linearity is again observed in the high temperature paramagnetic region of the inverse susceptibility against temperature plot (Figure 3.15 inset). The calculated moment (μ_{eff} = 5.08

μ_B per mole, θ = -20.9±0.6 K) obtained from the high temperature region (110 ≤ T ≤ 300 K) suggests the presence of mixed high spin Co^{2+}/Co^{3+} (Co^{3+}, high spin, spin only moment = 4.90 μ_B) due to the relatively high moment for a slightly cobalt deficient main phase. However, high spin Co^{3+} contradicts the more commonly observed low spin state for this ion (S = 0). It is difficult to conclude on the evidence presented to what extend cobalt oxidation has occurred, if any, but it is believed that some is possible. This would make a highly valuable XANES study to provide more conclusive evidence. It was clear that a reduction in the Weiss constant indicates a strengthening of the exchange process between magnetic ions.

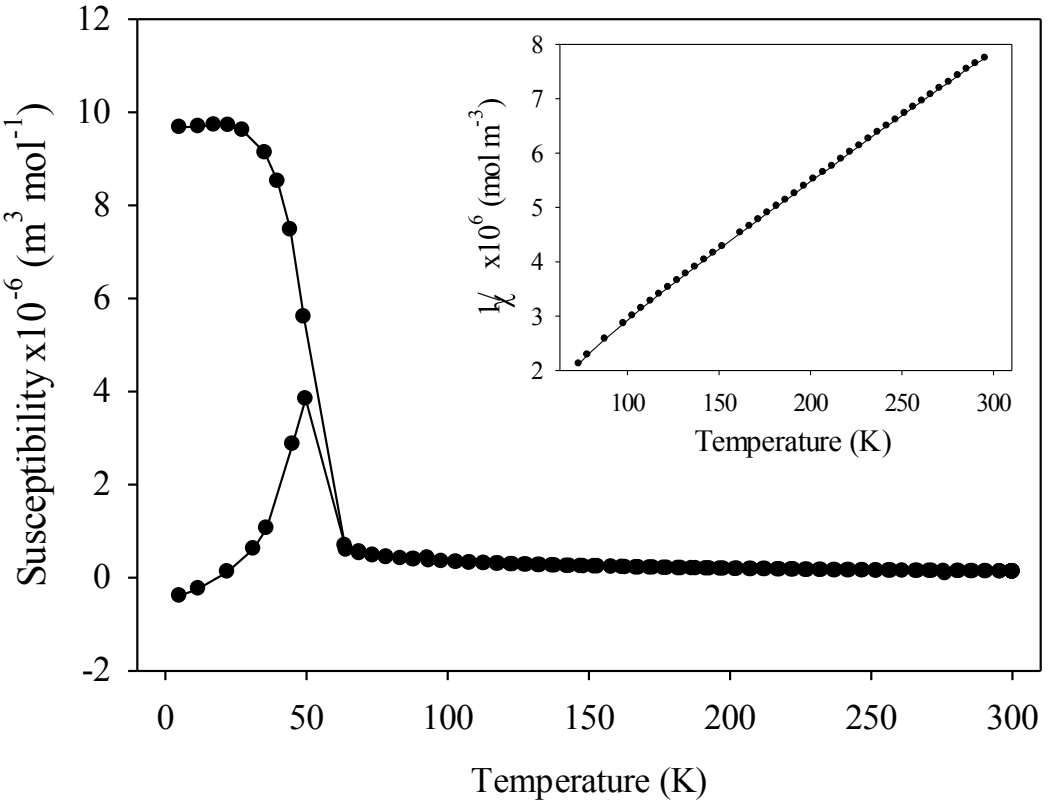

Figure 3.15 The susceptibility plot for $CoSb_{1.50}Pb_{0.50}O_4$ showing ZFC (●) and FC (○) measurements taken in a field of 100 Oe under temperature sweep conditions. Inset shows the inverse susceptibility trend in the temperature range 77≤ T ≤ 295 K.

3.11 Thermogravimetric analysis of $CoSb_2O_4$

Thermogravimetric analysis demonstrated the appreciable resistance of the material to oxidation as evidenced by the absence of a mass increase below 500˚C (Figure 3.16). Above 550˚C $CoSb_2O_4$ began to rapidly uptake oxygen. Coincidence of the large mass increase with large exotherm (dashed line) was indicative of a significant structural alteration upon heating. The formation of $CoSb_2O_6$ was confirmed by mass increase calculations and XRPD as the high temperature product.

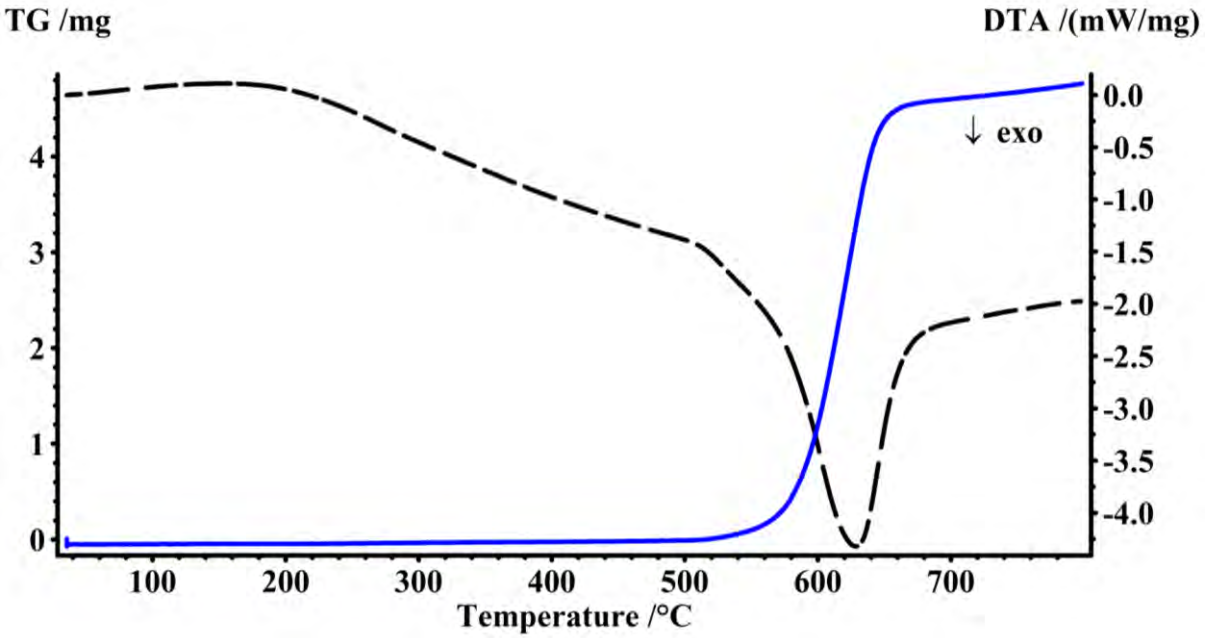

Figure 3.16 A TGA plot representative of $CoSb_2O_4$. Mass increases (solid blue line) and associated enthalpy change (dashed black line) measurements were taken from a sample of around 50mg in an atmosphere of O_2, using N_2 as a protective gas.

3.12 Variable temperature XRPD of $CoSb_2O_4$

Variable temperature XRPD (VT-XRPD) was performed on a polycrystalline sample of $CoSb_2O_4$ under standard atmospheric conditions between 303-753 K (*see Appendix 1.1* for the calibrated temperatures). The resultant powder patterns were refined and the results, as displayed in Figure 3.17, show a linear expansion of both *a* (Δa = 0.0561 Å) and *c* (Δc = 0.0275 Å) upon heating. A similar trend is seen in $MnSb_2O_4$ [23] where expansion of *a* over a

similar temperature range is nearly also double that of *c*; however, the expansion of *a* in $MnSb_2O_4$ agrees better with an exponential type increase than is presented here for $CoSb_2O_4$. This implies that the Co-O_{ap} bond is perhaps the weakest in the octahedral coordination sphere resulting in greater changes in *a*; however, NPD studies are required to gain more accurate oxygen positions for detailed analysis. It should be noted that the 736 K, and subsequent, powder patterns contained a $CoSb_2O_6$ impurity which was accounted for in the refinements. The lattice parameters refined for the main phase, based upon data acquired during cooling the sample once the maximum temperature had been reached, differ slightly from those initially refined upon heating. This most likely reflects the sample degradation upon heating.

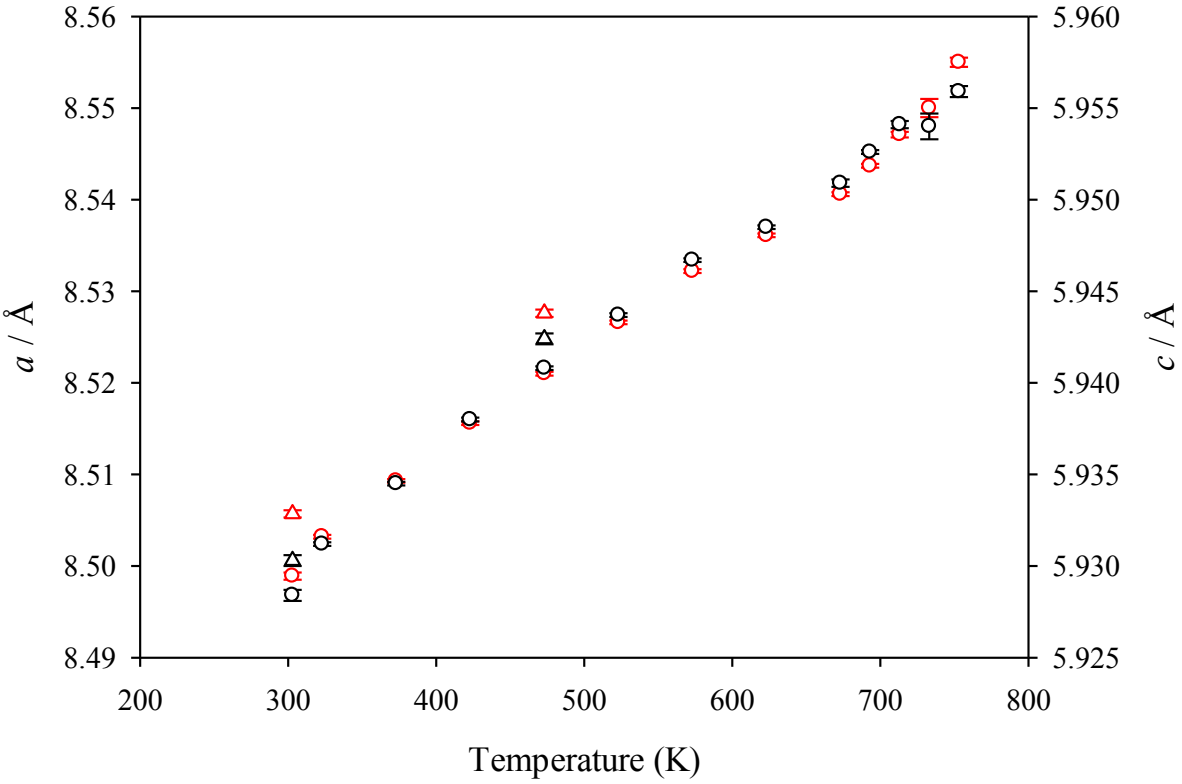

Figure 3.17 A plot presenting the results from a VT-XRPD study showing how lattice parameters of $CoSb_2O_4$ change on heating (○) to 753 ±30 K and cooling to 303 K (Δ). Red and Black symbols represent changes in *a* and *c* respectively.

3.13 Absorption characteristics

Absorption characteristics of $CoSb_2O_4$ were investigated by placing a small quantity of pre-dried (high vac, 5hrs) and X-ray verified sample in separate baths of deionised water and 1M NaOH solution. Samples were left submerged at both room temperature and under reflux conditions for 1 hour. Excess water was removed and the samples interrogated by XRPD. There was no pronounced change in any of the lattice parameter.

3.14 Conclusions

This chapter has shown the nuclear and magnetic characterisation of $CoSb_2O_4$ for the first time. The nuclear structure is seen to be consistent with $P4_2/mbc$ symmetry in analogy to schafarzikite and its equivalent (MSb_2O_4) synthetic variants (where M = Mn, Ni, Zn). The magnetic structure was determined to be of C- type, with FM ordering within a chain and AFM ordering in the plane, orientated along the primary *z* axis. This was explained by a reduction in strength of direct exchange between adjacent intrachain TM ions as a result of an extension of *c*, hence increase in TM-TM separation distance. This increased the dominance of the 90˚ superexchange resulting in ferromagnetic ordering within a chain. The moment magnitude 3.72(2) μ_B determined from NPD indicated a large orbital contribution to the moment. This was supported by the high temperature paramagnetic moment (5.06 μ_B) determined from the magnetic susceptibility measurements.

$CoSb_2O_4$ was found to be a canted antiferromagnetic system which possessed a highly unusual, rare magnetic phenomenon. The negative susceptibility, seen in ZFC/FC sweeps under 100 Oe, is believed to be related to the high coercivity of the ferromagnetic component of the canted system, which was observed as a result of trapped flux within the magnet of the magnetometer. This was supported by the findings of Kumar *et al* [22].

TGA data showed that the system is resistant to oxidation up to around 500˚C, in an atmosphere of O_2, where after rapid reaction with oxygen occurs resulting in the oxidation of Sb^{3+} to Sb^{5+} and formation of $CoSb_2O_6$.

Partial oxidation of Co^{2+} to Co^{3+} was attempted by the substitution of Sb^{3+} with Pb^{2+} as had been previously tried in the $MnSb_2O_4$ and $FeSb_2O_4$ phases. $CoSb_{1.50}Pb_{0.50}O_4$ could not be synthesised as a pure product; $Co_{2.33}Sb_{0.66}O_4$ was the main impurity although at relatively low concentrations. Despite this, refinement of NPD data suggested the simultaneous oxidation of Co^{2+} and Sb^{3+} where some Co was subsequently substituted by Sb^{5+}. The magnetic structure was mainly consistent with a C_z mode for the same reasons as in $CoSb_2O_4$ but that a small G_x component coexisted as a result of the substitution of Co for Sb^{5+}. Magnetic susceptibility measurements indicated further that some cobalt had been oxidised by a change in the materials magnetic susceptibility but the extent of the oxidation remains uncertain. This, in conjunction with the TGA data from $CoSb_2O_4$ showed that it is difficult to solely oxidise Co^{2+} in this phase, as had been shown in the lead doped $MnSb_2O_4$ compounds, but crucially suggested that it is possible to oxidise some Co^{2+} to Co^{3+}.

3.15 References

[1] J. R. Gavarri, A. W. Hewat, *J. Solid State Chem.* **49** (1983) 14.
[2] J. A. Gonzalo, D. E. Cox, G. Shirane, *Phys. Rev.* **147** (1966) 415.
[3] E. Koyama, I. Nakai, K. Nagashima, *Nippon Kagaku Kaishi* **6** (1979) 793.
[4] H. T. Witteveen, *Solid State Commun.* **9** (1971) 1313.
[5] E. G. Puebla, E. G. Rios, A. Monge, I. Rasines, *Acta Crystallogr.* **B 38** (1982) 2020.
[6] R. Fischer, F. Pertlik, *Tschermaks Min. Petr. Mitt.* **22** (1975) 236.
[7] S. Ståhl, *Arkiv för Kemi, Min. och Geol.* **B 17** (1943) 1.
[8] A. M. Abakumov, M. G. Rozova, E. V. Antipov, J. Hadermann, G. Van Tendeloo, M. V. Lobanov, M. Greenblatt, M. Croft, E. V. Tsiper, A. Llobet, K. A. Lokshin, Y. S. Zhao, *Chem. Mater.* **17** (2005) 1123.
[9] M. J. Whitaker, R. D. Bayliss, F. J. Berry, C. Greaves, *J. Mater. Chem.* **21** (2011) 14523.
[10] R. Chater, K. Chhor, J. R. Gavarri, C. Pommier, *Mat. Res. Bull.* **20** (1985) 1427.
[11] T. Hahn, "*International Tables for Crystallography*", Fifth ed, (2005).

[12] R. Chater, J. R. Gavarri, A. Hewat, *J. Solid State Chem.* **60** (1985) 78.
[13] R. D. Shannon, *Acta Crystallogr.* **A 32** (1976) 751.
[14] C. J. Howard, *J. Appl. Crystallogr.* **15** (1982) 615.
[15] P. Thompson, D. E. Cox, J. B. Hastings, *J. Appl. Crystallogr.* **20** (1987) 79.
[16] J. N. Reimers, J. E. Greedan, C. V. Stager, R. Kremer, *J. Solid State Chem.* **83** (1989) 20.
[17] B. C. Frazer, P. J. Brown, *Phys. Rev.* **125** (1962) 1283.
[18] P. Gambardella, M. Blanc, H. Brune, K. Kuhnke, K. Kern, *Phys. Rev.* **B 61** (2000) 2254.
[19] R. Chater, J. R. Gavarri, *J. Solid State Chem.* **59** (1985) 123.
[20] K. Motida, S. Miyahara, *J. Phys. Soc. Japan* **28** (1970) 1188.
[21] D. J. Craik, "*Magnetic Oxides: Part 1*", John Wiley and Sons, London (1975).
[22] N. Kumar, A. Sundaresan, *Solid State Commun.* **150** (2010) 1162.
[23] H. Fjellvåg, A. Kjekshus, *Acta Chem. Scand.* **A 39** (1985) 389.

Chapter 4

Synthesis and characterisation of $Co_{1-x}Fe_xSb_2O_4$ (x = 0.25, 0.50 and 0.75)

4.1 Introduction

Reports of mixed TM schafarzikite systems are limited [1-2]. Hence a large area of science appeared amenable to detailed enquiry. The recently reported success of oxidising iron in the lead doped $FeSb_2O_4$ system [3], without the associated oxidation of antimony as seen in the manganese [4] and cobalt variants [5] offered a powerful route for oxidising the cations in the octahedral chains and thereby inducing different magnetic, electrical and oxidative properties. The $Co_{1-x}Fe_xSb_2O_4$ (x = 0.25, 0.50 and 0.75) compounds were therefore synthesised as a foundation for creating mixed Co/Fe (4*d*), Sb/Pb (8*h*) systems with partially oxidised chains of TMs, whilst maintaining the original $P4_2/mbc$ symmetry. Another goal of this work was to ascertain at which point the main magnetic ordering of the system changed from a dominant A mode ($FeSb_2O_4$ [3, 6]) to a dominant C mode ($CoSb_2O_4$ *Chapter 3*). This chapter presents for the first time the detailed structural, magnetic and oxidative properties of the $Co_{1-x}Fe_xSb_2O_4$ system which were found to retain their original $P4_2/mbc$ symmetry whilst displaying highly complex magnetic and oxidative properties.

4.2 Synthesis

The materials were synthesised by the ceramic method using intimately ground mixtures of anhydrous reagents (Sb_2O_3, CoO, Fe_2O_3 (<5 micron powder, ≥ 99%, Sigma-Aldrich), and Sb (100 mesh, 99.5% trace metals basis, Sigma-Aldrich) in the stoichiometric

ratio dictated by the final composition under static vacuum. The materials were initially heated at 700˚C for extended periods of 24 hrs. This produced products which showed similar symmetry to that of $CoSb_2O_4$ but which also contained minor impurity components ($CoFe_2O_4$, and possibly $CoSb_3$). The addition of excess antimony oxide (3 wt %) to the reaction mixture to compensate for Sb_2O_3 loss at high temperatures led to the removal of the impurities and to pure single phase products. The phases reported in this chapter were formed by heating stoichiometric mixtures of reactants within alumina inserts inside evacuated fused silica tubes for two 6 hour periods at 700˚C with intermittent grinding. All samples were furnace cooled before analysis.

4.3 Structural characterisation

4.3.1 Characterisation by XRPD

The XRPD patterns obtained from $Co_{1-x}Fe_xSb_2O_4$ (x = 0.25, 0.50, 0.75) (Figure 4.1) showed no sign of any impurity phases. Each ideal composition could be indexed with a high figure of merit (> 20) where all reflections were included (Table 4.1) demonstrating that single phases had been synthesised. The values of the lattice parameters varied roughly between the limits set by $CoSb_2O_4$ (a = 8.49340(9) Å, c = 5.92387(8) Å) and $FeSb_2O_4$ (a = 8.61574(9) Å, c = 5.92068(8) Å) [3]. The similarity between the powder patterns of $CoSb_2O_4$ and the $Co_{1-x}Fe_xSb_2O_4$ phases and systematic shifting of the (220) peak to higher d spacing upon insertion of the larger Fe^{2+} (ionic radius, all high spin (HS): Co^{2+} = 0.745 Å; Fe^{2+} = 0.780 Å) [7] species indicated successful mixing of Co^{2+} and Fe^{2+} and retention of original symmetry. Full structural analysis of these samples was performed and the main structural details are discussed in *section 4.3.2*.

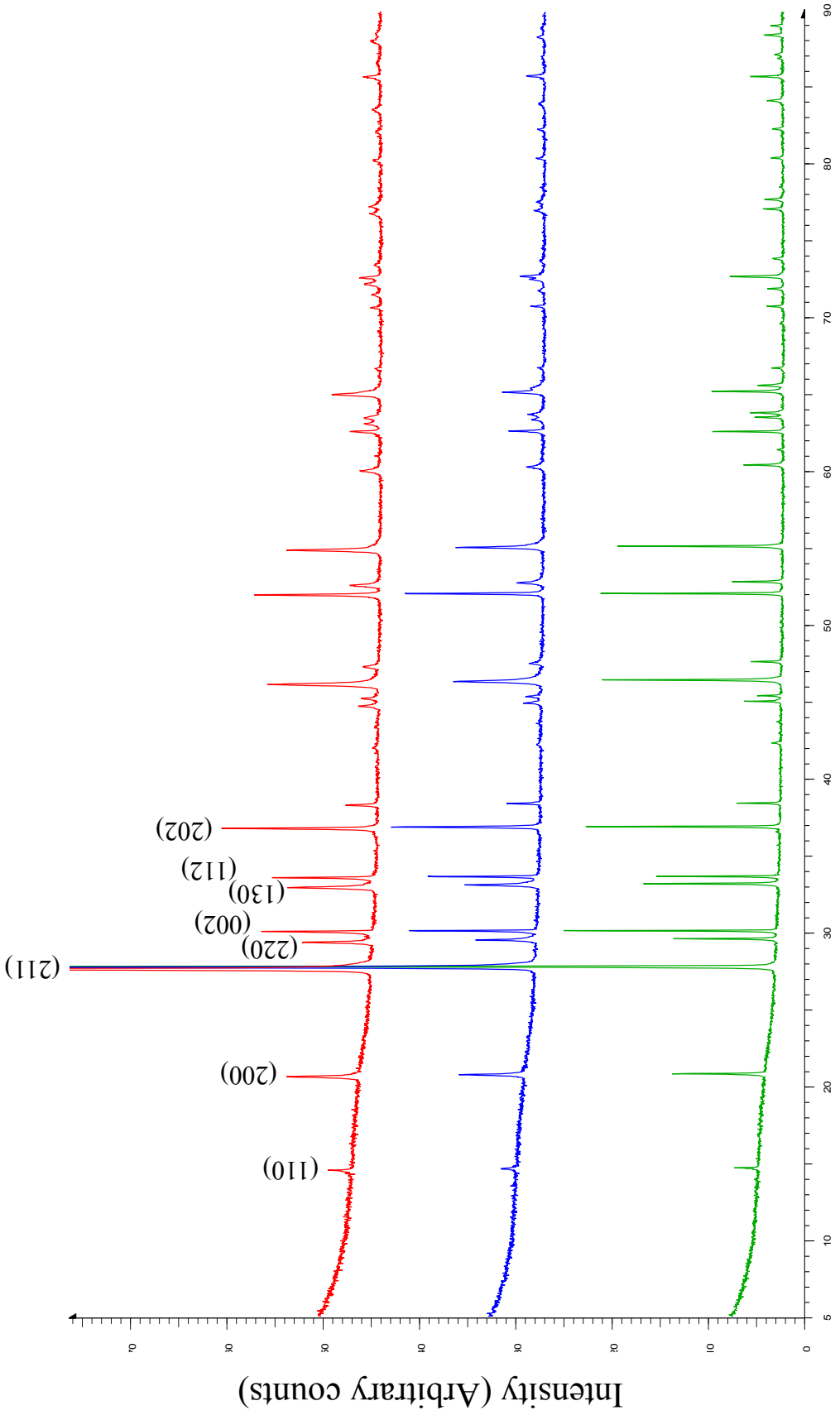

Figure 4.1 Overnight powder patterns collected on the D8 transmission diffractometer. The plots represent $Co_{0.75}Fe_{0.25}Sb_2O_4$ (green), $Co_{0.50}Fe_{0.50}Sb_2O_4$ (blue) and $Co_{0.25}Fe_{0.75}Sb_2O_4$ (red) respectively.

Table 4.1 A selection of comparable ˚2θ, (*hkl*), and *d* spacing's from indexing of the overnight XRPD patterns for $Co_{0.75}Fe_{0.25}Sb_2O_4$, $Co_{0.50}Fe_{0.50}Sb_2O_4$, and $Co_{0.25}Fe_{0.75}Sb_2O_4$. λ = 1.5406 Å.

$Co_{0.75}Fe_{0.25}Sb_2O_4$			$Co_{0.50}Fe_{0.50}Sb_2O_4$			$Co_{0.25}Fe_{0.75}Sb_2O_4$		
˚2θ	(*hkl*)	d_{obs}	˚2θ	(*hkl*)	d_{obs}	˚2θ	(*hkl*)	d_{obs}
14.692	(110)	6.0245	14.604	(110)	6.0605	14.488	(110)	6.1088
20.819	(200)	4.2632	20.726	(200)	4.2823	20.600	(200)	4.3082
27.806	(211)	3.2058	27.719	(211)	3.2158	27.609	(211)	3.2283
29.619	(220)	3.0136	29.520	(220)	3.0235	29.358	(220)	3.0398
30.157	(002)	2.9610	30.098	(002)	2.9667	30.049	(002)	2.9715
33.214	(310)	2.6951	33.092	(310)	2.7048	32.929	(310)	2.7179
33.687	(112)	2.6584	33.638	(112)	2.6622	33.569	(112)	2.6675
36.936	(202)	2.4317	36.871	(202)	2.4358	36.779	(202)	2.4417
38.458	(212)	2.3390	38.394	(212)	2.3426	38.301	(212)	2.3481
42.392	(400)	2.1305	42.254	(400)	2.1371	42.034	(400)	2.1478
43.762	(410)	2.0669	43.629	(410)	2.0729	43.401	(410)	2.0833
45.095	(330)	2.0088	44.967	(330)	2.0143	44.750	(330)	2.0236
45.466	(312)	1.9933	45.379	(312)	1.9969	45.226	(312)	2.0034
46.500	(411)	1.9513	46.359	(411)	1.9570	46.163	(411)	1.9649
47.669	(420)	1.9062	47.543	(420)	1.9110	47.304	(420)	1.9201
52.115	(213)	1.7535	52.082	(213)	1.7546	51.992	(213)	1.7575
52.884	(402)	1.7298	52.781	(402)	1.7330	52.610	(402)	1.7383
55.203	(332)	1.6625	55.099	(332)	1.6655	54.909	(332)	1.6708
60.492	(521)	1.5292	60.335	(521)	1.5328	60.068	(521)	1.5390
62.682	(004)	1.4809	62.674	(004)	1.4812	62.636	(004)	1.4820
63.616	(530)	1.4614	63.418	(530)	1.4656	63.141	(530)	1.4713
63.889	(512)	1.4558	63.756	(512)	1.4586	63.526	(512)	1.4633
65.288	(413)	1.4280	65.203	(413)	1.4297	65.057	(413)	1.4325
66.815	(204)	1.3991	66.765	(204)	1.4000	66.719	(204)	1.4008
70.841	(224)	1.3290	70.804	(224)	1.3297	70.706	(224)	1.3313
a (Å) =	8.5230(3)			8.5394(6)			8.5660(4)	
c (Å) =	5.9243(3)			5.9197(6)			5.9177(3)	
Volume ($Å^3$) =	430.35			431.67			434.22	
c/*a*	0.695			0.693			0.691	

4.3.2 Structural and magnetic characterisation by NPD

NPD patterns of the samples were collected at PSI-Zurich ($Co_{0.25}Fe_{0.75}Sb_2O_4$ at 300 and 1.5 K; $Co_{0.75}Fe_{0.25}Sb_2O_4$ at 300 and 2 K) and the ILL ($Co_{0.50}Fe_{0.50}Sb_2O_4$ at 300 and 4 K). Full intensity data sets were used unless otherwise stipulated. Least squares analysis of all samples initiated using $P4_2/mbc$ symmetry, the atomic coordinates obtained from the refinement of $CoSb_2O_4$, lattice parameters from the indexed XRPD patterns, and the

occupancies of the Co/Fe (4*d*) site were set to be consistent with stoichiometry. Several differences were noticed between the data sets and will be discussed later. The neutron wavelength used in the refinement of all samples was calibrated in an analogous fashion to that used for $CoSb_2O_4$ (*Chapter 3*).

4.3.2.1 Characterisation of $Co_{0.25}Fe_{0.75}Sb_2O_4$ at 300 K

Inspection of the powder pattern showed a weak magnetic (101) reflection at 21.7 ˚2θ which indicated a small Fe_3O_4 impurity. All refinements of this compound thereafter included both a nuclear and magnetic cell for the impurity for which lattice and profile parameters were initially refined and then fixed throughout. The refinement proceeded by initially obtaining a fit where all fractional coordinates, IDPs, ZPE, lattice constants, scale factors, profile parameters for profile function 2 (Pseudo-Voigt) and preferred orientation (March-Dollase [001]) were refined ($\lambda_{refined}$ = 1.88434(2) Å from λ_{PSI} = 1.8851810 Å). In all refinements of this nature (i.e. where two different cations coexisted on the same site) constraints were placed on atomic coordinates and IDPs to ensure unified variation. In later discussion, mention of all parameters varying independently excludes these species (e.g. the U_{iso} value for Co and Fe on the 4*d* site remains constrained to vary as a single unit). The fit parameters (χ^2 = 6.764, R_{wp} = 0.0550, 31 variables) indicated the necessity for further improvement. Visual inspection of the difference plot where all peak intensities were closely matched as were peak positions suggested the structural model was correct. It was apparent that the elevated figure of merit was due to poor profile fitting. Equivalent refinement methods were tested using profile functions 3 (Finger-Cox-Jephcoat) and 4 with the improvement of χ^2 = 6.588 R_{wp} = 0.0547 and χ^2 = 6.652, R_{wp} = 0.0549 respectively. Inclusion of the anisotropic micro strain parameters for the three profile functions resulted in a significant improvement of the fits for functions 3 and 4 only (χ^2 = 6.082, R_{wp} = 0.0521, 34

variables; χ^2 = 4.528, R_{wp} = 0.0453, 36 variables and χ^2 = 4.165, R_{wp} = 0.0435, 36 variables for profile functions 2, 3, and 4 respectively). It was decided on the basis of goodness of fit that profile function 4 should be used. Whilst the model appeared correct the slightly higher U_{iso}*100 value for the O_{ap} position (2.17(4) Å^2 compared with values centred about 1.5 Å^2 for all other positions) prompted further improvement. By allowing anisotropic displacement the final fit was improved further (Figure 4.2, χ^2 = 3.772 R_{wp} = 0.0413, 39 variables) and demonstrated significant atomic displacement in the *xy* plane (2.53(5) Å^2) when compared with *z* (1.42(8) Å^2). The Fe_3O_4 impurity was calculated as being ~1 wt%, below the threshold of detection for the D8 diffractometer. Significant crystal morphology effects were observed in the intensities of the XRPD refinement and a preferred orientation correction (March-Dollase, refined ratio = 0.936 (4)) was applied along [001]. Some evidence of preferred orientation was seen in the NPD data but the contribution was small, consequently a similar correction was included in the NPD refinement.

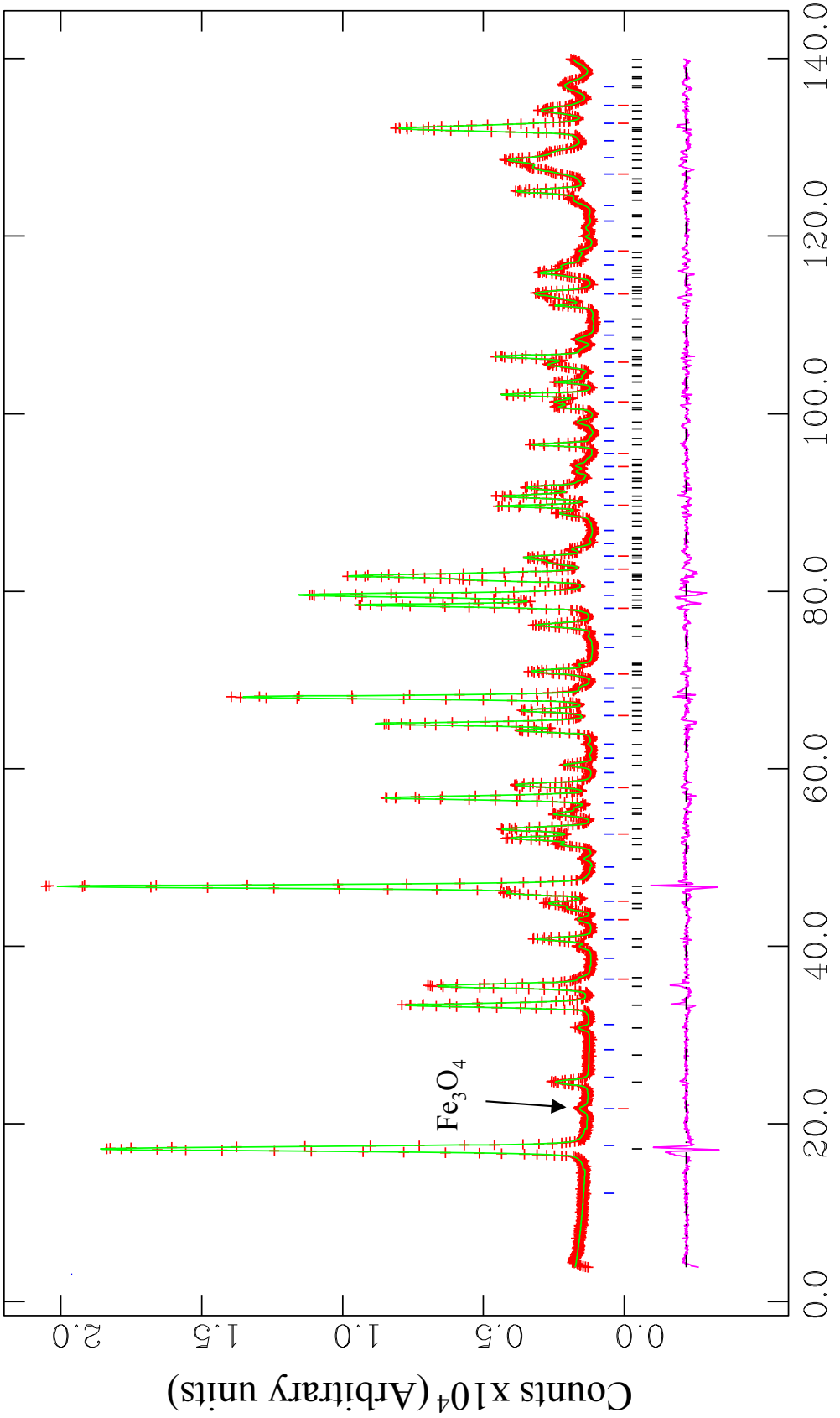

Figure 4.2 The final 300 K NPD Rietveld refinement of $Co_{0.25}Fe_{0.75}Sb_2O_4$ in $P4_2/mbc$. The (+) observed (|) calculated and (|) difference profiles are as indicated and the tick marks represent $Co_{0.25}Fe_{0.75}Sb_2O_4$ nuclear phase (Black), Fe_3O_4 nuclear phase in $Fd3m$, a = 8.3996 Å (Red), and the Fe_3O_4 magnetic phase in $P1$ (Blue). The magnetic (101) peak of magnetite is indicated.

4.3.2.2 Characterisation of $Co_{0.25}Fe_{0.75}Sb_2O_4$ at 1.5 K

The nuclear structure was first satisfactorily refined. Nuclear and magnetic structures for the Fe_3O_4 impurity were included for completeness and the neutron wavelength set to that used for the refinement at 300 K. Varying the anisotropic displacement parameters for the O_{ap} position again showed significant variation in the *xy* plane over *z* and was therefore included throughout. The emergence of new intense reflections at discrete 2θ values were attributed to the magnetic ordering of the system, evident from satisfactory nuclear phase refinement. It was immediately apparent from visual inspection that two sets of magnetic peaks were present and so at least two different magnetically ordered components of the system existed. Indexing revealed the most intense magnetic peaks (11.93 and 25.06 $^{\circ}2\theta$) of each set to be the (100) and (111) reflections indicative of a C and A mode respectively (Figure 4.3). Initially a magnetic cell, consisting of Co ions only, with lattice parameters consistent with the refined nuclear phase was added to the refinement and used to test all orientations of each mode including tilting models where spin directions were allowed to vary between *x* and *z* as applied in the case of $CoSb_2O_4$ (*Section 3.5.2*). The symmetry-free space group *P*1 was again used (as in all refinements reported) to refine the magnetic structures since it allowed unrestricted orientation of the spins to be examined. The form factor was set for Co^{2+}, consistent with the applied magnetic cell. The findings corroborated the indexing and an A mode was found to be orientated in the *x* direction and the C mode along *z*. Constraints, as for all magnetic refinements, were two fold and enabled the identified modes to be combined into a single phase whilst being refined independently. The first constraint ensured the moments lay only in the directions specified where the spin magnitude in each direction was initially fixed. The total moment for the model was initially set to reflect the total spin-only value (2*S*) [8]. The second type of constraint ensured that, when varying the

moment magnitude for a particular mode, spins remained parallel and the magnitudes for each vector component were equal, i.e. all M_x components for an A mode had the same magnitude for their respective direction. The magnitude of the individual mode components when combined into a single phase was maintained. Combination of the two magnetic structures into a single model (Table 4.2) and allowing the magnetic moment magnitudes to vary provided a very good fit ($\chi^2 = 4.780$, $A_x = 2.45(2)\ \mu_B$ and $C_z = 1.25(1)\ \mu_B$). The suitability of the magnetic form factor was investigated for effects on the overall refined moments; the cobalt-containing magnetic cell was substituted for one of iron only and the form factor set to be consistent with Fe^{2+}. The final fit, chosen as the representative structure, was for lattice constants, all atomic coordinates, preferred orientation, ZPE, IDPs (ADP for O_{ap} only), profile parameters, scale factor and back ground being refined. It showed an improvement (Figure 4.3, $\chi^2 = 4.442$, 42 variables, $R_{wp} = 0.0463$, $A_x = 2.51(2)\ \mu_B$ and $C_z = 1.27(1)\ \mu_B$; $a = 8.5677(1)$ Å, $c = 5.90455(9)$ Å) with significantly differently magnetic moments but within 3 standard deviations of each other and was chosen as the best representation of the structure.

Table 4.2 A Typical magnetic arrangement used to initially refine the magnetic structure, using the space group *P*1. The positive and negative sign of the moment indicate the spin direction assigned to that site. The model shows an A mode along *x* and a C mode along *z*. Moment values are typical of those used as the basis for refinement and reflect the relative ratio of intensity for the magnetic peaks corresponding to each mode.

Atom	Position(*x, y, z*)	M_x	M_y	M_z
Co1	(0, 0.5, 0.25)	2	0	1
Co2	(0, 0.5, 0.75)	-2	0	1
Co3	(0.5, 0, 0.25)	2	0	-1
Co4	(0.5, 0, 0.75)	-2	0	-1

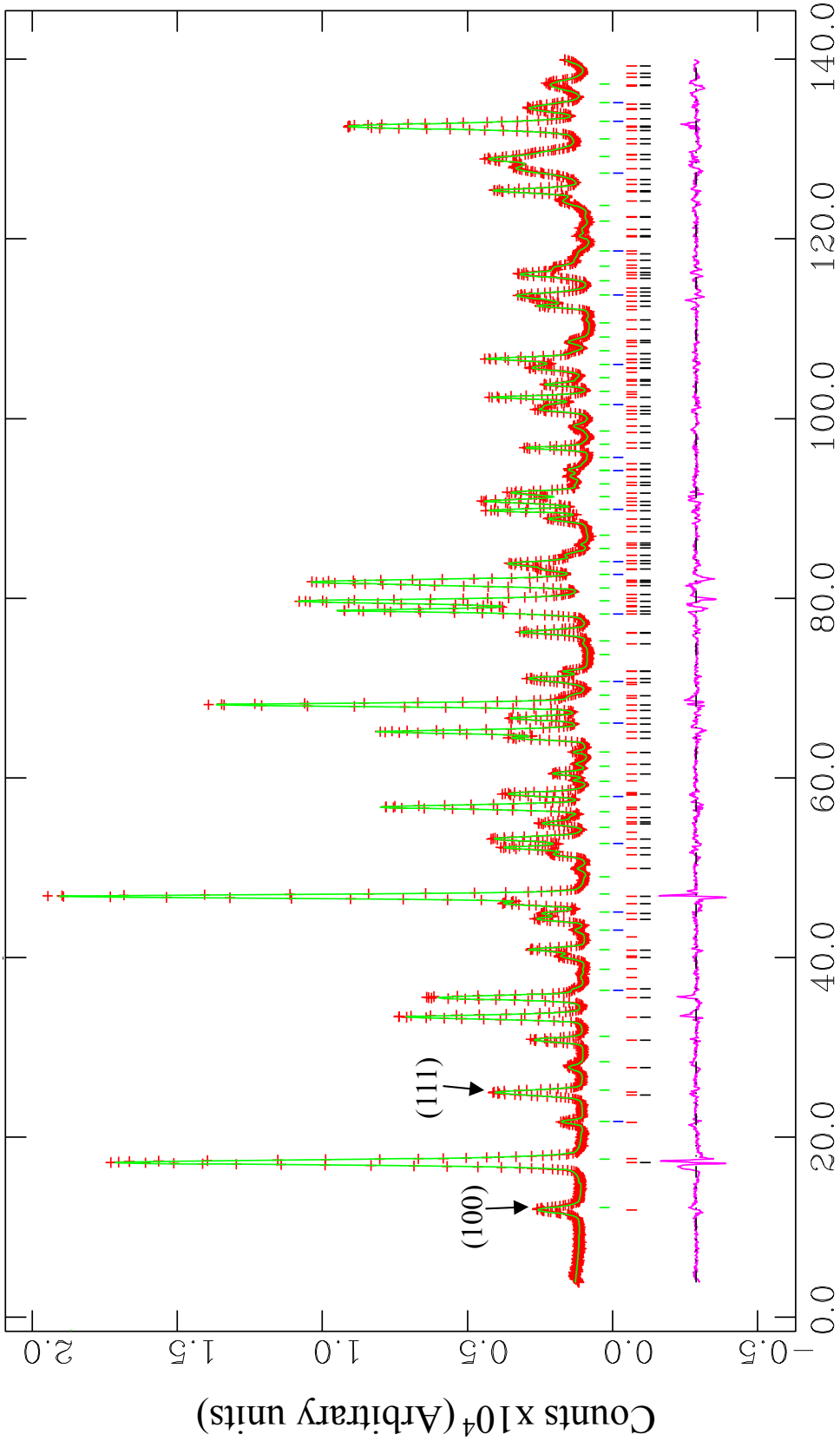

Figure 4.3 (+) observed (|) calculated and (|) difference profiles from the final fit of 1.5 K NPD data for $Co_{0.25}Fe_{0.75}Sb_2O_4$. Tick marks represent $Co_{0.25}Fe_{0.75}Sb_2O_4$ nuclear phase in spacegroup $P4_2/mbc$ (black), $Co_{0.25}Fe_{0.75}Sb_2O_4$ magnetic phase in $P1$ (red), Fe_3O_4 nuclear phase in $Fd3m$, $a = 8.3836$ Å (blue), and Fe_3O_4 magnetic phase in $P1$ (green). The (100) and (111) peaks indicative of C and A modes are indicated.

4.3.2.3 Characterisation of $Co_{0.50}Fe_{0.50}Sb_2O_4$ at 300 K

Nuclear structure refinement was performed in the same manner as that used for previous refinements, no evidence for Fe_3O_4 was observed. For this compound both high intensity and high resolution data sets were investigated due to significant broadening of the first magnetic peak in the data measured at 4 K (discussed in section 4.3.2.4). High intensity data sets at 300 K were used for better comparison throughout the series. Neutron wavelengths were set to 1.59178 Å, concordant with those calibrated for $CoSb_2O_4$. The initial refinement showed no change of symmetry but the fit produced had a high value of χ^2 (8.269) whilst displaying excellent symmetry coincidence with the model. It was apparent from profile fitting and miss matching of intensities that improvement was possible. Profile Functions 2, 3, and 4 were tested (*Appendix 2.1*), the statistics shown in (Table 4.3) are for all atomic positions, IDPs, ZPE, back ground, scaling, profile parameters and preferred orientation being refined independently. The lower statistical values produced for profile function 2 (Table 4.3) and visual inspection of the fit demonstrated that this was the most suitable function for phase analysis.

Table 4.3 Obtained statistics, atomic positions, lattice constants and various other parameters obtained from the refinement of $Co_{0.50}Fe_{0.50}Sb_2O_4$ at 300 K. HI data used as a guide to determine the most suitable profile function to use.

		Profile Fn 2	Profile Fn 3	Profile Fn 4
Co/Fe	$100*U_{iso}$	0.95(3)	0.83(4)	0.77(4)
Sb	(x,y,0)	0.1760(2), 0.1642(2)	0.1759(2), 0.1645(2)	0.1760(2), 0.1646(2)
	$100*U_{iso}$	1.14(3)	0.99(3)	0.94(3)
O1	(x,y,0)	0.0984(2), 0.6400(2)	0.0988(2), 0.6403(2)	0.0986(2), 0.6402(2)
	$100*U_{iso}$	1.27(3)	1.14(4)	1.08(3)
O2	(x,y,0)	0.6790(1), 0.1790(1)	0.6794(1), 0.1794(1)	0.6794(1), 0.1794(1)
	$100*U_{iso}$	1.76(3)	1.60(3)	1.52(3)
χ^2		7.095	8.958	8.680
R_{wp}		0.0405	0.0455	0.0448
R_{F^2}		0.0386	0.0378	0.0373
a (Å)		8.5462(1)	8.5453(2)	8.5464(2)
c (Å)		5.9188(1)	5.9180(1)	5.9188(1)
Density (g cm^{-3})		5.606	5.608	5.606
Variables		32	32	32
Preferred orientation [001]		0.985(2)	0.987(3)	0.982(3)

It was observed that profile fitting and the variation of crystallite broadening/strain effects had not achieved satisfactory fitting of the first reflection at 15.203 °2θ, the (110) peak. This is most likely due to low angle peak asymmetry common to NPD data which was visibly reduced in the HR dataset. The IDP for the O_{ap} positions was also relatively high. Anisotropic variation of this site gave the clearest example of the tendency for the O_{ap} positions to vary in the xy directions where a large discrepancy lay between xy (2.28(5) Å) and z (0.82(6) Å). This is the result of disorder caused by mixed cation occupancy of the Co/Fe site. The final fit (Figure 4.4, χ^2 = 5.048, R_{wp} = 0.0339) is for all atomic positions, lattice constants, ZPE, PO, back ground, profile parameters and IDPs (ADP for O_{ap}) being refined. All structural details are shown in Table 4.4.

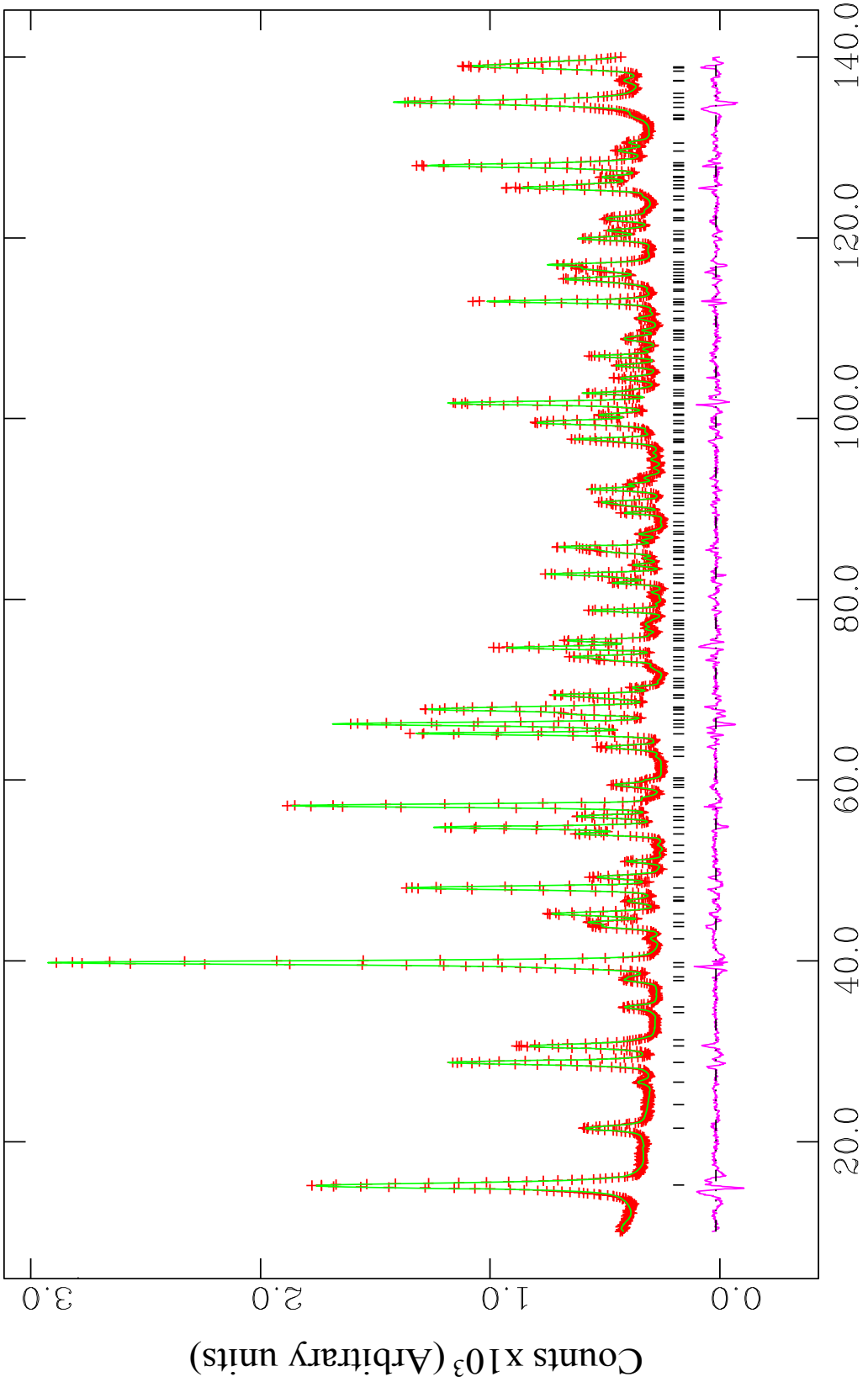

Figure 4.4 The fit obtained from the final refinement of $Co_{0.50}Fe_{0.50}Sb_2O_4$ at 300 K in $P4_2/mbc$. (+) observed, (|) calculated and (|) difference profiles are displayed. The black tick marks represent the $Co_{0.50}Fe_{0.50}Sb_2O_4$ nuclear phase. No impurities were observed.

4.3.2.4 Characterisation of $Co_{0.50}Fe_{0.50}Sb_2O_4$ at 4 K

A satisfactory nuclear structure was initially achieved before investigation of the magnetic structure from the HI data was performed. Several new intense reflections attributable to the magnetically ordered system were indexed for a cell consistent with the nuclear structure. The indexed peaks ((100), (210), and (300), at 10.758, 24.122, and 32.538 $^{\circ}2\theta$ respectively) suggested the presence of a C mode. The (100) peak was found to be significantly broadened and asymmetrically distributed. Attempts to fit this peak (Figure 4.5) were unsuccessful hence the HR dataset was used to resolve the magnetic structure. Investigation of the spin orientation for the C mode (based on a Co^{2+} magnetic cell with Co^{2+} form factor) found that whilst intensity was generated along both *x* and *z*, the poor fit of the *x* component suggested the moments lay significantly along *z*. A tilting model where the magnitude of the moments was varied resulted in instability and unsatisfactory errors for the M_x (M_x = 0.3(8), M_z = 2.00(4)) component, hence the moment orientated solely along *z* was most plausible. The presence of other magnetic modes were sought and an A mode was evidenced along *x*. It is noted that the (111) peak from the A mode is almost coincident with the (200) nuclear peak; however, addition of the A_x component improved the fit (from χ^2 = 3.121 to χ^2 = 3.036). Both C_z and A_x modes were combined into a single phase and the magnitudes of the spins refined. Both Fe^{2+} and Co^{2+} form factors were tested where the statistics identified the better form factor as Co^{2+} (χ^2 = 3.121, R_{wp} = 0.0584, 38 variables for Fe^{2+}; χ^2 = 3.036, R_{wp} = 0.0576, 38 variables for Co^{2+}) but no significant difference between the moments was observed. The final fit (χ^2 = 2.761, R_{wp} = 0.0547: A_x = 1.02(5) μ_B, C_z = 1.86(2) μ_B) is for all atomic displacement parameters, IDPs (ADP for O_{ap}), ZPE, profile parameters, lattice constants, PO and the magnetic moments magnitude being refined independently (Figure 4.6). More detailed refinement results are displayed in Table 4.4.

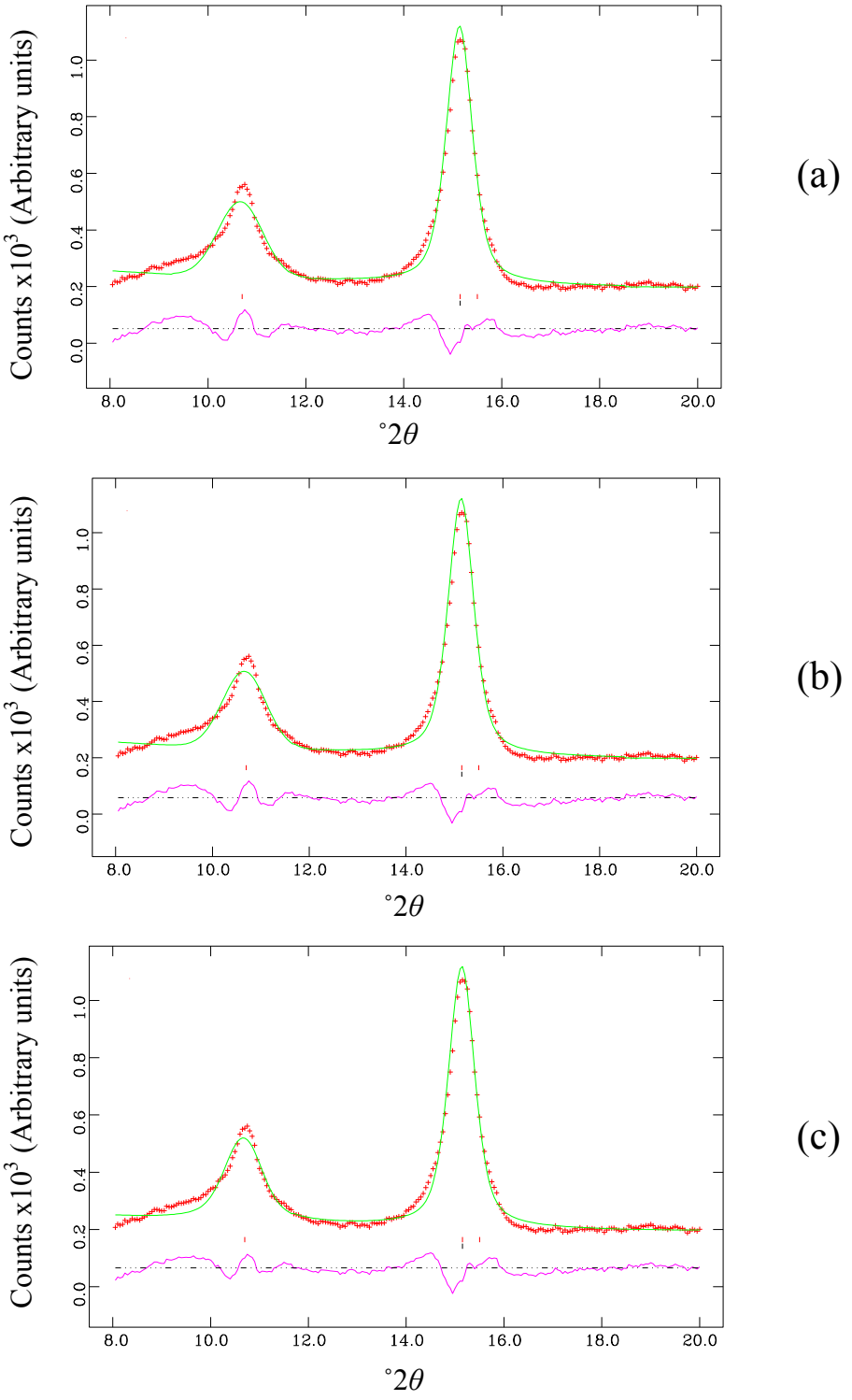

Figure 4.5 Attempts to fit the (100) magnetic peak for $Co_{0.50}Fe_{0.50}Sb_2O_4$ by varying profile functions and profile parameters for the magnetic cell. The nuclear phase profile was refined using profile function 2. Fits represent profile functions 4 (a) χ^2 = 6.395; 3 (b) χ^2 = 6.455; and 2 (c) χ^2 = 6.257. Observed (+), calculated (|) and difference (|) profiles are displayed. The tick marks represent the $Co_{0.50}Fe_{0.50}Sb_2O_4$ nuclear phase (black) in $P4_2/mbc$ and $Co_{0.50}Fe_{0.50}Sb_2O_4$ magnetic phase in $P1$ (red).

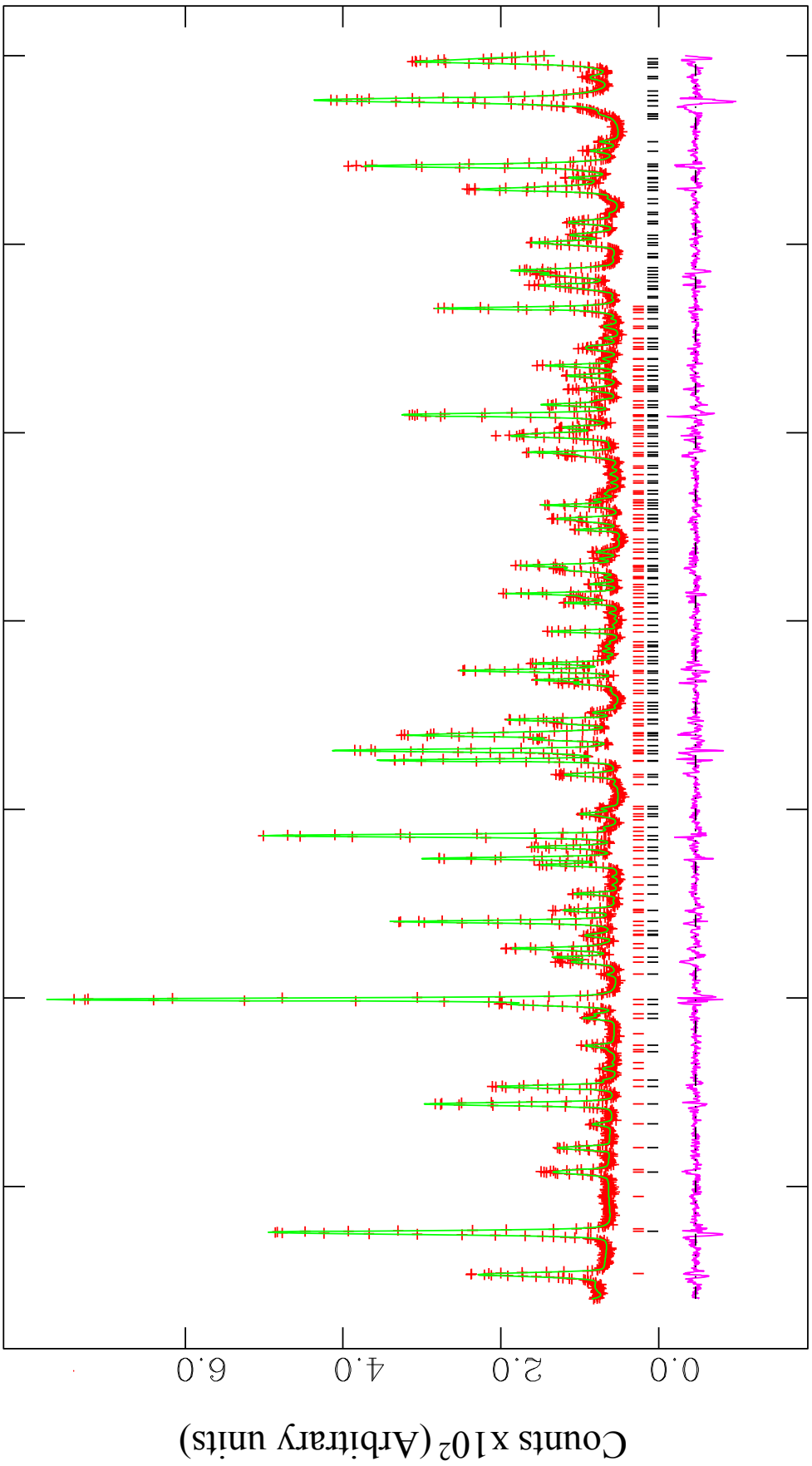

Figure 4.6 The observed (+), calculated (|), and difference profiles (|) obtained from the final refinement of $Co_{0.50}Fe_{0.50}Sb_2O_4$ based on 4 K NPD data. Tick marks represent the $Co_{0.50}Fe_{0.50}Sb_2O_4$ nuclear phase in $P4_2/mbc$ (black) and the $Co_{0.50}Fe_{0.50}Sb_2O_4$ magnetic phase refined in $P1$ with lattice constants set to equal the nuclear phase (red).

4.3.2.5 Characterisation of $Co_{0.75}Fe_{0.25}Sb_2O_4$ at 300 K

The refinement of $Co_{0.75}Fe_{0.25}Sb_2O_4$, performed as before, gave an extremely good fit for a single phase product. A calibrated neutron wave length ($\lambda_{refined}$ = 1.88643 Å, from λ_{PSI} = 1.88518 Å) was used. A small discrepancy was seen for the O_{ap} IDP when compared with all other atoms (χ^2 = 2.212; U_{iso}*100 = 2.166). Applying an ADP resulted in improvement of the fit where the difference between values for the *xy* and *z* positions was not as pronounced as previously seen (χ^2 = 1.924, $U_{11/22}$*100 = 2.31(4) Å and U_{33}*100 = 1.59(9) Å respectively). For a more accurate representation the ADP was justified. The final fit (Figure 4.7, χ^2 = 1.924, R_{wp} = 0.0395) is for all atomic positions, lattice constants, IDPs (ADP for O_{ap}), ZPE, background, profile parameters, scale factor and preferred orientation being refined independently. Table 4.4 displays the results of the final fit.

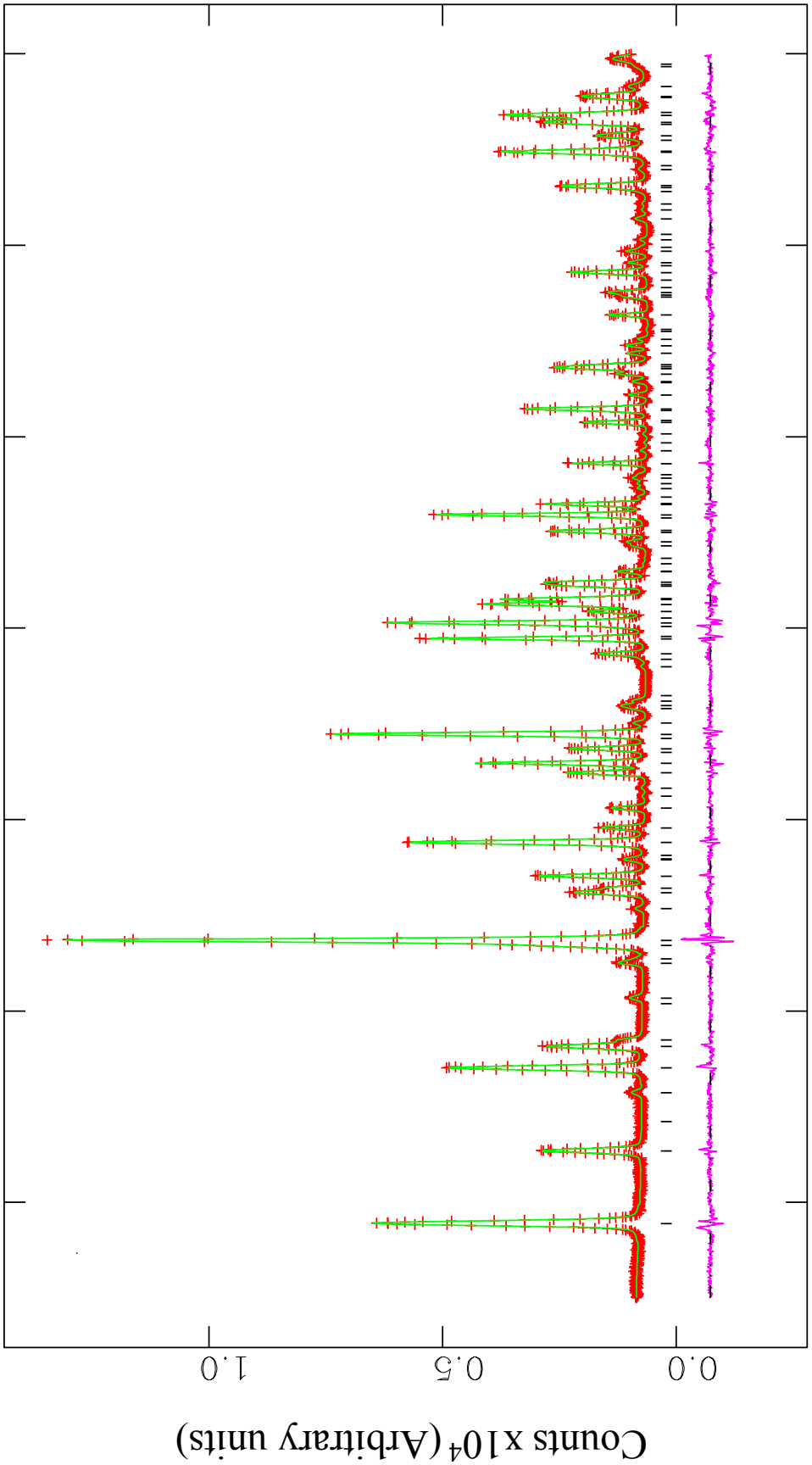

Figure 4.7 The observed (+), calculated (|), and difference (|) profiles from the refinement of 300 K NPD data of $Co_{0.75}Fe_{0.25}Sb_2O_4$. The black tick marks represent the $Co_{0.75}Fe_{0.25}Sb_2O_4$ nuclear phase in $P4_2/mbc$. $\chi^2 = 1.924$.

4.3.2.6 Characterisation of $Co_{0.75}Fe_{0.25}Sb_2O_4$ at 2 K

On cooling to 2 K new intense reflections at low angles of 2θ were observed and attributed to the magnetic ordering of the compound. The absence of any broadening or new reflections from the nuclear phase suggested retention of the original $P4_2/mbc$ symmetry. Subsequently refinement of the nuclear structure was carried out as for the 300 K data set, it was unnecessary to apply an ADP to the O_{ap} position. Indexing of the main magnetic reflections at 12.558, 28.516 and 38.650 ˚2θ ((100), (210), and (300) respectively) indicated the presence of a C mode. All other modes and spin orientations were investigated. An A_x mode could be identified; the final magnitude of this component (A_x = 0.53(6) μ_B, obtained from different initial values) and stability of the fit was highly dependent on the profile parameters used in the refinement. The profiles from refinements which contained and excluded an A mode (Figure 4.8) showed minimal difference; furthermore when an A_x component was added to the final 300 K fit, a moment of 0.38(7) μ_B was obtained (initial value: 0.2 μ_B) with minimal alteration to the profile. These findings suggested with a greater degree of certainty that the magnetic structure was a collinear C mode along *z*, but that a small component along *x* could not be ruled out. The final fit (χ^2 = 4.240, R_{wp} = 0.0428, C_z = 3.03(1) μ_B) is displayed in Figure 4.9. The model details are shown in Table 4.4.

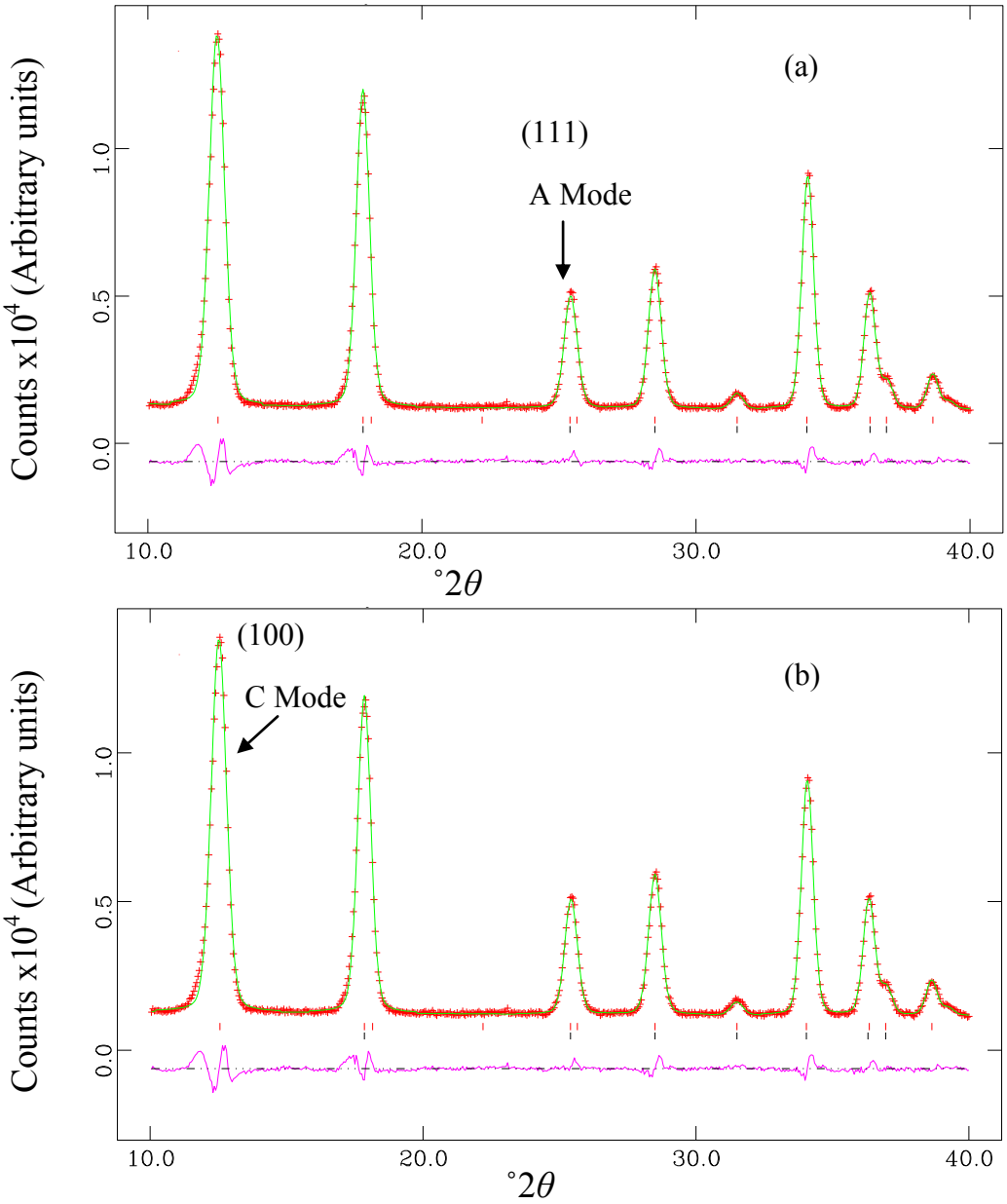

Figure 4.8 Magnified sections of the magnetic refinements of $Co_{0.75}Fe_{0.25}Sb_2O_4$ at 2 K two models are displayed; (a) is the refinement based upon non-collinear C_z and A_x components being refined in a single phase ($\chi^2 = 4.188$; $C_z = 3.03(1)$ and $A_x = 0.53(6)$ μ_B); (b) is the refinement based upon a C_z magnetic component only ($\chi^2 = 4.240$; $C_z = 3.03(1)$ μ_B). It is noted that the (111) magnetic peak was coincident with the (200) of the nuclear phases. Magnetic phases are refined in *P*1 whilst the nuclear phase was refined in $P4_2/mbc$. The observed (+), calculated (|) and difference profiles (|) are displayed and tick marks represent the nuclear (black) and magnetic (red) phases.

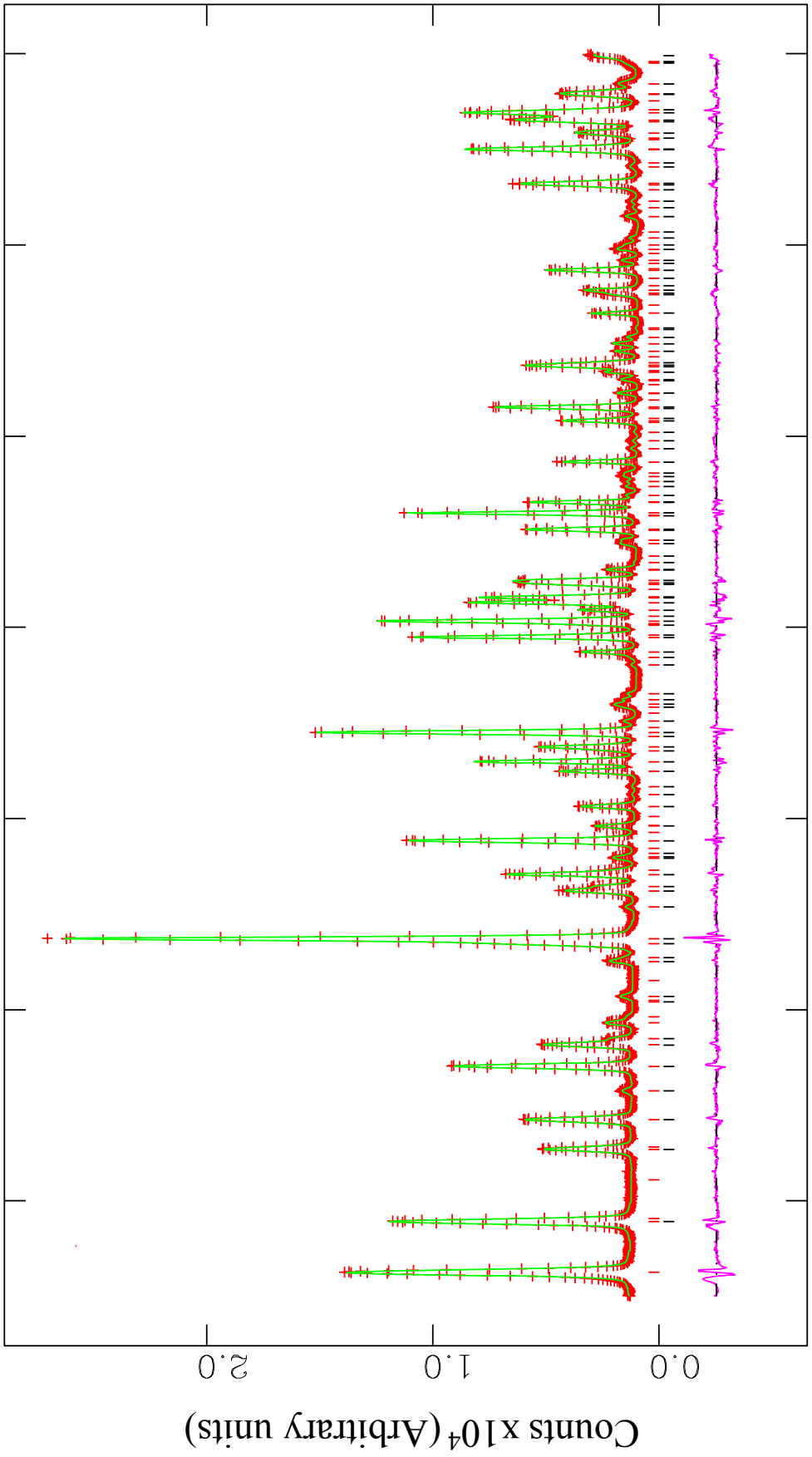

Figure 4.9 The final fit of $Co_{0.75}Fe_{0.25}Sb_2O_4$ based upon 2 K NPD data. The observed (+), calculated (|) and difference profiles (|) are displayed; the tick marks represent the $Co_{0.75}Fe_{0.25}Sb_2O_4$ nuclear phase in $P4_2/mbc$ (black) and $Co_{0.75}Fe_{0.25}Sb_2O_4$ magnetic cell in the spacegroup $P1$ (red). The magnetic structure is consistent with a C_z (3.03(1) μ_B) mode, $\chi^2 = 4.240$.

Table 4.4 Atomic coordinates, ADPs, and selected statistics associated with the refinements of all samples. * Isotropic displacement used.

		$Co_{0.25}Fe_{0.75}Sb_2O_4$		$Co_{0.50}Fe_{0.50}Sb_2O_4$		$Co_{0.75}Fe_{0.25}Sb_2O_4$	
		300 K	1.5 K	300 K	4 K	300 K	2 K
Co/Fe **4*d***	U_{iso}*100 (Å^2)	1.19(3)	0.58(3)	1.24(4)	0.30(5)	1.08(5)	0.53(4)
Sb **8*h***	(*x*, *y*, 0)	0.1761(2), 0.1651(2)	0.1753(2), 0.1647(1)	0.1748(2), 0.1647(2)	0.1753(2), 0.1649(2)	0.1757(1), 0.1650(1)	0.1753(1), 0.1647(1)
	U_{iso}*100 (Å^2)	1.38(3)	0.53(3)	1.38(3)	0.19(4)	1.37(3)	0.57(3)
O1 **8*h***	(*x*, *y*, 0)	0.0996(1), 0.6410(1)	0.0995(1), 0.6417(1)	0.0987(1), 0.6399(1)	0.0990(2), 0.6406(2)	0.0995(1), 0.6398(1)	0.0995(1), 0.6404(1)
	U_{iso}*100 (Å^2)	1.63(3)	0.81(3)	1.50(3)	0.39(4)	1.48(3)	0.82(3)
O2 **8*g***	(*x*, *x*+½, ¼)	0.67896(9), 0.17896(9)	0.67837(9), 0.17837(9)	0.6792(1), 0.1792(1)	0.6788(1), 0.1788(1)	0.67889(8), 0.17881(8)	0.67834(7), 0.17826(7)
	$U_{11} = U_{22}$*100 (Å^2)	2.53(5)	1.20(5)	2.57(5)	0.77(6)	2.31(5)	0.96(3)*
	U_{33}*100 (Å^2)	1.42(8)	0.68(8)	1.02(7)	0.23(8)	1.59(9)	
	U_{11}/U_{33}	1.78	1.76	2.52	3.35	1.45	
χ^2		3.772	4.442	5.048	2.761	1.924	4.240
R_{wp}		0.0413	0.0463	0.0339	0.0547	0.0395	0.0428
R_F^2		0.0171	0.0200	0.0259	0.0280	0.0247	0.0257
Volume (Å^3)		434.85(2)	433.43(2)	432.22(2)	430.85(2)	430.88(2)	429.62(1)
Density (g cm^{-3})		5.562	5.580	5.607	5.625	5.637	5.653
Moment (μ_B)	C_z	-	1.27(1)	-	1.86(2)	-	3.03(1)
	A_x	-	2.51(2)	-	1.02(5)	-	-
	μ_{Total}		2.81(3)		2.12(4)		3.03(1)
a (Å)		8.5728(2)	8.5677(1)	8.5457(1)	8.5382(1)	8.5265(1)	8.5172(1)
c (Å)		5.9170(1)	5.90455(9)	5.91843(9)	5.90999(9)	5.92675(9)	5.92236(8)

4.3.3 Results analysis

The results from Table 4.5 show several trends on increasing the cobalt content which directly affect the lattice parameters and are linked to the change in magnetic ordering. It is firstly seen that increasing the cobalt content of the system induces a decrease in *a* and an increase in *c* (Figure 4.10). The octahedral coordination sphere is reduced in size reflecting the increased Coulombic attraction between the TM and oxygen when substituting Fe^{2+} by the higher effective nuclear charge Co^{2+} species. There is a larger reduction in the Co-O_{ap} bond length as compared with the Co-O_{eq} bond but all octahedra remain slightly elongated. The larger reduction of the Co-O_{ap} bond length (-0.0134 Å) could be a contributing factor to the greater reduction of *a* (Δa = -0.0463 Å) when compared with *c* (Δc = 0.00975 Å). The seemingly anomalous increase in *c* with decreasing octahedral coordination sphere is best rationalised by the observed flattening of the Sb trigonal pyramidal geometry shown by an increase in the O-Sb-O bond angles. Such a simultaneous arrangement of elongation and contraction may suggest an increase in internal crystal strain as the two competing trends take place. The anisotropic displacement parameter for O_{ap} is unsurprising given the greater flexibility in the bond length and reflects the cation distribution amongst octahedral sites.

Table 4.5 A selection of bond angles and lengths obtained from the Rietveld refinement of the 300 K and T < 5 K NPD datasets.

	$Co_{0.25}Fe_{0.75}Sb_2O_4$		$Co_{0.50}Fe_{0.50}Sb_2O_4$		$Co_{0.75}Fe_{0.25}Sb_2O_4$	
	300 K	1.5 K	300 K	4 K	300 K	2 K
Co-O1 (Å) x4	2.0928(8)	2.0927(8)	2.0808(9)	2.083(1)	2.0823(7)	2.0835(7)
Co-O2 (Å) x2	2.170(1)	2.161(1)	2.165(1)	2.159(2)	2.1566(9)	2.1477(9)
Sb-O1 (Å)	1.934(2)	1.939(2)	1.947(2)	1.938(3)	1.929(2)	1.929(1)
Sb-O2 (Å)	1.994(1)	1.997(1)	1.993(1)	1.991(2)	1.9922(9)	1.9949(8)
O1-Sb-O2 (˚)	93.39(5)	93.18(5)	93.11(6)	93.26(8)	93.51(5)	93.39(5)
O2-Sb-O2 (˚)	95.78(7)	95.33(7)	95.87(7)	95.8(1)	96.09(6)	95.82(5)
O1-Co-O1 (˚)	90.04(4)	90.28(4)	89.35(5)	89.65(6)	89.27(4)	89.43(4)
O1-Co-O1 (˚)	166.22(7)	165.97(7)	166.27(7)	166.13(9)	166.58(5)	166.42(5)
O1-Co-O1 (˚)	91.60(5)	91.43(5)	92.29(5)	92.02(7)	92.29(4)	92.17(4)
Co-O1-Co (˚)	89.96(4)	89.72(4)	90.65(5)	90.35(6)	90.73(4)	90.57(4)

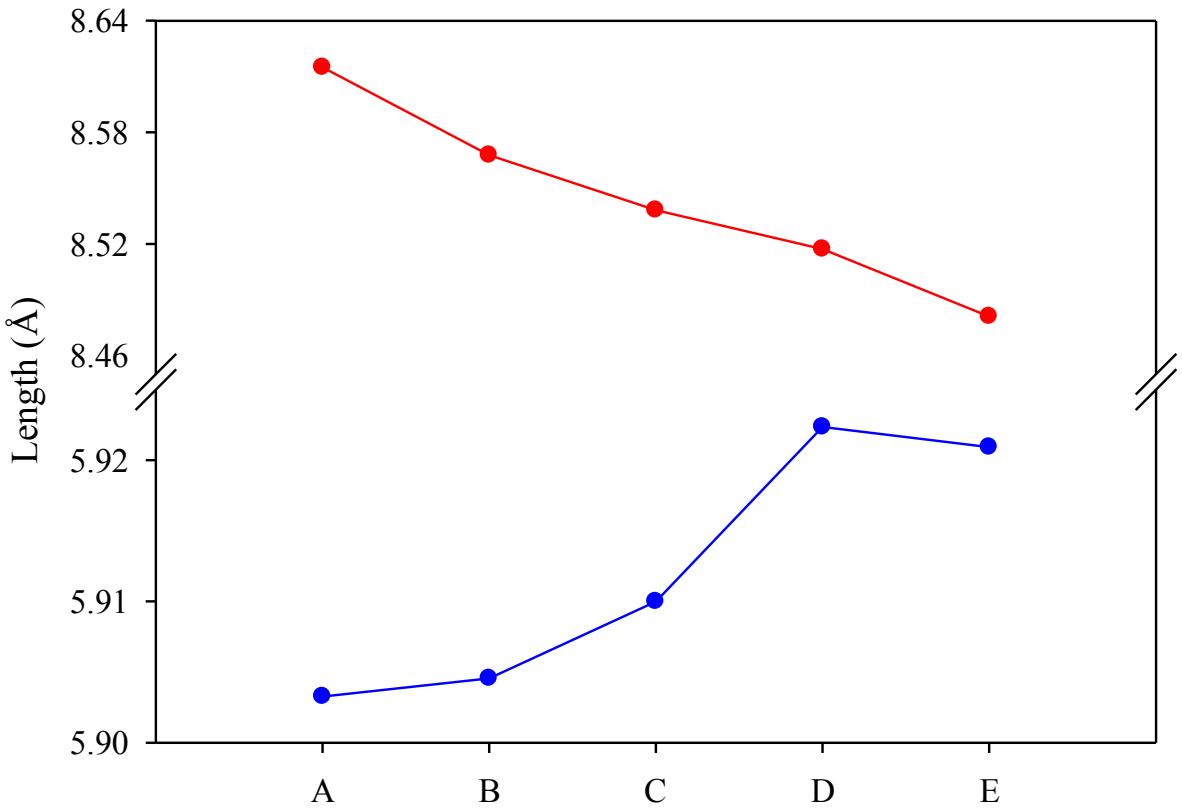

Figure 4.10 A plot showing the variation in lattice parameters with increasing iron content. Results are arranged from A to E in order of decreasing iron content; A, B, C, D, E represent $FeSb_2O_4$ [3], $Co_{0.25}Fe_{0.75}Sb_2O_4$, $Co_{0.50}Fe_{0.50}Sb_2O_4$, $Co_{0.75}Fe_{0.25}Sb_2O_4$, and $CoSb_2O_4$. The red and blue variations reflect changes in *a* and *c* respectively and are based on T < 5 K NPD data.

The transition of the predominant A mode to the C mode and orientation is found, for the first time, to occur between $Co_{0.50}Fe_{0.50}Sb_2O_4$ and $Co_{0.75}Fe_{0.25}Sb_2O_4$. A theory for the apparent preferential change in orientation of the moments has as yet not been established however it is possible to offer reasons for the change in mode of ordering using the principles summarised by Witteveen [9]. The general increasing length of *c* reflects the increase in magnitude of the C mode with increasing cobalt content. It is known that $CoSb_2O_4$ displays C type ordering [5]. The findings therefore, of a C mode only for $Co_{0.75}Fe_{0.25}Sb_2O_4$ support the suggestion that the *c* parameter is a key contributor to reducing the dominant direct exchange process between adjacent intrachain TMs by reducing orbital overlap. The consequence of this is that the weaker but ever present 90˚ superexchange increases its relative strength resulting in increasing dominance of FM coupling within a chain. The change in mode of ordering upon varying the Co/Fe ratio is shown in Figure 4.11.

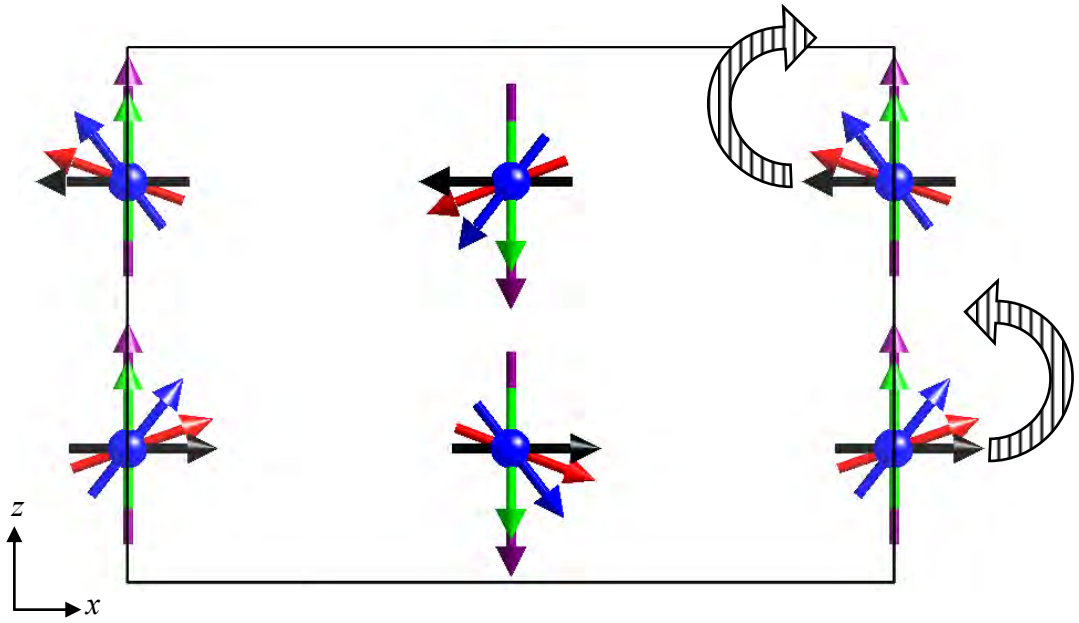

Figure 4.11 A presentation of the change in mode of ordering and orientation upon increasing the iron content. The arrows represent the magnetic structures of $FeSb_2O_4$ (Black), $Co_{0.25}Fe_{0.75}Sb_2O_4$ (red), $Co_{0.50}Fe_{0.50}Sb_2O_4$ (blue), $Co_{0.75}Fe_{0.25}Sb_2O_4$ (green), and $CoSb_2O_4$ (purple). The Striated arrows clearly show how the intrachain magnetic structure changes with increasing cobalt content.

4.4 SEM analysis

SEM confirmed the significant preferred orientation effects identified by Rietveld refinements of XRPD patterns (particularly prominent in $Co_{0.25}Fe_{0.75}Sb_2O_4$ and $Co_{0.50}Fe_{0.50}Sb_2O_4$). Increasing the iron content resulted in the formation of long needle like crystals (Figure 4.12). These were found to increase in size with iron content. Synthesis of all NPD samples (brown powders) resulted in sintered clumps which sparkled. It was found that by heating pressed pellets for 10 hrs at 700˚C followed by 2 hrs at 800˚C in successive heats, pellets made entirely of crystals (on the micron scale) could be produced.

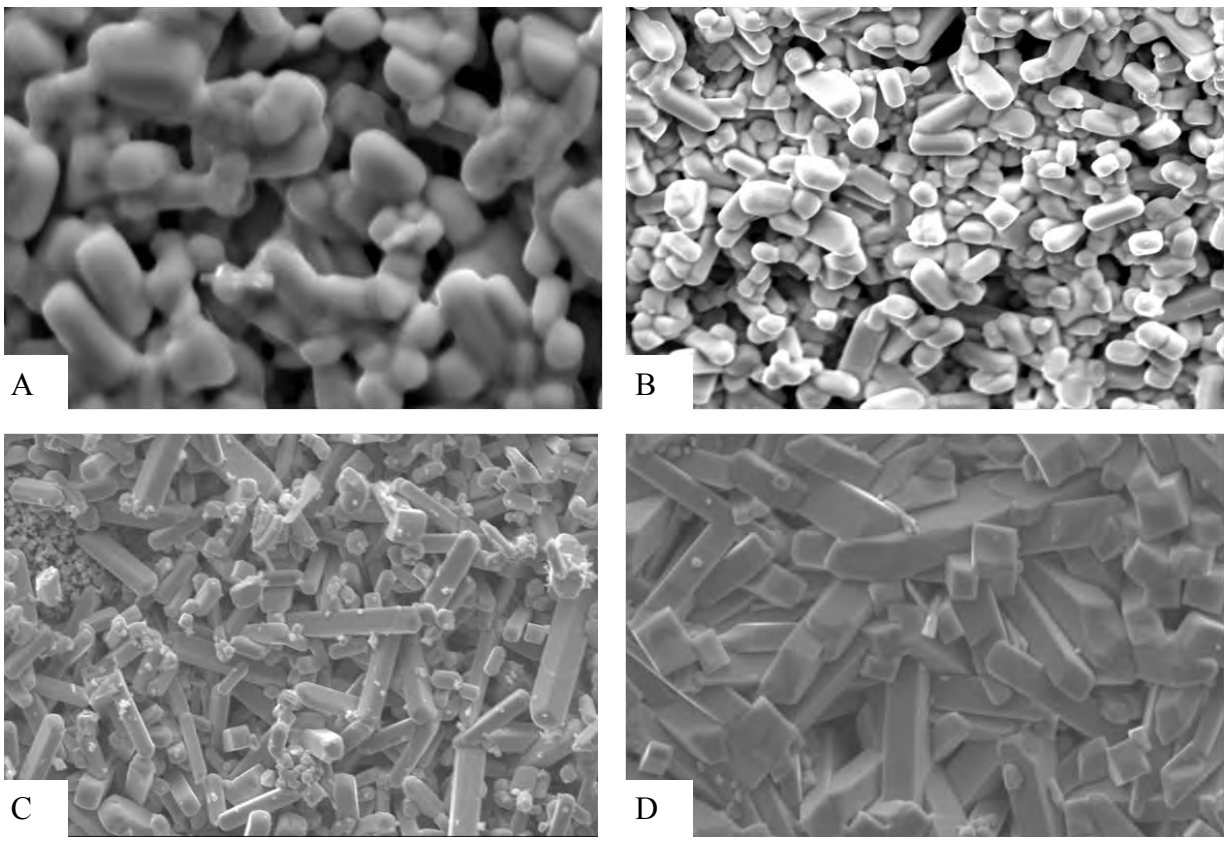

Figure 4.12 Crystal morphologies of: A - $CoSb_2O_4$, B - $Co_{0.75}Fe_{0.25}Sb_2O_4$, C - $Co_{0.50}Fe_{0.50}Sb_2O_4$, and D – $Co_{0.25}Fe_{0.75}Sb_2O_4$. Typical particle size in: $CoSb_2O_4$ > 5 μm; $Co_{0.25}Fe_{0.75}Sb_2O_4$ in excess of 60 μm long and 10 μm wide.

4.5 Magnetic susceptibility of the $Co_{1-x}Fe_xSb_2O_4$ phases

The magnetic susceptibility of all samples were recorded under ZFC-FC conditions, (applied field: 100 Oe) in the temperature range 5-300 K. All samples demonstrate ordering of the main phase associated with a canted antiferromagnetic system (Figure 4.13-4.16). Attempts to replicate a canted system in the NPD data were unsuccessful.

4.5.1 Susceptibility measurements for $Co_{0.25}Fe_{0.75}Sb_2O_4$

The measured susceptibility data for $Co_{0.25}Fe_{0.75}Sb_2O_4$ (Figure 4.13) had two main points of interest. The sharp decrease in susceptibility, more prominent in the ZFC data, occurring at around 126 K coincided well with the Verwey transition (T_v = 120 K), [10-11] and supported the findings in the NPD data (*Section 4.3.2.1/2*) for the presence of small amounts of magnetic Fe_3O_4. This is a previously cited problem [3, 6] for iron containing compounds. The subsequent calculation of any moment from the paramagnetic region was prevented. The AFM ordering of the system (T_N = 55 K) appeared consistent with a canted material: the FC susceptibility increases below 55 K and there is a very shallow drop in ZFC susceptibility.

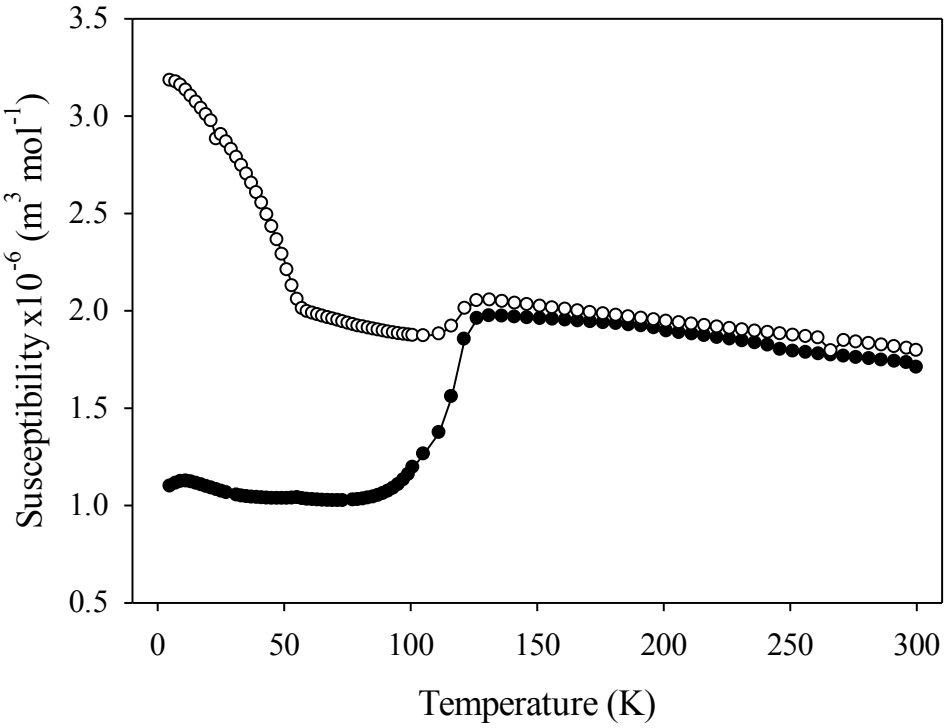

Figure 4.13 The magnetic susceptibility data for $Co_{0.25}Fe_{0.75}Sb_2O_4$. Measurements were recorded in an applied field of 100 Oe: ZFC (●) and FC (○) data are displayed.

4.5.2 Susceptibility measurements of $Co_{0.50}Fe_{0.50}Sb_2O_4$

The susceptibility plot (Figure 4.14) shows features consistent with a canted antiferromagnetic system. The structure surrounding the Néel temperature is particularly complex. The magnified ZFC susceptibility about T_N (Figure 4.15) shows that the susceptibility increases sharply up to 61 K where after a broad slightly positive increase is seen and the expected decrease in susceptibility due to AFM ordering occurs at 35 K. A residual paramagnetic response is observed below 20 K and a small broad shoulder between $63 < T < 79$ K, indicating short range ferromagnetic ordering, is seen in the FC measurements. The FC and ZFC paramagnetic susceptibilities ($80 < T < 300$ K) are not coincident suggesting a ferromagnetic impurity was present. This could be attributed to a very small amount of a Co/Fe spinel (discussed below).

The 1/χ versus T plot (Figure 4.14 inset) shows a deviation from Curie Weiss behaviour between 71-300 K. The magnetic moment was evaluated by separating the plot into two roughly linear regions and fitting the Curie-Weiss formalism for the high temperature paramagnetic region (200 < T < 296 K). A moment of 8.44 μ_B mol^{-1}, θ = -191±3 K was obtained. Such a value for the moment is obviously larger than can be obtained from a spin only moment, even when orbital contributions are considered. It is proposed therefore that this result indicates the presence of small FM clusters with AFM exchange between clusters; similar results have been seen in layered manganese oxides [12-13].

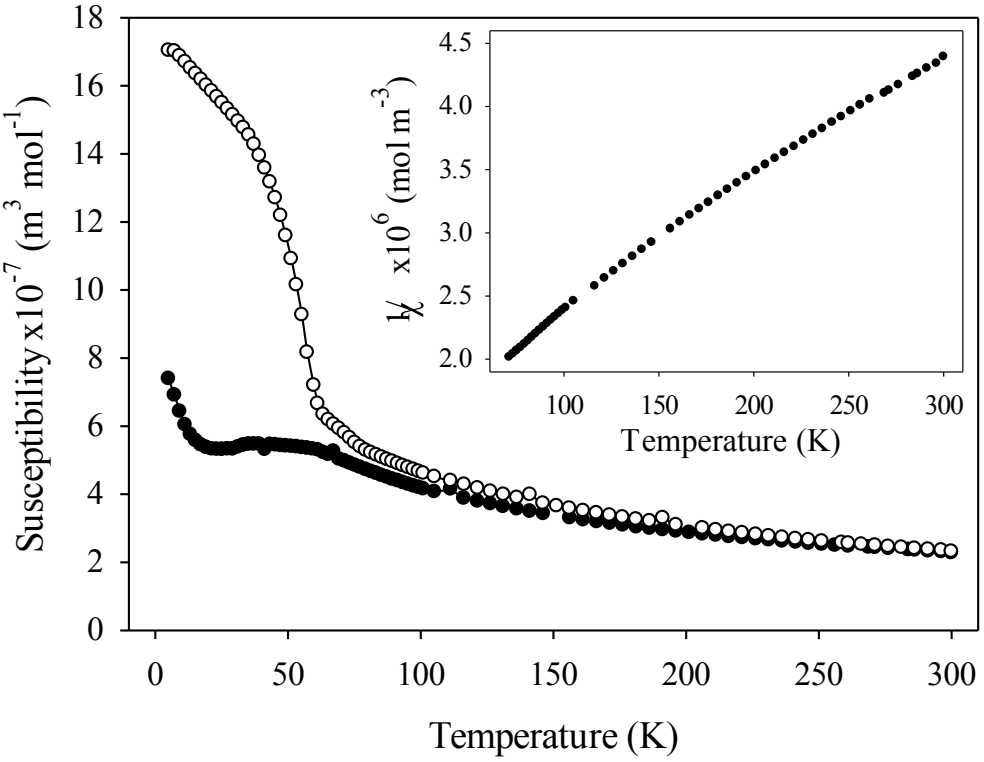

Figure 4.14 Magnetic susceptibility measurement of $Co_{0.50}Fe_{0.50}Sb_2O_4$. Measurements taken in an applied field of 100 Oe; ZFC (●) and FC (○) data are shown. Inset: the inverse susceptibility plot of $Co_{0.50}Fe_{0.50}Sb_2O_4$ showing the paramagnetic region 80-300 K.

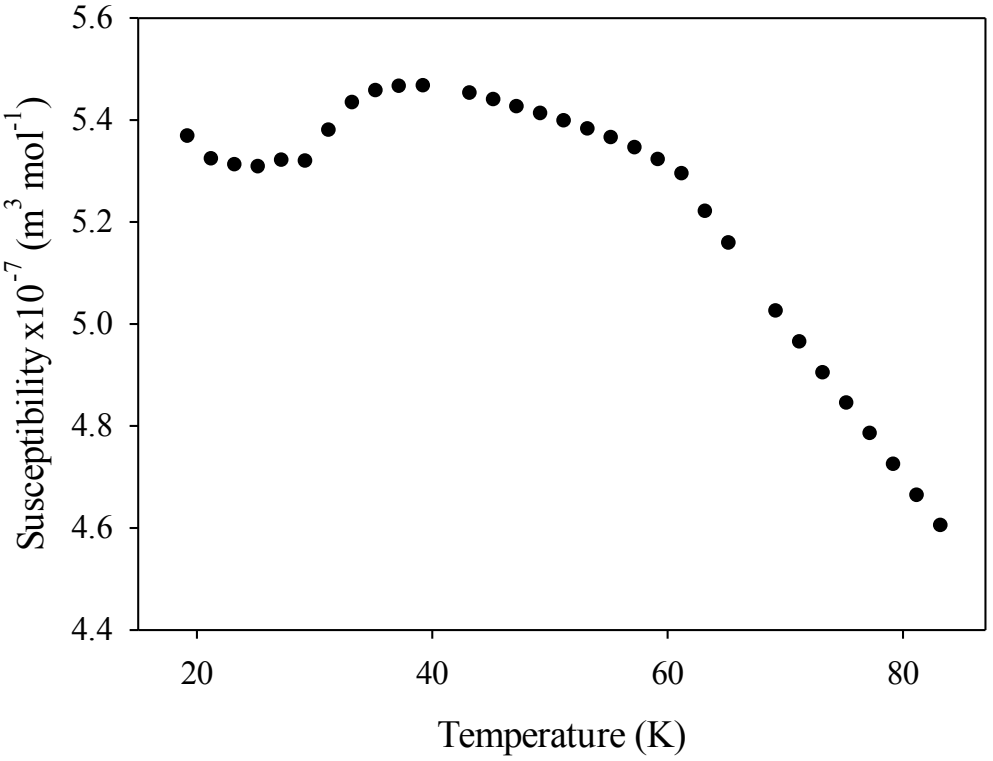

Figure 4.15 A magnified view of the magnetic structure surrounding T_N of $Co_{0.50}Fe_{0.50}Sb_2O_4$ ZFC data.

4.5.3 Susceptibility measurements of $Co_{0.75}Fe_{0.25}Sb_2O_4$

From the susceptibility plot (Figure 4.16) of $Co_{0.75}Fe_{0.25}Sb_2O_4$, long range AFM order of the canted system occurs at 57 K but divergence of the ZFC and FC data does not coincide with this temperature. The slight deviation between the FC and ZFC paramagnetic susceptibility ($77 < T < 300$ K) suggests the presence of a small ferromagnetic component in the sample possibly a mixed cobalt/ iron ferrimagnetic inverse spinel [14] without the associated Verwey transition [15]. The unusual FM upturn immediately prior to long range ordering ($59 < T < 77$ K) is not understood. The FC susceptibility was shown to substantially increase below 57 K coincident with T_N and is attributed to ordering of the main phase. The upturn in susceptibility seen at very low temperatures ($T < 27$ K) for both the ZFC and FC measurements is most likely attributed to a residual paramagnetic response from isolated paramagnetic ions dispersed throughout the sample.

The variation of the inverse susceptibility with temperature plot, for the ZFC data, (Figure 4.16 inset) shows slight deviation from linearity at temperatures below 150 K indicating Curie-Weiss behaviour is not strictly followed. The highest temperature region 151 < T < 296 K gives a moment of 5.27 μ_B mol^{-1} and the Weiss constant $\theta = -11.5 \pm 4$ K which supports the overall findings for dominant antiferromagnetic exchange. Between phases a reduction in the Weiss constant from -11.5(4) K to -191(3) K on increasing Fe^{2+} content suggests a strengthening of the AFM exchange processes occurring supporting further the findings in the NPD data of an increasingly dominant A mode component with iron content (*Section 4.3.3*.).

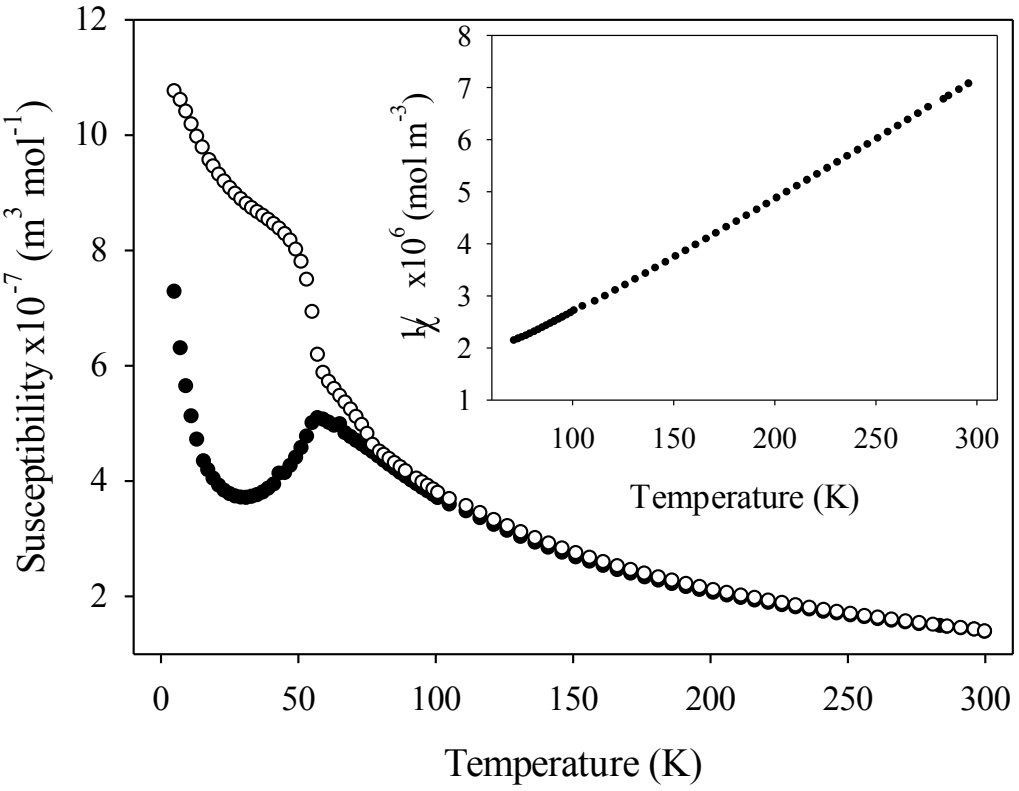

Figure 4.16 A magnetic susceptibility plot for $Co_{0.75}Fe_{0.25}Sb_2O_4$. Measurements taken in an applied field of 100 Oe; ZFC (●) and (○) FC data are shown. Inset displays the inverse susceptibility plot of $Co_{0.75}Fe_{0.25}Sb_2O_4$ showing the paramagnetic region 70-300 K.

It is noteworthy that the similar values of T_N for $Co_{0.25}Fe_{0.75}Sb_2O_4$ and $Co_{0.75}Fe_{0.25}Sb_2O_4$ appear to demonstrate an independence of the Néel temperature with iron

content over a whole composition range and reflect the findings of Abe *et al* [1] for the mixed Mn/V phases. Furthermore T_N is roughly equidistant between $FeSb_2O_4$ (45 K) [3] and $CoSb_2O_4$ (79 K) [5].

4.6 Thermogravimetric analysis

4.6.1. Heating in O_2

Samples in the order of 50 mg were heated in an atmosphere of pure oxygen at a rate of 10˚C/min to 1000˚C for oxidative characteristics testing, where the end products were identified as $CoSb_2O_6$ and $FeSbO_4$. Preliminary trials (Figure 4.17) indicated a vast difference in the oxidative characteristics of the system upon substitution of Fe^{2+} for Co^{2+} where a stepwise transition is seen on heating the samples indicating the formation of a transient intermediate. Three key findings are discussed:

1. It can be seen that the apparent formation of an intermediate phase is dependent on iron, given by the lack of intermediate step in the pure $CoSb_2O_4$ sample (Figure 4.17).
2. The amount of oxygen absorbed by the sample is intrinsically linked to the amount of iron in the starting material where a greater concentration of iron results in a larger oxygen uptake. It is noted that no mass losses were observed in any measurements.
3. The temperature at which oxidation is initiated is significantly reduced (260-320˚C).

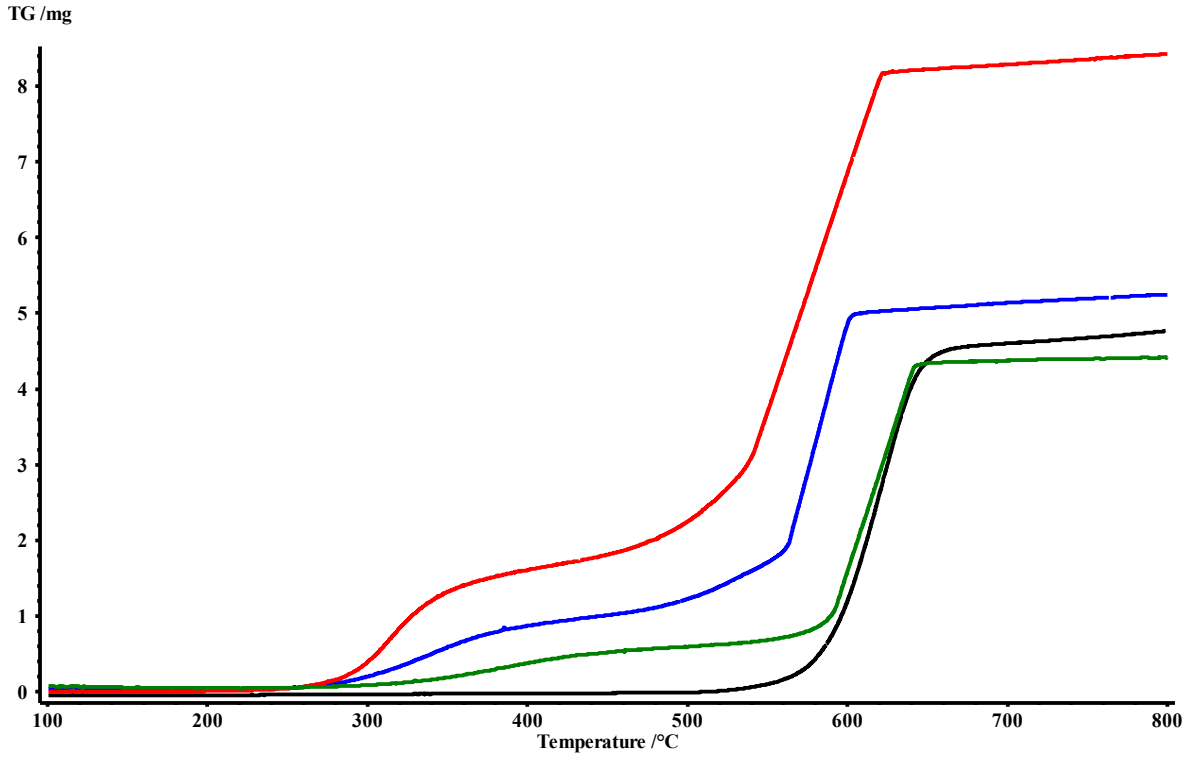

Figure 4.17 The TGA results of heating $CoSb_2O_4$ (black), $Co_{0.75}Fe_{0.25}Sb_2O_4$ (green), $Co_{0.50}Fe_{0.50}Sb_2O_4$ (blue), and $Co_{0.25}Fe_{0.75}Sb_2O_4$ (red) in O_2 up to 800˚C.

4.6.2 Analysis of the mass changes

The $CoSb_2O_4$ phase did not shown any sign to support the formation of an intermediate phase (*Section 3.11*), this has made these materials of significant interest and formed the focus of subsequent studies reported herein. Changes in enthalpy associated with the 1st and 2nd mass increases (Figure 4.18) for each sample show that a much smaller exotherm accompanies the first oxygen uptake. The relative magnitude of each exotherm implies small structural changes are involved on forming the intermediate and large structural changes are observed on the sample decomposing.

When calculating the oxygen stoichiometry of the intermediate phases it was initially assumed that all mass increases resulted from the accommodation of an O^{2-} species. The most likely site for the oxygen excess was believed to be within the channel running through the structure. The resultant distribution of oxidation states, based on this assumption are shown

in Table 4.6. It has been demonstrated that cobalt is highly resistive to oxidation by this mechanism, in contrast to the findings of the schafarzikite phase and lead doped variants [16] which displayed a similar ability to the $Co_{1-x}Fe_xSb_2O_4$ compounds to form intermediate phases. This suggested that the oxidation process was predominantly dependent on Fe and the amount able to oxidise to Fe^{3+}; hence, determining the final oxidation state of the TM species was based primarily on the oxidation of Fe but it is recognised that some Co oxidation may occur. The resultant compositions are shown in Table 4.6. These findings justified a rethink of the oxygen species accommodated by the parent structure because, as seen, the insertion of an O^{2-} species crucially, and in all cases, would result in the simultaneous oxidation of Fe^{2+} and Co^{2+}. A new oxygen species was sought which would only result in the oxidation of iron and give the observed mass increases. It was possible that a peroxide species would satisfy these criteria and the results show consistency with the hypothesis (Table 4.6).

Table 4.6 Results and analysis of the TGA data for the $Co_{1-x}Fe_xSb_2O_4$ compounds based on the inclusion of O^{2-} and O_2^{2-} species. *This is based upon the Fe content.

Starting compound	T_{max} intermediate formation (˚C)	Calculated oxygen excess	Oxidation states		Expected O^{2-} excess*
			O^{2-}	O_2^{2-}	
$Co_{0.25}Fe_{0.75}Sb_2O_4$	325	$O_{4.40}$	$Co^{2+}_{0.20}(Fe^{3+}_{0.75}Co^{3+}_{0.05})$	$Co^{2+}_{0.25}Fe^{2+}_{0.35}(Fe^{3+}_{0.40})$	$O_{4.375}$
$Co_{0.50}Fe_{0.50}Sb_2O_4$	448	$O_{4.36}$	$Co^{2+}_{0.28}(Fe^{3+}_{0.50}Co^{3+}_{0.22})$	$Co^{2+}_{0.50}Fe^{2+}_{0.14}(Fe^{3+}_{0.36})$	$O_{4.250}$
$Co_{0.75}Fe_{0.25}Sb_2O_4$	509	$O_{4.25}$	$Co^{2+}_{0.50}(Fe^{3+}_{0.25}Co^{3+}_{0.25})$	$Co^{2+}_{0.75}Fe^{3+}_{0.25}$	$O_{4.125}$

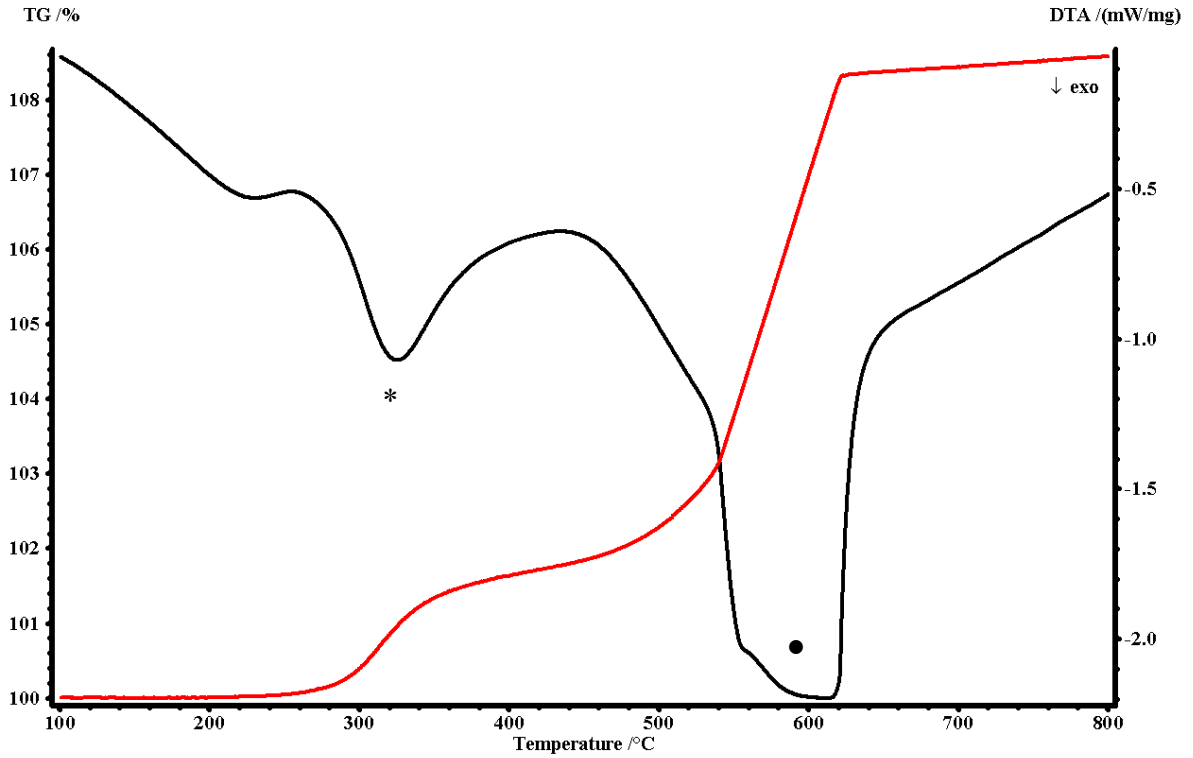

Figure 4.18 A TGA plot showing the mass change (red line) and enthalpy change (black line) for the $Co_{0.25}Fe_{0.75}Sb_2O_4$ sample whilst heating in O_2. Two exotherms are of interest: (*) coinciding with the 1st mass increase forming an intermediate and (●) associated with breakdown of the main phase into the high temperature oxidised components.

4.6.3 XRPD analysis of the intermediate phases

Isolating the proposed intermediate phases employed further TGA studies, where samples were heated to within 5˚C of the midpoint of the plateau (e.g. 442˚C Figure 4.18) before cooling to room temperature. It was later found that oxidised samples of comparable quality could be synthesised by heating unoxidised samples in a muffle furnace at the intermediate formation temperature for 30 minutes. XRPD showed that in each case a stable intermediate was formed (Figure 4.19), where indexing of each powder pattern revealed lattice parameters similar to the starting material and tetragonal symmetry, except $Co_{0.25}Fe_{0.75}Sb_2O_{4+x}$ (Table 4.7). Focussing on $Co_{0.75}Fe_{0.25}Sb_2O_{4+x}$, the resultant shifting of the (002) and (112) peaks to higher *d*-space gives the appearance of coalescence with the (220) and (310) respectively. No signs to indicate a change of crystal system or new reflections

owing to the parent compound were used as an early indication of the oxygen being located within the channels. At present, no NPD data has been obtained for these compounds and further work is required before reliable conclusions can be made about the residence of the excess oxygen. A clear trend in increasing peak broadening is seen which links oxygen excess to the molar amount of iron and sample degradation, further implicating iron in the oxidation process. However, there appeared to be a limit to the amount of excess oxygen a sample can accommodate before impurities are observed (Figure 4.19, see $Co_{0.25}Fe_{0.75}Sb_2O_{4+x}$). It is acknowledged that most oxidised samples showed some impurities (Sb_2O_4 and Fe_2O_3) in early work but modification of the heat treatment process removed these except in the case of $Co_{0.25}Fe_{0.75}Sb_2O_4$ which were persistent.

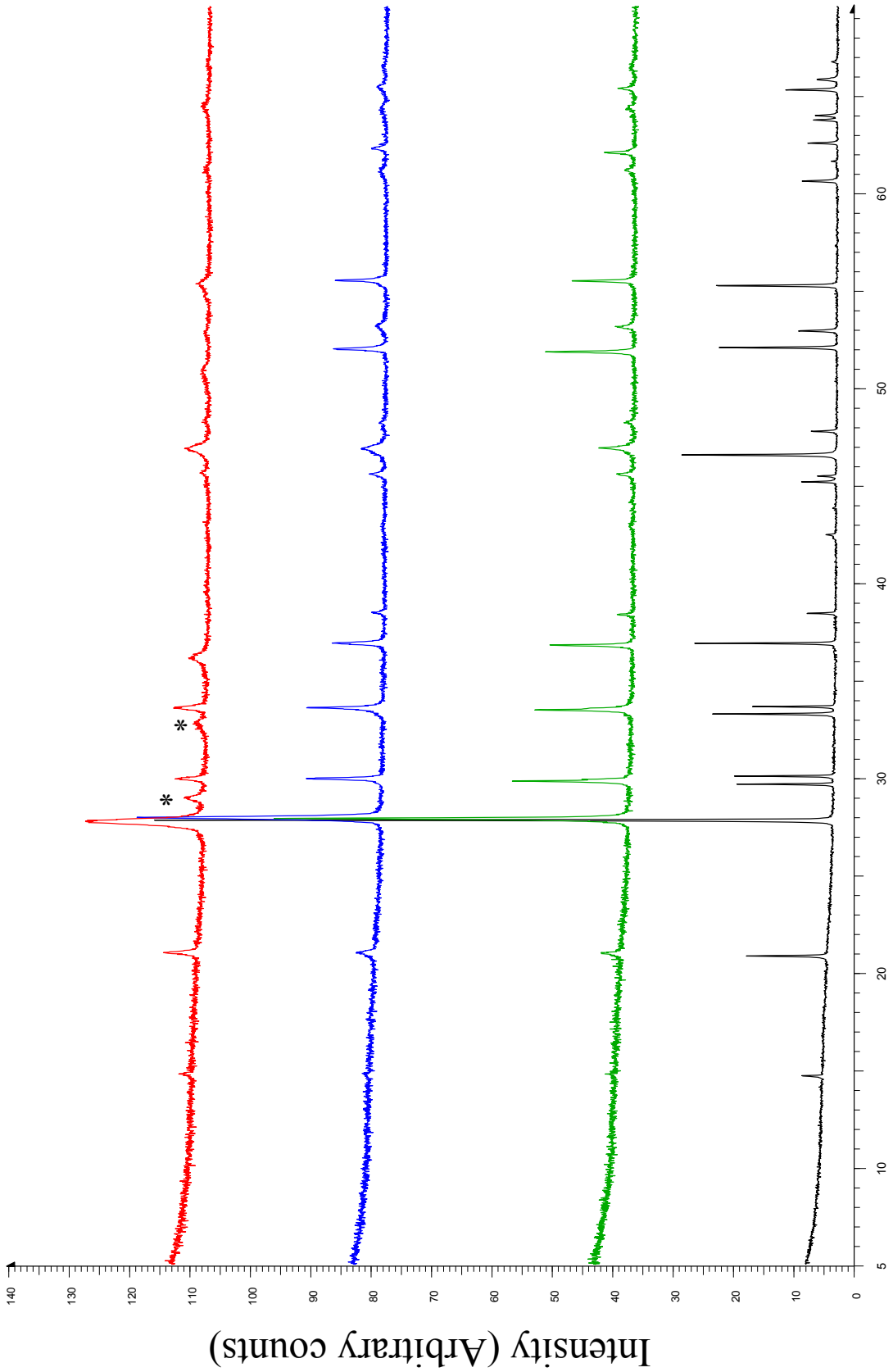

Figure 4.19 XRPD patterns of the intermediates formed by: $Co_{0.75}Fe_{0.25}Sb_2O_{4+x}$ (Green), $Co_{0.50}Fe_{0.50}Sb_2O_{4+x}$ (blue) and $Co_{0.25}Fe_{0.75}Sb_2O_{4+x}$ (Red). $CoSb_2O_4$ (Black) is added as a guide for ease of comparison of the initial and final compounds. (*) indicates impurity phase.

Table 4.7 A table of selected *d* spaces used to calculate the lattice parameters. All but $Co_{0.25}Fe_{0.75}Sb_2O_{4+x}$ represent tetragonal symmetry.

$Co_{0.25}Fe_{0.75}Sb_2O_{4+x}$		$Co_{0.50}Fe_{0.50}Sb_2O_{4+x}$		$Co_{0.75}Fe_{0.25}Sb_2O_{4+x}$	
d (Å)	(hkl)	*d* (Å)	(hkl)	*d* (Å)	(hkl)
5.9333	(110)	5.98289	(110)	4.21761	(111) or (200)
4.1953	(200)	4.22483	(111) or (200)	3.18754	(211)
3.19594	(102)	3.18839	(211)	2.98769	(002)
2.9664	(220)	2.97873	(002) or (220)	2.66881	(112)
2.6541	(310)	2.66492	(112) or (221) or (310)	2.43653	(202)
2.4732	(131)	2.43242	(202) or(311)	2.33924	(212)
1.9779	(330)	2.33721	(212) or (320)	1.98441	(312) or (330)
1.9293	(322)	1.98735	(312) or (330) (401)	1.93074	(411)
1.87288	(240)	1.93456	(411)	1.88041	(331) or (420)
1.7895	(042)	1.88442	(113) or (331) (420)	1.75908	(213)
1.6529	(422)	1.75597	(213)	1.71864	(402)
1.5070	(052)	1.65245	(223) or (332)	1.65098	(332) or (510)
1.44072	(530)	1.48815	(004)	1.49268	(004)
a (Å)	8.413(3)		8.434 (3)		8.410(2)
b (Å)	8.367(3)				
c (Å)	6.922(7)		5.952(2)		5.971(2)
Volume ($Å^3$)	487.29		423.34		422.30

4.6.4 Reduction of the oxidised compounds

Evidence to support the formation of stable intermediates led to the question of reversibility. This was tested by heating preoxidised samples in atmospheres of nitrogen and a nitrogen/ 10% hydrogen mix on the TGA. Only results for $Co_{0.50}Fe_{0.50}Sb_2O_{4+x}$ were obtained but in both cases the oxidised sample is seen to return to the original symmetry; however, the significant impurity phase ($CoSb_2O_6$) implies that the oxygen cannot be removed without first reacting with the parent compound. Narrowing of the peaks post reduction shows a more uniform distribution of crystallites (Figure 4.20). The temperature for which the reduction process appeared to initiate (above 550˚C) could be the reason for forming $CoSb_2O_6$ further suggesting irreversibility post oxygen insertion.

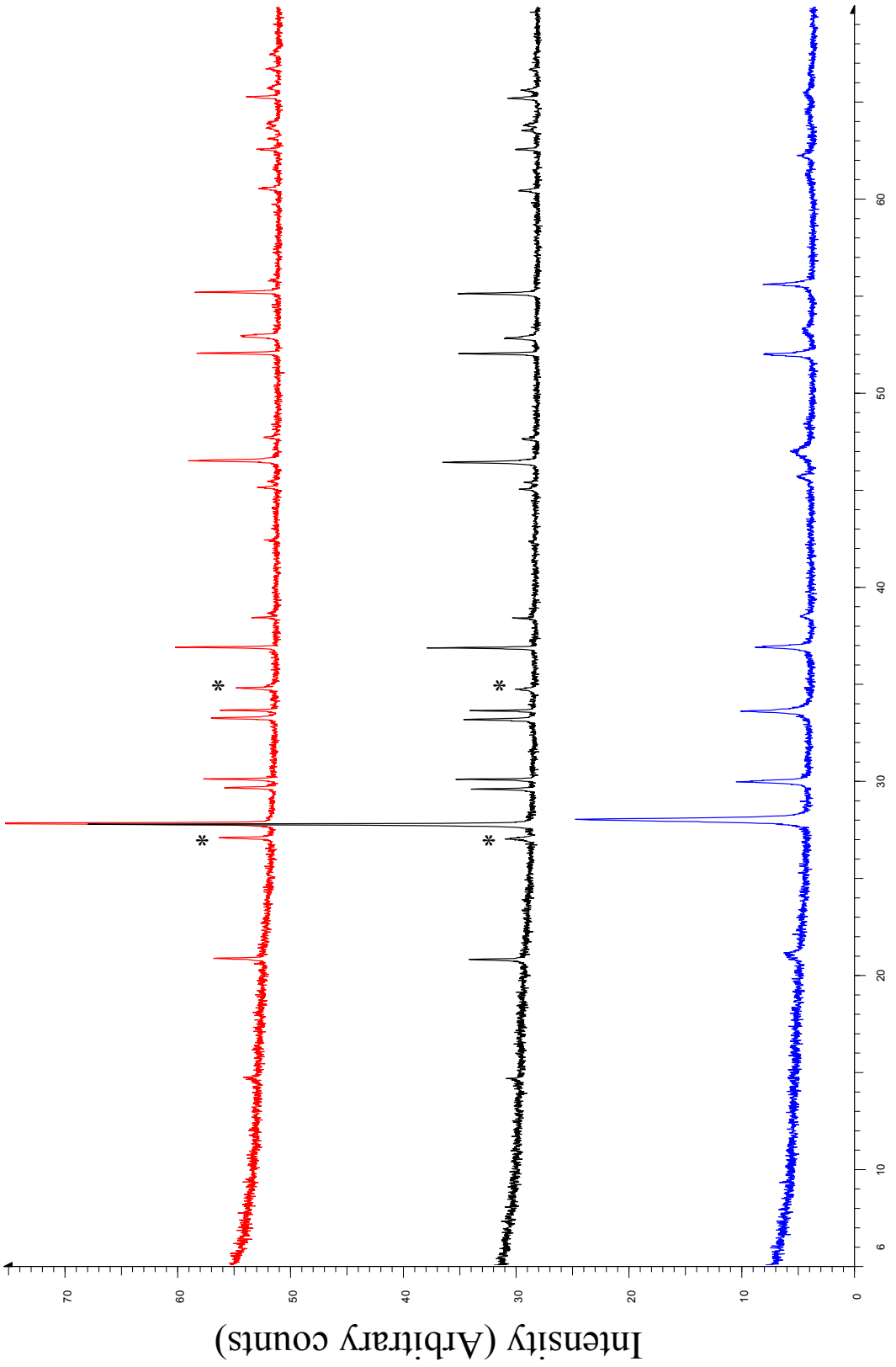

Figure 4.20 Powder plots of the reduced $Co_{0.50}Fe_{0.50}Sb_2O_{4+x}$ samples. Blue, black and red powder patters represent $Co_{0.50}Fe_{0.50}Sb_2O_{4+x}$, $Co_{0.50}Fe_{0.50}Sb_2O_{4+x}$ reduced in an atmosphere of N_2/10% H_2 up to 600°C and $Co_{0.50}Fe_{0.50}Sb_2O_{4+x}$ reduced in an atmosphere of N_2 to a maximum of 800°C. (*) indicates the impurity ($CoSb_2O_6$).

4.7 Magnetic susceptibility measurements of the $Co_{1-x}Fe_xSb_2O_{4+x}$ phases

4.7.1 Susceptibility measurements for $Co_{0.50}Fe_{0.50}Sb_2O_{4+x}$

The oxidised sample of $Co_{0.50}Fe_{0.50}Sb_2O_4$ displayed very similar magnetic behaviour to $Co_{0.50}Fe_{0.50}Sb_2O_4$ (*Section 4.5.2*) showing a canted antiferromagnetic response (Figure 4.21). Closer inspection of the structure around the transition temperature appeared to show two ordering temperatures which coincide in the ZFC and FC susceptibilities. The first at 79 K results in a shallow increase in the ZFC susceptibility and large FM increase in the FC susceptibility (almost double the magnitude when compared with the stoichiometric variant) extending towards lower temperature. At 63 K the second broadened transition is observed indicating long range AFM ordering of the system. Such an anomaly shows weak ferromagnetic ordering before long range AFM ordering takes place. It seemed unlikely however that the pre-T_N structure was related to clustering affects as a similar trend was seen (to a lesser extent) in the $Co_{0.75}Fe_{0.25}Sb_2O_4$ and $Co_{0.75}Fe_{0.25}Sb_2O_{4+x}$ (*vide infra*) samples where no clustering effects were observed in the susceptibility data. Better agreement between the ZFC and FC susceptibility in the high temperature paramagnetic region and no residual paramagnetic response at very low temperature, $T < 20$ K, were evident. Further studies possibly of an NPD nature would need to be employed to determine the structure in this region. Clustering effects evidenced from the calculated moment $\mu = 7.66\ \mu_B\ mol^{-1}$ ($151 < T < 296$ K; $\theta = -137(4)$ K) showed a marked reduction in magnitude, with a weakening of the overall AFM coupling when compared to the stoichiometric variant (Table 4.8).

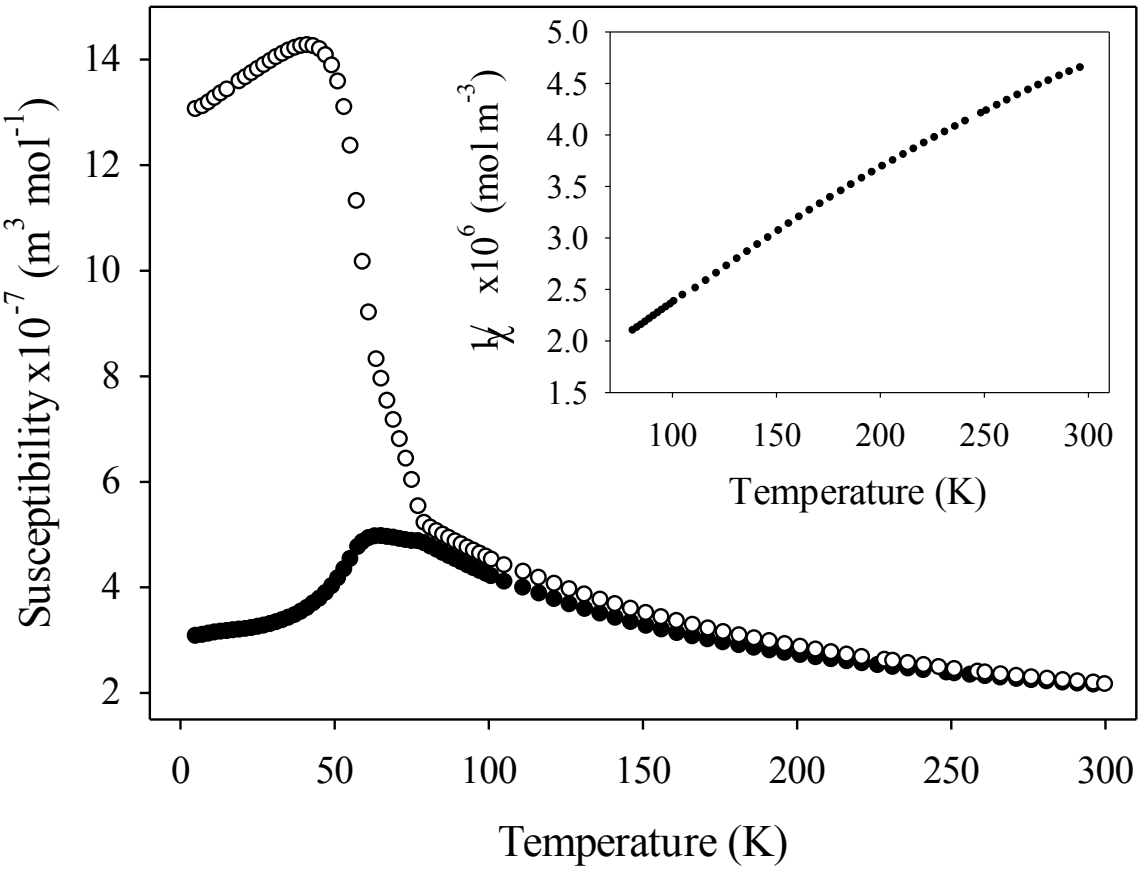

Figure 4.21 Magnetic susceptibility plot for $Co_{0.50}Fe_{0.50}Sb_2O_{4+x}$. ZFC (●) and FC (○) data are shown. The inset displays the inverse susceptibility with temperature plot for the paramagnetic region 81-296 K used to calculate the moment and Curie temperature.

4.7.2 Susceptibility measurements for $Co_{0.75}Fe_{0.25}Sb_2O_{4+x}$

This sample shows similar magnetic behaviour to the stoichiometric variant yet several differences are evident (Figure 4.22). The ZFC and FC susceptibility are coincident in the paramagnetic region ($81 < T < 296$ K) where a small shoulder between $71 < T < 77$ K shows weak reduction in the ZFC susceptibility before a sharp decrease in magnetisation indicating long range AFM ordering of the system at $T_N = 71$ K. The residual paramagnetic response seen in $Co_{0.75}Fe_{0.25}Sb_2O_4$ is replaced with a small decrease in ZFC susceptibility to a negative magnitude, possibly reflecting the findings of the $CoSb_2O_4$ system. The ordering temperature is the highest seen for this series and reflects a similar temperature to that of $CoSb_2O_4$.

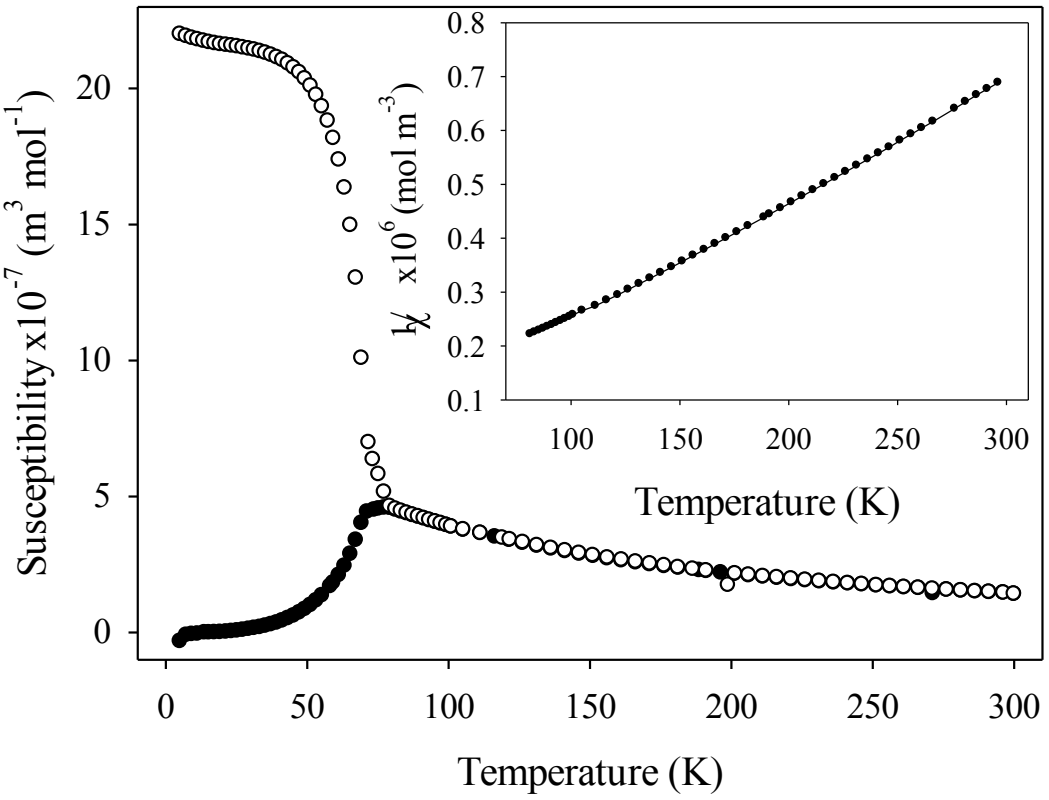

Figure 4.22 The magnetic susceptibility plot of $Co_{0.75}Fe_{0.25}Sb_2O_{4+x}$. ZFC (●) and FC (○) data are shown. Inset: the inverse susceptibility plot for the paramagnetic region 81-296 K showing slight deviation from linearity.

From the inverse susceptibility plot (Figure 4.22 inset) we see the typical deviation from linearity where the moment extrapolated from high temperature paramagnetic region ($171 < T < 296$ K) is 5.25 μ_B, θ = -1.1±8 K. The considerable increase in ordering temperature for the oxidised samples (Table 4.8) is indicative of the increasing strength of interactions between intrachain TMs resulting from their oxidation and shows that it is possible to preferentially oxidise the A site over Sb whilst retaining original structural features. Furthermore the increase in positivity of θ upon oxidation of $Co_{0.75}Fe_{0.25}Sb_2O_4$ implies weakening of AFM exchange; interestingly the values of T_N and θ are very similar to those of $CoSb_2O_4$.

All systems show negative values of the Weiss constant consistent with overall antiferromagnetic ordering of the systems but this is seen to reduce in strength upon

oxidation. The existence of shoulders before T_N in the oxidised and stoichiometric samples with the absence of any impurity in the $Co_{0.75}Fe_{0.25}Sb_2O_{4+x}$ sample suggests that this is linked with ordering of the main phase and requires further investigation. It is acknowledged that trace amounts of a $CoFe_2O_4$ derivative [17] could be responsible for the separation between FC and ZFC paramagnetic susceptibilities for most samples. It is expected that a random distribution of Co^{2+} (d^7) and Fe^{2+} (d^6) should prevent any possible ferrimagnetic ordering. $Co_{0.25}Fe_{0.75}Sb_2O_4$ was excluded from further study due to impurities presented upon oxidation.

Table 4.8 Collated magnetic results from the $Co_{1-x}Fe_xSb_2O_4$ and $Co_{1-x}Fe_xSb_2O_{4+x}$ samples. Fe_3O_4 prevented the determination of the magnetic moments for some samples.

Compound	Moment (μ_B mol^{-1})	Temperature range (K)	T_N (K)	θ (K)
$FeSb_2O_4$ [3]	-	-	45	-
$Co_{0.25}Fe_{0.75}Sb_2O_4$	-	-	55	-
$Co_{0.50}Fe_{0.50}Sb_2O_4$	8.45	200 – 296	35	-191±3
$Co_{0.75}Fe_{0.25}Sb_2O_4$	5.27	151-293	57	-11.5±4
$CoSb_2O_4$	5.06	160-300	79	3.28±1
Oxidised Samples				
$Co_{0.50}Fe_{0.50}Sb_2O_{4+x}$	7.66	151-296	63	-137±4
$Co_{0.75}Fe_{0.25}Sb_2O_{4+x}$	5.25	171-296	71	-1.1±8

4.8 Raman spectra

Raman data were collected with the aim of identifying the location of the excess oxygen and, if possible, its nature. The Raman spectrum shown in Figure 4.23 is typical for the schafarzikite system and a recent publication by Bahfenne *et al* [18] enabled assignment of the vibration bands. They found that most bands in the region 250-900cm^{-1} could be attributed to the Sb-O stretching frequencies, reflecting little variation in frequencies on varying the Co/Fe ratio (Table 4.9). The main band of interest for this particular study was the large intense peak at ~671 cm^{-1} corresponding to a Sb-O stretching frequency. Two factors were of interest; firstly modification of any stretching Sb-O frequency could be used as a

guide to locating sites for the excess oxygen. Secondly a vibration in the region 760-876 cm^{-1} [19] corresponding to an O-O stretch could be used to identify a peroxide species [20-21].

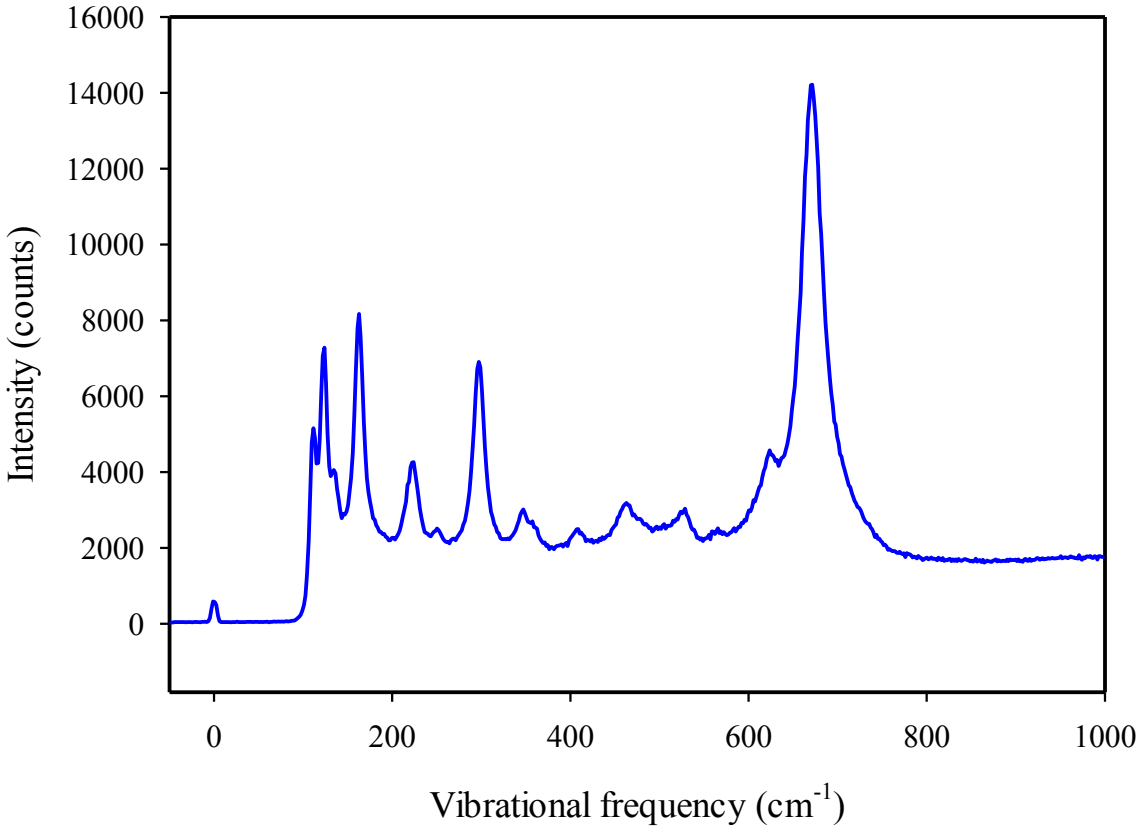

Table 4.9 A list of Raman stretching frequencies for the $Co_{1-x}Fe_xSb_2O_4$ compounds. No peak fitting software was used in the determination of stretching frequencies**.**

Stretching frequency (cm^{-1})		
$Co_{0.25}Fe_{0.75}Sb_2O_4$	$Co_{0.50}Fe_{0.50}Sb_2O_4$	$Co_{0.75}Fe_{0.25}Sb_2O_4$
110	111	111
121	123	124
132	135	136
160	163	163
221	223	223
249	250	249
296	297	297
348	347	345
-	360	360
405	407	409
466	462	462
-	-	481
527	527	528
560	566	564
620	624	628
669	671	672

Difficulties were met when trying to obtain well resolved spectra for the oxidised samples, where a variety of approaches were used, including using a cooling stage to reduce thermal contributions from the laser possibly giving rise to the observed broadened peaks. This did not significantly help.

It was clear that the Sb-O frequency had been significantly altered (Figure 4.24) providing evidence for inclusion of the excess oxygen within the channels bound to Sb. The broad but unmistakeable shoulder in the region of 750 cm^{-1} is a possible indicator of the presence of a peroxide species but further studies will need to be conducted for conclusive evidence.

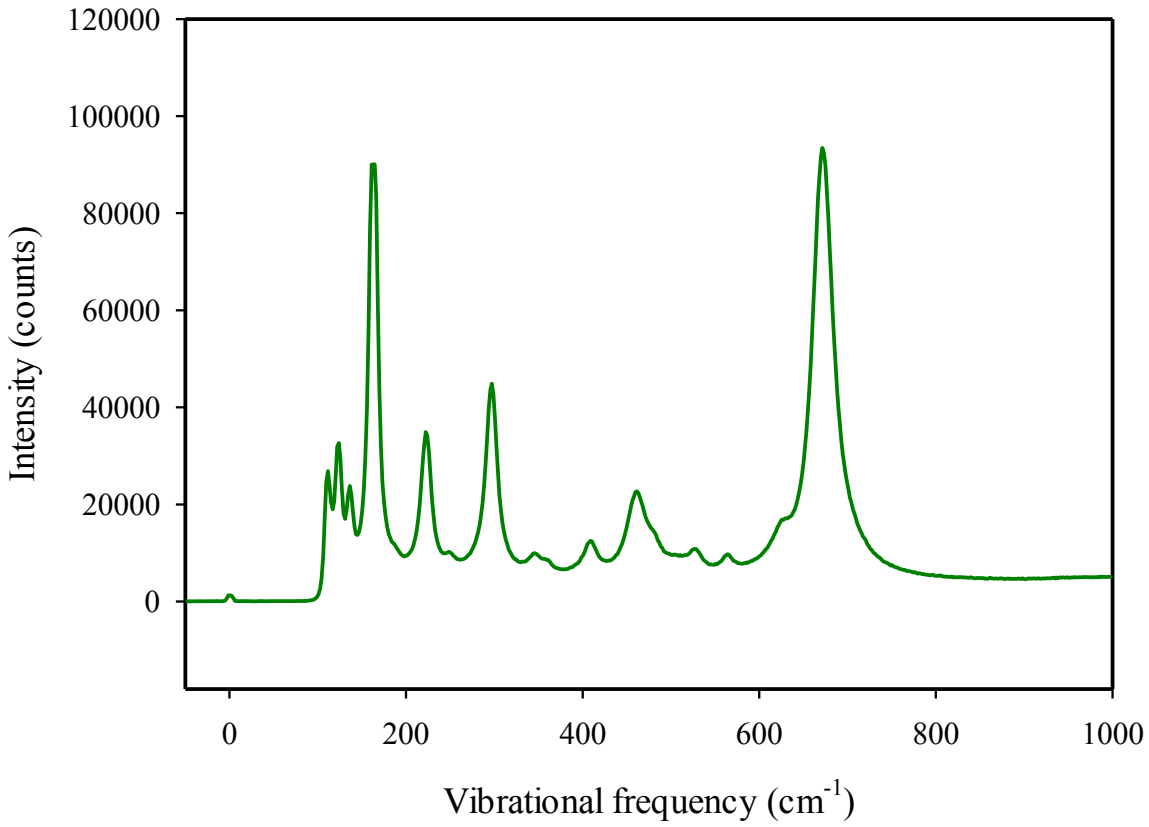

Figure 4.24 A comparison between $Co_{0.75}Fe_{0.25}Sb_2O_4$ (Dark Green) and $Co_{0.75}Fe_{0.25}Sb_2O_{4+x}$ (Red) Raman spectra.

4.9 Conclusions

The samples in this chapter have all shown nuclear structures consistent with the tetragonal spacegroup $P4_2/mbc$. Magnetic structures characterised by NPD have revealed for the first time that a change from a dominant A to C type magnetically ordered system occurs between $Co_{0.50}Fe_{0.50}Sb_2O_4$ and $Co_{0.75}Fe_{0.25}Sb_2O_4$. This has been linked to an expansion of *c* resulting in weakening of the direct exchange and increasing the dominance of the ferromagnetic 90˚ superexchange mechanism. Magnetic susceptibility measurements have revealed highly complex ordering in the systems where further work is required to gain more detail, but it has been demonstrated that the $Co_{0.50}Fe_{0.50}Sb_2O_4$ sample is the most peculiar, with apparent cation segregation and the formation of ferromagnetic aligned clusters. Detailed thermogravimetric analysis has revealed for the first time the oxidative capabilities

of these samples resulting in the accommodation of excess oxygen and oxidation of the TM species over antimony whilst retaining some semblance of the original symmetry. This was crucially found to be dependent on iron and the amount available to oxidise to Fe^{3+} where too large an oxygen excess can lead to sample degradation. Magnetic susceptibility studies have shown this process results in TM oxidation. Whilst more evidence is required, preliminary studies suggest the excess oxygen species to be peroxide.

4.10 References

[1] H. Abe, K. Yoshii, H. Kitazawa, *Phys. Status Solidi* **A 189** (2002) 429.
[2] B. Y. Brach, N. V. Chezhina, Y. V. Shapoval, *Inorg. Mater.* **25** (1989) 601.
[3] M. J. Whitaker, R. D. Bayliss, F. J. Berry, C. Greaves, *J. Mater. Chem.* **21** (2011) 14523.
[4] A. M. Abakumov, M. G. Rozova, E. V. Antipov, J. Hadermann, G. Van Tendeloo, M. V. Lobanov, M. Greenblatt, M. Croft, E. V. Tsiper, A. Llobet, K. A. Lokshin, Y. S. Zhao, *Chem. Mater.* **17** (2005) 1123.
[5] B. P. de Laune, C. Greaves, *J. Solid State Chem.* **187** (2012) 225.
[6] J. A. Gonzalo, D. E. Cox, G. Shirane, *Phys. Rev.* **147** (1966) 415.
[7] R. D. Shannon, *Acta Crystallogr.* **A 32** (1976) 751.
[8] G. E. Bacon, "*Neutron Diffraction*", 3rd ed, Clarendon Press, Oxford (1975).
[9] H. T. Witteveen, *Solid State Commun.* **9** (1971) 1313.
[10] E. J. W. Verwey, P. W. Haayman, *Physica* **8** (1941) 979.
[11] V. Skumryev, H. J. Blythe, J. Cullen, J. M. D. Coey, *J. Magn. Magn. Mater.* **196** (1999) 515.
[12] R. K. Li, C. Greaves, *J. Solid State Chem.* **153** (2000) 34.
[13] H. El Shinawi, A. Bertha, J. Hadermann, T. Herranz, B. Santos, J. F. Marco, F. J. Berry, C. Greaves, *J. Solid State Chem.* **183** (2010) 1347.
[14] D. H. Martin, "*Magnetism in Solids*", Iliffe books Limited, London (1967).
[15] J. Abellan, M. Ortuno, *Phys. Status Solidi* **A 96** (1986) 581.
[16] M. J. Whitaker, *Personal Communication* (2012).
[17] P. A. Joy, S. K. Date, *J. Magn. Magn. Mater.* **222** (2000) 33.
[18] S. Bahfenne, L. Rintoul, R. L. Frost, *Am. Miner.* **96** (2011) 888.
[19] V. Vacque, B. Sombret, J. P. Huvenne, P. Legrand, S. Suc, *Spectroc. Acta Pt. A-Molec. Biomolec. Spectr.* **53** (1997) 55.
[20] H. H. Eysel, S. Thym, *Z. Anorg. Allg. Chem.* **411** (1975) 97.
[21] J. Oxley, J. Smith, J. Brady, F. Dubnikova, R. Kosloff, L. Zeiri, Y. Zeiri, *Appl. Spectrosc.* **62** (2008) 906.

Chapter 5

Synthesis and characterisation of the $Co_{1-x}Fe_xSb_{2-y}Pb_yO_4$ phases (x = 0.25, 0.50, 0.75 and y = 0.10-0.75) and their oxidised products

5.1 Introduction

As we have seen in previous chapters the substitution of lead for antimony has been used for oxidising Fe^{2+} to Fe^{3+} in $FeSb_2O_4$. There is mounting evidence to suggest that other cations are less amenable to oxidation of this type [1-3]. We saw in *Chapter 4* that an additional method of oxidising the TM species is possible by heating an iron rich sample in O_2 to form stable intermediate phases of the type $Co_{1-x}Fe_xSb_2O_{4+x}$. It has, at present, been shown that this is only possible for phases containing Fe^{2+}, and is relevant to both naturally occurring and synthetic variants [4-5]. When considering the redox potentials associated with the TM species [6]:

$$Fe^{3+}_{(aq)} + e^- \rightarrow Fe^{2+}_{(aq)} \qquad +0.77\ V$$
$$Mn^{3+}_{(aq)} + e^- \rightarrow Mn^{2+}_{(aq)} \qquad +1.54\ V$$
$$Co^{3+}_{(aq)} + e^- \rightarrow Co^{2+}_{(aq)} \qquad +1.92\ V$$

it becomes clearer that Mn^{3+} and Co^{3+} are considerably more oxidising than Fe^{3+}, although data for this particular solid will be different from those in aqueous media. Empirically, this gives evidence for the absence of compounds of the form $CoSb_{1.50}Pb_{0.50}O_4$ [3] and the $MnSb_{2-x}Pb_xO_4$ series [2], and implies that it is impossible to oxidise Co and Mn to the same extent as Fe^{2+} in the presence of Sb^{3+}. This shows the importance of Fe to these systems in order to achieve greater functionality of the material.

To date, few phases exist with mixed A or B site cations [1-3, 7-8] and it is the aim of this chapter to explore the combination of mixed A (containing Fe which can be readily oxidised) and mixed B site (Sb^{3+}/Pb^{2+}; the mechanism for oxidation) elements in a variety of ratios within a single phase. In all cases reported the lead content was limited to the maximum Fe content of the phase based upon the observations described above.

5.2 Experimental

All reported samples were produced using the same methodology previously detailed. Reaction mixtures consisted of CoO (325mesh Aldrich), Sb_2O_3 (99% Reagent Plus, 5 micron powder), Fe_2O_3 (<5 micron powder, ≥ 99%, Sigma-Aldrich), Fe (fine powder, ≥ 99%, Sigma-Aldrich), and PbO (≥ 99%, Puriss) in a ratio dictated by the desired final composition. Samples were heated between 625 and 675˚C for a maximum of two six hour sessions with intermittent grinding; this was sample dependent, *see Section 5.3*. All samples were analysed by XRPD (absorption correction applied) and NPD (PSI Zurich, SINQ, 8mm V can, HRPT; 300 and 1.5 K). Magnetic susceptibility measurements (ZFC/FC) were collected on the MPMS between 5 and 300 K; sample set up as previously detailed (*Section 2.4*). Oxidative properties were investigated using TGA in an atmosphere of oxygen (N_2 protective gas) with an applied buoyancy and sensitivity correction. The findings were further corroborated by the use of VT-XRPD in the case of $Co_{0.25}Fe_{0.75}Sb_{1.75}Pb_{0.25}O_4$. Hour long scans were acquired at 25˚C intervals under standard atmospheric conditions between room temperature and 600˚C. Mössbauer data was collected and interpreted for $Co_{0.50}Fe_{0.50}Sb_{1.50}Pb_{0.50}O_4$ at 300 K by Professor Frank Berry.

5.3 XRPD analysis

The synthesis of these phases was more difficult than the previously synthesised $Co_{1-x}Fe_xSb_2O_4$ phases. The heating times and temperatures reagent mixtures were subjected to had to be varied between sample compositions in order to produce the purest samples possible. Consistency of methodology at the highest possible temperature with intermediate grindings was always intended during synthesis in order to limit the amount of residual Fe_3O_4 (a common impurity in iron containing phases). There was evidence to suggest that sample purity was impaired further by successive reheating. A compromise was reached in which lower heating temperatures and a reduced number of heat treatments were used to inhibit the formation of the unknown impurities to the greatest possible extent, at the cost of samples potentially containing more residual Fe_3O_4. The samples produced were highly crystalline; milk chocolate to dark chocolate brown in colour, all samples formed hard sintered masses after the first heating session which often had small crystals running throughout their mass. The products were indexed [9] for tetragonal cells; the lattice parameters obtained identified the phases as being related to the $Co_{1-x}Fe_xSb_2O_4$ compounds. In an attempt to rule out the impurity peaks as an indication of a change of symmetry they were included in the indexing procedure which allowed all but monoclinic and triclinic systems to be identified. None of the impurity peaks (e.g. at about 31.427˚ and 32.349 ˚2θ) could be indexed as part of the main phase and were taken to be the most intense peaks of an unidentifiable impurity phase.

Rietveld refinement of all XRPD patterns highlighted significant, sample dependent, differences in symmetry. Considering first the $Co_{0.25}Fe_{0.75}Sb_{2-x}Pb_xO_4$ series of compounds, the refinement initially proceeded, as detailed in previous chapters, with $P4_2/mbc$ symmetry but fits with poor figures of merit were achieved for the compositions (Pb = 0.10, 0.20, 0.25, and 0.30); e.g. a best fit with $\chi^2 = 3.940$ was achieved for $Co_{0.25}Fe_{0.75}Sb_{1.90}Pb_{0.10}O_4$. This was

far greater than expected for an acceptable XRPD refinement despite the small amount of impurity. Elements on the same crystallographic site were constrained to allow unified variation and U_{iso} values were fixed to 0.02 for the oxygen positions. It was evident that the profile fitting was unusually unstable; the profile was examined closely and implied the symmetry was incorrect by a noticeable shoulder on the (200) peak which could have been indicative of an orthorhombic distortion (Figure 5.1).

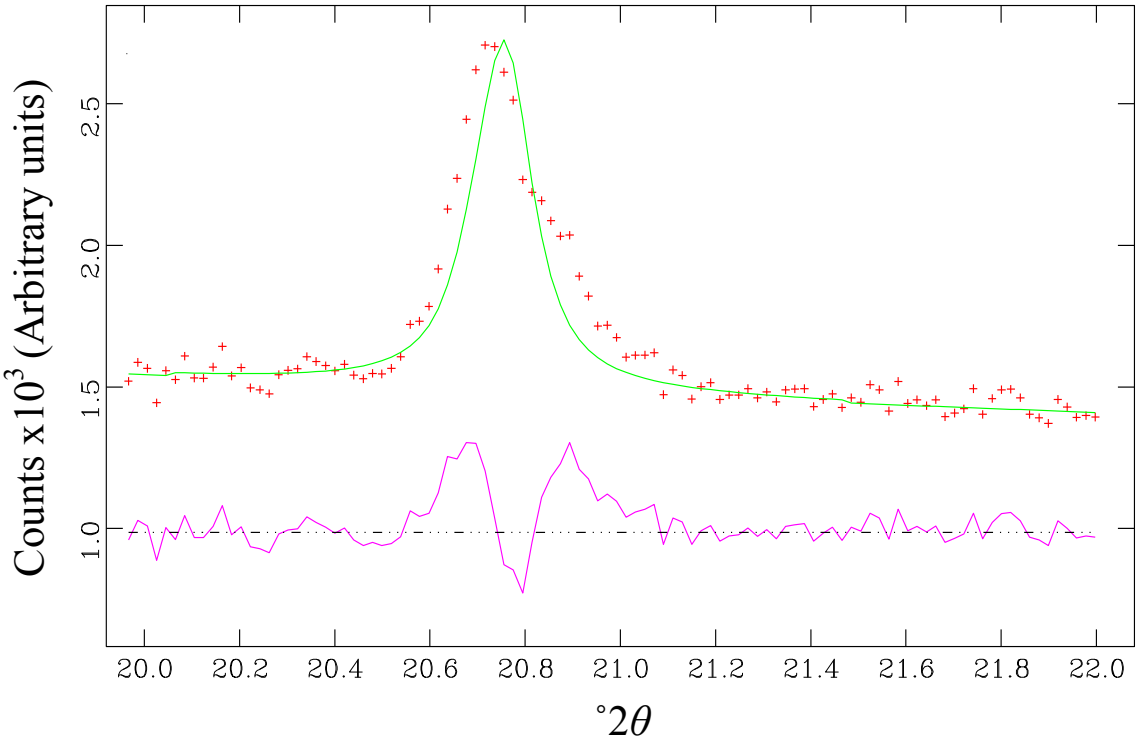

Figure 5.1 Isolation of the orthorhombic distortion during the refinement of $Co_{0.25}Fe_{0.75}Sb_{1.90}Pb_{0.10}O_4$ in $P4_2/mbc$. Displayed is a portion of the structural refinement in $P4_2/mbc$ showing the (200) peak where attempts to fit the peak shape (green line) with different profile parameters was fruitless. The small shoulder of the peak in the observed data (+) is a clear indication of a distortion from original symmetry to a possible orthorhombic spacegroup.

The orthorhombic space group *Pbam*, a maximal subgroup of $P4_2/mbc$ and previously used to describe the orthorhombic distortion seen in Pb_3O_4 at low temperatures [10-11], was used to further investigate the suspected distortion. The final fit of $Co_{0.25}Fe_{0.75}Sb_{1.80}Pb_{0.20}O_4$ in *Pbam* can be seen in Figure 5.2. The shoulder of the (200) peak seen in the $P4_2/mbc$ refinement (Figure 5.1) was accommodated by the change of spacegroup as shown in Figure

5.2 inset. The fits achieved were significantly better than for the $P4_2/mbc$ models; the slightly high values of χ^2 achieved for these phases, when compared with the samples which did not show a distortion, are a reflection of the small amounts of impurity which could not be catered for in the refinement. As the lead content is increased, a diminishing orthorhombic distortion is seen, where a threshold limit reached at $Pb_{0.30}$ (Table 5.1). Exceeding this limit shows strong evidence of the system reverting back to $P4_2/mbc$ symmetry. $Co_{0.25}Fe_{0.75}Sb_{1.70}Pb_{0.30}O_4$ was refined in both *Pbam* (χ^2 = 1.945, R_{wp} = 0.0474) and $P4_2/mbc$ (χ^2 = 2.041, R_{wp} = 0.0486) in order to verify the transition point. Whilst there was no clear shoulder of the (200) peak, the (410) and (140) peaks were visibly split; furthermore the statistics of the *Pbam* model were better (Table 5.1). The *a* lattice parameter (from the $P4_2/mbc$ model) was midway between *a* and *b* of the *Pbam* model suggesting that the distortion, although slight, was still present. The profile fitting was more stable once *Pbam* symmetry was assigned to these phases indicating that the profile functions were trying, inadequately, to fit the small distortion as a morphological rather than crystallographic effect.

The remaining lead compositions could easily be refined in $P4_2/mbc$ without any sign of orthorhombic distortion and with good figures of merit. It is noted that three of the four orthorhombic compounds contained impurities; however, these are minimal especially in the case of $Pb_{0.20}$ (Figure 5.2) where a peak just exceeding the background intensity (31.611 °2θ) is visible representing an impurity in the order of ~3 wt% (the detection limit of the D8 diffractometer). It therefore seems unlikely that the distortion is linked to the impurity.

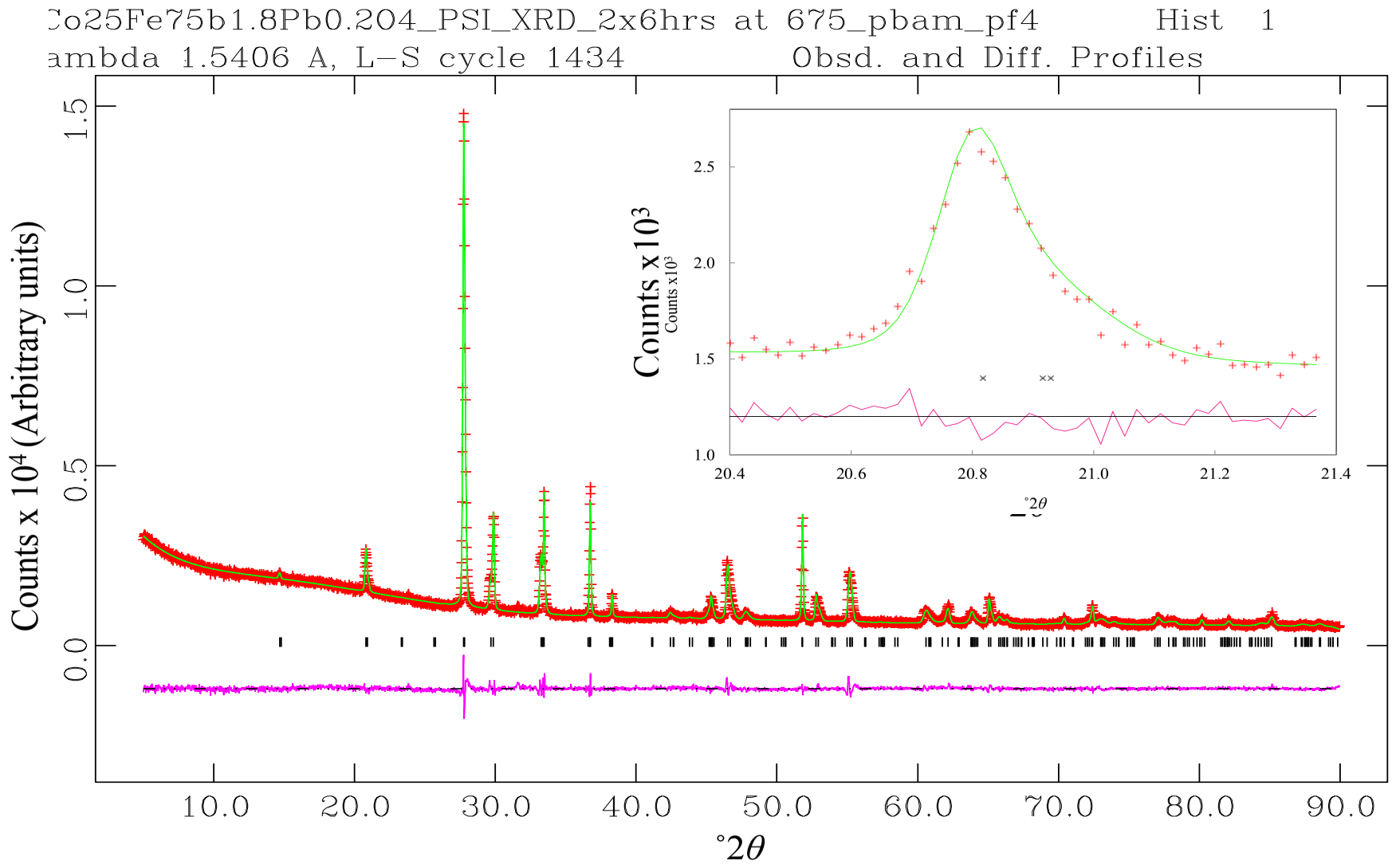

Figure 5.2 The final fit of $Co_{0.25}Fe_{0.75}Sb_{1.80}Pb_{0.20}O_4$ obtained from the Rietveld refinement of XRPD data in *Pbam*. The (+) observed (|) calculated and (|) difference profiles are as indicated. Whilst the tick marks (|) represent the nuclear structure of $Co_{0.25}Fe_{0.75}Sb_{1.80}Pb_{0.20}O_4$. Inset shows the fit of the (200) peak split into the (200) at 20.817 °2θ , (020) at 20.916 °2θ, and (111) peak at 20.929 °2θ.

Figure 5.2 The final fit of $Co_{0.25}Fe_{0.75}Sb_{1.80}Pb_{0.20}O_4$ obtained from the Rietveld refinement of XRPD data in *Pbam*. The (+) observed (|) calculated and (|) difference

Table 5.1 Parameters obtained from the final fits of the $Co_{0.25}Fe_{0.75}Sb_{2-x}Pb_xO_4$ series of compounds based upon the refinement of XRPD data. The amount of unknown impurity is estimated based on a detection limit of 3 wt%. All oxygen U_{iso}*100 values were fixed to 2.00.

	$Co_{0.25}Fe_{0.75}Sb_{2-x}Pb_xO_4$									
	$Pb_{0.10}$	$Pb_{0.20}$	$Pb_{0.25}$	$Pb_{0.30}$		$Pb_{0.30}$	$Pb_{0.40}$	$Pb_{0.50}$	$Pb_{0.60}$	$Pb_{0.75}$
Co/Fe **4*f***	0.253(7)	0.251(6)	0.253(6)	0.238(4)	Co/ Fe **4*d***					
(0, ½, *z*)					(0, ½, ¼)					
U_{iso} *100	2.0(2)	1.7(2)	2.2(2)	2.2(2)	U_{iso}*100	2.4(2)	2.5(2)	2.1(2)	1.8(2)	0.9(1)
Sb/Pb **4*h***	0.175(1),	0.172(1),	0.171(1),	0.170(1),	Sb/Pb **8*h***	0.1687(5),	0.1672(6),	0.1649(5),	0.1624(4),	0.1596(4),
(*x*, *y*, ½)	0.164(1)	0.163(1)	0.162(2)	0.161(2)	(*x*, *y*, 0)	0.1616(5)	0.1611(6)	0.1601(5)	0.1589(4)	0.1577(4)
U_{iso} *100	1.7(3)	2.0(3)	2.6(4)	3.1(5)	U_{iso}*100	3.03(7)	3.09(6)	2.90(6)	2.8(1)	2.91(5)
Sb/Pb **4*g***	0.163(1),	0.163(1),	0.162(1),	0.162(1),	O_{eq} **8*h***	0.093(2),	0.094(2),	0.095(2),	0.100(1),	0.092(2),
(*x*, *y*, 0)	0.832(2)	0.836(1)	0.834(2)	0.831(2)		0.632(2)	0.631(2)	0.631(2)	0.640(2)	0.626(2)
U_{iso} *100	3.0(3)	3.0(3)	1.8(4)	2.9(5)	O_{ap} **8*g***	0.676(2),	0.678(1),	0.676(1),	0.674(1),	0.675(1),
					(*x*, *x*+½, ¼)	0.176(2)	0.178(1)	0.176(1)	0.174(1)	0.175(1)
O_{eq} **4*h***	0.091(5),	0.104(4),	0.111(4),	0.105(5),						
	0.616(7)	0.618(6)	0.626(7)	0.609(6)						
O_{eq} **4*g***	0.141(6),	0.144(5),	0.141(5),	0.166(5),						
	0.588(6)	0.608(5)	0.602(5)	0.588(6)						
O_{ap} **8*i***	0.685(4),	0.666(3),	0.669(3),	0.686(5),						
(*x*, *y*, *z*)	0.191(4),	0.191(3),	0.190(3),	0.183(5),						
	0.240(6)	0.246(6)	0.232(6)	0.24(1)						
Impurity- (wt%)	≈ 6	≈ 3	≈ 6	N/A		N/A	N/A	N/A	N/A	N/A
χ^2	2.763	2.010	2.483	1.945		2.041	1.769	1.999	1.620	1.658
R_{wp}	0.0480	0.0415	0.0450	0.0474		0.0486	0.0457	0.0475	0.0339	0.0424
R_F^2	0.1082	0.1047	0.0722	0.1041		0.1024	0.0919	0.0835	0.0841	0.0759
Space group	*Pbam*	*Pbam*	*Pbam*	*Pbam*		$P4_2/mbc$	$P4_2/mbc$	$P4_2/mbc$	$P4_2/mbc$	$P4_2/mbc$
Lattice parameters (Å)										
a	8.5329(5)	8.5023(4)	8.4926(3)	8.4968(3)		8.4896(2)	8.4735(4)	8.4575(3)	8.4542(1)	8.4459(1)
b	8.4832(7)	8.4634(6)	8.4631(5)	8.4823(3)						
c	5.9450(2)	5.9636(2)	5.9693(1)	5.9714(1)		5.9709(1)	5.9892(3)	6.0056(2)	6.02845(8)	6.0459(1)

The $Co_{0.50}Fe_{0.50}Sb_{2-x}Pb_xO_4$ phases showed no clear evidence to suggest a distortion from $P4_2/mbc$ symmetry and very good fits were achieved. All phases appeared to be free from impurity. The $Co_{0.75}Fe_{0.25}Sb_{2-x}Pb_xO_4$ phases again showed excellent coincidence with $P4_2/mbc$ symmetry but $Co_{0.75}Fe_{0.25}Sb_{1.90}Pb_{0.10}O_4$ clearly contained impurities, the most intense peak being at the foot of the (211) peak at 27.798 ˚2θ. All samples showed preferred orientation along [001] (e.g. $Co_{0.75}Fe_{0.25}Sb_{1.75}Pb_{0.25}O_4$, ratio = 0.946(4)). The final fits of all XRPD refinements can be seen in Appendix 3.1.

Inspection of all powder patterns, post refinement, showed a diminishing intensity of the (110) peak, at around 14.5 ˚2θ, with increased lead compositions (see Appendix 3.1). Intensities of the (110) peaks are sensitive to the Sb/Pb positions and full disorder on these sites could explain this. To some extent the high U_{iso} values could further support this observation (Tables 5.1 and 5.2).

Table 5.2 Parameters obtained from the final fits of the $Co_{0.50}Fe_{0.50}Sb_{2-x}Pb_xO_4$ and $Co_{0.75}Fe_{0.25}Sb_{2-x}Pb_2O_4$ compounds based on the refinement of XRPD data in $P4_2/mbc$.

	$Co_{0.50}Fe_{0.50}Sb_{2-x}Pb_xO_4$						$Co_{0.75}Fe_{0.25}Sb_{2-x}Pb_xO_4$		
	$Pb_{0.10}$	$Pb_{0.20}$	$Pb_{0.25}$	$Pb_{0.30}$	$Pb_{0.40}$	$Pb_{0.50}$	$Pb_{0.10}$	$Pb_{0.20}$	$Pb_{0.25}$
Co/Fe **4*d***	1.9(1)	2.3(2)	2.0(2)	1.8(2)	2.0(2)	1.2(1)	2.0(2)	2.3(2)	1.5(2)
U_{iso}*100									
Sb/Pb **8*h***	0.1742(3), 0.1642(3)	0.1701(5), 0.1625(5)	0.1692(5), 0.1623(5)	0.1687(5), 0.1624(5)	0.1666(5), 0.1607(5)	0.1637(4), 0.1603(4)	0.1750(5), 0.1637(5)	0.1722(5), 0.1633(5)	0.1696(6), 0.1634(6)
U_{iso}*100	2.30(6)	2.69(8)	2.45(6)	2.39(6)	2.53(7)	2.59(5)	2.64(8)	2.74(7)	2.54(7)
O_{eq} **8*h***	0.103(2), 0.643(2)	0.097(2), 0.632(2)	0.101(2), 0.628(2)	0.095(2), 0.624(2)	0.097(2), 0.639(2)	0.097(1), 0.643(2)	0.093(2), 0.629(2)	0.094(2), 0.624(2)	0.096(2), 0.630(2)
O_{ap} **8*i***	0.684(1), 0.184(1)	0.679(1), 0.179(1)	0.678(1), 0.178(1)	0.677(1), 0.177(1)	0.677(1), 0.177(1)	0.678(1) 0.178(1)	0.683(2), 0.183(2)	0.682(1), 0.182(1)	0.681(1), 0.181(1)
χ^2	1.765	1.779	1.821	1.821	1.689	1.620	1.878	1.814	1.856
R_{wp}	0.0332	0.0433	0.0421	0.0436	0.0409	0.0361	0.0445	0.0428	0.0385
R_F^2	0.0951	0.0980	0.0729	0.0710	0.0698	0.0722	0.1291	0.1031	0.0893
Impurity (wt %)	-	-	-	-	-	-	≈ 6	-	-
Lattice parameters (Å)									
a	8.5289(2)	8.4861(7)	8.4738(2)	8.4694(6)	8.4553(2)	8.4572(1)	8.5002(2)	8.4783(5)	8.4708(7)
c	5.9407(2)	5.9573(5)	5.9659(1)	5.9737(4)	5.9951(1)	6.0216(1)	5.9313(1)	5.9534(4)	5.9672(5)

5.4 Refinement of NPD data

The following compositions were examined by NPD at 300 and 1.5 K: $Co_{0.25}Fe_{0.75}Sb_{2-y}Pb_yO_4$ (where y = 0.25, 0.50, 0.75), $Co_{0.50}Fe_{0.50}Sb_{2-y}Pb_yO_4$ (y = 0.25, 0.40, 0.50) and $Co_{0.75}Fe_{0.25}Sb_{1.75}Pb_{0.25}O_4$. The refinement procedure was carried out as in previous chapters testing profile functions, different magnetic modes and orientations, applying ADPs where appropriate etc before arriving at the final model. The neutron wavelength was set to be consistent with that refined from the $Co_{0.25}Fe_{0.75}Sb_2O_4$ sample (λ = 1.88434 Å, data collected during the same beam time allocation). Most samples except $Co_{0.75}Fe_{0.25}Sb_{1.75}Pb_{0.25}O_4$ and $Co_{0.50}Fe_{0.50}Sb_{1.50}Pb_{0.50}O_4$ were found to contain trace amounts of Fe_3O_4, below the limit of detection for the D8 diffractometer. Nuclear and magnetic contributions to the profile from the known impurity were accommodated throughout all applicable refinements. ADPs were applied to the O_{ap} site for most compositions in order to see if there was any correlation between Pb content and the thermal motion of the O_{ap} site in the *ab* plane.

5.4.1 NPD at 300 K

The 300 K data sets were first refined using the models obtained from the XRPD refinements as the basis. The reduced resolution associated with NPD meant that no obvious sign of a shoulder to the (200) peak for $Co_{0.25}Fe_{0.75}Sb_{1.75}Pb_{0.25}O_4$ was visible however for consistency the structure was refined in *Pbam* the final fit is shown in Figure 5.3. It should be noted that $P4_2/mbc$ was tested and the fit was slightly worse ($P4_2/mbc$: χ^2 = 2.540, R_{wp} = 0.0433); examination of the FWHM values of the (*h*00) and (*h*10) peaks showed these to be slightly broader than neighbouring reflections supporting the assignment of *Pbam* symmetry.

The refined lattice parameters from the $Co_{0.25}Fe_{0.75}Sb_{1.75}Pb_{0.25}O_4$ *Pbam* model (a = 8.5083(3) Å, b = 8.4985(4) Å, c = 5.9683(1) Å) returned comparable a and c parameters to the XRPD refinement (a = 8.4926(3) Å, b = 8.4631(5) Å, c = 5.9693(1) Å). In the case of b, which showed a large difference, this could be a consequence of the discrepancy between resolution capabilities of the two techniques where the distortion is less clearly visible in the NPD data. For much better identification of the distortion a synchrotron radiation source would be required with much greater resolution which should be able to distinguish between the a and b parameters more clearly. All remaining fits which have not been shown here can be seen in Appendix 3.2.

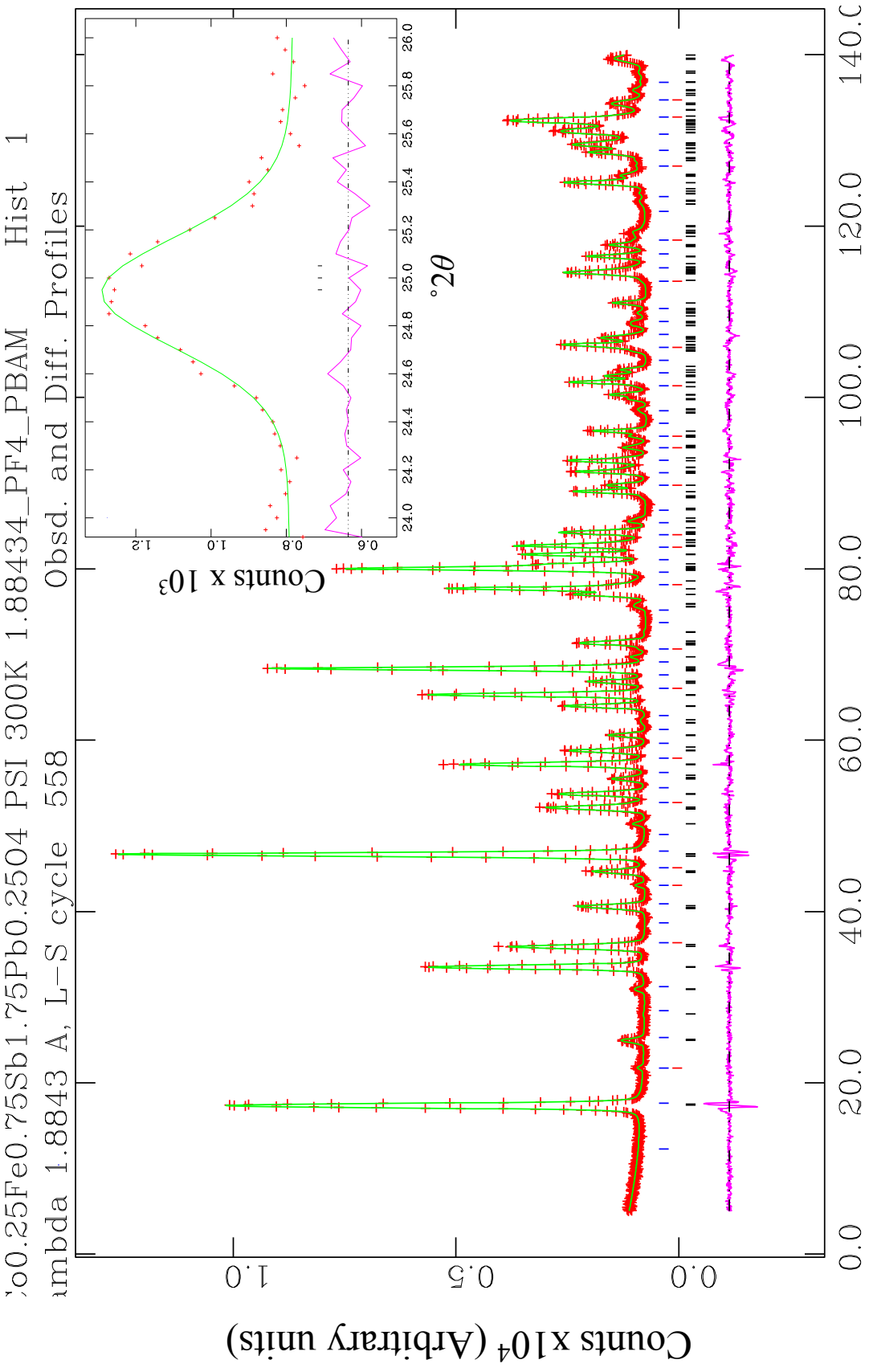

Figure 5.3 The final refinement of $Co_{0.25}Fe_{0.75}Sb_{1.75}Pb_{0.25}O_4$ in *Pbam* at 300 K; the (+) observed (|) calculated and (|) difference profiles are as indicated whilst the tick marks represent the $Co_{0.25}Fe_{0.75}Sb_{1.75}Pb_{0.25}O_4$ nuclear (|), Fe_3O_4 nuclear (|), and Fe_3O_4 magnetic structures (|). The inset shows the (200) at 24.975 °2θ, (020) at 25.005 °2θ and the (111) peak at 25.088 °2θ.

Table 5.3 Details obtained from the final NPD refinements of the $Co_{1-x}Fe_xSb_{2-y}Pb_yO_4$ compounds at 300 K. (λ used 1.88434 Å) for all samples

	$Co_{0.25}Fe_{0.75}Sb_{1.75}Pb_{0.25}O_4$		$Co_{0.25}Fe_{0.75}Sb_{2-x}Pb_xO_4$		$Co_{0.50}Fe_{0.50}Sb_{2-x}Pb_2O_4$			$Co_{0.75}Fe_{0.25}Sb_{1.75}Pb_{0.25}O_4$
			$Pb_{0.50}$	$Pb_{0.75}$	$Pb_{0.25}$	$Pb_{0.40}$	$Pb_{0.50}$	
Co/Fe **4*f***	0.2405(7)	Co/Fe **4*d***						
U_{iso} *100	1.36(3)	U_{iso} *100	1.31(3)	1.32(3)	1.41(4)	1.29(4)	1.22(4)	1.27(6)
Sb/Pb **4*h***	0.1728(6), 0.1624(7)	Sb/Pb **8*h***	0.1651(2), 0.1592(2)	0.1594(1), 0.1573(1)	0.1698(2), 0.1619(2)	0.1667(2), 0.1601(2)	0.1639(2), 0.1598(2)	0.1695(2), 0.1620(2)
U_{iso} *100	1.6(1)	U_{iso} *100	1.98(3)	2.11(3)	1.86(3)	1.95(3)	2.12(3)	1.86(3)
Sb/Pb **4*g***	0.1611(7), 0.8324(6)	O_{eq} **8*h***	0.0966(2), 0.6354(2)	0.0963(1), 0.6324(2)	0.0980(2), 0.6380(2)	0.0970(2), 0.6360(1)	0.0970(2), 0.6351(2)	0.0975(2), 0.6378(1)
U_{iso} *100	2.0(1)	U_{iso} *100	2.00(4)	1.94(4)	2.01(4)	2.10(4)	2.16(4)	1.96(4)
O_{eq} **4*h***	0.0978(7), 0.6359(7)	O_{ap} **8*g***	0.6743(1), 0.1743(1)	0.6721(1), 0.1721(1)	0.6767(1), 0.1767(1)	0.6753(1), 0.1753(1)	0.6747(1), 0.1747(1)	0.6768(1), 0.1768(1)
U_{iso} *100	2.1(1)	U_{11} = U_{22}*100	2.32(6)	2.38(6)	2.40(6)	2.47(6)	2.63(6)	2.56(6)
O_{eq} **4*g***	0.1403(7), 0.5978(8)	U_{33}*100	2.3(1)	2.33(9)	1.9(1)	2.3(1)	2.2(1)	1.9(1)
U_{iso} *100	2.0(1)	U_{11}/U_{33}	1.01	1.02	1.26	1.07	1.20	1.35
O_{ap} **8*i***	0.6709(4), 0.1829(4), 0.2446(9)							
U_{iso} *100	2.16(4)							
Impurity	Fe_3O_4 - < 1 wt%		Fe_3O_4 - < 1 wt%	Fe_3O_4 - < 2 wt%	Fe_3O_4 - < 2 wt%	Fe_3O_4 - < 1 wt%	-	-
χ^2	2.322		1.966	3.278	3.449	2.624	3.408	3.855
R_{wp}	0.0414		0.0414	0.0384	0.0392	0.0377	0.0419	0.409
R_F^2	0.0243		0.240	0.0256	0.0290	0.0286	0.0387	0.0322
Space group	*Pbam*		$P4_2/mbc$	$P4_2/mbc$	$P4_2/mbc$	$P4_2/mbc$	$P4_2/mbc$	$P4_2/mbc$
Lattice parameters (Å)								
a	8.5083(3)		8.4604(1)	8.4492(2)	8.4866(2)	8.4596(1)	8.4546(2)	8.4724(2)
b	8.4985(4)							
c	5.9683(1)		6.0085(1)	6.0483(1)	5.9662(2)	5.9960(1)	6.0194(2)	5.9661(2)

5.4.2 NPD at 1.5 K

The refinement of magnetic structures was implemented as in previous chapters. The structures obtained from the 300 K refinements were used as the basis for refinement; $Co_{0.25}Fe_{0.75}Sb_{1.75}Pb_{0.25}O_4$ was refined in *Pbam* whilst all other samples were refined in $P4_2/mbc$. All samples clearly showed the dominant magnetic ordering to be consistent with a C mode due to the relative strength of the (100) magnetic peak. Other types of ordering were investigated and the indexing rules discussed by Gonzalo [12] used to identify other magnetic components. There was no apparent increase in intensity of the weak (201) nuclear reflection upon cooling for any phase which can be used as a guide to suggest the presence of an A mode. Comparison between the obtained lattice parameters of each phase with $CoSb_2O_4$ (a = 8.4809(1) Å, c = 5.92092(9) Å at 4 K) showed that all of the lead containing phases possessed a larger c parameter at 1.5 K. The magnitude of c is critically linked to the TM-TM orbital overlap [13], and hence to the strength of direct exchange. $CoSb_2O_4$ has been shown to possess the smallest c parameter to display simple C- type ordering, and this supports the assignment of dominant C- type ordering to all phases.

The direction of the C mode was, in most cases, consistent with the C_z model where significantly better statistics and fit were obtained solely for this arrangement; however, $Co_{0.25}Fe_{0.75}Sb_{1.75}Pb_{0.25}O_4$ presented a different situation. A C_z cell was initially fitted to the data but the significantly reduced moment was of concern (χ^2 = 3.792 C_z = 2.752(9) μ_B; $CoSb_2O_4$, C_z = 3.73(2) μ_B). Theoretically the maximum spin only moment achievable from NPD equates to 4 μ_B, the same as expected for $FeSb_2O_4$, yet the moment was significantly lower than those previously reported [1, 12, 14]. Despite a good fit being achieved for just a C_z mode (Figure 5.4) it was clear another component to the model was missing, evident from the shoulder of the (300/030) peak (Figure 5.4 inset) which could possibly explain the lower

than expected refined moment magnitude. Other components were investigated in the *ab* plane. The nature of the tetragonal nuclear cell had in previous cases precluded the distinction between *x* and *y* directions but with a refined orthorhombic nuclear cell distinction was subsequently possible and all variations were investigated as shown in Table 5.4.

Table 5.4 The refined moments and associated statistics for $Co_{0.25}Fe_{0.75}Sb_{1.75}Pb_{0.25}O_4$ at 1.5 K.

	Magnetic model	Form factor	χ^2, R_{wp}
$Co_{0.25}Fe_{0.75}Sb_{1.75}Pb_{0.25}O_4$	C_z = 2.752(9)	Fe^{2+}	3.793, 0.0409
	C_x = 3.52(2)	Fe^{2+}	8.688, 0.0618
	C_y = 3.51(2)	Fe^{2+}	8.848, 0.0624
	C_{zxy}:	Fe^{2+}	Would not converge
	C_{xz} : C_z =2.60(2) C_x = 1.41(7)	Fe^{2+}	3.679, 0.0402
	C_{yz}: C_z= 2.60(2) C_y = 1.41(7)	Fe^{2+}	3.675, 0.0402

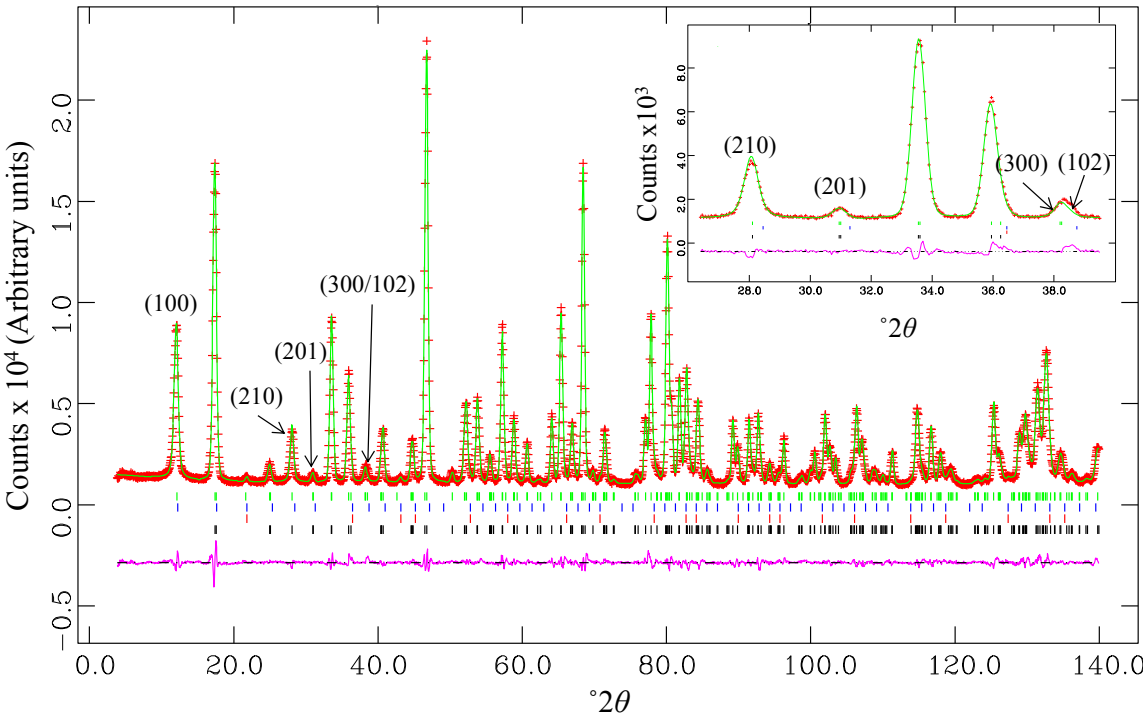

Figure 5.4 A plot of the Rietveld refinement of $Co_{0.25}Fe_{0.75}Sb_{1.75}Pb_{0.25}O_4$ in *Pbam* with a C_z magnetic model. The observed (+), calculated and difference profiles (continuous lines) are as indicated whilst the tick marks represent the $Co_{0.25}Fe_{0.75}Sb_{1.75}Pb_{0.25}O_4$ nuclear (|), Fe_3O_4 nuclear (|), and Fe_3O_4 magnetic (|), and $Co_{0.25}Fe_{0.75}Sb_{1.75}Pb_{0.25}O_4$ magnetic (|) structures. The inset shows the region 26.2-39.5 °2*θ* note that intensity has not been calculated for the (102) reflection. The (030) and (012) peaks have not been marked to simplify the display but the lattice parameters of the magnetic cell were consistent with the orthorhombic nuclear cell.

The insignificant difference between the moment obtained in the *x* and *y* directions is a result of the small difference between a = 8.4902(3) Å and b = 8.5004(4) Å. A model where the C_x and C_z modes were combined into a single phase was chosen to be representative of the magnetic structure. The final fit was stable and all magnetic reflections were suitably refined (Figure 5.5); a total moment of μ_{total} = 2.96(5) μ_B was achieved which is significantly lower than the spin only moment of 4.0 μ_B. It is usual for the spin only moments of TM's which have been refined from NPD data, and do not show any orbital contribution, to be lower than 2*S* because of covalence effects. However, the value obtained here is significantly lower than expected.

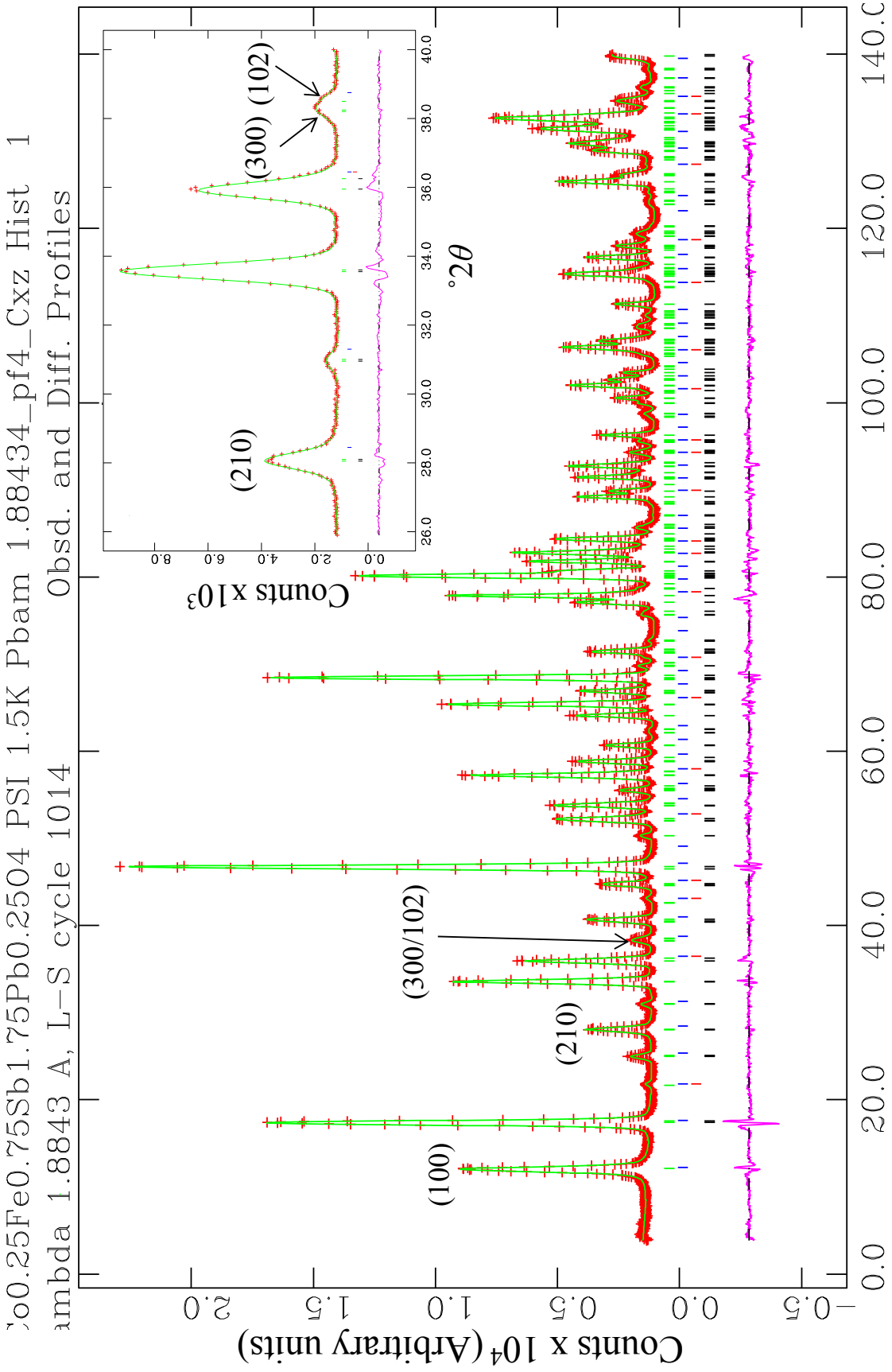

Figure 5.5 The final fit of $Co_{0.25}Fe_{0.75}Sb_{1.75}Pb_{0.25}O_4$ at 1.5 K with *Pbam* symmetry and a magnetic structure consistent with a C_{xz} mode. The fit includes $Co_{0.25}Fe_{0.75}Sb_{1.75}Pb_{0.25}O_4$ nuclear (|), Fe_3O_4 nuclear (|), Fe_3O_4 magnetic (|) and the $Co_{0.25}Fe_{0.75}Sb_{1.75}Pb_{0.25}O_4$ magnetic (|) structures. The inset shows the improved fit of the (300), (030), (012), and (102) reflections.

The remaining phases consistently showed the main magnetic component of the system to be related to a C_z mode and indicators of an A- type ordering were absent. The possible presence of a G mode received careful consideration. As demonstrated in (Figure 5.6) the addition of a Fe_3O_4 impurity was insufficient to satisfactorily match the observed intensity as it had done in the previous refinements of other phases; this is despite refining the atomic positions, lattice parameters and profile parameters for the Fe_3O_4 magnetic phase. The small but clear difference in $^{\circ}2\theta$ between the red and green tick marks in a preliminary refinement of $Co_{0.50}Fe_{0.50}Sb_{1.60}Pb_{0.40}O_4$ indicated that the observed shoulder could be attributed to a G type (101) reflection. Where this phenomenon was seen, i.e. contributions from magnetite were insufficient, a G component was refined and returned a small moment in many samples (see Tables 5.5 and 5.6). These values were lower than could perhaps be refined with a high degree of accurately but it is an indication that a small G- type component exists. For completeness, the G- type ordering in the *ab* plane was combined with the main C_z component into a single phase. It is seen that there is a rough consistency between the magnitude of G_x and C_z. Refining the magnetic components individually did not provide significantly different values of G_x for a statistically worse fit (e.g. $Co_{0.50}Fe_{0.50}Sb_{1.75}Pb_{0.25}O_4$: $\chi^2 = 4.707$, $C_z = 3.40(1)$, $G_x = 0.84(3)$) but it is accepted that the accuracy of the magnitude of the G component is questionable. The increased complexity resulting from mixtures of Fe^{2+}/Fe^{3+} and possibly Co^{2+}/Co^{3+} and the effect on the magnetic form factor was considered in all cases and investigated once the magnetic structure was established. The magnetic form factor which gave the best fit and made the most chemical sense was always used. The details of the final fits can be seen in Tables 5.5 and 5.6.

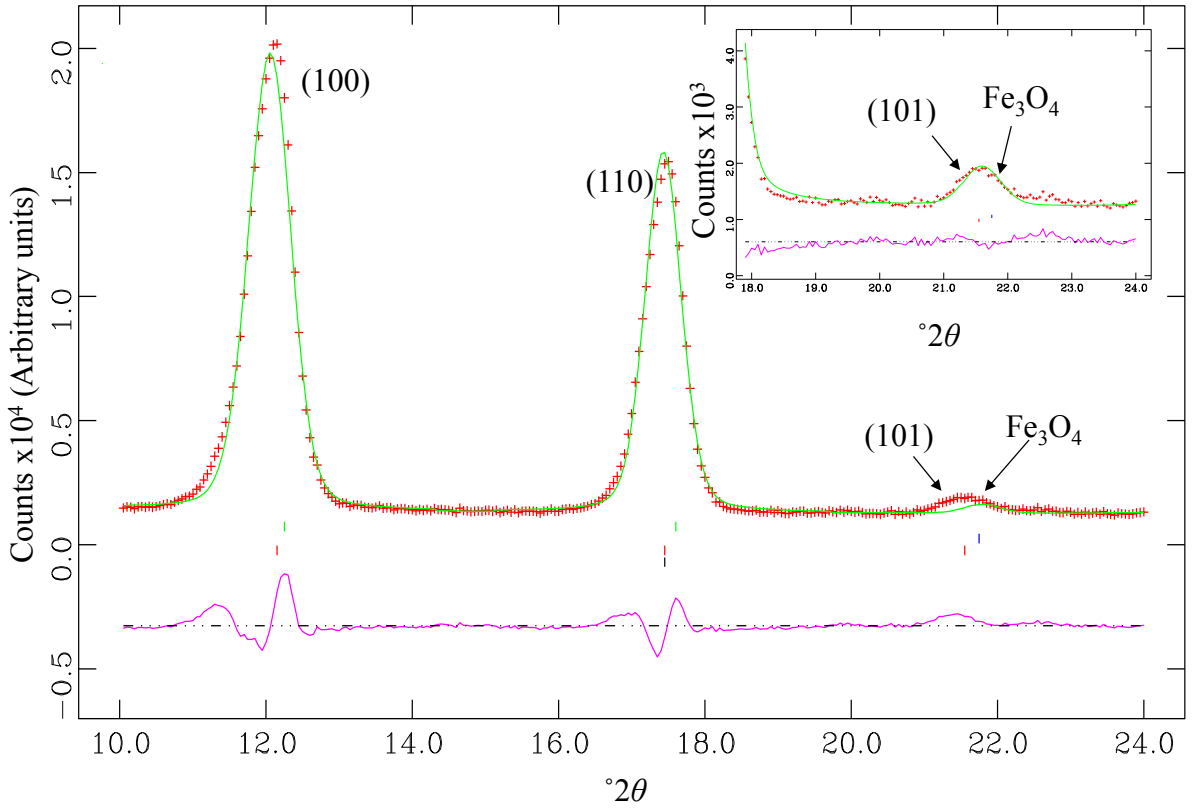

Figure 5.6 An enlarged plot from the preliminary refinement of the $Co_{0.50}Fe_{0.50}Sb_{1.60}Pb_{0.40}O_4$ nuclear phase (|) and C_z magnetic component (|). Fe_3O_4 nuclear (|) and magnetic (|) contributions are indicated. Note the Fe_3O_4 peak and (101) peak of a G mode are roughly coincident; however, the difference profile (purple line) clearly shows a discrepancy between the calculated (green line) and observed (+) intensities the maximum of which is coincident with the (101) reflection position. The inset shows the fit with the addition of a G- type magnetic component to the refinement (|), note how the previously missing intensity is now accounted for by the (101) peak.

The statistics for some of the final fits appear slightly high but despite this the fits are very good as shown by the difference profile. It is clear that in several of the phases e.g. $Co_{0.50}Fe_{0.50}Sb_{1.50}Pb_{0.50}O_4$ (Figure 5.7), the (100) peak was highly asymmetric and despite best attempts to fit the asymmetry the fits could not be improved. This is characteristic of low angle peaks in NPD data. All remaining final fits can be seen in Appendix 3.3.

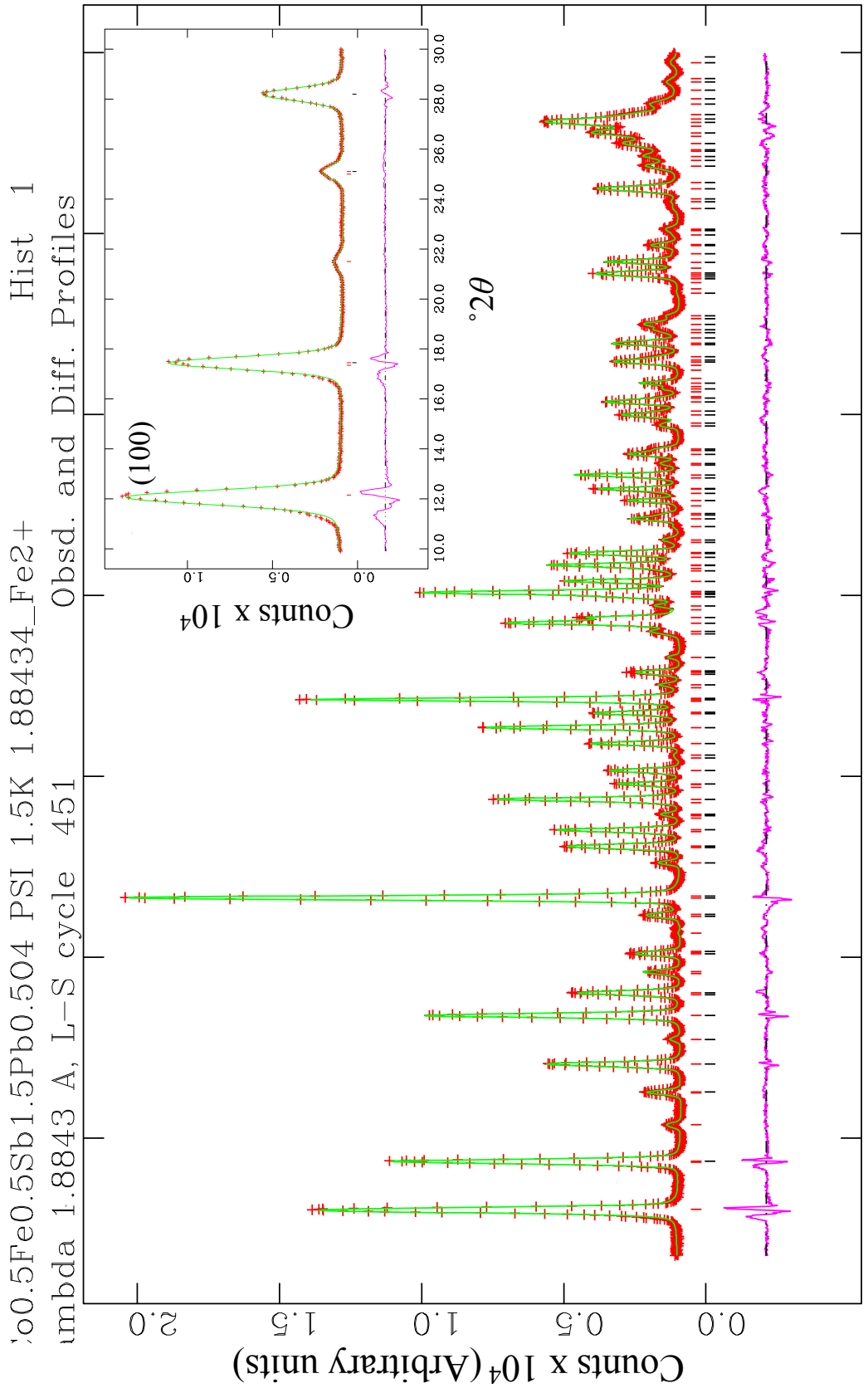

Figure 5.7 The final fit of $Co_{0.50}Fe_{0.50}Sb_{1.50}Pb_{0.50}O_4$ in $P4_2/mbc$ showing the C_z and G_x mode components combined into a single phase. The (+) observed, calculated, and difference profiles (continuous green and purple lines respectively) are as indicated. The tick marks represent the $Co_{0.50}Fe_{0.50}Sb_{1.50}Pb_{0.50}O_4$ nuclear (|), and magnetic (|) structures. The inset highlights the asymmetry of the (100) magnetic peak

Table 5.5 Details of the final structures obtained from the Rietveld refinement of the $Co_{0.25}Fe_{0.75}Sb_{2-x}Pb_xO_4$ phases at 1.5 K.

	$Co_{0.25}Fe_{0.75}Sb_{2-x}Pb_xO_4$			
	$Pb_{0.25}$		$Pb_{0.50}$	$Pb_{0.75}$
Co/Fe **4*f***	0.2559(8)	Co/Fe **4*d***		
U_{iso}*100	0.66(3)	U_{iso}*100	0.64(3)	0.78(3)
Sb/Pb **4*h***	0.1668(6), 0.1615(5)	Sb/Pb **8*h***	0.1653(1), 0.1588(2)	0.1596(1), 0.1567(1)
U_{iso}*100	1.0(1)	U_{iso}*100	1.11(3)	1.33(3)
Sb/Pb **4*g***	0.1628(6), 0.8279(6)	O_{eq} **8*h***	0.0964(2), 0.6365(2)	0.0960(1), 0.6334(2)
U_{iso}*100	1.1(1)	U_{iso}*100	1.33(4)	1.28(4)
O_{eq} **4*h***	0.0949(7), 0.6394(6)	O_{ap} **8*g***	0.6738(1), 0.1738(1)	0.6717(1), 0.1717(1)
U_{iso}*100	1.8(1)	U_{iso}*100	1.19(3)	1.40(4)
O_{eq} **4*g***	0.1389(6), 0.6013(5)			
U_{iso}*100	0.8(1)			
O_{ap} **8*i***	0.6773(5), 0.1748(5), 0.2525(9)			
U_{iso}*100	1.15(3)			
Impurity-	Fe_3O_4 <1wt%		Fe_3O_4 < 1 wt %	Fe_3O_4 < 2 wt%
χ^2	3.679		4.683	4.689
R_{wp}	0.0402		0.0448	0.0448
R_F^2	0.0196		0.0255	0.0243
Space group	*Pbam*		$P4_2/mbc$	$P4_2/mbc$
Lattice parameters (Å)				
a	8.4902(3)		8.4510(1)	8.4413(1)
b	8.5004(2)			
c	5.9581(1)		5.9988(1)	6.0379(1)
Magnetic moment (μ_B)	C_z = 2.60(2)		C_z = 3.76(1)	C_z = 3.33(1)
	C_x = 1.41(7)			G_x =0.44(6)
	μ_{total} = 2.96(5)			μ_{total} = 3.36(2)
Form factor	Fe^{2+}		Fe^{3+}	Fe^{3+}

Table 5.6 Details of the final structures obtained from the Rietveld refinement of the $Co_{0.50}Fe_{0.50}Sb_{2-x}Pb_xO_4$ (x = 0.25, 0.40, 0.50) and $Co_{0.75}Fe_{0.25}Sb_{1.75}Pb_{0.25}O_4$ phases at 1.5 K.

	$Co_{0.50}Fe_{0.50}Sb_{2-x}Pb_xO_4$			$Co_{0.75}Fe_{0.25}Sb_{1.75}Pb_{0.25}O_4$
	$Pb_{0.25}$	$Pb_{0.40}$	$Pb_{0.50}$	
Co/Fe **4*d***	0.52(4)	0.63(4)	0.52(4)	0.23(6)
U_{iso}*100				
Sb/Pb **8*h***	0.1700(2), 0.1619(2)	0.1668(1), 0.1601(2)	0.1644(2), 0.1594(2)	0.1697(2), 0.1621(2)
U_{iso}*100	0.90(3)	1.16(2)	1.32(3)	0.83(4)
O_{eq} **8*h***	0.0980(2), 0.6390(1)	0.0968(2), 0.6374(1)	0.0967(2), 0.6361(2)	0.0978(2), 0.6387(2)
U_{iso}*100	1.07(4)	1.37(4)	1.45(4)	0.91(5)
O_{ap} **8*g***	0.6761(1), 0.1761(1)	0.6748(1), 0.1748(1)	0.6741(1), 0.1741(1)	0.6763(1), 0.1763(1)
U_{iso}*100	0.87(4)	1.25(3)	1.33(4)	0.92(4)
Impurity	Fe_3O_4 < 2 wt%	Fe_3O_4 < 1 wt%	-	-
χ^2	4.620	5.268	5.006	5.994
R_{wp}	0.0437	0.433	0.0499	0.0502
R_F^2	0.0262	0.0250	0.0378	0.0382
Space group	*P4$_2$/mbc*	*P4$_2$/mbc*	*P4$_2$/mbc*	*P4$_2$/mbc*
Lattice parameters (Å)				
a	8.4775(1)	8.4508(1)	8.4463(2)	8.4633(2)
c	5.9594(1)	5.9890(1)	6.0115(1)	5.9607(2)
Magnetic moment (μ_B)	C_z = 3.55(1)	C_z = 3.64(1)	C_z = 3.53(1)	C_z = 3.55(2)
	G_x = 0.85(3)	G_x = 0.85(3)	G_x = 0.95(3)	G_x = 0.86(3)
	μ_{total} = 3.65(2)	μ_{total} = 3.74(1)	μ_{total} = 3.64(1)	μ_{total} = 3.65(3)
Form factor	Fe^{2+}	Fe^{3+}	Fe^{3+}	Co^{2+}

5.4.3 Analysis of results

There was very good agreement between the refined XRPD and NPD lattice parameters of all samples except $Co_{0.25}Fe_{0.75}Sb_{1.75}Pb_{0.25}O_4$, the *a* and *c* parameters for which were in good agreement but the *b* paramter (NPD = 8.4985(4) Å, XRPD 8.4631(5) Å) showed a large difference. This is believed to be caused by the better resolution of XRPD in which the distortion is more easily identified. As shown by Figure 5.8 the general trend as a result of increasing the lead content of the system is to increase *c* whilst simultaneously decreasing *a* reminiscent of the $FeSb_{2-x}Pb_xO_4$ phases [1]. As the lead conent is increased, the octahedral environment becomes more regular and this is facilitated primarily by a larger reduction in the Co-O_{ap} bonds (Tables 5.7 and 5.8): $Co_{0.25}Fe_{0.75}Sb_{2-x}Pb_xO_4$ (x = 0.25 to 0.75), ΔO_{ap} = -0.072 Å, $\Delta O_{eq} = 5.6x10^{-3}$ Å). This is akin to the introduction of Pb into $CoSb_2O_4$ (*Section 3.7*). The expansion of *c* is explained by the elongation of all Sb-O bonds to accomodate the contracting octahedra and insertion of larger Pb^{2+} ions on the Sb^{3+} site. Induced oxidation of the TM species (most likely Fe) would also cause *c* to expand through greater repulsion between intra chain octahedral cations. Interestingly the gradient of the Δc data for all samples at 300 K (based on XRPD data) appears to converge on a lead content of $Pb_{0.30}$ independent of the Co/Fe ratio where after there is a rapid expansion of *c*. This is not mirrored in Δa and suggests there could be a physical threshold for the changes in lattice parameters at this point.

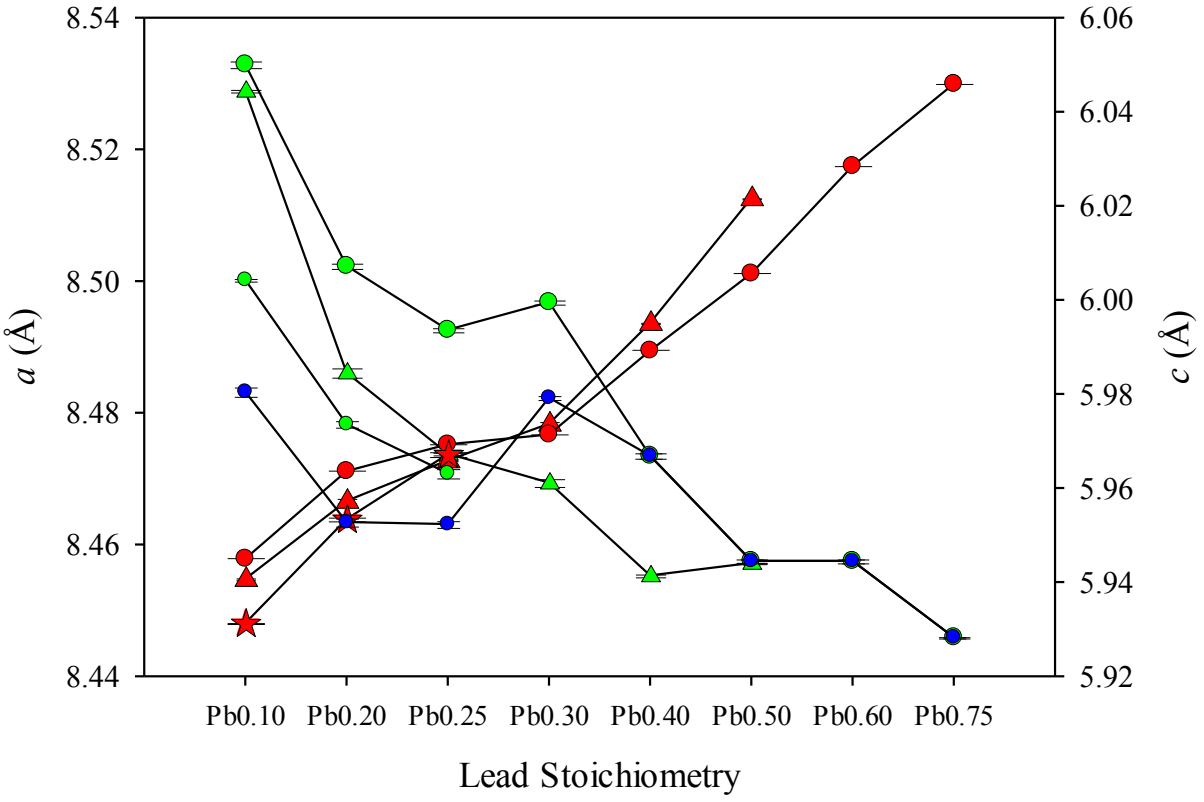

On cooling to 1.5 K distortion of the octahedral crsytal field is reduced in all phases except $Co_{0.25}Fe_{0.75}Sb_{1.75}Pb_{0.25}O_4$. The refined magnetic structures of all phases also show noncollinear spin alingment, except for $Co_{0.25}Fe_{0.75}Sb_{1.50}Pb_{0.50}O_4$, which are consistent with a dominant C mode and a minor G- type component. The G- type ordering is present in phases which are shown to be contaminanted with and Fe_3O_4 free which likely precludes any relationship. The intra TM separation distance ranges beteen 2.9797-3.0199 Å (excluding $Co_{0.25}Fe_{0.75}Sb_{1.75}Pb_{0.25}O_4$, discussed below) which is in all cases larger than that of $FeSb_2O_4$ (2.9500 Å [14]) but is smaller, in many cases, than seen in $MnSb_2O_4$ (2.9916 Å [15]) which display a dominant A mode. Kanamori [16] gives no details as to the outcome of a 90˚ superexchange between the possible intereactions present in the phases reported here. In any case, the complexity and potential range of cations (Co^{2+} (d^7); Fe^{2+} (d^6); Fe^{3+} (d^5); Co^{3+} (d^6)) interacting through a 90˚ super exchange mechanism surpasses the relatively simple phases

examined by Kanamori and it is difficult to predict the superexchange outcome. However, the 90˚ superexchange is likely to be important for generating ferromagnetic order within a chain in these phases, although in the structure above both double exchange and direct exchange can potentially occur also. Since direct exchange relies on orbital overlap there is a subtle interplay between TM-TM distance, oxidation state, and orbital contraction [13, 17-18]. This can begin to explain why some of these compounds with a smaller *c* parameter than $MnSb_2O_4$ display a dominant C mode, where all TM-O-TM bond angles range between 91.87(5)˚-94.83(5)˚.

As previously mentioned the refined moment for $Co_{0.25}Fe_{0.75}Sb_{1.75}Pb_{0.25}O_4$ is particularly low (μ_{total} = 2.96(5) μ_B ; $\mu_{expected}$ = 4 μ_B based upon 2*S*). The bond lengths show us that the Co-O_{4h} (2.042(5) Å) equatorial bonds are much shorter than the Co-O_{4g} (2.111(4) Å) at 1.5 K (Figure 5.9). This shows that intrachain pairs of very close magnetic (TM-TM distance = 2.909 Å) ions form separated by an inter pair distance of 3.049 Å. The magnitude of the (100) magnetic reflection is adequately matched and suggests that it is possible the orthorhombic distortion has partially removed the degeneracy of the t_{2g} orbitals. Removal of the degeneracy and hence removal of some/all of the orbital contribution explains a lower moment but not a moment lower than the spin only value. The remaining phases which do not display the distortion all represent moments which are more consistent with a 2*S* moment but are lower than expected, due to covalence effects. These findings are consistent with those reported in the lead doped schafarzikite phases e.g. $FeSb_{1.30}Pb_{0.70}O_4$ C_x = 1.3(2) μ_B , C_z = 3.29(4) μ_B [1].

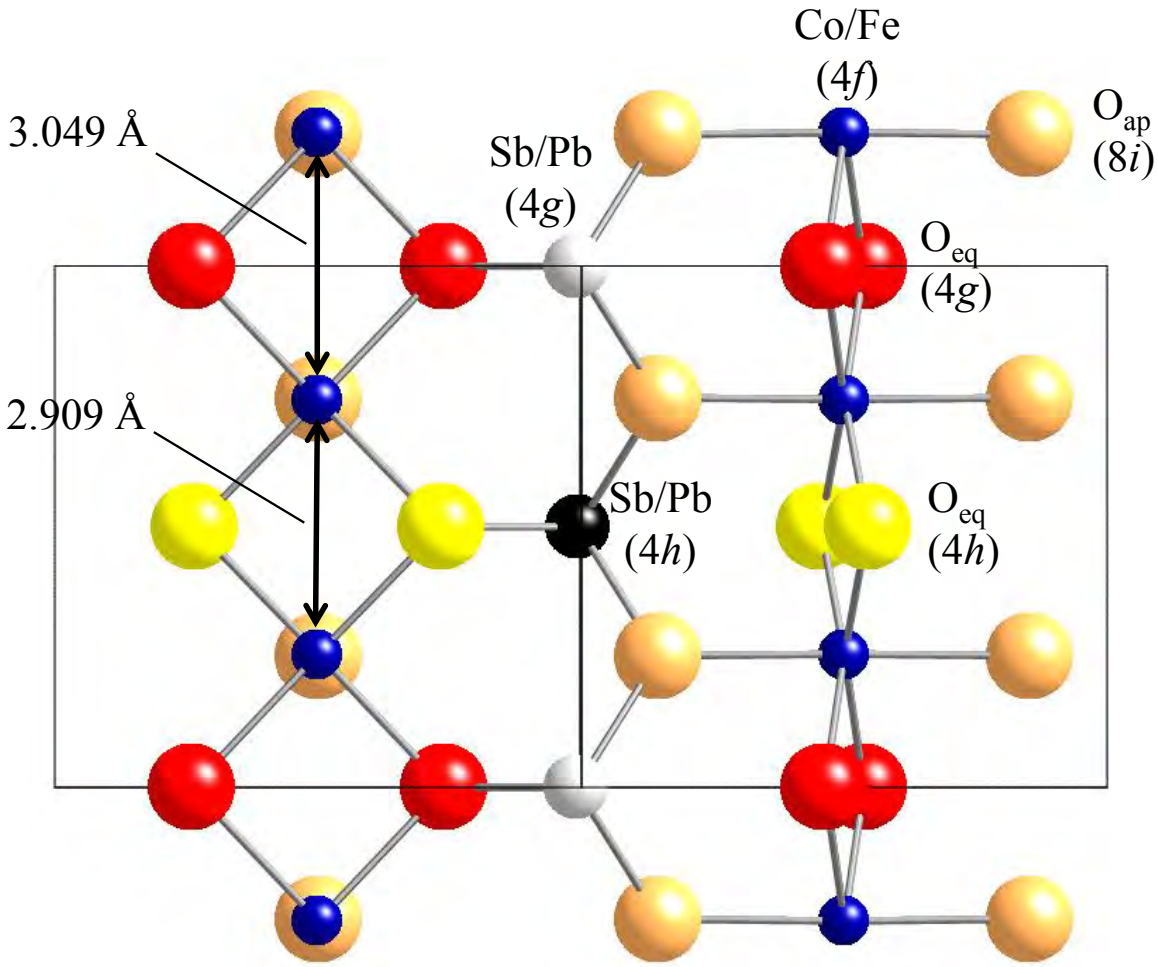

Figure 5.9 A diagram of the orthorhombic $Co_{0.25}Fe_{0.75}Sb_{1.75}Pb_{0.25}O_4$ structure at 1.5 K. The spheres represent the: Sb/Pb **4*g*** (grey), Sb/Pb **4*h*** (black), Co/Fe **4*f*** (blue), O_{eq} **4*g*** (red), O_{eq} **4*h*** (yellow), and O_{ap} **8*i*** (beige) sites.

Table 5.7 Selected bond distances and angles obtained from the refinement of NPD data for the $Co_{0.25}Fe_{0.75}Sb_{2-x}Pb_xO_4$ (x = 0.25, 0.50, 0.75) phases.

	$Co_{0.25}Fe_{0.75}Sb_{1.75}Pb_{0.25}O_4$			$Co_{0.25}Fe_{0.75}Sb_{1.50}Pb_{0.50}O_4$		$Co_{0.25}Fe_{0.75}Sb_{1.25}Pb_{0.75}O_4$	
	300 K	1.5 K		300 K	1.5 K	300 K	1.5 K
Co-O_{4g} (Å)	2.044(5)[3]	2.111(4)[3]	Co-O_{eq} (Å) x4	2.0585(9)	2.0599(9)	2.0496(8)	2.0502(9)
Co-O_{4h} (Å)	2.104(5)[3]	2.042(5)[3]	Co-O_{ap} (Å) x2	2.086(1)	2.077(1)	2.057(1)	2.0450(1)
Co-O_{ap} (Å)	2.129(1)	2.115(1)	Sb-O_{eq} (Å)	2.026(2)	2.023(2)	2.075(2)	2.072(2)
Sb_{4h}-O_{ap} x2 (Å)	2.013(6)	2.029(5)	Sb-O_{ap} (Å) x2	2.061(1)	2.063(1)	2.092(1)	2.095(1)
Sb_{4h}-O_{4h} (Å)	1.965(7)	2.032(7)	O_{ap}-Sb-O_{eq} (°) x2	91.71(5)	91.67(5)	91.06(5)	90.99(5)
Sb_{4g}-O_{ap} x2 (Å)	2.047(5)	2.027(6)	O_{ap}-Sb-O_{ap} (°)	93.59(7)	93.28(6)	92.57(6)	92.21(6)
Sb_{4g}-O_{4g} (Å)	2.002(8)	1.937(5)	O_{eq}-Co-O_{eq} (°)	86.27(5)	86.56(5)	84.92(5)	85.17(5)
O_{ap}-Sb_{4g}-O_{ap} (°)	91.0(3)	95.9(4)	O_{eq}-Co-O_{eq} (°)	167.04(7)	166.64(7)	167.92(7)	167.50(7)
O_{4g}-Sb_{4g}-O_{ap} (°)	89.9(2)	93.4(2)	O_{eq}-Co-O_{eq} (°)	95.19(6)	95.00(6)	96.35(5)	96.19(5)
O_{ap}-Sb_{4h}-O_{ap} (°)	98.5(3)	93.2(4)	Co-O_{eq}-Co (°)	93.73(5)	93.44(5)	95.08(5)	94.83(5)
O_{ap}-Sb_{4h}-O_{4h} (°)	94.8(2)	91.1(2)					
Co-O_{4g}-Co (°)	89.2(3)	92.5(3)					
Co-O_{4h}-Co (°)	94.8(3)	90.9(3)					

[3]The swap over of bond lengths for this composition confirms that we are close to the orthorhombic/tetragonal transition point.

Table 5.8 Selected bond distances and angles obtained from the refinement of NPD data for the $Co_{0.5}Fe_{0.5}Sb_{2-x}Pb_xO_4$ and $Co_{0.75}Fe_{0.25}Sb_{1.75}Pb_{0.25}O_4$ phases.

	$Co_{0.50}Fe_{0.50}Sb_{1.75}Pb_{0.25}O_4$		$Co_{0.50}Fe_{0.50}Sb_{1.60}Pb_{0.40}O_4$		$Co_{0.50}Fe_{0.50}Sb_{1.50}Pb_{0.50}O_4$		$Co_{0.75}Fe_{0.25}Sb_{1.75}Pb_{0.25}O_4$	
	300 K	1.5 K	300 K	1.5 K	300 K	1.5 K	300 K	1.5 K
Co-O_{eq} (Å) x4	2.0707(9)	2.0735(9)	2.0602(9)	2.0637(9)	2.0597(9)	2.061(1)	2.0666(9)	2.070(1)
Co-O_{ap} (Å) x2	2.121(1)	2.112(1)	2.098(1)	2.089(1)	2.089(1)	2.080(1)	2.119(1)	2.110(1)
Sb-O_{eq} (Å)	1.980(2)	1.976(2)	2.010(2)	2.007(2)	2.033(2)	2.027(2)	1.985(2)	1.977(2)
Sb-O_{ap} (Å) x2	2.026(1)	2.027(1)	2.047(1)	2.048(1)	2.057(1)	2.060(1)	2.023(1)	2.0239(1)
O_{ap}-Sb-O_{eq} (˚) x2	92.34(6)	92.34(6)	91.91(5)	91.86(5)	91.46(6)	91.53(6)	92.24(6)	92.32(6)
O_{ap}-Sb-O_{ap} (˚)	94.83(7)	94.63(7)	94.16(6)	93.97(6)	94.04(6)	93.72(6)	95.00(7)	94.83(7)
O_{eq}-Co-O_{eq} (˚)	87.84(5)	88.13(5)	86.63(5)	86.98(5)	86.13(5)	86.35(6)	87.61(5)	87.89(6)
O_{eq}-Co-O_{eq} (˚)	166.72(7)	166.38(7)	166.98(7)	166.52(7)	167.29(7)	166.89(7)	166.57(7)	166.43(7)
O_{eq}-Co-O_{eq} (˚)	93.70(5)	93.48(5)	94.85(5)	94.61(6)	95.28(5)	95.15(6)	93.96(5)	93.71(6)
Co-O_{eq}-Co (˚)	92.16(5)	91.87(5)	93.37(5)	93.02(5)	93.87(5)	93.65(6)	92.39(5)	92.11(6)

5.5 Thermogravimetric analysis

The oxidation properties of the mixed $Co_{1-x}Fe_xSb_{2-y}Pb_yO_4$ phases showed similarities to the $Co_{1-x}Fe_xSb_2O_4$ phases (Figures 5.10-5.12). The most obvious difference is clearly shown by $Co_{0.25}Fe_{0.75}Sb_{1.75}Pb_{0.25}O_4$ (Figure 5.13), with 2 intermediate plateaus prior to the formation of the high temperature products implying the formation of two discrete intermediate phases. This is considerably different to previous reports which only detail a single plateau in $FeSb_2O_4$ [4-5] and the $Co_{1-x}Fe_xSb_2O_4$ phases, see *Section 4.6*. The DTA signal accompanying the phase changes are however very shallow representing the possibility of a more transient/ reversibly oxidative intermediate when compared with the $Co_{1-x}Fe_xSb_2O_4$ phases. It is clear that as the stoichiometric amount of lead approaches the maximum level of Fe definition is lost between the steps associated with intermediate formation and the progressive oxidation approaching the high temperature product is more transient, i.e. the intermediates are no longer formed. This is consistent with the $Co_{1-x}Fe_xSb_2O_4$ phases which demonstrated the ability to absorb varying levels of oxygen dependent on the amount of Fe^{2+} to oxidise to Fe^{3+}.

Focusing on $Co_{0.25}Fe_{0.75}Sb_{1.75}Pb_{0.25}O_4$ (Figure 5.13) as it demonstrates most clearly the stepwise transition upon heating, it is shown that increases in the TGA and decrease in the DTA signals associated with the plateaux regions are coincident. The TGA signal can be broken into 3 segments relating to the formation of the 1st (250-488˚C) and 2nd (488-633˚C) intermediates before total sample decomposition T > 633˚C. The decomposition products were identified as predominantly being related to $Pb_2Fe_{0.50}Sb_{1.50}O_{6.50}$, $PbSb_2O_6$ and $CoSb_2O_6$ for all phases. The associated compositions at 430˚C and 580˚C, the approximate midpoint of each plateau, are calculated as $Co_{0.25}Fe_{0.75}Sb_{1.75}Pb_{0.25}O_{4.35}$ and $Co_{0.25}Fe_{0.75}Sb_{1.75}Pb_{0.25}O_{4.79}$. At 430˚C the amount of excess oxygen is less than that of $Co_{0.25}Fe_{0.75}Sb_2O_{4.40}$ at 325˚C but, on

the basis of the O_2^{2-} model, implies a greater final oxidation state for Fe. This oxygen increase represents 0.6 or 60% of the Fe being oxidised; this is inclusive of the oxidation caused by Pb^{2+}. However, at 580˚C the calculated composition $Co_{0.25}Fe_{0.75}Sb_{1.75}Pb_{0.25}O_{4.79}$ shows the greatest amount of excess oxygen recorded and crucially suggests two findings which have never been seen before. The first is that that the inserted oxygen species could have changed to O_2^- which would tie in with previous findings that the TM site cannot be fully oxidised or that it is possible to fully oxidise the TM site based upon the insertion of O_2^{2-} and O_2^-. In either case the mixture of Co/Fe and Pb is likely to be a key factor in stabilising the final compositions and this represents a significantly higher excess oxygen stoichiometry than is seen in any previously reported phases.

The lowering of the temperature at which oxygen is initially absorbed (T_{abs}) by the sample is again associated with the iron content of the phase where T_{abs} for the $Co_{0.75}Fe_{0.25}Sb_{2-x}Pb_xO_4$ phases is around 325˚C which lowers to around 250˚C for the $Co_{0.25}Fe_{0.75}Sb_{2-x}Pb_xO_4$ phases. The stoichiometric amount of lead appears to have little effect on T_{abs} but it does seem to increase the temperature at which the sample decomposes and therefore it seems likely it introduces a degree of stability to the material, hence enabling greater oxygen uptake. All samples which were heated to an intermediate phase region and cooled were visibly darker than before heating.

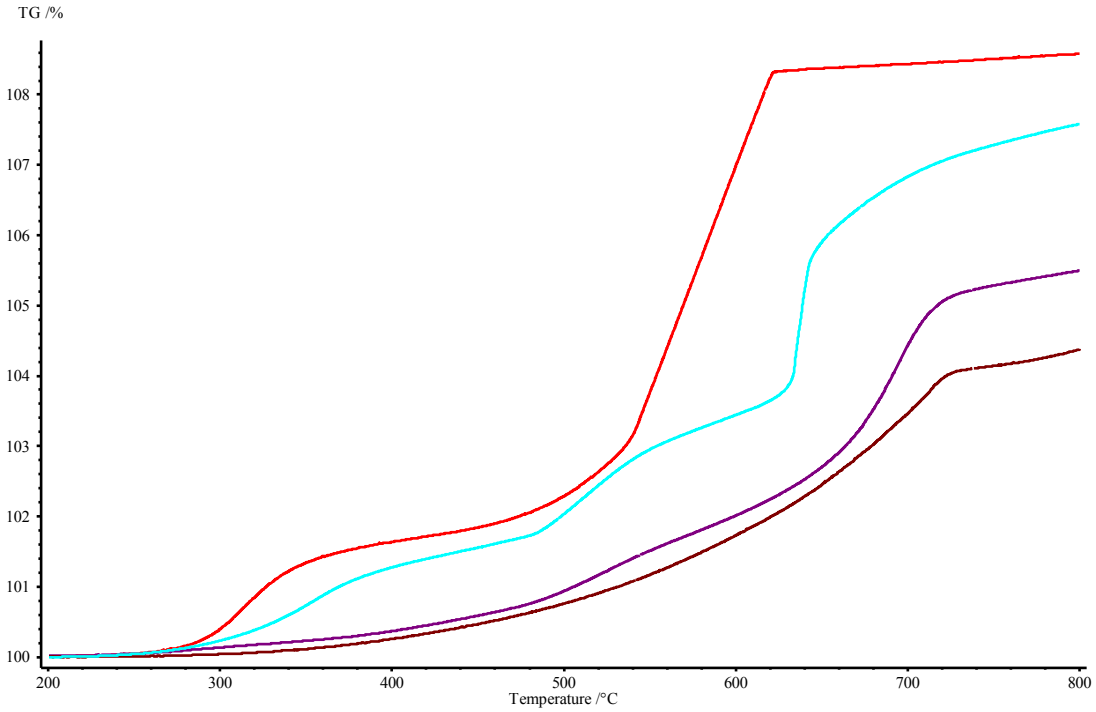

Figure 5.10 A TGA plot showing the mass increases exhibited by $Co_{0.25}Fe_{0.75}Sb_2O_4$ (Red), $Co_{0.25}Fe_{0.75}Sb_{1.75}Pb_{0.25}O_4$ (light blue), $Co_{0.25}Fe_{0.75}Sb_{1.50}Pb_{0.50}O_4$ (purple), and $Co_{0.25}Fe_{0.75}Sb_{1.25}Pb_{0.75}O_4$ (brown) when heated in an atmosphere of oxygen at a rate of 10˚C/ min. The samples were heated between 30˚C to 1000˚C.

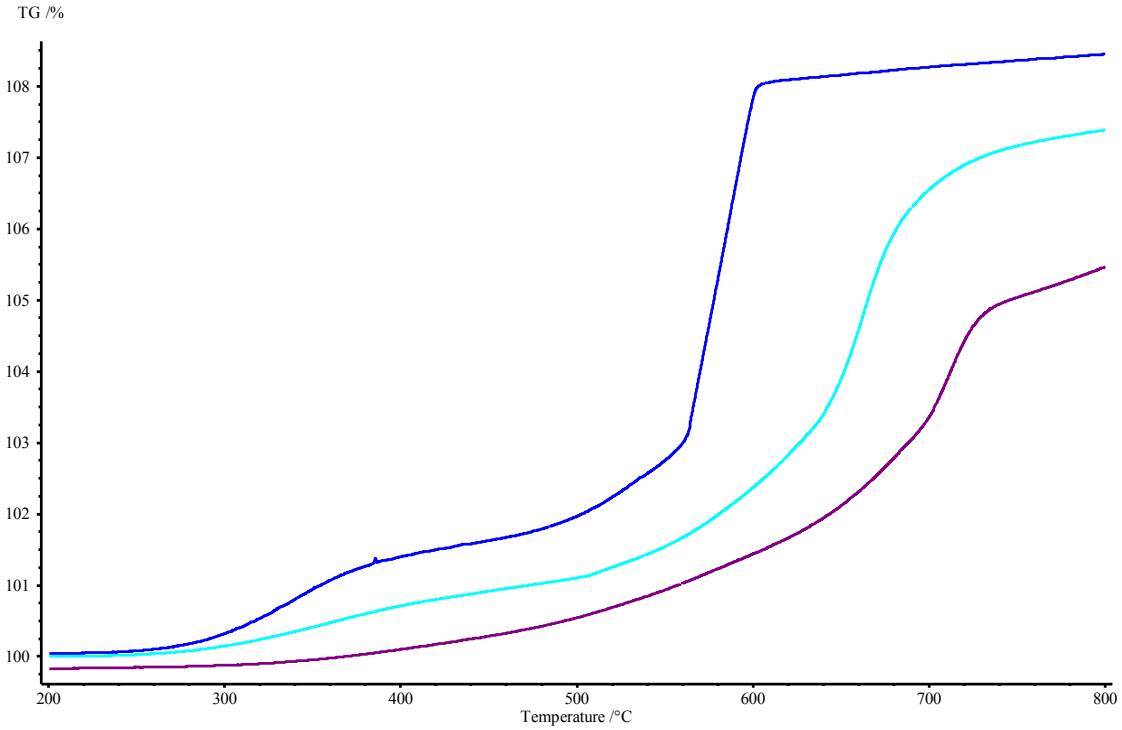

Figure 5.11 A TGA plot showing the mass increases exhibited by $Co_{0.50}Fe_{0.50}Sb_2O_4$ (blue), $Co_{0.50}Fe_{0.50}Sb_{1.75}Pb_{0.25}O_4$ (light blue) and $Co_{0.50}Fe_{0.50}Sb_{1.50}Pb_{0.50}O_4$ (purple) when heated in an atmosphere of oxygen at a rate of 10˚C/ min. The samples were heated between 30˚C to 1000˚C.

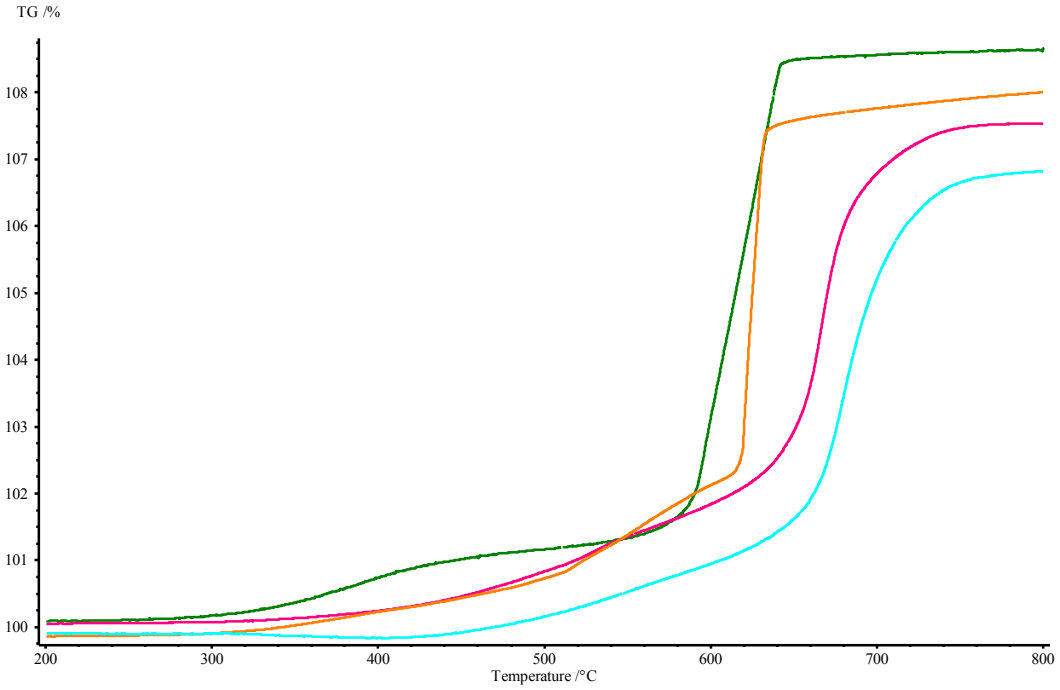

Figure 5.12 A TGA plot showing the mass increases exhibited by $Co_{0.75}Fe_{0.25}Sb_2O_4$ (green), $Co_{0.75}Fe_{0.25}Sb_{1.90}Pb_{0.10}O_4$ (orange), $Co_{0.75}Fe_{0.25}Sb_{1.80}Pb_{0.20}O_4$ (pink), and $Co_{0.75}Fe_{0.25}Sb_{1.75}Pb_{0.25}O_4$ (light blue) when heated in an atmosphere of oxygen at a rate of 10˚C/ min. The samples were heated between 30˚C to 1000˚C.

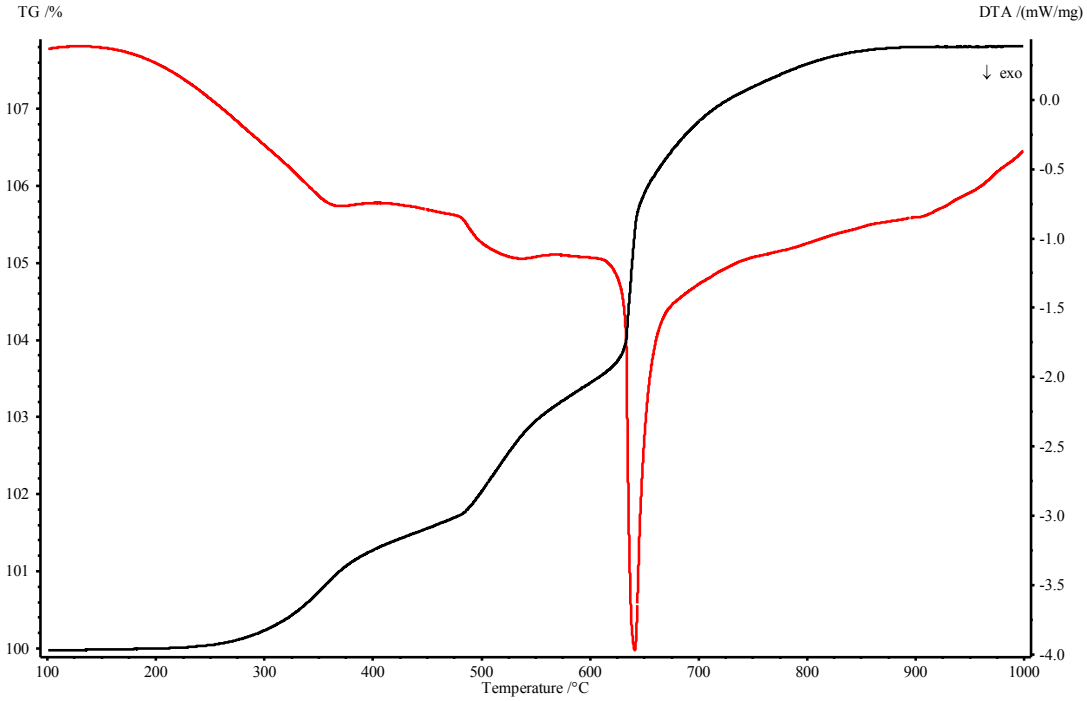

Figure 5.13 A TGA (black) and DTA plot (red) of $Co_{0.25}Fe_{0.75}Sb_{1.75}Pb_{0.25}O_4$ heated in an atmosphere of O_2 (N_2 is the protective gas) at a rate of 10˚C/min between 30-1000˚C.

5.6 XRPD of $Co_{0.25}Fe_{0.75}Sb_{1.75}Pb_{0.25}O_4$ and the $Co_{0.25}Fe_{0.75}Sb_{1.75}Pb_{0.25}O_{4+x}$ phases

Samples were heated on the TGA up to the midpoint of each plateaux region (430˚C and 590˚C) and cooled at a rate of 10˚C under continuously flowing oxygen in order to identify any possible stable intermediates. In both instances distinct phases were found (Figure 5.14). Comparing indexing results of the powder patterns showed the lattice parameters of $Co_{0.25}Fe_{0.75}Sb_{1.75}Pb_{0.25}O_4$ at 30˚C and 430˚C to be consistent with a tetragonal cell (a = 8.509(1) Å, c = 5.969(1) Å at 300 K; a = 8.360(1) Å, c = 6.019(1) Å at 430 K). The difference in symmetry of $Co_{0.25}Fe_{0.75}Sb_{1.75}Pb_{0.25}O_4$ at 30 ˚C with respect to Rietveld refinement values is of little surprise given the greater sophistication of GSAS. At 590˚C an orthorhombic cell (a = 8.399(5) Å, b = 8.350(9) Å, c = 6.061(4) Å at 590 K) with very low figure of merit was obtained. The loss of several peak intensities i.e. (the 110) and broadening of many others indicates a large range of crystallites with small differences of lattice parameters resulting from oxygen insertion. The volume of the oxidised products changes as follows: 432Å^3 (30˚C), 421Å^3 (430˚C), 425Å^3 (590˚C). The cause for the decrease in volume can be envisaged as the bridging oxygen channel species pulling adjacent Sb^{3+} sites closer together, whilst a threshold is reached in the more oxygenated samples which causes the system to distort. It is possible that a similar situation is occurring to the versiliaite and apuanite samples [19-22].

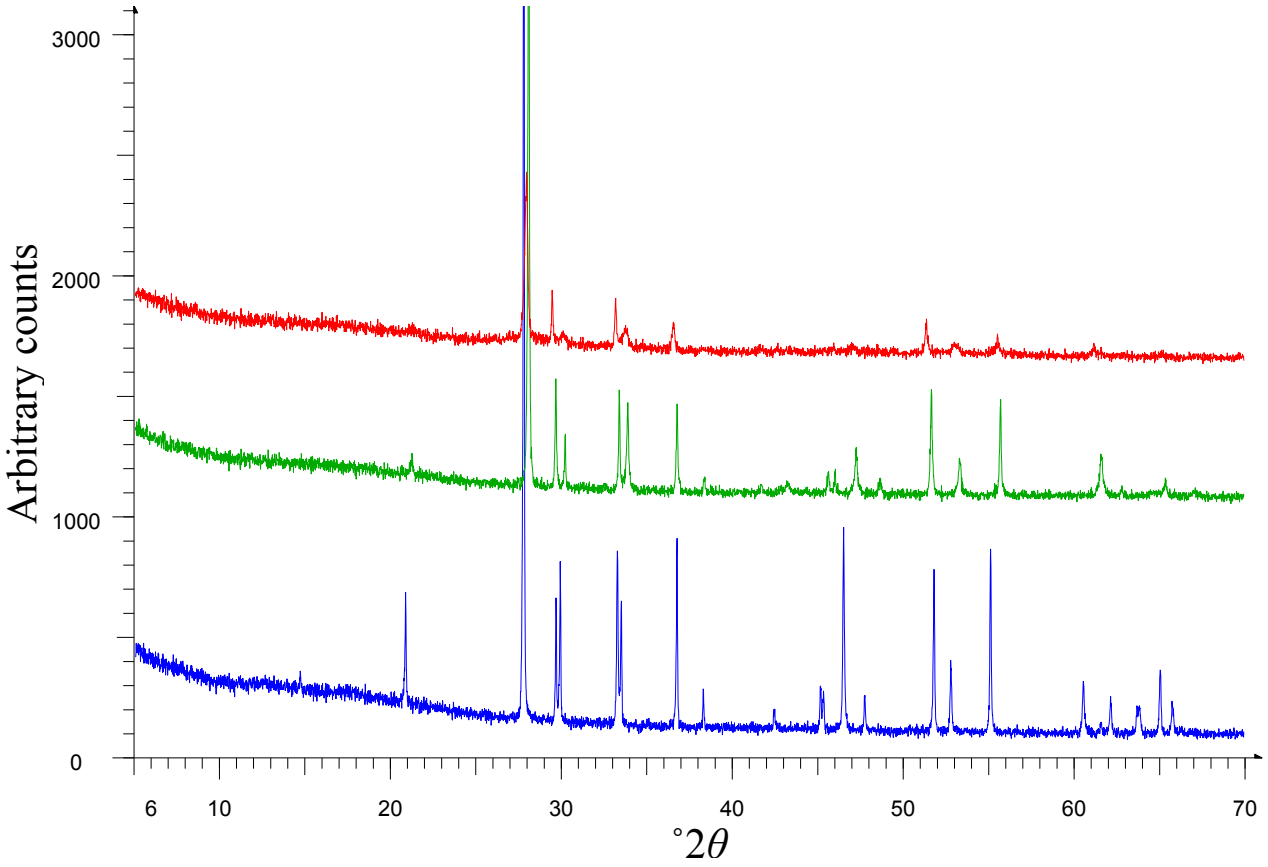

Figure 5.14 A plot showing the powder patterns of stoichiometric $Co_{0.25}Fe_{0.75}Sb_{1.75}Pb_{0.25}O_4$ at 30˚C (blue), $Co_{0.25}Fe_{0.75}Sb_{1.75}Pb_{0.25}O_4$ heated on a TGA up to 430˚C (green), and $Co_{0.25}Fe_{0.75}Sb_{1.75}Pb_{0.25}O_4$ heated on a TGA up to 590˚C (red) all in O_2.

5.7 Raman spectroscopy of the $Co_{0.25}Fe_{0.75}Sb_{1.75}Pb_{0.25}O_{4+x}$ phases

The unprecedented magnitude of oxygen uptake by $Co_{0.25}Fe_{0.75}Sb_{1.75}Pb_{0.25}O_4$ (at 430˚C and 590˚C) was further investigated by Raman spectroscopy with the aim of identifying the excess oxygen species. The exploratory study showed that there is a similarity between the spectra for all samples (Figure 5.15) which supports the XRPD data indicating retention of the crystal structure upon oxygen uptake. Furthermore all peaks are broadened and reduced in intensity; this could be associated with minor variations in crystalline environment caused by the insertion of oxygen. The main peak at around 675 cm^{-1} for $Co_{0.25}Fe_{0.75}Sb_{1.75}Pb_{0.25}O_4$ shows a similar degree of broadening upon oxidation when compared with the $Co_{1-x}Fe_xSb_2O_4$ (*Section* 4.8) phases. This initially suggested that oxygen had been inserted into the channels and was probably of the peroxide (O_2^{2-}) form. However,

extended scans over the range 0-3200 cm^{-1} showed a broad low intensity peak approximately between 1100-1500 cm^{-1}. This was not seen in $Co_{0.25}Fe_{0.75}Sb_{1.75}Pb_{0.25}O_4$ or the $Co_{1-x}Fe_xSb_2O_{4+x}$ phases. It is expected that the primary O-O frequency in a superoxide and peroxide species will vary with composition; however, there is broad agreement that the primary O-O stretching frequencies occur at around 1050-1150 cm^{-1} (O_2^-) [23-25] and 790-950 cm^{-1} (O_2^{2-}) [25-26]. Whilst it is not absolutely clear that the observed features represent the incorporation of peroxide and superoxide species their approximate overlap with literature values gives some support to the assertions made from the TGA data, i.e. their inclusion would result in a lower level of oxidation of the TM site with the observed large increase of oxygen. These findings would be consistent with the level of Fe^{2+} available to oxidise to Fe^{3+}, i.e. not all of the TM site has been oxidised. Clearly these preliminary studies require further investigation and characterisation to resolve the identity and locality of the excess oxygen; this would make an interesting and highly valuable EXAFS study.

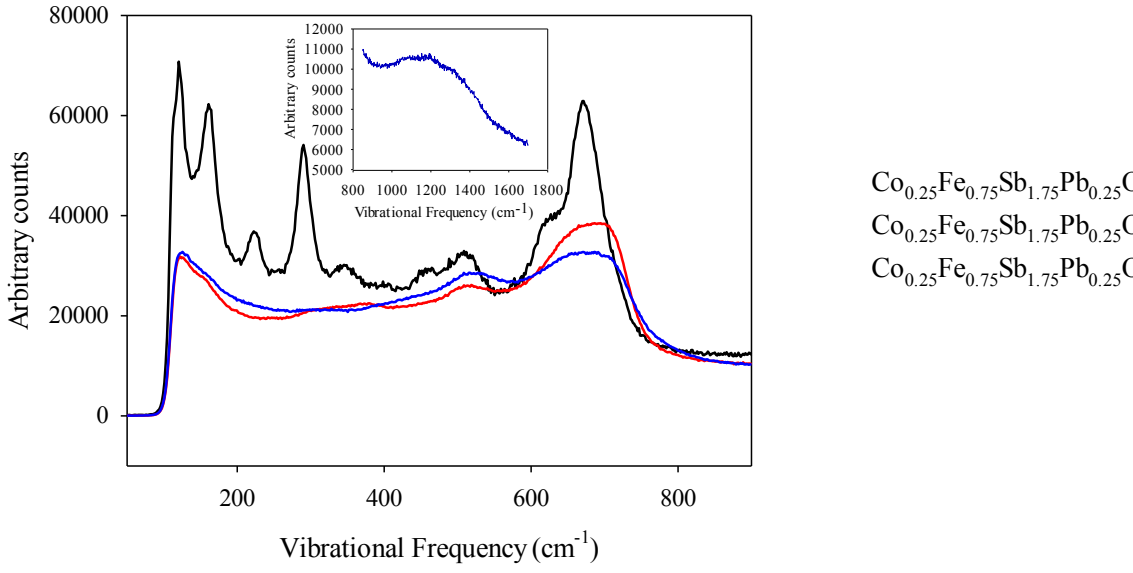

Figure 5.15 Raman spectra of $Co_{0.25}Fe_{0.75}Sb_{1.75}Pb_{0.25}O_4$ (black), $Co_{0.25}Fe_{0.75}Sb_{1.75}Pb_{0.25}O_{4.35}$ (red), and $Co_{0.25}Fe_{0.75}Sb_{1.75}Pb_{0.25}O_{4.79}$ (blue) collected at room temperature from samples oxidised on the TGA under flowing oxygen. Inset shows the broad peak at around 1100-1500 cm^{-1} for a $Co_{0.25}Fe_{0.75}Sb_{1.75}Pb_{0.25}O_{4.79}$ sample which could indicate a superoxide species.

5.8 SEM analysis

Of the few SEM images taken from these samples, Figure 5.16 shows the formation of a range of crystallite shapes which do not appear totally consistent with needles and in some cases e.g. $Co_{0.25}Fe_{0.75}Sb_{1.25}Pb_{0.75}O_4$ appears more consistent with platelets. Consequently the origins of the preferred orientation, along [001] in the XRPD data, are not entirely clear.

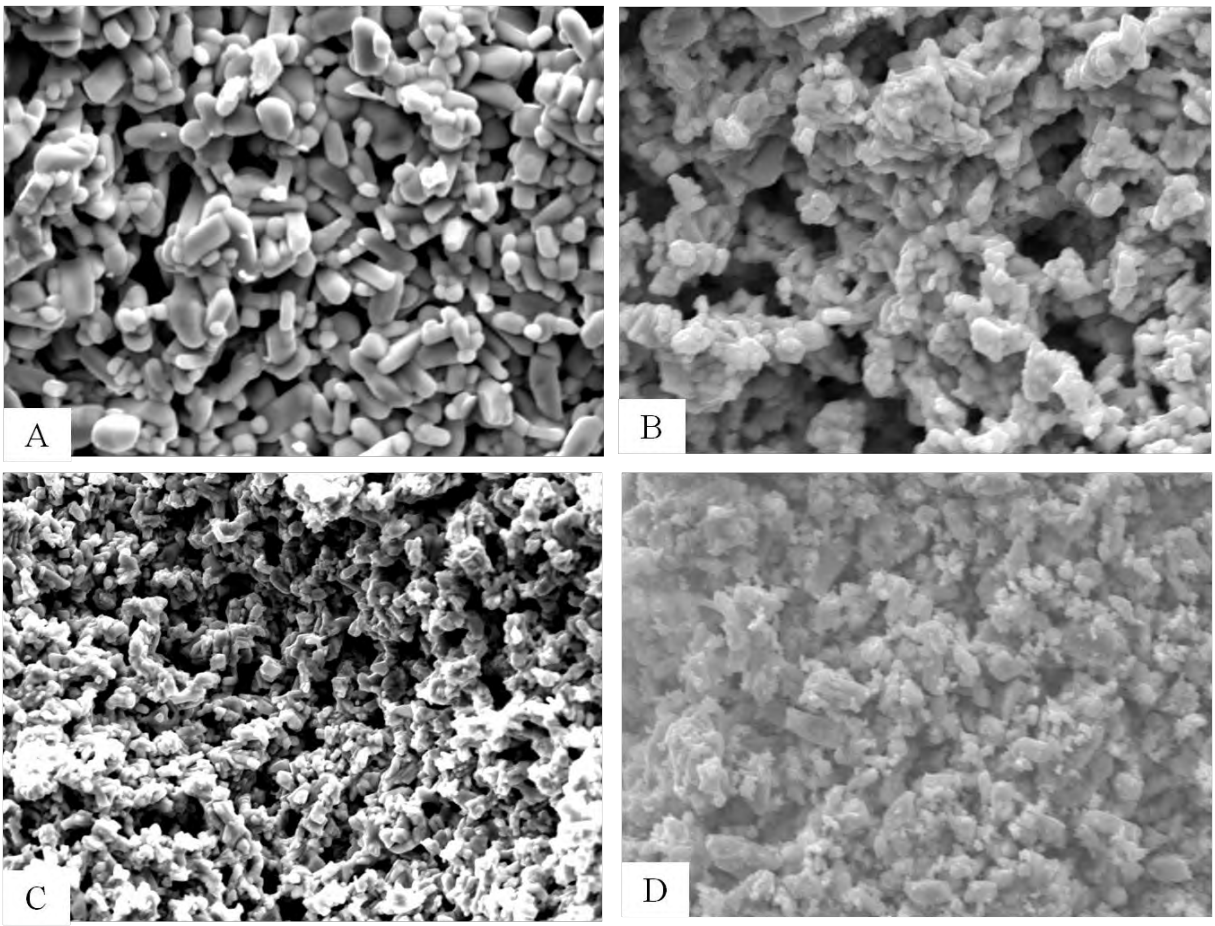

Figure 5.16 SEI images taken on a Joel 6060 SEM microscope. The samples are: $Co_{0.25}Fe_{0.75}Sb_{1.75}Pb_{0.25}O_4$ (A), $Co_{0.25}Fe_{0.75}Sb_{1.25}Pb_{0.75}O_4$ (B), $Co_{0.50}Fe_{0.50}Sb_{1.50}Pb_{0.50}O_4$ (C) and $Co_{0.75}Fe_{0.25}Sb_{1.75}Pb_{0.25}O_4$ (D) showing a mixture of long needle like crystals and round globular like crystals.

5.9 Magnetic susceptibility measurements

All samples show a magnetic structure consistent with a canted antiferromagnet. As in previous magnetic determinations attempts were made to refine the ferromagnetic component from the NPD data; however the magnitude was too small to be refined. Most

samples were found to contain small amounts of magnetite precluding any further analysis of the high temperature paramagnetic moment or Curie-Weiss constant. The Néel temperatures are however shown in (Table 5.9) and a general trend can be seen where T_N increases with Pb content similar to that of the lead doped schafarzikite systems [1]. This shows that as the stoichiometric amount of lead is increased the strength of magnetic interaction is also increased demonstrating oxidation of the TM species.

Table 5.9 The Néel temperatures obtained from the $Co_{1-x}Fe_xSb_{2-y}Pb_yO_4$ samples under ZFC/FC conditions in an applied field of 100 Oe. The Error in T_N is estimated to be ±3 K.

Compound	T_N (K)	Magnetite	Magnetic moment (μ_B mol^{-1})
$Co_{0.25}Fe_{0.75}Sb_{1.90}Pb_{0.10}O_4$	40	Y	-
$Co_{0.25}Fe_{0.75}Sb_{1.80}Pb_{0.20}O_4$	50	Y	-
$Co_{0.25}Fe_{0.75}Sb_{1.75}Pb_{0.25}O_4$	54	Y	-
$Co_{0.25}Fe_{0.75}Sb_{1.70}Pb_{0.30}O_4$	58	Y	-
$Co_{0.25}Fe_{0.75}Sb_{1.60}Pb_{0.40}O_4$	64	Y	-
$Co_{0.25}Fe_{0.75}Sb_{1.50}Pb_{0.50}O_4$	68	Y	-
$Co_{0.25}Fe_{0.75}Sb_{1.40}Pb_{0.60}O_4$	63	Y	-
$Co_{0.25}Fe_{0.75}Sb_{1.25}Pb_{0.75}O_4$	55	Y	-
$Co_{0.50}Fe_{0.50}Sb_{1.90}Pb_{0.10}O_4$	49	Y	-
$Co_{0.50}Fe_{0.50}Sb_{1.80}Pb_{0.20}O_4$	58	Y	-
$Co_{0.50}Fe_{0.50}Sb_{1.75}Pb_{0.25}O_4$	58	Y	-
$Co_{0.50}Fe_{0.50}Sb_{1.70}Pb_{0.30}O_4$	64	Y	-
$Co_{0.50}Fe_{0.50}Sb_{1.60}Pb_{0.40}O_4$	68	Y	-
$Co_{0.50}Fe_{0.50}Sb_{1.50}Pb_{0.50}O_4$	ZFC = 58	N	-
$Co_{0.75}Fe_{0.25}Sb_{1.90}Pb_{0.10}O_4$	67	Trace	-
$Co_{0.75}Fe_{0.25}Sb_{1.80}Pb_{0.20}O_4$	73	Trace	-
$Co_{0.75}Fe_{0.25}Sb_{1.75}Pb_{0.25}O_4$	73	N	6.21(2) θ = -61(2) K

Selected susceptibility plots for the $Co_{0.25}Fe_{0.75}Sb_{2-x}Pb_xO_4$ phases are shown in Figure 5.17, the remainder can be found in Appendix 3.4. Compositions where Pb = 0.10-0.25 all show a small ferromagnetic upturn in the magnetisation below T_N before decreasing at lower temperatures representing AFM long range order. This feature was absent in the remaining $Co_{0.25}Fe_{0.75}Sb_{2-x}Pb_xO_4$ phases. The ferromagnetic component of each phase was found to successively decrease with lead content up to $Pb_{0.60}$ where after a small increase in the

ferromagnetic component is seen for $Co_{0.25}Fe_{0.75}Sb_{1.25}Pb_{0.75}O_4$. $Co_{0.25}Fe_{0.75}Sb_{1.80}Pb_{0.20}O_4$ is the only phase to display a negative susceptibility and appears consistent with previously seen phases, e.g. $CoSb_2O_4$, although the origin of the negative susceptibility has not been determined in this case. All phases display the characteristic Verwey transition except for $Co_{0.25}Fe_{0.75}Sb_{1.25}Pb_{0.75}O_4$. It is clear from the 300 K NPD data that magnetite is present however a loss of the Verwey transition (T_v) can be explained by its sensitivity to slight compositional changes. Abellán *et al* [27] demonstrated that a Co concentration of 0.04 in $Co_xFe_{3-x}O_4$ is sufficient to destroy T_v and that the transition displayed hysteretic behaviour explaining the discrepancy of T_v between ZFC and FC sweeps. This therefore suggests that $Co_{0.25}Fe_{0.75}Sb_{1.25}Pb_{0.75}O_4$ has lost the greatest amount of Co from the main structure. Given the magnitude of the impurity and the amount required to destroy T_v this was not of concern to previous determinations but supports the findings of Abellán *et al* [27].

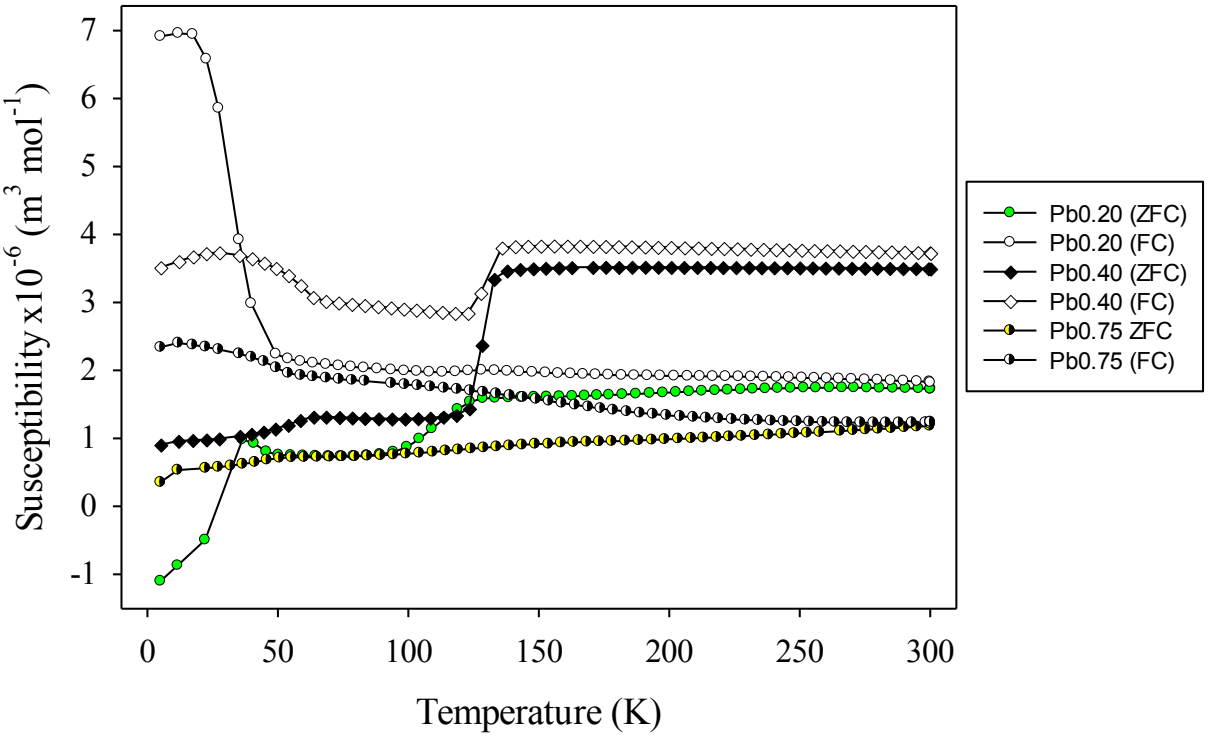

Figure 5.17 A comparison of selected magnetic susceptibilities for the $Co_{0.25}Fe_{0.75}Sb_{2-x}Pb_xO_4$ compounds taken under ZFC-FC conditions with an applied field of 100 Oe.

The $Co_{0.50}Fe_{0.50}Sb_{2-x}Pb_xO_4$ phases (selected susceptibility plots Figure 5.18) show a trend similar to the $Co_{0.25}Fe_{0.75}Sb_{2-x}Pb_2O_4$ phases where $Co_{0.50}Fe_{0.50}Sb_{1.90}Pb_{0.10}O_4$ possesses the largest ferromagnetic component. At lead concentrations higher than $Pb_{0.25}$ the ferromagnetic component decreases with increasing lead content. Furthermore $Co_{0.50}Fe_{0.50}Sb_{1.90}Pb_{0.10}O_4$ (Figure 5.19) shows a small ferromagnetic upturn in the ZFC data below T_N (49 K) before decreasing at 40 K and is similar to that seen in $CoSb_{1.50}Pb_{0.50}O_4$ (*Section 3.10*). This is unlike the remaining phases in the $Co_{0.50}Fe_{0.50}Sb_{2-x}Pb_xO_4$ series of compounds.

$Co_{0.50}Fe_{0.50}Sb_{1.50}Pb_{0.50}O_4$ resembles a magnetic structure unlike any other within this chapter. The absence of the Verwey transition and characteristic Fe_3O_4 magnetic peak in the NPD data is a clear mark of this samples purity. Two main magnetic ordering events are apparent; these occur at 58 K (T_N) showing long range order of the main phase ending in a canted antiferromagnetic arrangement and at 148 K where a broad ferromagnetic upturn initiates. The pre T_N event is similar to that seen in many of the $Co_{1-x}Fe_xSb_2O_4$ and $Co_{1-x}Fe_xSb_2O_{4+x}$ phases notably $Co_{0.75}Fe_{0.25}Sb_2O_4$ (*see Section 4.5 and 4.7*). Divergence between the ZFC and FC measurements initiates close to 300 K and indicates the presence of a small ferromagnetic component. It is not known if the pre T_N structure is borne from an impurity but its presence in several samples could be an indication of interesting magnetic structures forming at higher temperatures and requires further study. The high temperature paramagnetic susceptibility of $Co_{0.50}Fe_{0.50}Sb_{1.50}Pb_{0.50}O_4$ was not linear preventing a determination of the magnetic moment.

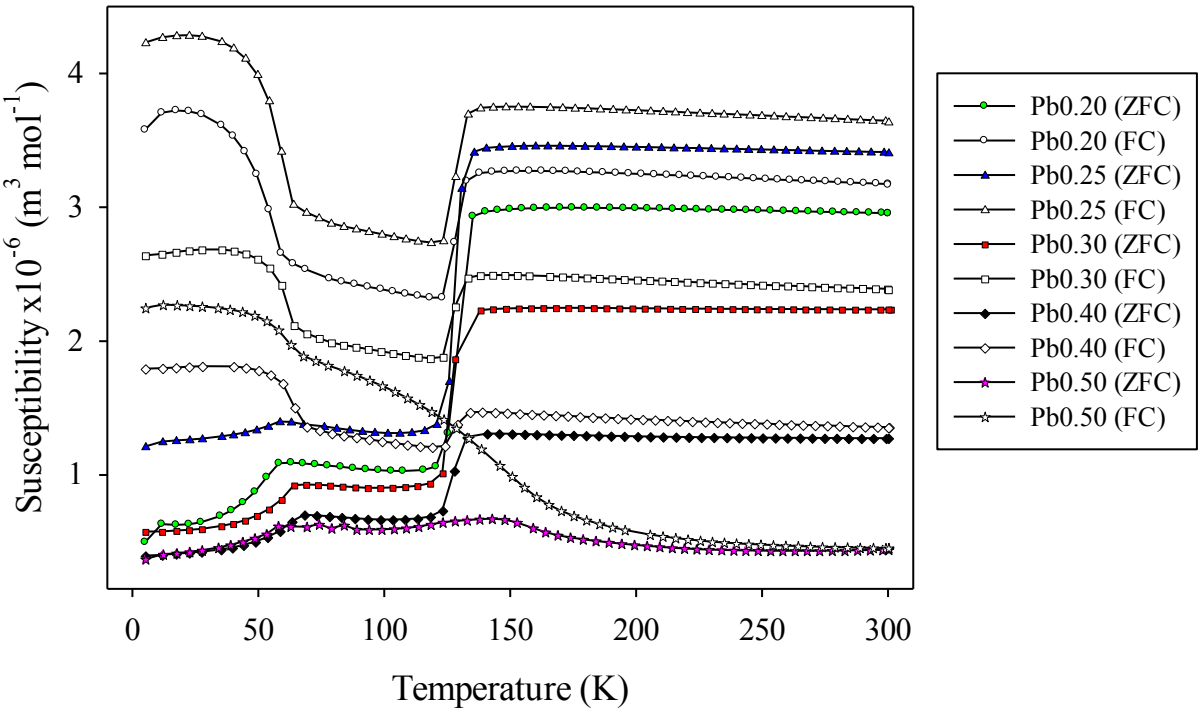

Figure 5.18 A comparison of selected magnetic susceptibilities for the $Co_{0.50}Fe_{0.50}Sb_{2-y}Pb_yO_4$ phases taken under ZFC-FC conditions with an applied field of 100 Oe.

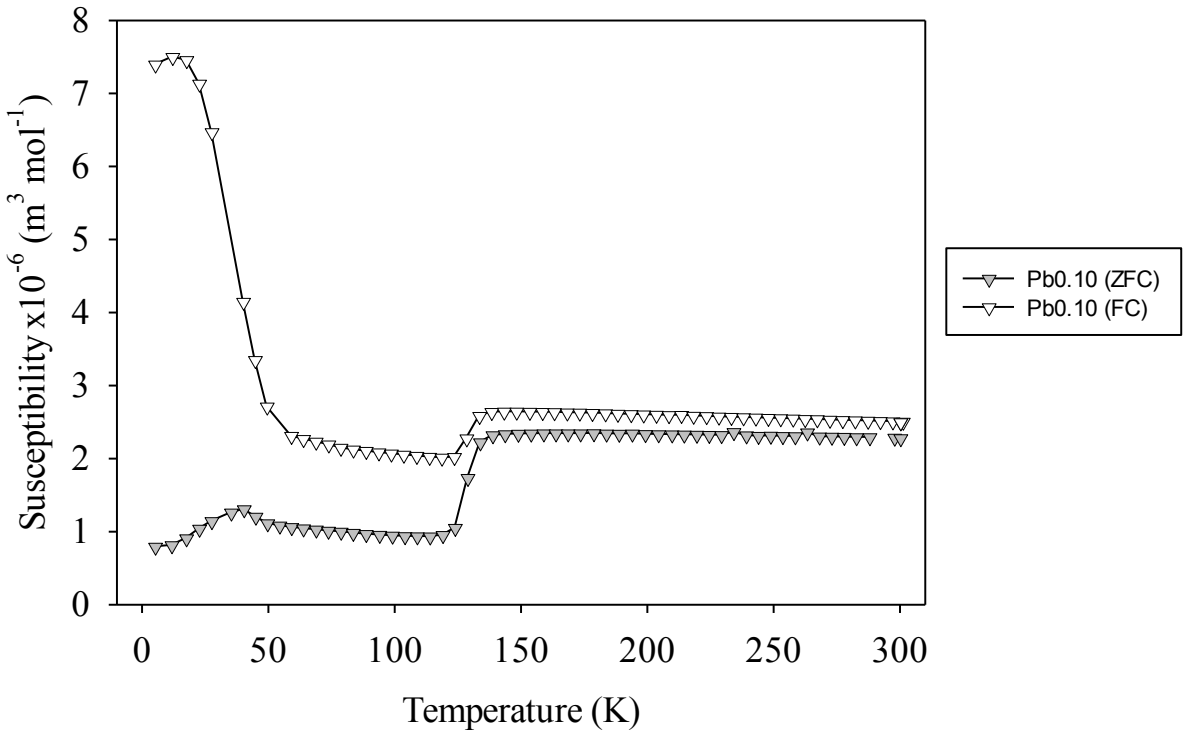

Figure 5.19 The magnetic susceptibility plot of $Co_{0.50}Fe_{0.50}Sb_{1.90}Pb_{0.10}O_4$ acquired under ZFC-FC conditions with an applied field of 100 Oe.

As previously seen, the lower the iron content of a phase the less likely magnetite is to be an impurity. All synthesised $Co_{0.75}Fe_{0.25}Sb_{2-x}Pb_xO_4$ phases possessed the lowest levels of magnetite, yet the magnetic moment could only be determined for $Co_{0.75}Fe_{0.25}Sb_{1.75}Pb_{0.25}O_4$ as it was the only sample to be free of magnetite (Figure 5.20). The moment obtained from the inverse susceptibility (Figure 5.20 inset) was high. The paramagnetic region could be fitted to 2 separate gradients: the whole range 77-300 K (μ = 6.21(2) μ_B mol^{-1}) and 216-300 K (μ = 6.69(5) μ_B mol^{-1}). The fit statistics (R^2 value) for the former were slightly better but in both cases demonstrated moments above the maximum spin only value. Assuming all Fe^{3+} and Co^{2+} high spin, the spin only moment would be in the region of 4.38 μ_B. This could represent ferromagnetic clusters e.g. pairs of ferromagnetically aligned TMs along the chains where the FM link is retained at high temperatures displaying this effect. The negative Weiss constant (θ = -61.2 K) would be an indication that the cluster are aligned in an AFM fashion. A similar result was seen in $Co_{0.50}Fe_{0.50}Sb_2O_4$ (8.45 μ_B, θ = -191 K) (*Section* 4.7) and has been seen in other compounds [28-29]. Compared to $Co_{0.75}Fe_{0.25}Sb_2O_4$, which also displayed a larger than spin only moment of 5.27 μ_B mol^{-1} between 151-293 K (expected moments: Co^{2+} = 4.5-5.2 μ_B; Fe^{2+} = 5.0 μ_B [13]) it is apparent that oxidation of the TM has occurred and that the large moment is most likely contributed to by a large component of orbital momentum common to Co containing compounds [13].

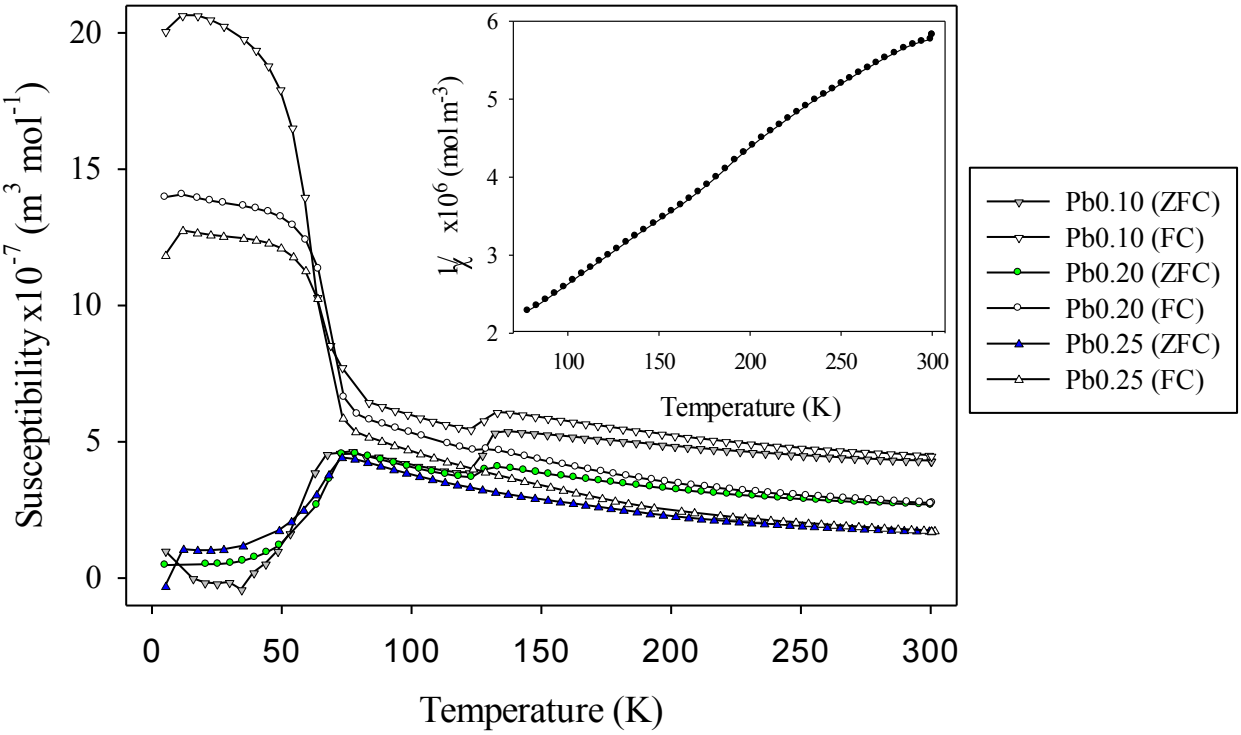

Figure 5.20 A comparison of the magnetic susceptibilities for the $Co_{0.75}Fe_{0.25}Sb_{2-y}Pb_yO_4$ phases taken under ZFC-FC conditions with an applied field of 100 Oe. The inset shows the inverse susceptibility plot for $Co_{0.75}Fe_{0.25}Sb_{1.75}Pb_{0.25}O_4$ within the temperature range 77-300 K.

5.10 Mössbauer study of $Co_{0.50}Fe_{0.50}Sb_{1.50}Pb_{0.50}O_4$

The Mössbauer data of $Co_{0.50}Fe_{0.50}Sb_{1.50}Pb_{0.50}O_4$ was collected and interpreted by Professor Frank Berry [30]. The 300 K spectrum is displayed in Figure 5.21. The data was fitted to two doublets with chemical isomer shifts of 0.36(2) mm s^{-1} and 1.05(2) mm s^{-1} which are characteristic of Fe^{3+} and Fe^{2+} respectively. The relative area of each peak shows 7% Fe^{2+} and 93% Fe^{3+} with an associated error of 3% in each. This is evidence to show that in this sample, where no deviation from stoichiometry is seen in the XRPD and NPD data, it appears possible to oxidise about 10% of Co^{2+} to Co^{3+}.

This could offer an explanation to the unusually low magnetic moment observed in the NPD data for $Co_{0.25}Fe_{0.75}Sb_{1.75}Pb_{0.25}O_4$ where the octahedral environment is shown to be significantly more distorted than all other $Co_{1-x}Fe_xSb_{2-y}Pb_yO_4$ phases. If some Co^{2+} is

oxidised to Co^{3+} which is more likely to adopt a low spin (d^6, $S = 0$) configuration e.g. as in Co_3O_4 [13] the moment would be reduced. It is accepted that the level of Co oxidation is probably low but in this situation a mixture of Co^{2+} (HS): Co^{3+} (LS): Fe^{2+} (HS): Fe^{3+} (HS) could begin to explain this anomaly. Disorder resulting in a reduced ordered moment is another possible explanation.

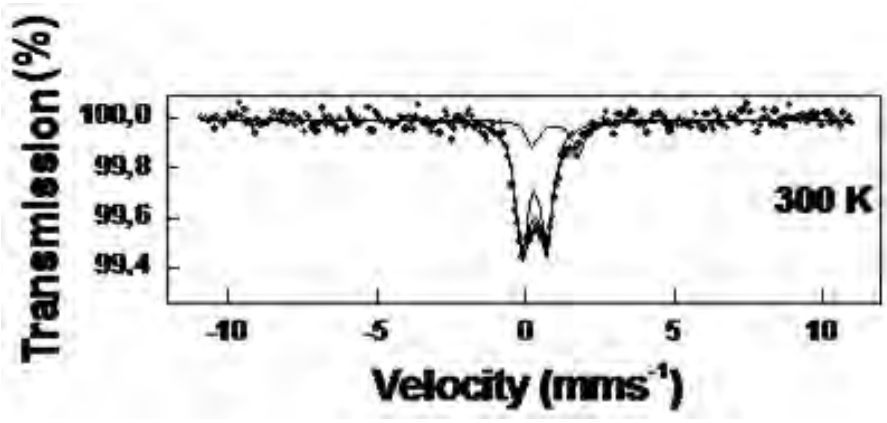

Figure 5.21 The ^{57}Fe Mössbauer spectrum recorded at 300 K from $Co_{0.50}Fe_{0.50}Sb_{1.50}Pb_{0.50}O_4$. Two doublets are shown with isomer shift values of: Fe^{2+} = 1.05(2) mm s^{-1} and Fe^{3+} = 0.36(2) mm s^{-1}.

5.11 Variable temperature XRPD of $Co_{0.25}Fe_{0.75}Sb_{1.75}Pb_{0.25}O_4$

A VT-XRPD study was conducted on $Co_{0.25}Fe_{0.75}Sb_{1.75}Pb_{0.25}O_4$ as it showed well defined intermediate phases upon heating. A clear transition from the staring compound to the decomposition products ($CoSb_2O_6$ and $Pb_2Fe_{0.5}Sb_{1.5}O_{6.5}$) at 600˚C (Figure 5.22) is seen. There is a large structural change between 246 and 272˚C indicating the formation of the 1st intermediate. This is at a significantly lower temperature than was seen in the TGA (*ca* 430˚C, midpoint of the intermediate formation) but coincides well with the temperature at which oxygen uptake is initiated. Isotherms were not run on the TGA for these phases. At 426˚C the peaks begin to broaden indicating formation of the second intermediate phase (consistent with Figure 5.14) and between 525-573˚C the structure begins to breakdown into the high temperature products, this is lower than the TGA data by around 60˚C. Isotherms

should be run on this sample to test the thermal stability at high temperatures for prolonged periods of time but the data seems to suggest that each intermediate phase is moderately stable within the defined temperature regions 272-375˚C and 426-525˚C. The rapid uptake of oxygen and relative implied stability of the first intermediate phase requires significant further investigation to ascertain the possible use as an oxygen conductor.

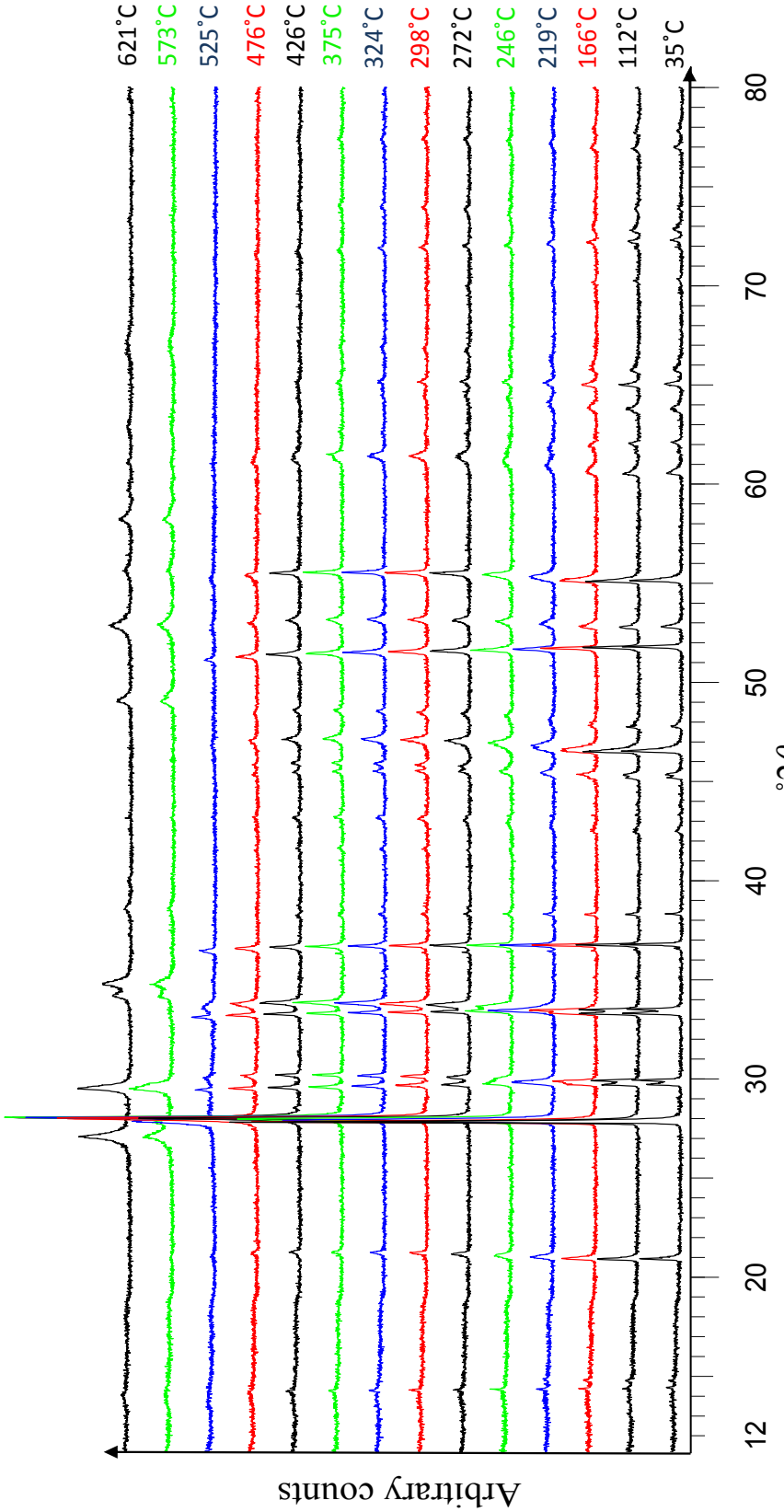

Figure 5.22 A variable temperature plot of $Co_{0.25}Fe_{0.75}Sb_{1.75}Pb_{0.25}O_4$ in the temperature range 35-621˚C. Hour long scans were acquired under standard atmospheric conditions. A structural change is seen in the region 219-272˚C. The temperatures displayed are the calibrated values with an associated error of ±5˚C.

5.12 Conclusions

This chapter has shown that it is possible to create mixed A and B site compounds whilst maintaining the schafarzikite structure. The previous assumption that Fe is the dominant species to be oxidised appears correct from Mössbauer data and the ability of only the iron containing samples to oxidise when heated in air. Sample purity is difficult to achieve when compared with iron free variants which has prevented the determination of magnetic moments from SQUID data. It is believed that this could be prevented by successive heats at much lower temperatures *ca* 500˚C but caution should be taken to prevent further impurities such as $Pb_2Fe_{0.50}Sb_{1.50}Pb_{6.50}$ forming. However, it is clear that the magnetic structures are all consistent with a dominant C mode which can be rationalised by a delicate interplay between direct exchange and 90˚ superexchange.

Clear evidence of a distortion from tetragonal symmetry has been seen for the first time in the schafarzikite phases. The greater resolution capabilities of a synchrotron should be employed to determine more definitively: a) the distortion and b) the range of oxidation states in the system through extended X-ray absorption fine structure (EXAFS) experiments.

TGA data has again revealed yet more interesting absorption characteristics of these phases where it appears that two separate isolable intermediates exist. This indicated two possibilities: the simultaneous oxidation of Co and Fe, which suggests that Pb could be important in tempering highly oxidative Co^{3+} and that the distortion could be influential in the absorption characteristics of the sample. This is supported by the Fe Mössbauer data which suggests it is possible to oxidise some Co^{2+} to Co^{3+}. Raman data however, appears to suggest that both a peroxide and superoxide species could be present, although perhaps tenuous, in the $Co_{0.25}Fe_{0.75}Sb_{1.75}Pb_{0.25}O_4$ sample which supports the oxidation of Fe only model. It is vital

that NPD studies are carried out on these phases to resolve these questions as it could present new technological application in the field of oxygen conductors. Furthermore a full and detailed characterisation of the electrical and oxygen conduction characteristics for these phases is required for potential applications in fuel cells and thermoelectric materials.

5.13 References

[1] M. J. Whitaker, R. D. Bayliss, F. J. Berry, C. Greaves, *J. Mater. Chem.* **21** (2011) 14523.
[2] A. M. Abakumov, M. G. Rozova, E. V. Antipov, J. Hadermann, G. Van Tendeloo, M. V. Lobanov, M. Greenblatt, M. Croft, E. V. Tsiper, A. Llobet, K. A. Lokshin, Y. S. Zhao, *Chem. Mater.* **17** (2005) 1123.
[3] B. P. de Laune, C. Greaves, *J. Solid State Chem.* **187** (2012) 225.
[4] J. Sejkora, D. Ozdin, J. Vitalos, P. Tucek, J. Cejka, R. Duda, *Eur. J. Mineral* **19** (2007) 419.
[5] E. Koyama, I. Nakai, K. Nagashima, *Nippon Kagaku Kaishi* **6** (1979) 793.
[6] C. E. Housecroft, A. G. Sharpe, "*Inorganic Chemistry*", Second ed, Pearson Education Limited, Harlow (2005).
[7] H. Abe, K. Yoshii, H. Kitazawa, *Phys. Status Solidi* **A 189** (2002) 429.
[8] B. Y. Brach, N. V. Chezhina, Y. V. Shapoval, *Inorg. Mater.* **25** (1989) 601.
[9] A. Boultif, D. Louer, *J. Appl. Crystallogr.* **37** (2004) 724.
[10] J. R. Gavarri, A. W. Hewat, *J. Solid State Chem.* **23** (1978) 327.
[11] J. R. Gavarri, G. Calvarin, D. Weigel, *J. Solid State Chem.* **14** (1975) 91.
[12] J. A. Gonzalo, D. E. Cox, G. Shirane, *Phys. Rev.* **147** (1966) 415.
[13] D. J. Craik, "*Magnetic Oxides: Part 1*", John Wiley and Sons, London (1975).
[14] R. Chater, J. R. Gavarri, A. Hewat, *J. Solid State Chem.* **60** (1985) 78.
[15] H. Fjellvåg, A. Kjekshus, *Acta Chem. Scand.* **A 39** (1985) 389.
[16] J. Kanamori, *J. Phys. Chem. Solids* **10** (1959) 87.
[17] K. Motida, S. Miyahara, *J. Phys. Soc. Japan* **28** (1970) 1188.
[18] J. B. Goodenough, "*Magnetism and the Chemical Bond*", John Wiley and Sons, New York-London (1963).
[19] M. Mellini, M. Amouric, A. Baronnet, G. Mercuriot, *Am. Miner.* **66** (1981) 1073.
[20] M. Mellini, S. Merlino, *Am. Miner.* **64** (1979) 1235.
[21] M. Mellini, S. Merlino, C. S. Geologia, *Acta Crystallogr.* **A 34** (1978) S184.
[22] M. Mellini, S. Merlino, P. Orlandi, *Am. Miner.* **64** (1979) 1230.
[23] J. A. Creighton, E. R. Lippincott, *J. Chem. Phys.* **40** (1964) 1779.
[24] S. A. Hunter-Saphir, J. A. Creighton, *J. Raman Spectrosc.* **29** (1998) 417.
[25] V. V. Pushkarev, V. I. Kovalchuk, J. L. d'Itri, *J. Phys. Chem.* **B 108** (2004) 5341.
[26] H. H. Eysel, S. Thym, *Z. Anorg. Allg. Chem.* **411** (1975) 97.
[27] J. Abellan, M. Ortuno, *Phys. Status Solidi* **A 96** (1986) 581.
[28] R. K. Li, C. Greaves, *J. Solid State Chem.* **153** (2000) 34.
[29] H. El Shinawi, A. Bertha, J. Hadermann, T. Herranz, B. Santos, J. F. Marco, F. J. Berry, C. Greaves, *J. Solid State Chem.* **183** (2010) 1347.

[30] R. D. Bayliss, F. J. Berry, B. P. de Laune, C. Greaves, O. Helgason, J. F. Marco, M. F. Thomas, L. Vergara, M. J. Whitaker, *J. Phys.: Condens. Matter* **24** (2012).

Chapter 6

Structural characterisation, oxidation and the ionic conductivity of $LiSbO_2$

6.1 Introduction

Given that $MgSb_2O_4$ adopts the schafarzikite structure [1], it was of interest to consider the structures of phases in which the Group 1 alkali metals replaced magnesium. It was found that of the antimonites with composition $ASbO_2$ (where A = K, Rb, Cs) none are structurally related to schafarzikite [2-3]. Isomorphic analogues to $ASbO_2$ were also found in the arsenites and bismuthites where a full range of compounds of general composition ABO_2 (where A = alkali metal; B = As [4-6], Bi [7-13]) were identified.

Of the reported systems three different space groups have been used to describe their structures:

M = monoclinic, *C*2/*c* (e.g. $NaBiO_2$)

O-I = orthorhombic, *Pbca* (e.g. $NaAsO_2$)

O-II = orthorhombic, *Ibam* ($LiBiO_2$)

It should be noted that of the three reported $AAsO_2$ (O-I type) compounds two different space-groups were used to describe their structure, *Pbca* for $NaAsO_2$ [4] and *Pbcm* for the K and Rb variants [5] but all are structurally comparable. Full details are given in Table 6.1.

Table 6.1 A summary of the structures adopted by the ABO_2 systems where A is a Group 1 alkali metal and the B site is occupied by a Group 15 element. * These materials have slightly different structures from O-I with *Pbcm* symmetry.

	As^{3+}	**Sb^{3+}**	**Bi^{3+}**
Li	—	—	O-II [8-9]
Na	O-I [4-6]	—	M [10-11]
K	O-I* [5]	M [2]	M [11-13]
Rb	O-I*[5]	M [2]	M[11, 13]
Cs	—	M [3]	M [11, 14]

Two factors are seen to be important in determining the structure adopted by each variant. It is clear from Table 6.1 that the symmetry is largely related to the B site, where all $AAsO_2$ compounds prefer O-I symmetry whilst all the remaining compounds (excluding A = lithium) adopt the monoclinic setting *C*2/*c*. This implies that the structure adopted is heavily dependent on the bonding preferences of the B site cation with a lone pair of electrons. The A site cations also seem to be important, as shown by $LiBiO_2$, but to a lesser extent. The effects of the alkali metal cations are more clearly seen in the lattice parameters (Table 6.2) where a general trend of increasing unit cell volume with increasing atomic number is observed.

Only compounds of O-I and O-II symmetry possess discrete BO_2 layers. In the M-type compounds each B site forms four bonds to surrounding oxygen providing a pseudo-trigonal-bipyramidal coordination geometry when including the lone pair. Each BO_4 polyhedron connects via a common edge to form infinite $[BO_2]^-$ chains parallel to [001] providing interstitial sites for the 6 coordinate [10] A cations (Figure 6.1a).

Table 6.2 Structural details for the ABO_2 compounds reported to date, and the respective X-ray sources used to determine the values. Structure types given in Table 6.1.

	Space Group	*a* (Å)	*b* (Å)	*c* (Å)	*β* (°)	Radiation
$NaAsO_2$ [4]	*Pbca*	14.314(5)	6.779(5)	5.086(5)	-	Cu K_α
$KAsO_2$ [5]	*Pbcm*	7.151(2)	7.48.0(1)	5.39.2(2)	-	Mo K_α
$RbAsO_2$[5]	*Pbcm*	7.297(5)	7.752(5)	5.411(3)	-	Mo K_α
$KSbO_2$ [2]	*C*2/*c*	7.854(3)	8.221(4)	5.587(3)	124.9	Mo K_α
$RbSbO_2$[2]	*C*2/*c*	7.996(1)	8.8632(7)	5.5932(5)	123.37	Mo K_α
$CsSbO_2$ [3]	*C*2/*c*	8.1023(8)	9.772(1)	5.5763(8)	121.90(8)	Mo K_α
$LiBiO_2$[9]	*Ibam*	17.97(8)	5.18(9)	4.97(8)	-	Mo K_α
$NaBiO_2$ [10]	*C*2/*c*	7.39(4)	7.26(2)	5.88(6)	127.7	Mo K_α
$KBiO_2$[13]	*C*2/*c*	7.8313(9)	7.909(1)	5.9686(8)	124.81(1)	Mo K_α
$RbBiO_2$[13]	*C*2/*c*	8.0620(5)	8.3888(4)	5.9814(4)	123.68	Mo K_α
$CsBiO_2$[14]	*C*2/*c*	8.274(2)	9.204(2)	5.9787(9)	122.51	Mo K_α

In contrast, the $AAsO_2$ compounds of O-I symmetry possess a layered structure constructed from infinite $[AsO_2]^-$ chains of corner linked AsO_3 trigonal pyramidal polyhedra which propagate along [001] (Figure 6.1b) to form zigzag chains due to the nature of the linkages. Each chain contains two long bridging Sb-O_B bonds and one short terminal Sb-O_T bond (e.g. $KAsO_2$ Sb-O_B =1.845(3) Å, Sb-O_T = 1.693(6) Å [5]). Layers are formed by the arrangement of the chains into opposing sheets, where the terminal oxygen is directed into the layer. The sheets then sandwich the seven coordinate (A = Na) or eight coordinate (A = K, Rb) A site cations between them where it is believed that the interlayer region provides a suitable environment for the As lone pairs [6].

Early single crystal XRD studies of $LiBiO_2$ proposed the system had O-II symmetry and a layered structure [9]. Each layer can be described as consisting of common edge sheets of 5-coordinate square-pyramidal Bi^{3+} (Figure 6.1c, including the lone pair) with the base of the pyramid forming the BiO plane and the terminal oxygen projecting into the interlayer

region occupied by Li in tetrahedral coordination. A later NPD study by Andersen *et al* [7] supported these findings: however the unacceptable R-factor (27.6%) for their fit was notable. It was apparent from the unacceptably high IDPs for the O1 and O2 positions (9.0 Å^2 and 5.9 Å^2 respectively) that the space-group was incorrect. A more detailed NPD study [8] suggested that the local structure was distorted generating three short Bi-O bonds and trigonal pyramidal Bi which is probably consistent with *Iba*2 symmetry.

It was surprising to find a lack of structural details for the Li-containing As^{3+} and Sb^{3+} systems and, although the likelihood of structural similarities between $LiSbO_2$ and $LiBiO_2$ has been suggested [15-16] no evidence has been found to support this. Only diffraction data derived from an original synthesis of $LiSbO_2$ by Sauvage *et al* [17] where crystals obtained from a LiCl/KCl flux were investigated by single crystal diffraction are available. The results suggest an orthorhombic cell of lattice parameters (a = 4.068 Å, b = 9.790 Å, c = 5.650 Å) and possible symmetry described by the space groups *Pmmn* or $P2_1mn$, implying no structural relationship to $LiBiO_2$ (*Ibam,* a = 17.976(4) Å, b = 5.179(1) Å, c = 4.972(1) Å) [8]. It therefore seemed unlikely that the structure is related to any of the compounds previously reported. No further characterisation was performed by Sauvage *et al* [17] presenting an opportunity for full characterisation of the structure and properties of $LiSbO_2$. This chapter examines in detail the thermal stability and ionic conductivity of $LiSbO_2$ and assigned definitive symmetry to the system for the first time.

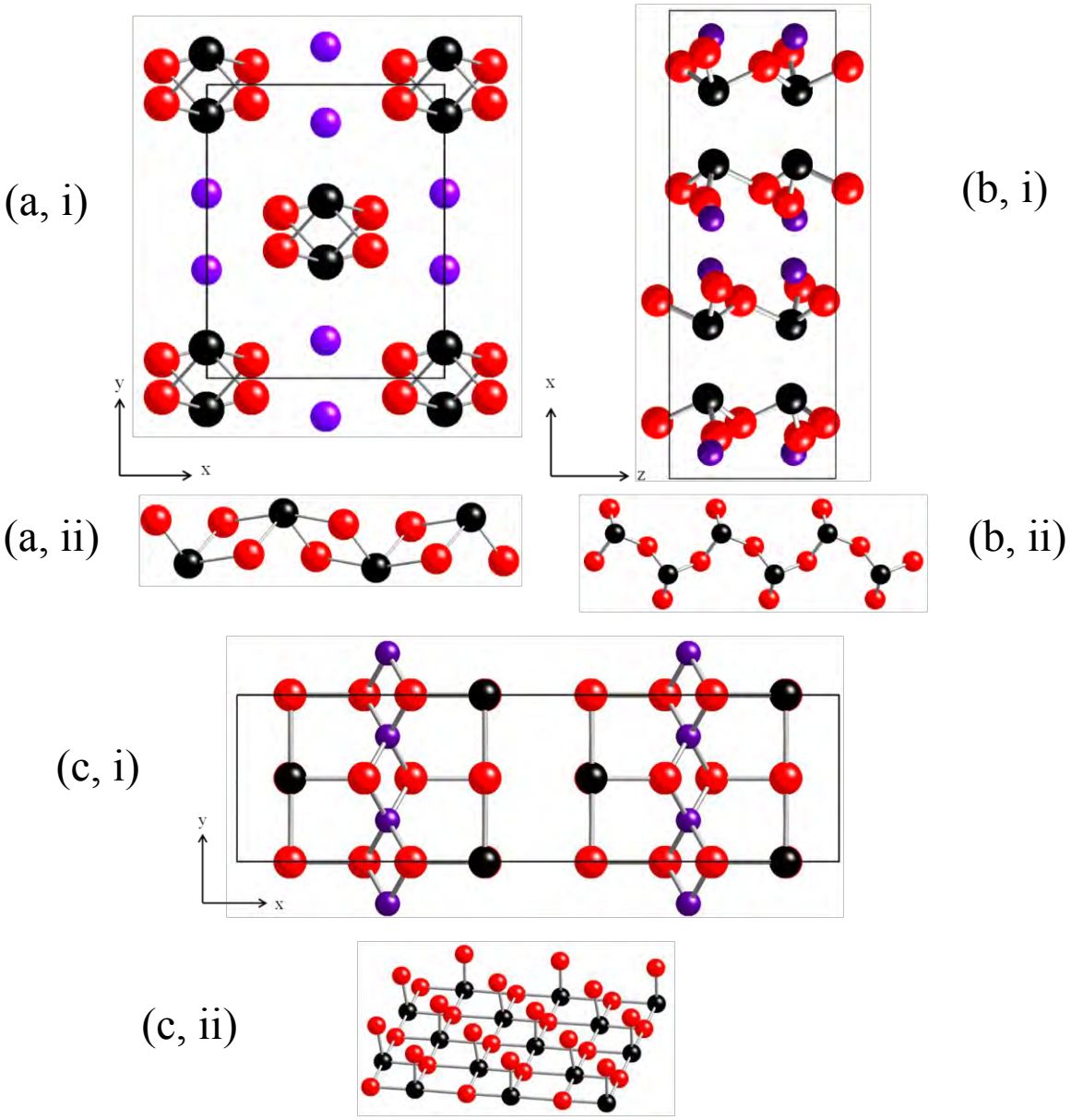

Figure 6.1 The structures adopted by the ABO_2 systems: (a) M type e.g. $NaBiO_2$ [10-11]; (b) O-I e.g. $NaAsO_2$ [4-6] and (c) O-II type e.g. $LiBiO_2$ [8-9]. The M structures (a); (i) a view along [001] showing the channels which accommodate the A site cations; (ii) a $[BO_2]^-$ chain showing edge linked trigonal bipyramidal BO_4 units roughly perpendicular to [010] and [001] (red, black and purple spheres represent O, B, and A sites respectively). O-I structures (b); (i) a view along [010] showing layers of corner linked BO_3 (B (black) and O (red spheres) respectively) trigonal pyramidal units parallel to [001] which sandwich the 7 coordinate (Na) or 8 coordinate (K, Rb) A site cations (purple spheres) between them; (ii) corner linked AsO_3 trigonal pyramidal units viewed along [100]. The O-II structure formed by $LiBiO_2$ (c); (i) a view along [001] showing layers of square pyramidal Bi (black spheres) parallel to [010] and Li (purple spheres) in tetrahedral geometry; (ii) edge linked BiO_4 polyhedra forming sheets perpendicular to [100].

6.2 Experimental

Samples were prepared by a solid state reaction of Li_2O (Sigma-Aldrich, 97%, in 5% excess) and Sb_2O_3 (Sigma-Aldrich, 99%). Intimately ground mixtures were contained in silver tubes with the ends crimped within evacuated fused silica tubes and were heated for 48 and 72 hrs at 500˚C with intermittent grinding. All sample preparation was carried out within a glove box under an anhydrous atmosphere of pure-shield Ar. Antimony oxide was dried prior to use under dynamic vacuum at 150˚C for a minimum of 4 hrs. Li_2O remained within the glovebox from opening.

Pellets for conductivity, were formed by pressing (uniaxial applied force of 0.5 tonnes) around 0.5g of $LiSbO_2$, analysed by NPD, in an 8mm die set and sintered in a silver tube within an evacuated fused silica tube for 24 hrs at 550˚C. The resultant pellet faces were coated in Ag-paste and allowed to dry overnight. AC impedance measurements were made by spring tensioned electrodes under variable temperature conditions in air (*see Chapter 2*).

Mixed $Li_{1-3x}A_xSbO_2$ and $Li_{1-2y}B_ySbO_2$ compounds (where A = Ga^{3+}, Al^{3+}; B = Zn^{2+}; x = 0.1, 0.01 and y = 0.1) were synthesised in the same manner as above by heating reaction mixtures (Equations 6.1-6.3) in the temperature region 500-550˚C for up to 96 hrs with intermittent grinding.

$$0.35Li_2O + 0.5Sb_2O_3 + 0.05Al_2O_3 \rightarrow Li_{0.7}Al_{0.1}SbO_2 \quad (6.1)$$

$$0.35Li_2O + 0.5Sb_2O_3 + 0.05Ga_2O_3 \rightarrow Li_{0.7}Ga_{0.1}SbO_2 \quad (6.2)$$

$$0.4Li_2O + 0.1ZnO + 0.5Sb_2O_3 \rightarrow Li_{0.8}Zn_{0.1}SbO_2 \quad (6.3)$$

6.3 Identification and characterisation of $LiSbO_2$.

Reaction mixtures were initially heated at 500˚C and 700˚C in an attempt to identify a suitable synthesis procedure; shorter heating times were used at higher temperatures. Several sample containment vessels were tested including silica, alumina crucibles and silver tubes with the ends crimped. Silver tubes were found to give the least amount of residual Sb_2O_3 indicating better retention of Li_2O during synthesis. Temperatures of 600˚C and above also produced samples of poor quality. Samples produced by heating at 500˚C were predominantly single phases; however a persistent Sb_2O_3 impurity, despite varying the reaction time, prompted the use of a small excess of Li_2O. A comparison between the XRPD data (Figure 6.2) and a simulated powder pattern obtained from the relative peak intensities presented by Sauvage *et al* [17] (Figure 6.3) clearly showed significant differences between the two structures. The possibility of the flux grown crystals being a lower temperature polymorph or of partially oxidised composition when compared to the main phase was considered.

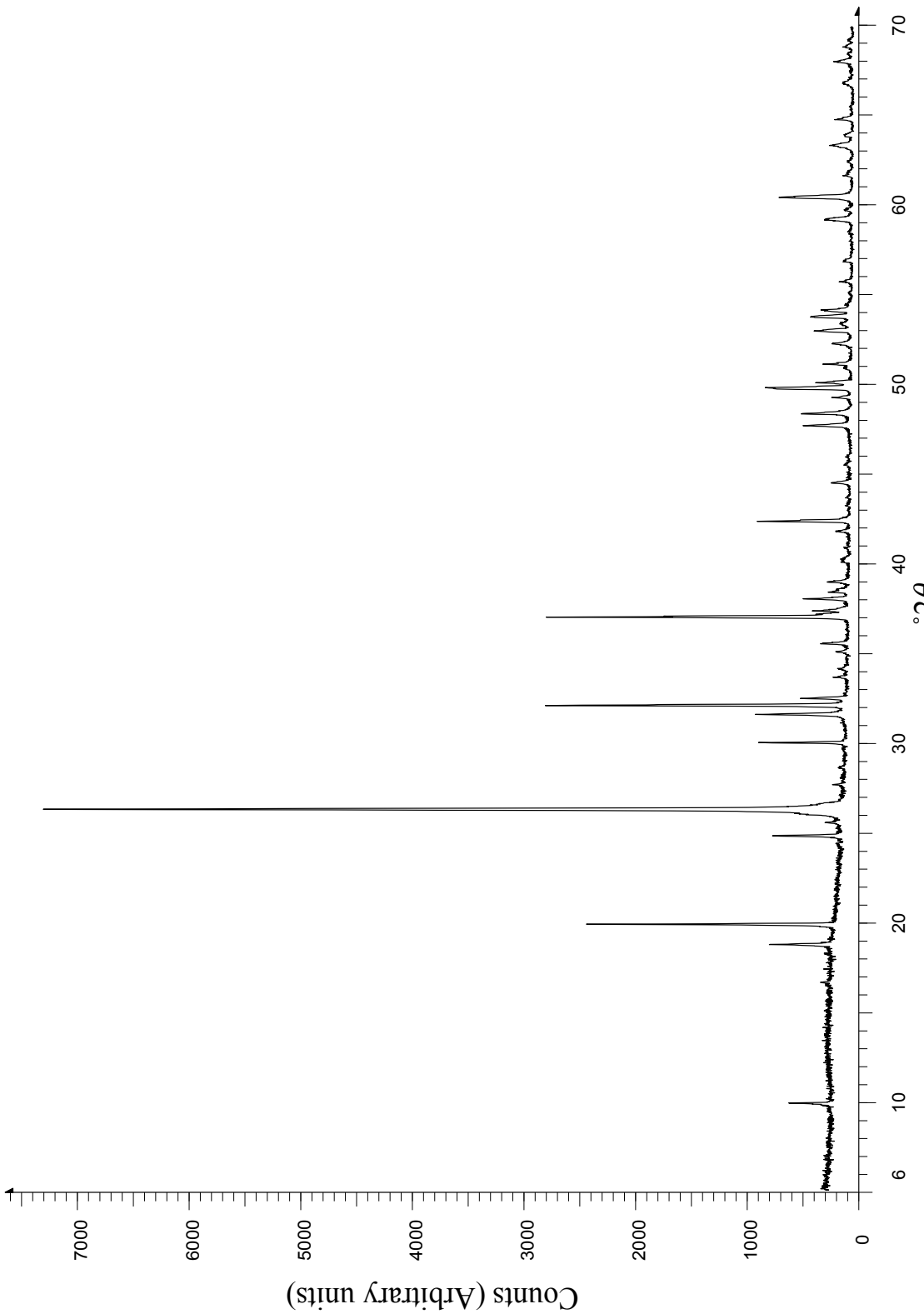

Figure 6.2 A XRPD pattern of $LiSbO_2$ synthesised at 500°C for a total of 120 hrs with an excess of Li_2O (5% by mass). Monochromatic Cu K_α X-rays, λ= 1.5406 Å were used.

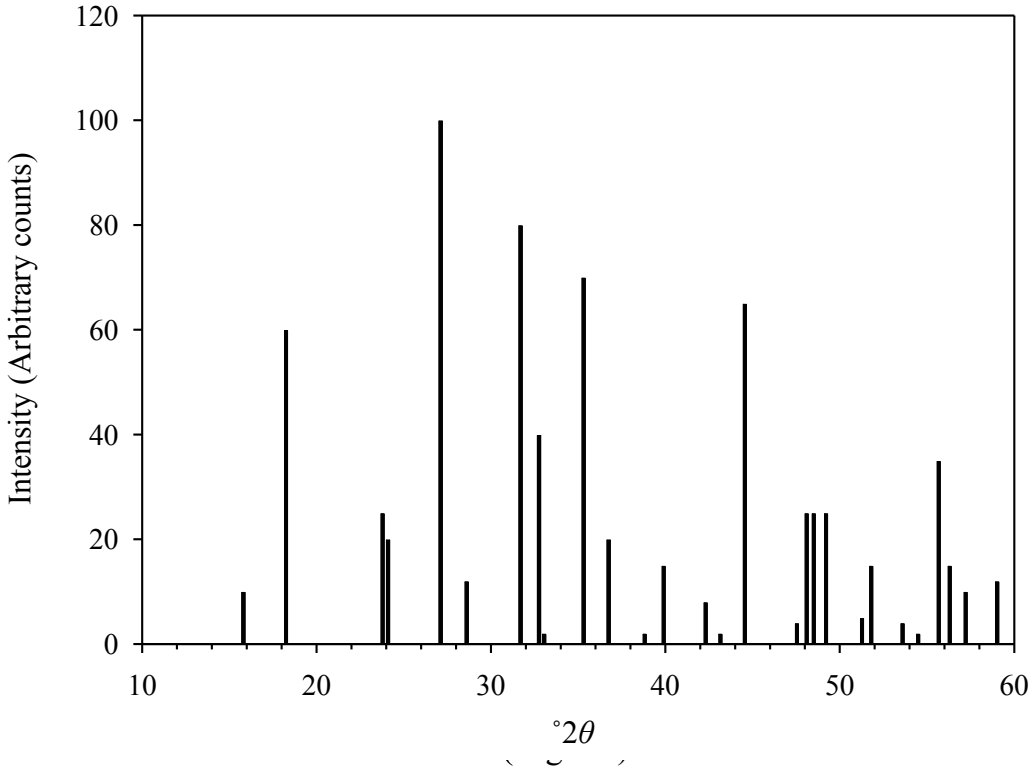

Figure 6.3 A simulated powder pattern of $LiSbO_2$ based upon the relative intensities and *d*-space values reported by Sauvage in a single crystal diffraction study, Cu K_α.

An isostructural template was sought in order to refine the structure; $LiBiO_2$ was possible due it allegedly being isostructural to $LiSbO_2$ [15-16]. Indexing of the XRPD data indicated the system to be orthorhombic with lattice parameters a = 17.855(6) Å, b = 5.572(1) Å, c = 4.8490(9) Å and showed similarities to that of $LiBiO_2$ (a = 17.976(4) Å, b = 5.179(1) Å, c = 4.972(1) Å [8]). However, indexing of the most intense peaks (Table 6.3) across the 2θ range (5-70 ˚2θ) did not satisfy the general selection rules of the *Ibam* space group, e.g. $h+k+l = 2n$, and suggested a primitive cell. A lower symmetry space group which contained 2_1 screw axes along all directions linking it to *Ibam* and simultaneously satisfying the calculated Miller indices had to be isolated. The orthorhombic spacegroup $P2_12_12_1$ was identified as being of suitable symmetry and was used as the basis for refinement.

Table 6.3 A selection of the most intense peaks obtained from a sample of $LiSbO_2$ within the range 5-70 ˚2θ and their associated (*hkl*) values for an orthorhombic cell.

˚2θ	(*hkl*)
9.860	(200)
18.739	(210)
19.862	(400)
24.814	(111)
25.560	(410)
26.291	(211)
28.636	(311)
30.017	(600)
31.602	(411)
32.101	(020)
32.492	(120)
37.045	(002)
42.395	(402)
49.815	(022)
53.818	(213) or (1010)
54.158	(422)
60.489	(213)

6.4 XRPD refinement

Refinement proceeded as previously detailed (*see Chapter 3*), where $P2_12_12_1$ symmetry, the lattice parameters obtained from indexing and atomic positions from the structure of $LiBiO_2$ were used. Only Sb and O were included in the model as lithium contributed relatively little to the powder pattern. Significant reduction in the intensities of the (020) and (002) peaks indicated strong preferred orientation (ratio = 1.480(6)) along the long axis; this was corrected using the March-Dollase function orientated along [100]. The final fit (Figure 6.4; χ^2 = 3.021, a = 17.8316(6) Å, b = 5.5678(1) Å, c = 4.8477(1) Å) whilst clearly requiring further analysis also demonstrated reasonable agreement between with the Sb-O framework and symmetry. This further supported significant differences between our sample and that produced by Sauvage *et al* [17].

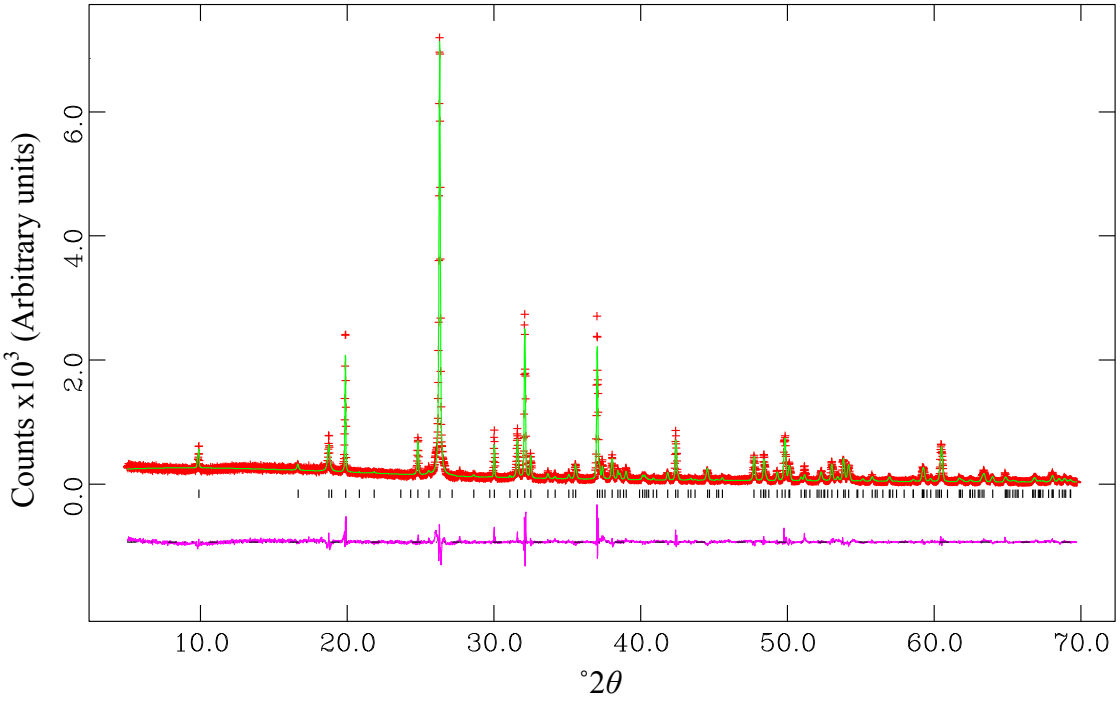

Figure 6.4 The Rietveld refinement of $LiSbO_2$ based upon XRPD data in $P2_12_12_1$ showing observed data (+), calculated and difference profiles (continuous lines) and reflection positions (|). This model only included the atomic positions of Sb and O.

6.5 Structural characterisation by NPD

Refinement of the 300 K NPD data set, collected at PSI Zurich on the HRPT beam line, proceeded using the XRPD refined model. It quickly became apparent from the best fit (Figure 6.5), where all acceptable variables were refined, that the space group was not suitable due to the miss match of intensities. However, the coincidence between many of the simulated peak positions and the observed data suggested a possible retention of some symmetry elements and that a related space group was required.

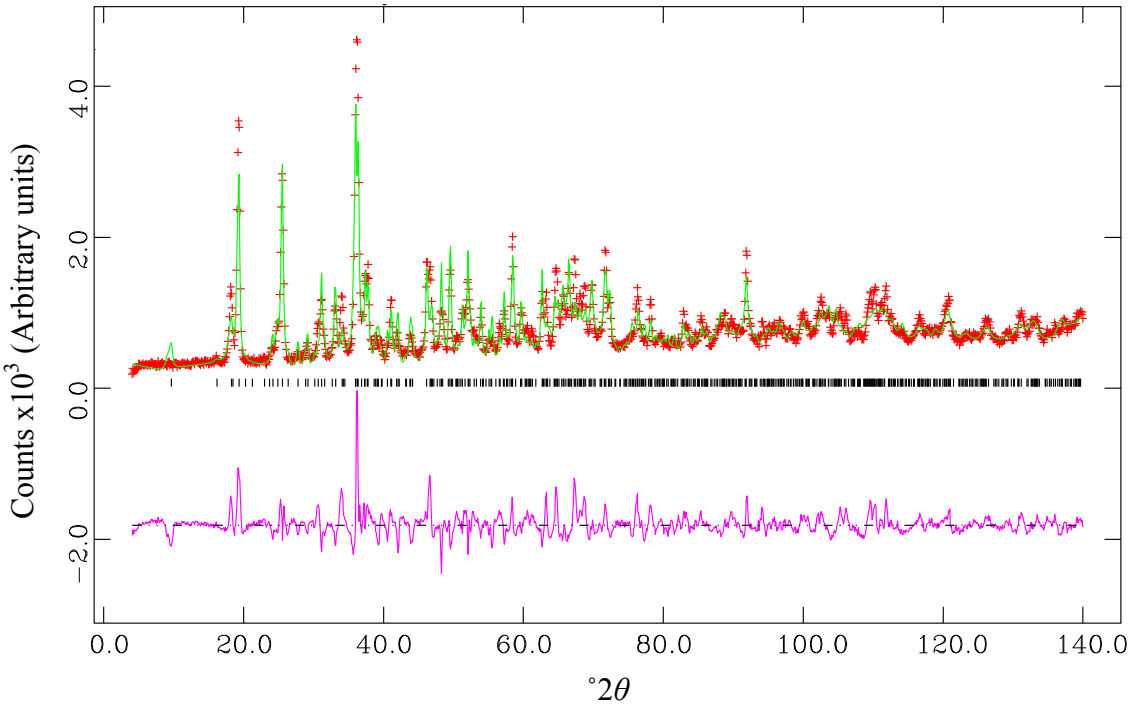

Figure 6.5 Refinement of $LiSbO_2$ NPD data at 300 K in $P2_12_12_1$, showing observed data (+), calculated and difference profiles (continuous lines) and reflection positions (|); $\chi^2 = 17.94$. This preliminary refinement does not contain Li in the model.

The difference in scattering properties of the elements within the sample by X-rays and neutrons (scattering lengths set to: Li -1.90, Sb 5.57, O 5.81 all $x10^{-15}$m) was an initial guide to the identification of a new suitable space-group. Considering first the XRPD refinement, the good agreement between the observed and calculated models indicated relatively high accuracy of the Sb positions and to a much lesser degree, oxygen. The rough coincidence between the raw data and model in the NPD refinement using $P2_12_12_1$ where the difference in scattering between Sb and O was much smaller suggested that the deficiency in the model related primarily to the oxygen positions. This enabled the antimony and to some extent the oxygen positions to be used to identify symmetry elements linking the sites. It was apparent at this point that the structures of $LiSbO_2$ and $LiBiO_2$ were significantly different.

A structure from the $P2_12_12_1$ XRPD refinement was generated where two distinct layers centred at roughly $z = 0.25$ and 0.75 were identified. Atoms which were closest to

sitting on the planes perpendicular to [001], namely the Sb1, Sb2 and O1 positions, were simulated as shown in Figure 6.6 and symmetry elements sought.

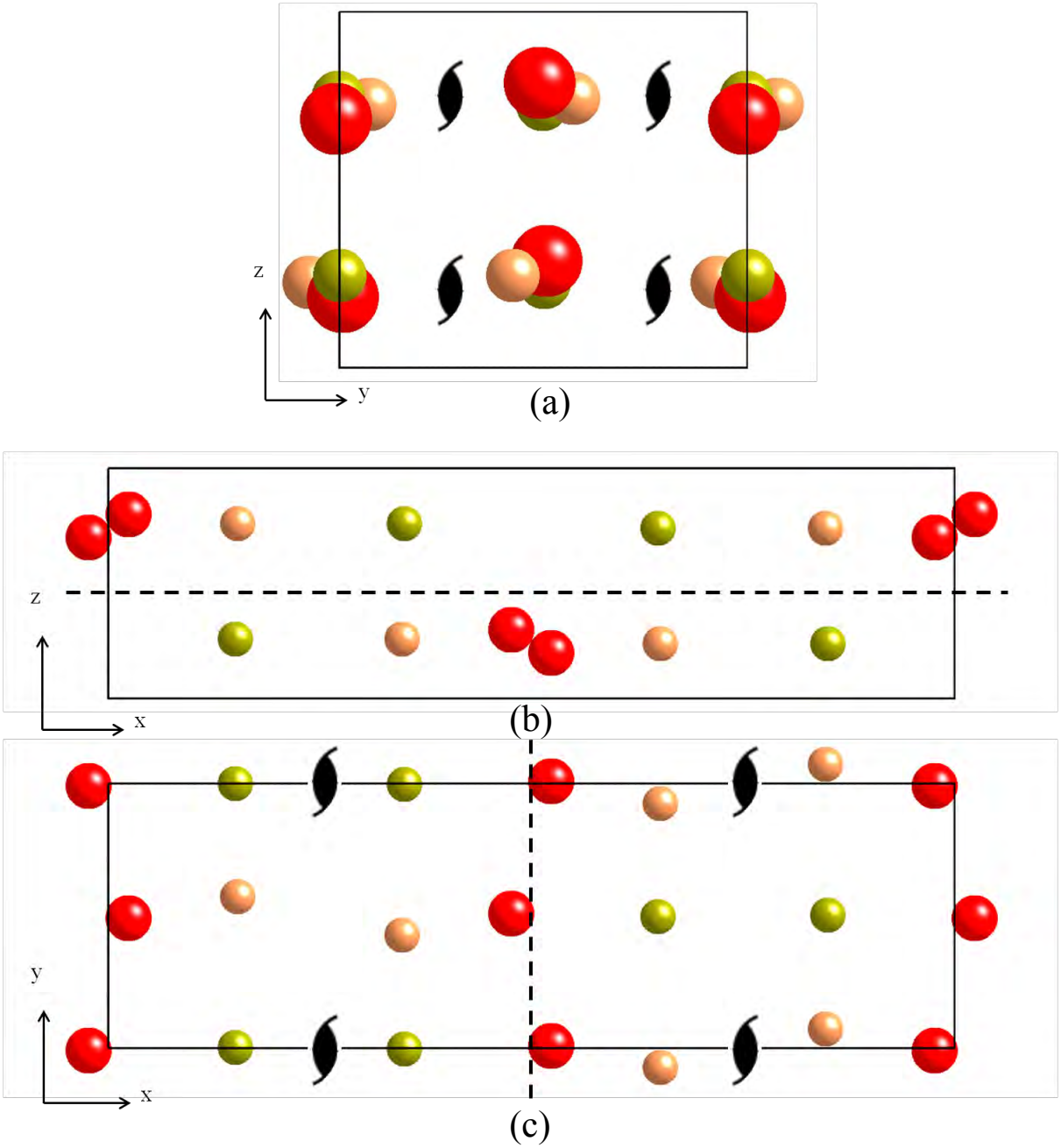

Figure 6.6 The simulated structure of $LiSbO_2$ based upon the final XRPD refinement in $P2_12_12_1$. Isolation of possible symmetry elements are indicated and were used to identify a more suitable spacegroup. The spheres represent Sb1 (beige), Sb2 (green) and O1 (red) with views along: (a) [100], (b) [010] and (c) [001].

Evidence for 2_1 screw axes and glide planes were identified. Of the remaining lower symmetry orthorhombic space groups none contained a glide plane so attention was directed to monoclinic space groups. Of these, several possibilities were identified where $P2_1/c$ was

one of the highest symmetry which accommodated the identified symmetry elements. $P2_1/c$ was also one of the highest symmetry maximal subgroups of *Pbam* (the same symmetry as displayed for $LiBiO_2$ once the body centring was removed). This was used as the subsequent basis for refinement. The axes were converted to accord with the monoclinic setting, a = 4.8477(1) Å, b = 17.8316(6) Å, c = 5.5678(1) Å, $\beta = 90^\circ$ and the atomic positions of Sb and O only, obtained from the $P2_12_12_1$ refinement, were used. Li was initially excluded due to its limited contribution to the profile. The fit was better (Figure 6.7; χ^2 = 7.219,) supporting the space-group assignment.

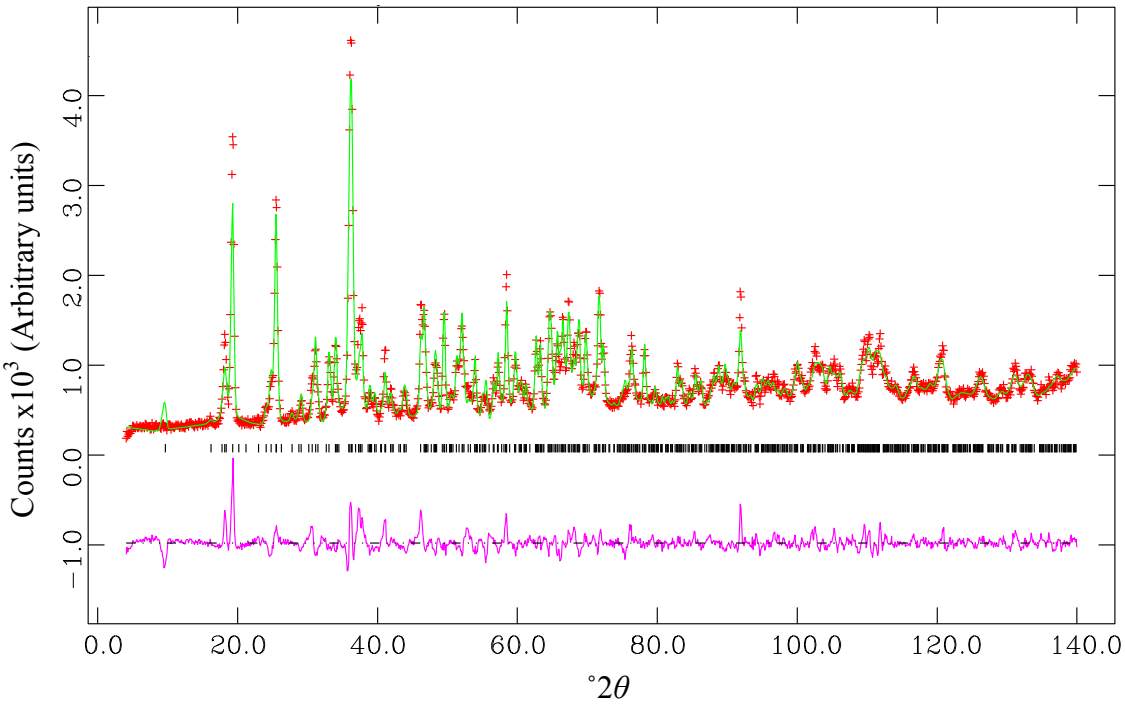

Figure 6.7 A plot of the fit obtained from the refinement of $LiSbO_2$ in $P2_1/c$ showing observed data (+), calculated and difference profiles (continuous lines) and reflection positions (|) of the main phase. The refinement excludes lithium.

Simulation of the resultant structure (Figure 6.8) enabled two highly electronegative regions to be isolated at roughly b = 0.25 and 0.75 which seemed most likely to accommodate the lithium ions.

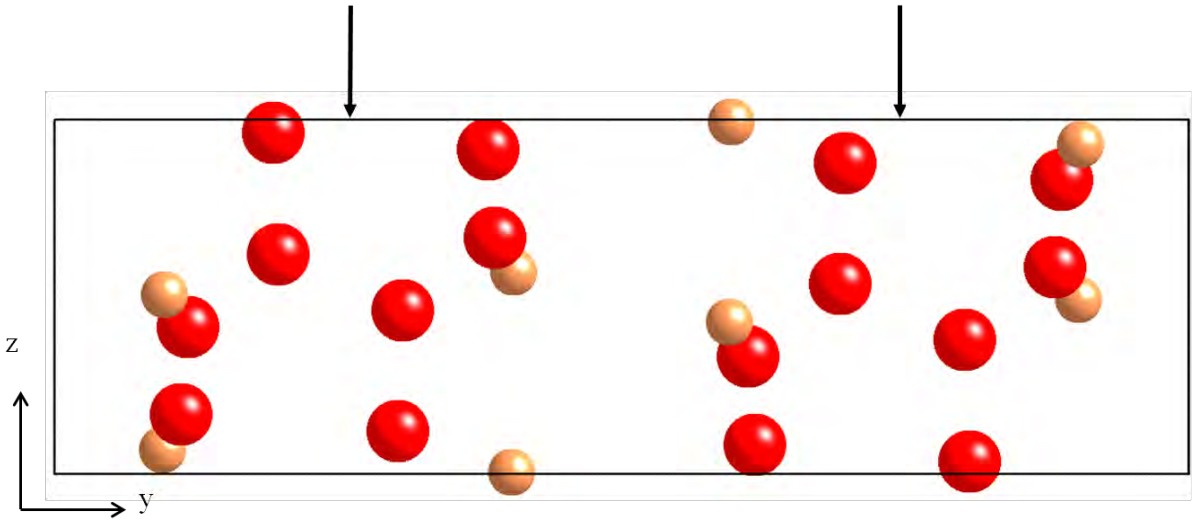

Figure 6.8 A structural simulation based on the refined (NPD) atomic positions of Sb and O in the $P2_1/c$ setting. The red and beige spheres represent O and Sb where the arrows indicate likely locations for Li ions.

Difference Fourier synthesis was used to more accurately locate the regions of negative scattering, representing lithium; a map was generated which was centred within one of these regions at (0.50, 0.25, 0.50). Slices of scattering were taken above and below the central plane. The resultant plot (Figure 6.9) showed negative scattering in two symmetry unrelated regions consistent with the theoretical model. The addition of the two lithium ions located at (0.263, 0.211, 0.040) and (0.783, 0.211, 0.321) to the model resulted in considerable improvement to the fit further supporting their locality.

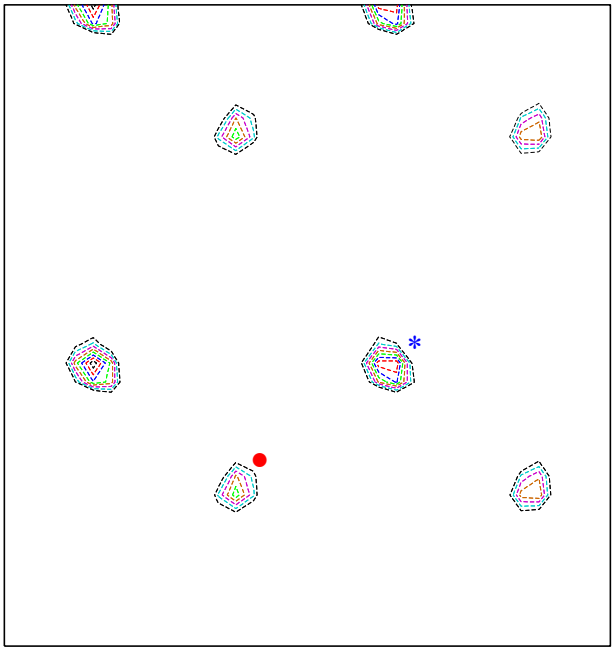

Figure 6.9 A Fourier map plot of $LiSbO_2$ used to locate the lithium positions. Centred at 0.50, 0.25, 0.50 and viewed along [010] two distinct regions of previously unaccounted for nuclei attributed to lithium are shown. Lithium positions were located at (0.263, 0.211, 0.040) ● and (0.783, 0.211, 0.321) *.

The final fit (Figure 6.10; $\chi^2 = 1.849$, $R_{wp} = 0.0476$) is for all atomic positions, IDPs, profile lattice parameters, background, ZPE, and SF being refined independently. The refined preferred orientation correction along [010] was small (1.087(4)) but still included. The final structural details are displayed in Table 6.4 where the small monoclinic distortion is a possible contributing factor to the initial assignment of an orthorhombic cell during indexing. It should be noted that no correction for the absorption effects of Li were added, however the IDPs were all reasonable and a high correlation between occupancy and IDPs would indicate if such a correction was necessary.

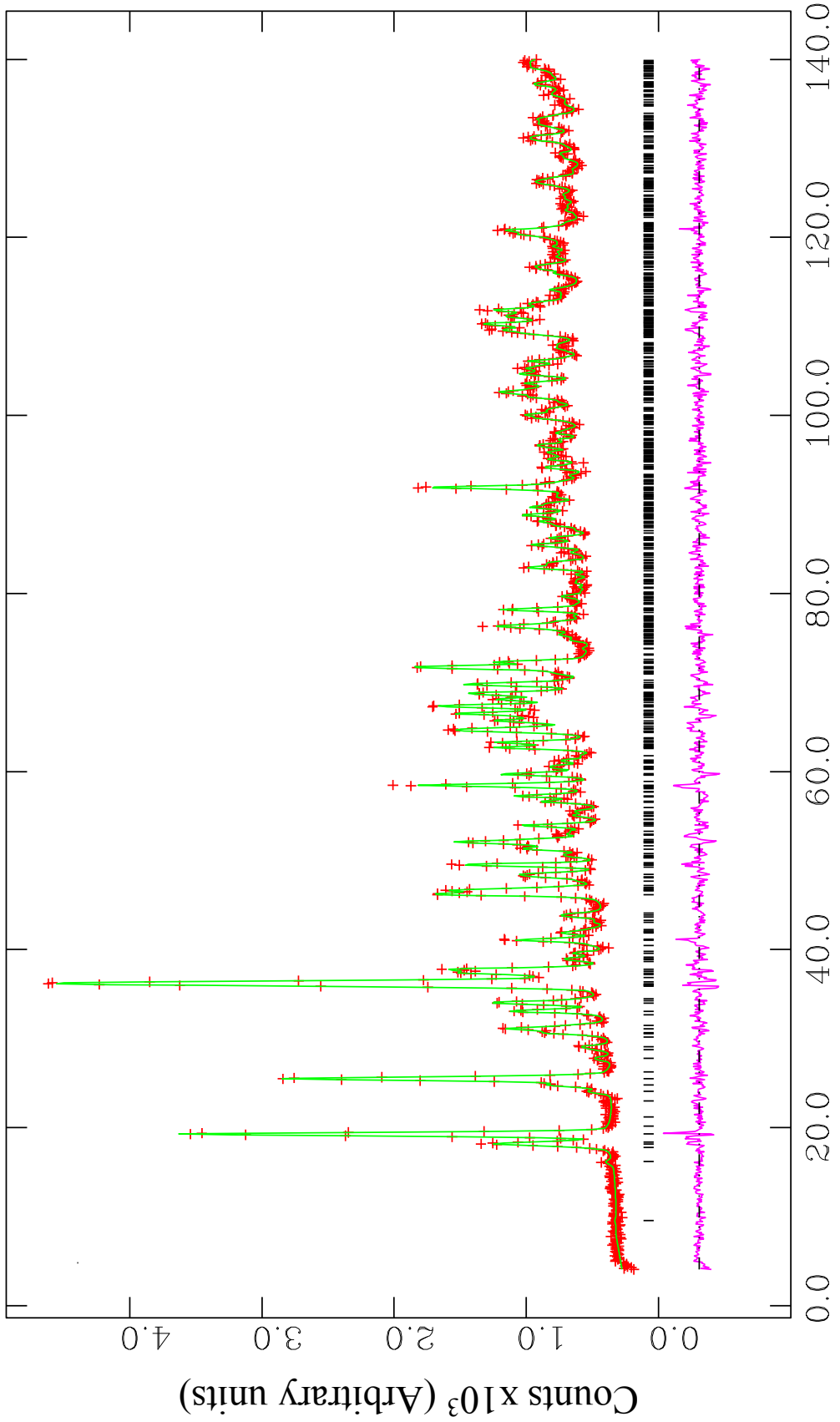

Figure 6.10 The final fit of $LiSbO_2$ in $P2_1/c$; observed data (+), calculated (|) and difference profiles (|) and reflection positions (black tick marks) of the main phase are shown. $\chi^2 = 1.849$.

Table 6.4 Showing the details obtained from the final refinement of $LiSbO_2$ in a $P2_1/c$ setting.

Atom	*x*	*y*	*z*	$100*U_{iso}$ (Å^2)
Sb1	0.259(2)	0.5994(4)	0.5711(8)	1.1(2)
Sb2	0.237(2)	0.4032(4)	0.994(1)	0.7(1)
O1	0.339(1)	0.6942(4)	0.463(1)	0.9(1)
O2	0.170(2)	0.3034(6)	0.878(1)	2.0(2)
O3	0.367(1)	0.6167(5)	0.920(1)	1.2(2)
O4	0.138(1)	0.3848(5)	0.333(1)	1.4(2)
Li1	0.254(5)	0.219(1)	0.042(3)	1.6(5)
Li2	0.770(5)	0.211(1)	0.376(3)	0.9(4)
a = 4.8550(3) Å; b = 17.857(1) Å; c = 5.5771(4) Å; β = 90.061(6)°				

6.6 Structure analysis

The structure shown in Figure 6.11 depicts a layered compound with sheets perpendicular to [010]. Each layer is comprised of discrete parallel chains of corner linked SbO_3 pyramidal units (Figure 6.11b) propagating along [100]. Individual SbO_3 chains consist of two types of Sb-O linkage: every Sb can be seen to be bound to two bridging O atoms (O_B; O3 and O4) and a single non-bonding terminal oxygen (O_T; O1 to Sb1 and O2 to Sb2). If the Sb-O_B chains are considered as the backbone, opposing layers are formed into which the terminal oxygens project roughly parallel to [010] (Figure 6.11a) consequently forming regions of negative charge at y = 0.25 and 0.75. This creates a suitable environment for the accommodation of lithium. Lithium ions were found to coordinate nearest neighbour chains into their observed parallel arrangement whilst simultaneously occupying distorted tetrahedra (Figure 6.11c) where a larger distortion, away from the ideal 109.5˚ bond angles, was found for Li1 (Table 6.5). Comparison with other compounds containing lithium tetrahedra showed comparable Li bond lengths (1.841(6) - 2.358(6) Å, for the distorted site and 1.9112(7) Å for the non distorted tetrahedral site in $Li_6SrLa_2Nb_2O_{12}$ [18]). It was also found, Figure 6.12, that the lithium sites ordered forming alternating sheets of same site tetrahedra perpendicular to [100].

The inter layer region at $y = 0$ and 0.5 was presumed to be occupied by the antimony lone pairs where repulsion was minimised by their non direct orientation between opposite layers. However, it was clear that forces of attraction must exist between each layer for the compound to form a thermodynamically stable crystalline solid. Consideration given to other layered compounds which possess atoms with lone pairs suggest that this structural feature was seen to commonly exist, e.g. in PbO (yellow massicot, *Pbcm*) [19]. Constructed from layers of zig-zag Pb-O chains of 4 coordinate lead, it was proposed by Dickens [19] that the reason the layers were in such close proximity was due to the van der Waals forces between $6s^2$ lone pairs on adjacent Pb atoms. Whilst the same argument could hold for $LiSbO_2$ detailed calculations are necessary to verify this.

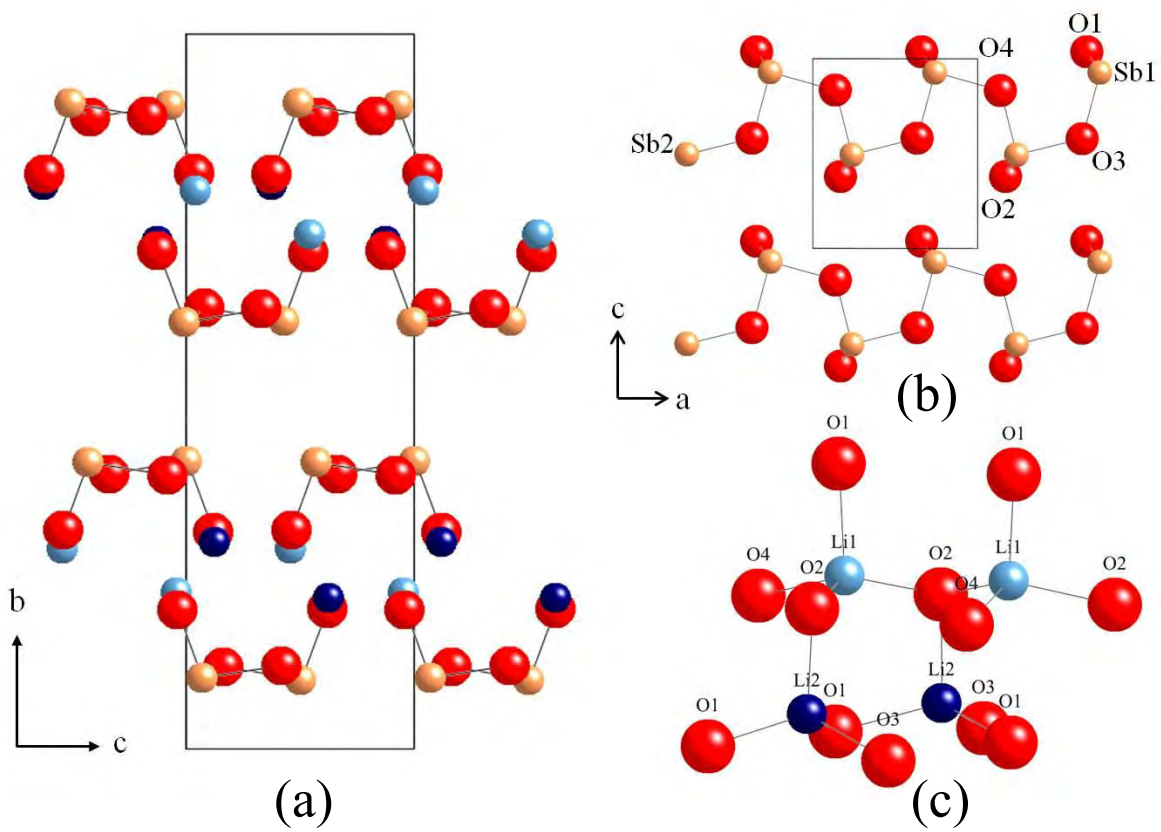

Figure 6.11 (a) A representation of the structure along [100]; (b) shows linking of the SbO_3 trigonal-pyramidal units to form infinite $[SbO_2]^-$ chains parallel to [100]; (c) shows the tetrahedral coordination and linking of the lithium sites.

Table 6.5 Selected bond lengths and angles obtained from the final Rietveld refinement of $LiSbO_2$

Bond Lengths (Å)		Angles (°)	
Li 1 – O1	2.03(3)	O1 – Li 1 – O2	113(1)
Li 1 – O2	1.81(2)	O1 – Li 1 – O2	100(1)
Li 1 – O2	1.96(2)	O2 – Li 1 – O2	128(1)
Li 1 – O4	2.26(2)	O1 – Li 1 – O4	93.1(9)
		O2 – Li 1 – O4	111.5(9)
		O2 – Li 1 – O4	106(1)
Li 2 – O1	1.98(2)	O1 – Li 2 – O1	119(1)
Li 2 – O1	1.99(2)	O1 – Li 2 – O2	104.5(8)
Li 2 – O2	1.96(2)	O1 – Li 2 – O2	112(1)
Li 2 – O3	2.14(2)	O1 – Li 2 – O3	108(1)
		O1 – Li 2 – O3	110(2)
		O2 – Li 2 – O3	101.7(9)
Sb 1 – O1	1.84(1)	O1 – Sb1 – O3	96.9(4)
Sb 1 – O3	2.036(8)	O1 – Sb1 – O4	99.2(5)
Sb 1 – O4	2.02(1)	O3 – Sb1 – O4	88.3(3)
Sb 2 – O2	1.92(1)	O2 – Sb2 – O3	94.5(4)
Sb 2 – O3	2.02(1)	O2 – Sb2 – O4	97.3(4)
Sb 2 – O4	1.978(9)	O3 – Sb2 – O4	88.6(4)

Comparison with other layered compounds indicated that the structure most closely resembled that of orthorhombic $NaAsO_2$ (*Pbca*) [4-6] where the Na environment has been described as consisting of four short tetrahedral type bonds and three longer bonds; however this was clearly different from the environment of lithium in $LiSbO_2$.

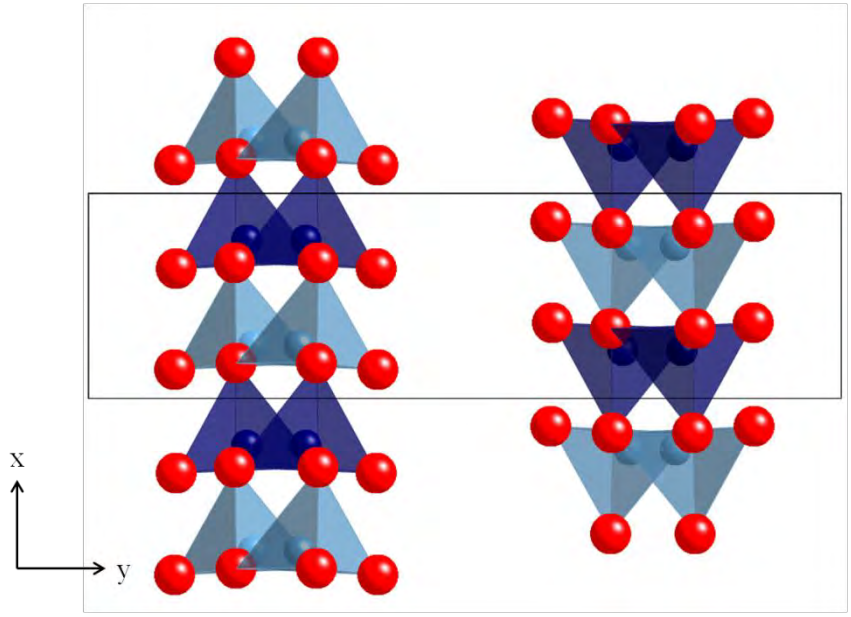

Figure 6.12 A view of $LiSbO_2$ along [001] showing ordering of the Li1 (light blue) and Li2 (dark blue) tetrahedra into sheets perpendicular to [100].

A clear distinction was seen between Sb-O (1 and 2) and Sb-O (3 and 4) bonds reflecting their bridging and terminal nature, where the bridging bonds (1.978(9)-2.036(8) Å) were significantly longer than the terminal bonds (1.84(1) Å and 1.92(1) Å). This was analogous to the trend seen in $NaAsO_2$ where the average bridging and terminal distances were 1.822(3) and 1.684(4) Å respectively [6]. Whilst the Sb-O bond distances were larger than the Sb-O bonds in the schafarzikite related materials (*see Chapter 3*) they compare favourably with the other $ASbO_2$ systems (Cs = 1.954(5) Å and 2.168(5) Å [3]; Rb = 1.957(5) Å and 2.179(5) Å [2]; K = 1.958(4) Å and 2.188(4) Å [2]). If the Sb coordination sphere is considered as tetrahedral when including the lone pair, the severely reduced bond angles demonstrate the strong repulsive force that the inert pair exerts over the surrounding bonds. Furthermore, the purely O_B-Sb-O_B bonds angles were shown to be 6-10˚ smaller than those possessing a terminal oxygen reflecting the greater electronic repulsion afforded by the electrons in the shorter terminal bonds.

The final model was verified by bond valence sum calculations (Table 6.6) [20] and showed the oxidation states of Sb and Li to be in excellent agreement with their ideal values.

Table 6.6 The calculated oxidation states worked out by BVS calculations from the final Rietveld refinement model.

Atom	BVS
Li1	0.99
Li2	0.93
Sb1	3.19
Sb2	3.00

6.7 SEM analysis

Strong evidence for preferred orientation in the XRPD refinement and to a lesser degree in the NPD data suggested the possible formation of platelets with large crystal faces growing perpendicular to [010] (preferred orientation along [010] in the XRPD refinement ≈ 1.5). A SEI image (Figure 6.13) showed the crystal morphology adopted large platelets with facial diameters in the region of 10 μm verifying the refinement findings.

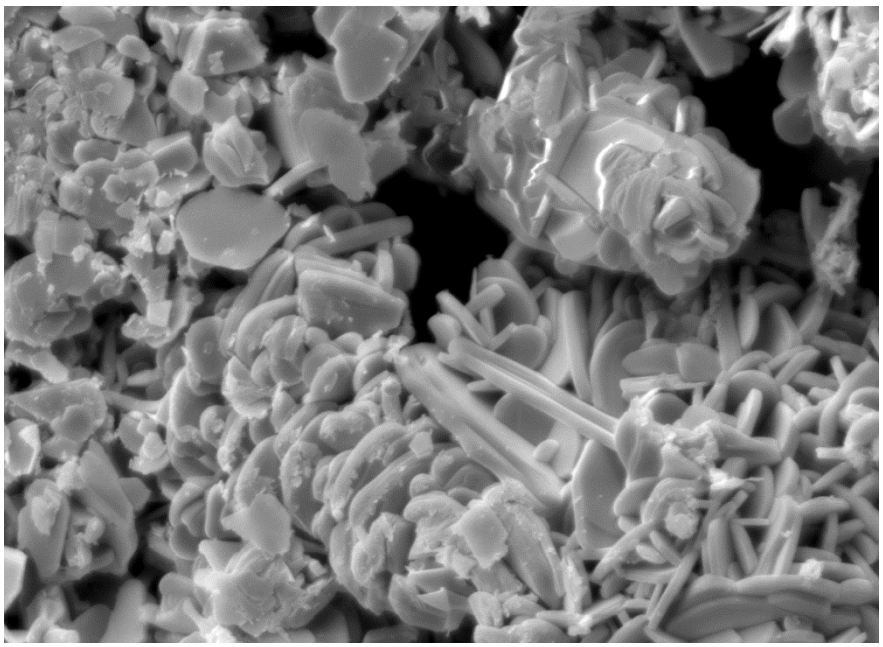

Figure 6.13 A SEM image of $LiSbO_2$ taken with an applied acceleration voltage of 15 kV.

6.8 Thermogravimetric analysis

Small polycrystalline samples (~50mg) were heated in an atmosphere of oxygen (N_2 protective gas) at a heating rate of 10˚C min^{-1} in order to investigate the oxidative characteristics and stability of the system. Unexpectedly high resistance to oxidation was observed up to ~400˚C after which the rate of oxygen absorption accelerated. TGA data (Figure 6.14) showed a large stepwise mass increase initiating at around 480˚C where each point of inflection was accompanied by a large exotherm in the DTA signal at *ca.* 500 and 580˚C, which is characteristic behaviour for the formation of an intermediate phase.

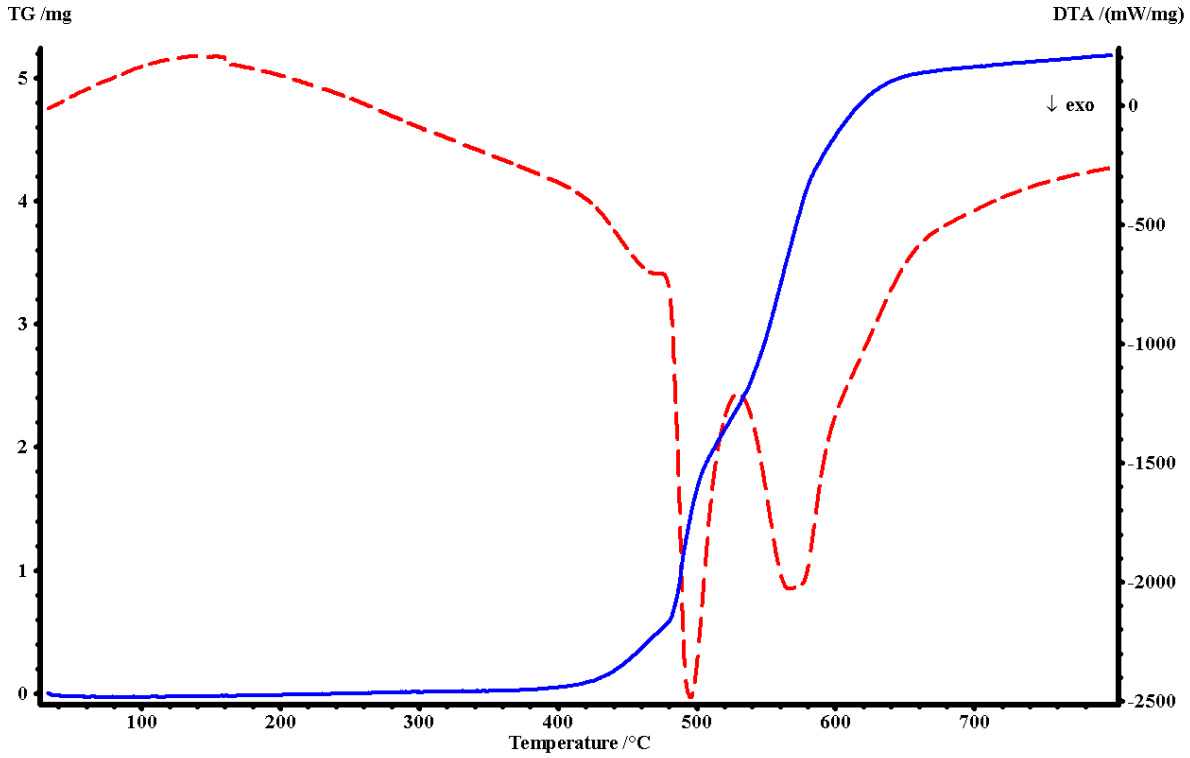

Figure 6.14 The TGA (Blue) and DTA (Red) traces for $LiSbO_2$ heated in an atmosphere of oxygen at a rate of 10˚C/ min up to 800˚C. The TGA axis reflects changes in mass relative to the initial mass represented as 0mg.

Calculations showed the total mass change at 800˚C was due to a 9.6% mass increase to give the composition $LiSbO_3$ and which was verified by XRPD. The expected mass

increase would be 10%. The intermediate plateau region with calculated composition $LiSbO_{2.5}$ appeared to suggest the formation of a mixed Sb^{3+}/Sb^{5+} species. An attempt was made to isolate this compound by heating samples to the appropriate temperature under identical conditions before cooling to room temperature. The XRPD patterns showed only the formation of $LiSbO_3$. The experiment was repeated where the oxygen gas supply was terminated at the maximum applied temperature in an attempt to prevent further reaction; this resulted in the formation of a mixed $LiSbO_2/LiSbO_3$ sample. Two possibilities were implied from this: the first, and most likely reason, was that the high temperature intermediate was metastable. The second was that the mass increase was due to a mixture of $LiSbO_2$ and $LiSbO_3$ in an equimolar ratio 1:1 but this was considered unlikely given the large and sharp DTA exotherm which indicated a phase change at temperatures above those applied.

6.9 Variable temperature XRPD

Evidence was sought to evaluate the possible formation of a metastable intermediate by VT-XRPD. Samples were heated in air at 15˚C increments between 400 and 580˚C, where 30 minute long scans were collected at each step. A gradual transition from $LiSbO_2$ to $LiSbO_3$ was observed (Figure 6.15) with the disappearance of peaks attributed to $LiSbO_2$ and appearance of peaks corresponding to poorly crystalline $LiSbO_3$. The emergence of new peaks, the most intense of which were at 27.5˚ and 28.3˚ 2θ, were attributed to the formation of the intermediate phase due to their absence in both the starting and end materials.

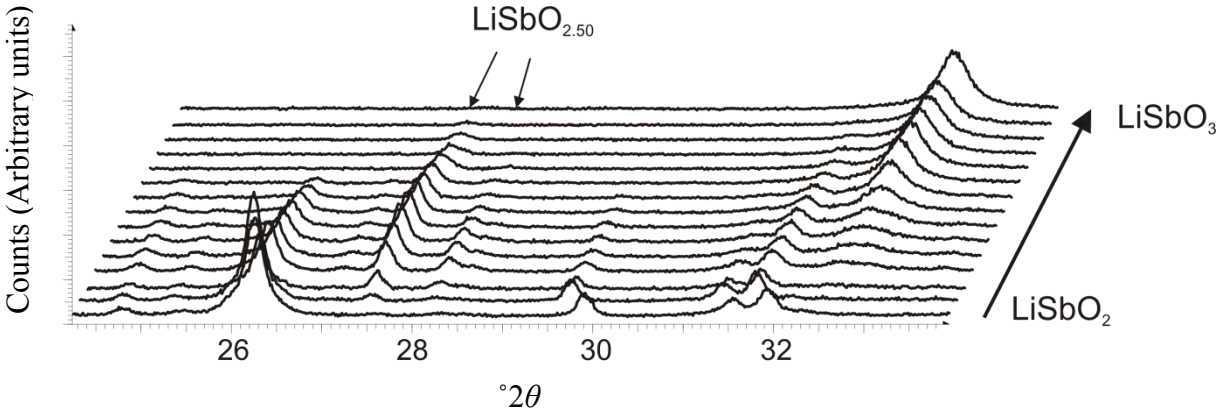

Figure 6.15 VT-XRPD traces for $LiSbO_2$ heated in air; the data have been electronically stripped of the $K\alpha_2$ component. The bottom and top traces correspond to the starting material ($LiSbO_2$) and product ($LiSbO_3$), respectively, at 25˚C. The intermediate plots are, from the bottom, at increasing temperatures between 400-580˚C in regular intervals of 15˚C.

Several strategies were adopted in an attempt to synthesis the intermediate by the solid state reaction. The first was the direct reaction of $LiSbO_2$ with $LiSbO_3$, assuming the ideal composition $LiSbO_{2.5}$, within evacuated fused silica tubes for 24 hrs at 500 and 550˚C on separate samples. The second method involved the equimolar reaction of Li_2CO_3 and Sb_2O_3 at 550˚C for 24 hrs in air (Li_3SbO_4 and $LiSbO_3$ resulted) and the final method was the reaction between Li_2O and Sb_2O_4 at 500˚C for 24 hrs. No method provided any indication as to the formation of an intermediate. This further implied that the intermediate was most likely metastable and thermodynamically unstable at the reaction temperatures required for synthesis. Comparison of the simulated powder pattern (Figure 6.3) obtained by Sauvage *et al* [17] with the intermediate showed a rough coincidence between the most intense peaks at around 27.5 ˚2θ. It therefore seems likely that the obtained intermediate is related to the flux grown sample by Sauvage [17] suggesting an oxidised composition and thereby providing a basis for the discrepancy between the reported structures. It is acknowledged that more peaks of the intermediate must be isolated before firm conclusions can be asserted.

6.10 Conductivity measurements

Lithium ion conductivity was of interest due to the commercial importance of lithium ion batteries and the nature of the layered structure containing planes of Li ions. Conductivity measurements were made on a pellet with a density 82% of the theoretical within the thermally stable region (below 400˚C) at 10˚C steps. Deconvolution of the bulk and grain boundary resistance values was not possible; consequently the total resistance values (i.e. $resistance_{bulk}$ + $resistance_{grain\ boundary}$) were used to calculate the conductivity. Resistance values were determined from the low frequency intercept of the impedance semicircle in the complex plane. The Arrhenius plot (Figure 6.16) showed two regions of differing conductive behaviour. The activation energy below 220˚C was calculated as 0.88 eV and was seen to decrease to 0.74 eV above 220˚C. The structural origins of the slight change in activation energy associated with the conduction mechanism, most likely ion migration, were not visible in the VT-XRPD experiment and more detailed NPD studies are needed for accurate conclusions. The relative magnitude of conductivity when compared with $LiBiO_2$ at 300˚C is comparable (ca. 10^{-6} S cm^{-1}) as is the activation energy (0.72 eV) [7]. However, the conductivity values when compared to the recently published solid electrolyte [21] with a room temperature conductivity of 12 mS cm^{-1} at 27˚C and activation energy of 24 kJ mol^{-1} (0.249 eV) [21] did not make this material of significant interest. This is unsurprising for a highly ordered material with few defects and a large migration distance of around 3 Å between sites.

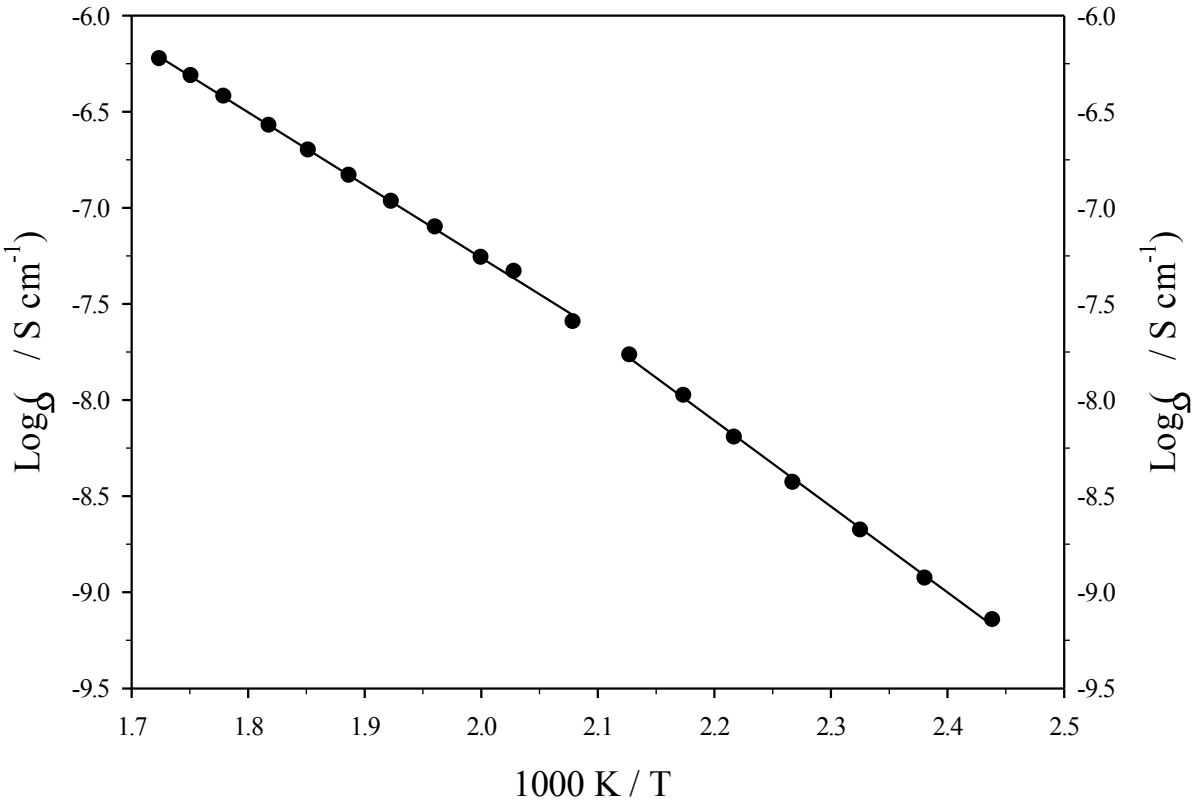

Figure 6.16 An Ahrrenius plot showing how the conductivity of $LiSbO_2$ changes within the temperature range 137-307˚C. Resistance values could not be obtained below 130˚C.

6.11 Synthesis and characterisation of defective $LiSbO_2$

Several hetero-valent elements known to adopt tetrahedral geometry (Zn^{2+}, Ga^{3+}, and Al^{3+}) were used in an attempt to introduce vacancies on the lithium sites and reduce the activation barrier for ion migration. Initially 10% dopant levels were chosen to be appropriate. In all cases a portion of the compound was shown to resemble $LiSbO_2$ in the XRPD patterns (Figure 6.17); however significant impurities, largely Sb_2O_3, suggested a loss of key elements, e.g. Li and the dopant possibly through the formation of more stable impurities which were not identifiable. Despite varying the reaction temperature, heating time and in certain cases adding an excess of Li_2O the outcome did not change. A lower dopant limit of 1% was subsequently investigated for the Ga and Al variants. $Li_{0.97}Ga_{0.01}SbO_2$ showed an almost coincident powder pattern to $LiSbO_2$ however, a single relatively large peak at 28.23 ˚2θ which could be indexed for a monoclinic cell (a = 5.852(2)

Å, b = 17.841(4) Å, c = 3.915(2) Å, β = 107.82(5)˚ FOM = 13.2 for 19 reflections across a 5-70 ˚2θ range) suggested major structural changes. The reliability of the indexing results was questionable and, given the effects seen by adding a 10% dopant, it was decided not to proceed further with the analysis of this composition. $Li_{0.97}Al_{0.01}SbO_2$ showed the same symmetry as $LiSbO_2$, however the characteristic semi-circles representing conduction in the complex impedance plane did not initiate until above 300˚C indicating worsening of conductive behaviour. Given the knowledge that impurities were likely at higher dopant levels and the decline of the conductive behaviour doping of this sample also seemed unlikely to result in the desired outcome.

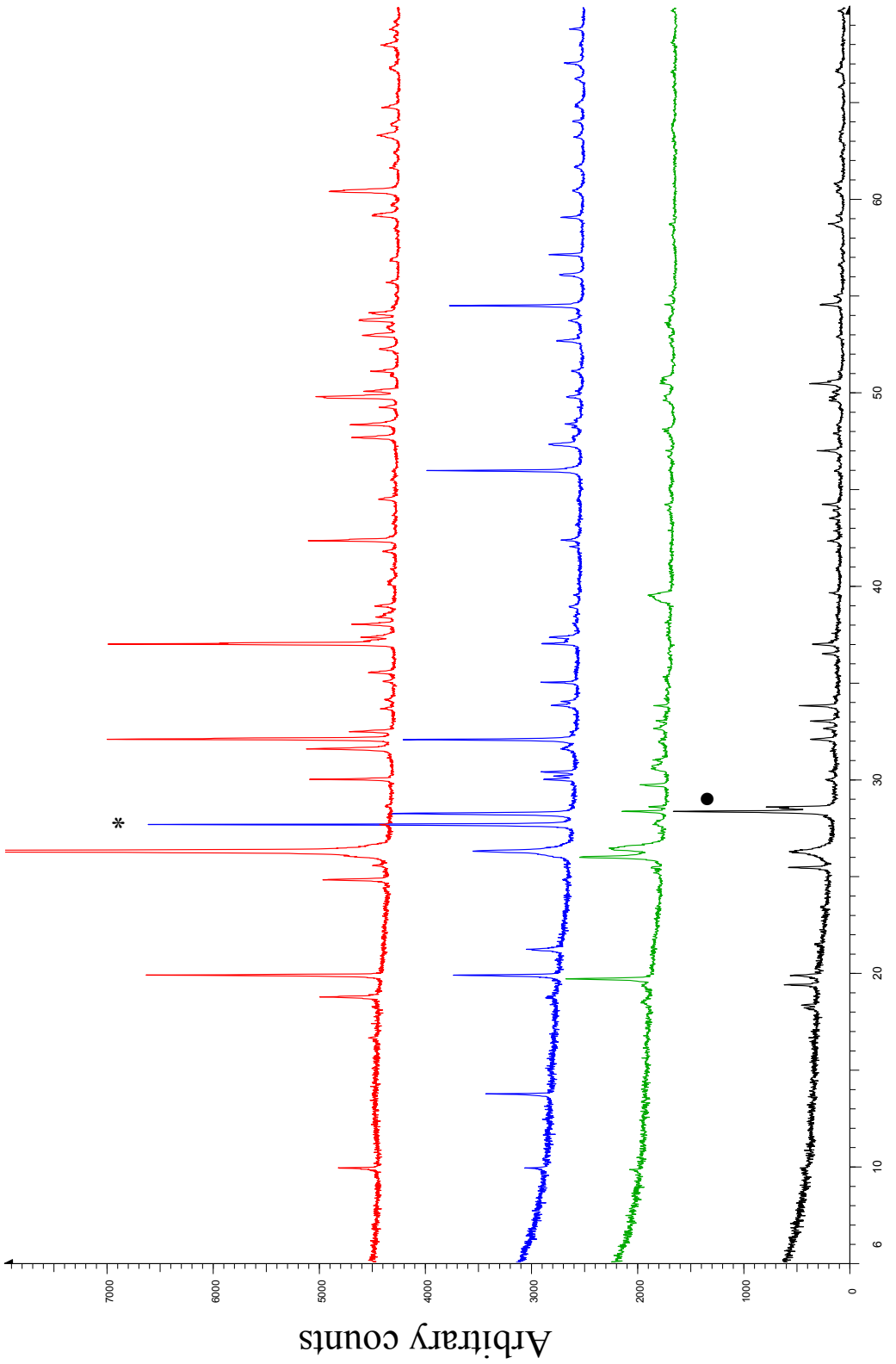

Figure 6.17 A selection of powder patterns showing the typical outcomes of from doping $LiSbO_2$ with Zn, Al, and Ga. $Li_{0.7}Al_{0.1}SbO_2$ (black), $Li_{0.8}Zn_{0.2}SbO_2$ (green), $Li_{0.7}Ga_{0.1}SbO_2$ (blue) and $LiSbO_2$ (NPD sample red) are displayed. Significant differences are observed between $LiSbO_2$ and the doped samples. Significant impurities include: cubic Sb_2O_3 senarmontite main peak (*) and orthorhombic Sb_2O_3 valentianite, main peak (●)

Arbitrary Counts

6.11 Conclusions

A pure sample of $LiSbO_2$ has been synthesised and characterised by NPD to show $P2_1/c$ symmetry (a = 4.8550(3) Å, b = 17.857(1) Å, c = 5.5771(4) Å, β = 90.061(6)˚). It is a layered compound with similar structural features to the previously reported systems of O-I and O-II symmetry; however, it is not isostructural to $LiBiO_2$ as previously believed. Little similarity between the sample presented and that previously reported by Sauvage [17] has been found, however the lack of structural refinement of their previously reported compound [17] cannot rule out the possibility of the flux grown sample to be a lower temperature polymorph or of partially oxidised composition. The material has appreciable resistance to oxidation up to 400˚C with a relatively low ionic conductivity below this temperature when compared with other solid electrolytes. Evidence for a transient intermediate was found, however attempts to isolate this compound of theoretical composition $LiSbO_{2.5}$ were unsuccessful and it is believed to be a metastable intermediate.

6.12 References

[1] C. Girouxmaraine, G. Perez, *Rev. Chim. Miner.* **12** (1975) 427.
[2] C. Hirschle, C. Röhr, *Z. Anorg. Allg. Chem.* **626** (2000) 1305.
[3] C. Hirschle, C. Röhr, *Acta Crystallogr.* **C 54** (1998) 1219.
[4] J. W. Menary, *Acta Crystallogr.* **11** (1958) 742.
[5] F. Emmerling, C. Röhr, *Z. Naturforsch.* **B 58** (2003) 620.
[6] C. Lee, W. T. A. Harrison, *Acta Crystallogr.* **C 60** (2004) m215.
[7] N. H. Andersen, F. W. Poulson, G. Eichinger, Studies in Inorganic Chemistry. *Proceedings of the Second European Conference*, Veldhoven, The Netherlands, 7-9 June 1982, (1982). R. Metselaar, H.J.M. Heijligers, J. Schoonman (Eds), Elsevier Amsterdam,1983; Volume 3
[8] C. Greaves, S. M. A. Katib, *J. Chem. Soc., Chem. Commun.* (1989) 902.
[9] R. Hoppe, B. Schwedes, *Rev. Chim. Miner.* **8** (1971) 583.
[10] B. Schwedes, R. Hoppe, *Z. Anorg. Allg. Chem.* **391** (1972) 313.
[11] E. Keller, C. Röhr, *Z. Krist.* **223** (2008) 431.
[12] B. Schwedes, R. Hoppe, *Z. Anorg. Allg. Chem.* **392** (1972) 97.
[13] N. Zoche, M. Jansen, *Z. Anorg. Allg. Chem.* **624** (1998) 205.
[14] N. Zoche, M. Jansen, *Z. Anorg. Allg. Chem.* **623** (1997) 832.
[15] F. Hulliger, "*Structural Chemistry of Layer-type Phases*", D. Reidel, Dordrecht, Holland (1976).

[16] H.-D. Von Stöver, R. Hoppe, *Z. Anorg. Allg. Chem.* **468** (1980) 137.
[17] J. P. Sauvage, P. Maraine, G. Perez, *C. R. Hebd. Acad. Sci.* **C 282** (1976) 835.
[18] J. Percival, P. R. Slater, *Solid State Commun.* **142** (2007) 355.
[19] B. Dickens, *J. Inorg. Nucl. Chem.* **27** (1965) 1495.
[20] I. D. Brown, D. Altermatt, *Acta Crystallogr.* **B 41** (1985) 244.
[21] N. Kamaya, K. Homma, Y. Yamakawa, M. Hirayama, R. Kanno, M. Yonemura, T. Kamiyama, Y. Kato, S. Hama, K. Kawamoto, A. Mitsui, *Nature Materials* **10** (2011) 682.

Chapter 7

Conclusions and further work

A number of cobalt containing phases related to the schafarzikite system have been synthesised and characterised in this study. The main focus of this thesis has been to isolate new cobalt containing phases and attempt to oxidise the octahedral TM species, modifying physical properties, whilst maintaining the original structure.

Chapter 3 details the synthesis and characterisation of $CoSb_2O_4$, chosen as the basis for this study as it had never been fully characterised previously. NPD studies at 300 and 4 K showed that the nuclear structure was consistent with the previously synthesised MSb_2O_4 phases (where M = Mn, Fe, Ni and Zn) and that no distortion from $P4_2/mbc$ symmetry was seen. The magnetic structure was determined as being of C- type which displays a collinear spin alignment of FM ordering within a chain (along z) and AFM ordering in the basal ab plane for the first time. Previous magnetic structure determinations of $MnSb_2O_4$ [1] and $FeSb_2O_4$ [2] showed both to possess dominant A- type ordering orientated along x. The lattice parameters: a = 8.49340(9) Å, c = 5.92387(8) Å (at 300 K) showed a contraction of a and c on cooling to 4 K (a = 8.4809(1) Å and c = 5.92092(9) Å).

Origins of the C- type magnetic structure were rationalised as dominance of the 90˚ superexchange between adjacent intrachain TM sites. A larger TM-TM distance exists in $MnSb_2O_4$ when compared with $CoSb_2O_4$. However, the difference in magnetic structure is probably related to the smaller ionic radius of Co^{2+} when compared with Mn^{2+} which inhibits/reduces orbital overlap, and hence direct exchange, leading to an increasing dominance of the 90˚ superexchange which should be enhanced by increased covalence.

Substitution of Pb^{2+} for Sb^{3+} in the $CoSb_{1.50}Pb_{0.50}O_4$ phase has shown that both Co^{2+} and Sb^{3+} are oxidised which is probably due to the high oxidising power of Co^{3+}. As a result, some Co is substituted by Sb^{5+} within the chains of octahedra. A similar result was seen in the mixed $(Mn_{1-x}Sb_x)(Sb_{1-y}Pb_y)_2O_4$ phases [3]. The oxidation of a small amount of Co^{2+} to Co^{3+} was later supported by the Mössbauer spectrum of $Co_{0.50}Fe_{0.50}Sb_{1.50}Pb_{0.50}O_4$ which suggested the oxidation of about 10% Co^{2+} to Co^{3+}.

Thermogravimetric analysis of $CoSb_2O_4$ proved highly useful in the determination of oxidised products in later chapters, e.g. the $Co_{1-x}Fe_xSb_2O_4$ phases, as it showed that upon heating the sample in an atmosphere of O_2 no intermediate phase was formed. The high temperature products ($CoSb_2O_6$) showed that, in this phase, only Sb was oxidised by this mechanism.

Magnetic susceptibility measurements showed a highly unusual negative susceptibility in $CoSb_2O_4$ which is believed to be related to the high coercivity of the ferromagnetic component of the canted magnetic system which interacted with trapped flux within the SQUID at zero applied field. The calculated moment from the paramagnetic region was consistent with a large orbital contribution (5.06 μ_B mol^{-1}).

Chapter 4 detailed the successful formation of mixed $Co_{1-x}Fe_xSb_2O_4$ phases (x = 0.25, 0.50, 0.75) which also maintained $P4_2/mbc$ symmetry in the range 300-1.5 K. The lattice parameters obtained (a = 8.5728(2)-8.5265(1) Å, c = 5.92675(9)-5.9170(1) Å) at 300 K showed that the a parameter varied between those of $FeSb_2O_4$ (a = 8.61574(9) Å, c = 5.92069(8) Å) [2] and $CoSb_2O_4$ (a = 8.49340(9) Å, c = 5.92387(8) Å), Chapter 3. At T < 5 K a transition from a dominant A_x mode to C_z mode was evidenced for the first time by NPD. $Co_{0.25}Fe_{0.75}Sb_2O_4$ and $Co_{0.50}Fe_{0.50}Sb_2O_4$ showed non-collinear spin alignment with mixtures of

A_x and C_z modes; however, $Co_{0.75}Fe_{0.25}Sb_2O_4$ was shown to display a C_z mode of ordering only. The lattice parameters showed that the *c* parameter for $Co_{0.75}Fe_{0.25}Sb_2O_4$ at 2 K (*c* = 5.92236(8) Å) was larger than that of $CoSb_2O_4$ at 4 K (*c* = 5.92093(9) Å) whilst those which displayed A_x type ordering had smaller *c* parameters. This supported the findings in Chapter 3 that a delicate balance is struck between the TM-TM separation distance and ionic radii in which small changes can significantly enhance the dominance of the 90˚ superexchange over direct exchange, generating FM ordering within a chain.

TGA data in conjunction with XRPD presented the isolation of one stable intermediate, of the form $Co_{1-x}Fe_xSb_2O_{4+x}$, for each $Co_{1-x}Fe_xSb_2O_4$ phase. Such oxygen-rich phases have never before been observed in schafarzikite related phases or characterised. Isolation of the intermediates was linked, crucially, to the presence of Fe; this is due to the absence of any intermediates in the TGA of $CoSb_2O_4$ which suggests that Fe^{2+} is oxidised to Fe^{3+} in the process. The amount of excess oxygen a given phase could retain was shown to increase with iron content at the expense of sample degradation. Susceptibility data did not show any significant increase in the magnetic moments upon oxidation of these phases but this was unsurprising given that there was always a large orbital contribution to the moment. The excess oxygen is believed to be consistent with a peroxide species based upon mass increases and the amount of Fe^{2+} available for oxidation. It should be noted that Co oxidation is not ruled out entirely for these phases, but Fe is considerably more likely to oxidise.

Raman spectroscopy attempted to clearly identify the interstitial oxygen species and its locality. In all samples the Raman spectra lost considerable resolution upon oxidation. A broadening of the very intense peak at around 672 cm^{-1}, associated with a Sb-O_{eq} stretching vibration [4] was seen. Furthermore a visible shoulder to this peak, at around 750 cm^{-1} in $Co_{0.75}Fe_{0.25}Sb_2O_{4+x}$, is evidence to support an interstitial peroxide species (consistent with the

O-O stretching frequency, dependent on species environment [5-6]) which is attached to the trigonal pyramidal Sb^{3+} site.

Chapter 5 builds upon the findings of Chapters 3 and 4 to synthesise, for the first time, a series of mixed A and B site phases ($Co_{1-x}Fe_xSb_{2-y}Pb_yO_4$ where: x = 0.25, 0.50, 0.75 and y = 0.10-0.75). Most were found to have $P4_2/mbc$ symmetry but a small orthorhombic distortion was deduced for $Co_{0.25}Fe_{0.75}Sb_{2-x}Pb_xO_4$ (x = 0.10-0.30), as indicated by a shoulder on the (200) peak. This would make an excellent study for synchrotron XRPD with a resolution which should be easily capable of resolving any orthorhombic distortions present. The distortion was believed to be similar to that seen in Pb_3O_4, [7-8] below 170 K, and so these phases were refined in *Pbam*. XANES experiments could also be used to more conclusively show the oxidation states of the TMs, in conjunction with X-ray photoelectron studies, within the various phases reported.

Nuclear structures at 1.5 K again showed a range of values for the *c* parameter (5.9581(1)-6.0379(1) Å) whilst all magnetic structures were determined as being consistent with dominant C- type ordering. This further supported previous arguments (*Section* 3.7) as to the importance of considering orbital contraction as well as TM-TM distance when considering spin alignment and the exchange processes generating magnetic ordering within these compounds. Mössbauer data for $Co_{0.50}Fe_{0.50}Sb_{1.50}Pb_{0.50}O_4$ supported the assertion that it is possible to oxidise a small amount of Co^{2+} to Co^{3+}. With a large range of newly characterised phases which accurately pinpoint the transition between dominant A- and C-type ordering it would be of fundamental interest to perform detailed calculations to ascertain the exchange constants within these samples. The NPD magnetic structures could be investigated further to assign magnetic symmetry to the systems reported.

A consistent problem with Fe containing phases is the presence of magnetite co-formed upon synthesis. Although reheating usually removes this, the tendency for these phases to form impurities upon reheating prevents such heat treatments. This could possibly be overcome by reheating in the region 500-600˚C for longer periods of time and ball milling reagent mixture to achieve smaller particles. As a direct consequence the magnetic moment of most phases could not be calculated. $Co_{0.75}Fe_{0.25}Sb_{1.75}Pb_{0.25}O_4$ however, demonstrated a large effective moment of 6.21(2) μ_B mol^{-1} and is most likely representative of oxidation of the TM species inclusive of a large orbital component to the moment. The ferromagnetic upturn before T_N in many of the reported samples, e.g. $Co_{0.50}Fe_{0.50}Sb_{1.50}Pb_{0.50}O_4$, and equally unusual negative susceptibility which appears not to be an isolated incidence, e.g. $Co_{0.25}Fe_{0.75}Sb_{1.80}Pb_{0.20}O_4$, would make an highly interesting fundamental study.

Thermogravimetric analysis again returned some of the most interesting results for these compounds. It showed that in the case of $Co_{0.25}Fe_{0.75}Sb_{1.75}Pb_{0.25}O_4$ two stable intermediate phases can be formed. This is the first time this has ever been seen. Furthermore the mass increases appeared to suggest total oxidation of all TM species at temperatures of around 590˚C, inferred by the calculated oxygen excess. This suggested that a complex balance between composition and a reduction of the redox potential (primarily for Co^{3+}) could be occurring and/or the excess oxygen species was modified once again. Raman spectroscopy was again employed to provide empirical clues as to the nature of the species. A broadening of the intense Sb-O stretching peak (at around 675 cm^{-1}) indicted some peroxide was still present, but a broad shallow peak between 1100-1500cm^{-1} could be indicative of some superoxide species. This would again relate the excess amount of oxygen to primarily oxidising Fe^{2+} to Fe^{3+} concordant with previous findings. The formation of two plateaus was observed in some phases but not as well defined as in $Co_{0.25}Fe_{0.75}Sb_{1.75}Pb_{0.25}O_4$ which has

shown signs of a distortion to lower symmetry at room temperature. It is uncertain if the definition of the second plateau is the result of the distortion or largely dependent on the composition at this point and will require further investigation. The large range of oxidised products is of considerable fundamental interest and has the potential for applications. These phases require detailed characterisation by: NPD, EXAFS, ^{17}O NMR, and both electrical and ionic conductivity testing. This is in order to better understand the oxygen species present, the mechanism for incorporation, its location and mobility.

Chapter 6 can be considered a separate topic from the main body of work. The synthesis and characterisation of the novel compound $LiSbO_2$ is described for the first time. The compound is shown to be consistent with $P2_1/c$ symmetry rather than *Ibam* as previously believed. $LiSbO_2$ has a layered structure (a = 4.8550(3) Å, b = 17.857(1) Å, c = 5.5771(4) Å, β = 90.061(6)˚) formed from discrete chains of corner lined SbO_3 trigonal pyramidal units. The chains are coordinated by tetrahedral Li^+ ions and Sb^{3+} is presumed to project its lone pair into the interlayer region. Attempts to dope the phase with various heterovalent elements (e.g. Al^{3+}, Ga^{3+} and Zn^{2+}) were unsuccessful. However, $ZnAs_2O_4$ (leiteite; a = 4.542(1) Å, b = 5.022(1) Å, c = 17.597(5) Å, β = 90.81(3)˚) is reported to adopt a structure very similar to that of $LiSbO_2$ with tetrahedral Zn^{2+} and is believed to form at very low temperatures, around 40˚C [9]. The lowest synthesis temperature used in this chapter was 500˚C and so it may be possible to synthesise the desired compound at much lower temperatures. Similarly $ZnAs_2O_4$ could be a low temperature polymorph of schafarzikite. Measurements of electrical conductivity for $LiSbO_2$ showed a relatively high activation energy of 0.88 eV below 220˚C which compares poorly with $Li_{10}GeP_2S_{12}$ (0.249 eV at 27˚C) [10]. There is no mention of $LiAsO_2$ in the literature and this could prove to have a similar structure to $LiSbO_2$ which

would then enable doping of the structure with the possibility of enhancing electrical conductivity.

TGA indicated the formation of an intermediate phase of composition $LiSbO_{2.5}$ in the temperature region 480-580˚C. VT-XRPD isolated new peaks within the same temperature region indicating the formation of a new phase but this could not be isolated as a stable intermediate nor was it possible to synthesise under the conditions used. The schafarzikite related arsenites of composition (MAs_2O_4) are an area in which extensive research is yet to be undertaken.

A wide variety of manipulations and characterisations of new ABO_2 (where A = alkali metal, B = group 15 element) phases are possible e.g. the synthesis of $LiAsO_2$ whilst more accurate structural descriptions of $LiBiO_2$ are yet to be determined.

7.1 References

[1] H. Fjellvåg, A. Kjekshus, *Acta Chem. Scand.* **A 39** (1985) 389.
[2] M. J. Whitaker, R. D. Bayliss, F. J. Berry, C. Greaves, *J. Mater. Chem.* **21** (2011) 14523.
[3] A. M. Abakumov, M. G. Rozova, E. V. Antipov, J. Hadermann, G. Van Tendeloo, M. V. Lobanov, M. Greenblatt, M. Croft, E. V. Tsiper, A. Llobet, K. A. Lokshin, Y. S. Zhao, *Chem. Mater.* **17** (2005) 1123.
[4] S. Bahfenne, L. Rintoul, R. L. Frost, *Am. Miner.* **96** (2011) 888.
[5] J. Oxley, J. Smith, J. Brady, F. Dubnikova, R. Kosloff, L. Zeiri, Y. Zeiri, *Appl. Spectrosc.* **62** (2008) 906.
[6] H. H. Eysel, S. Thym, *Z. Anorg. Allg. Chem.* **411** (1975) 97.
[7] J. R. Gavarri, G. Calvarin, D. Weigel, *J. Solid State Chem.* **14** (1975) 91.
[8] J. R. Gavarri, A. W. Hewat, *J. Solid State Chem.* **23** (1978) 327.
[9] S. Ghose, P. K. Sengupta, E. O. Schlemper, *Am. Miner.* **72** (1987) 629.
[10] N. Kamaya, K. Homma, Y. Yamakawa, M. Hirayama, R. Kanno, M. Yonemura, T. Kamiyama, Y. Kato, S. Hama, K. Kawamoto, A. Mitsui, *Nat. Mater.* **10** (2011) 682.

Appendix 1.1: Calibrated VT-XRPD temperatures for $CoSb_2O_4$

Applied temperature (˚C)	Calibrated temperature (˚C); Error = ±5˚C
30	35.2
50	57.3
100	112.1
150	166.1
200	219.4
250	272.1
300	324.0
350	375.2
400	425.7
420	445.7
440	465.6
460	485.4
480	505.1

A table of the calibrated temperatures the $CoSb_2O_4$ sample was exposed to during heating in the VT-XRD experiments.

Appendix 2.1: HI NPD Rietveld refinements of $Co_{0.50}Fe_{0.50}Sb_2O_4$ at 300 K

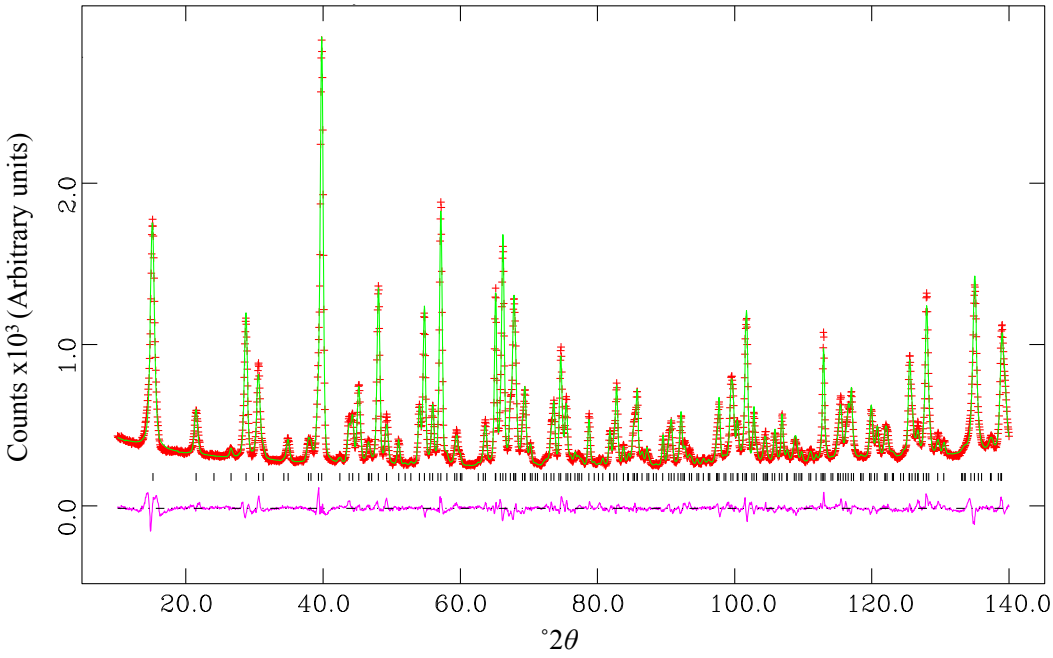

The fit obtained from the refinement of $Co_{0.50}Fe_{0.50}Sb_2O_4$ NPD data at 300 K using profile function 2 for HI data set. The (+) observed (|) calculated and (|) difference profiles are shown. The black tick marks represent the nuclear phase in $P4_2/mbc$.

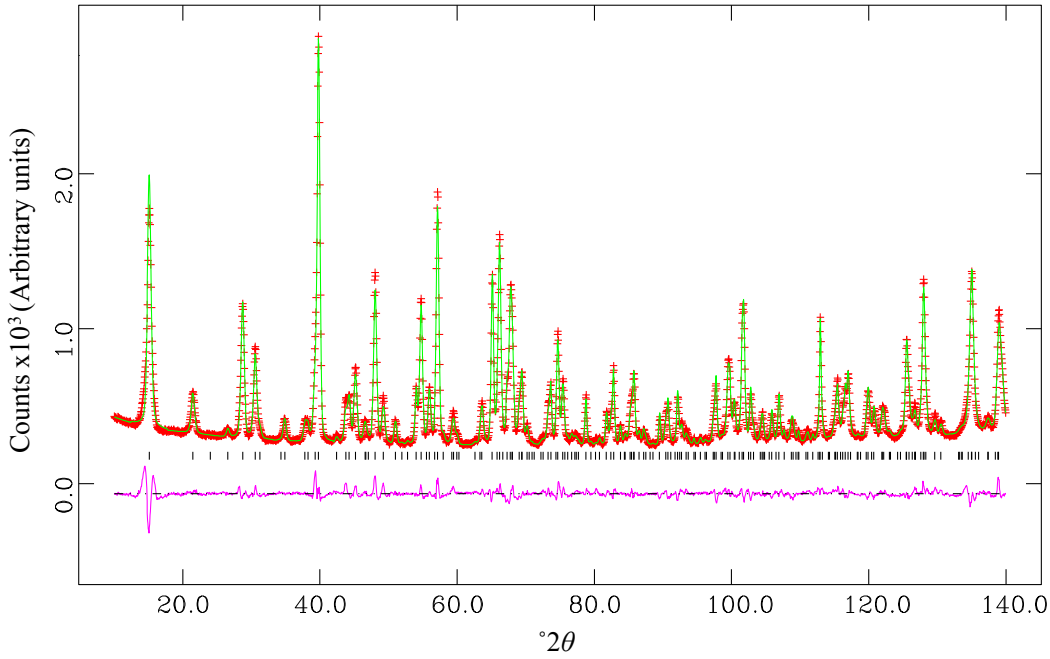

The refinement of $Co_{0.50}Fe_{0.50}Sb_2O_4$ NPD data at 300 K using profile Fn3 based upon HI data. The (+) observed (|) calculated and (|) difference profiles are shown. The black tick marks represent the nuclear phase in $P4_2/mbc$.

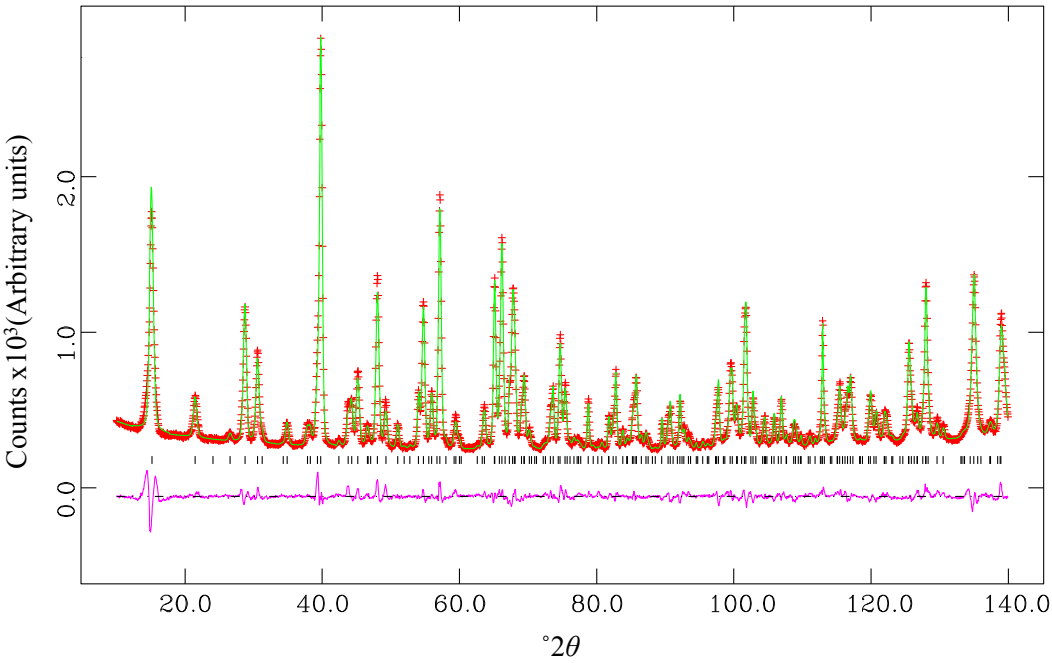

The fit obtained from the Rietveld refinement of $Co_{0.50}Fe_{0.50}Sb_2O_4$ at 300 K using profile Function 4. The (+) observed (|) calculated and (|) difference profiles are as indicated. The black tick marks represent the nuclear phase in $P4_2/mbc$.

Appendix 3.1: XRPD refinements of the $Co_{1-x}Fe_xSb_{2-y}Pb_yO_4$ phases

The $Co_{0.25}Fe_{0.75}Sb_{2-x}Pb_xO_4$ phases (x = 0.10 - 0.75)

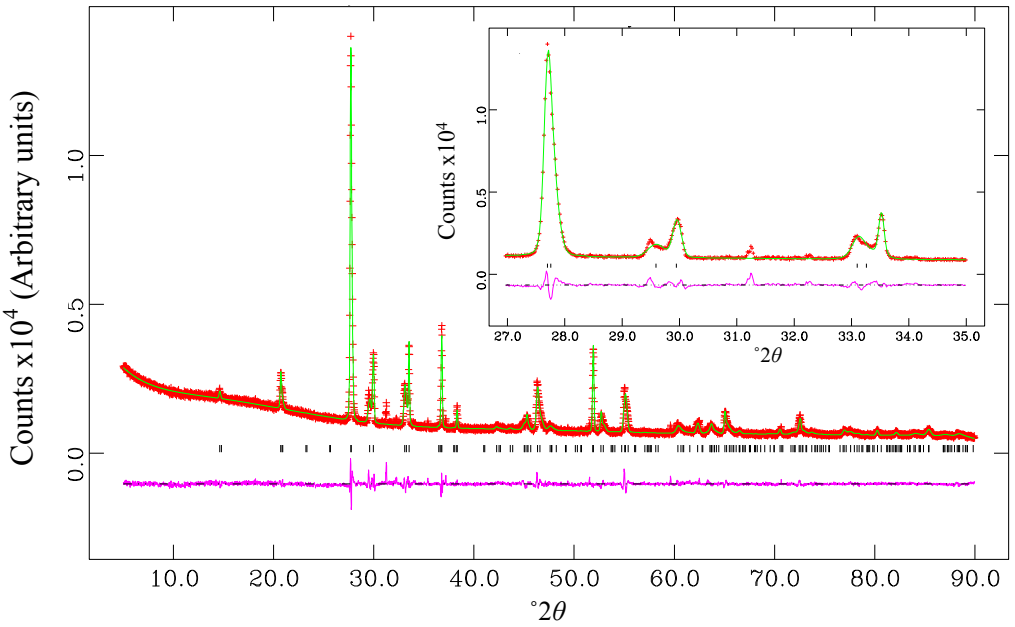

The final fit of $Co_{0.25}Fe_{0.75}Sb_{1.90}Pb_{0.10}O_4$ obtained from the Rietveld refinement of XRPD data in *Pbam*. The (+) observed (|) calculated and (|) difference profiles are as indicated whilst the tick marks (|) represent the nuclear structure of $Co_{0.25}Fe_{0.75}Sb_{1.90}Pb_{0.10}O_4$. Inset shows the fit of the region 27-35 °2*θ*.

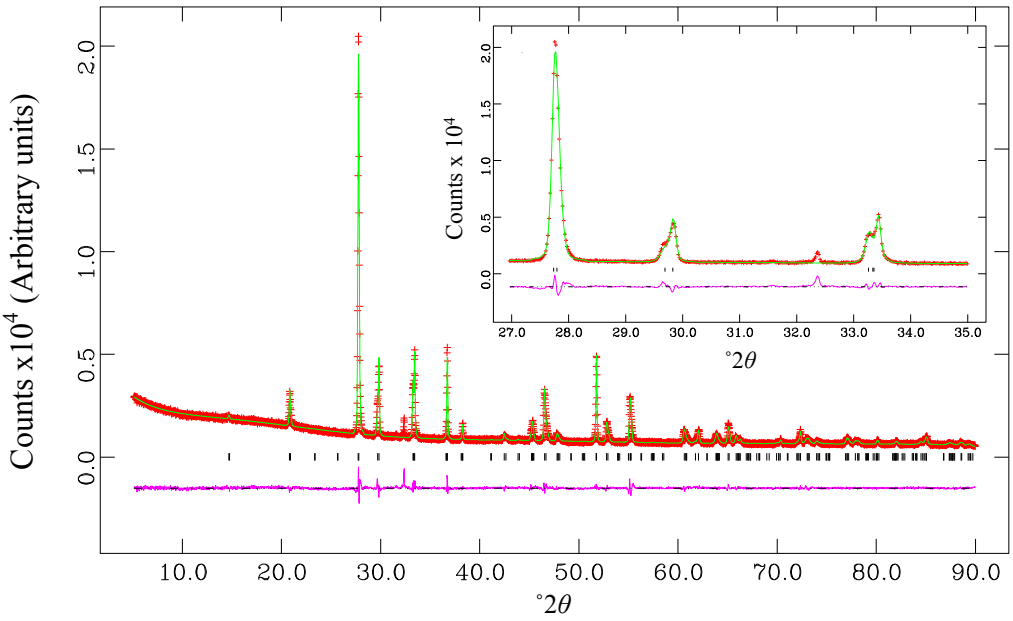

The final fit of $Co_{0.25}Fe_{0.75}Sb_{1.75}Pb_{0.25}O_4$ obtained from the Rietveld refinement of XRPD data in *Pbam*. The (+) observed (|) calculated and (|) difference profiles are as indicated whilst the tick marks (|) represent the nuclear structure of $Co_{0.25}Fe_{0.75}Sb_{1.75}Pb_{0.25}O_4$. Inset shows the fit of the region 27-35 °2*θ*.

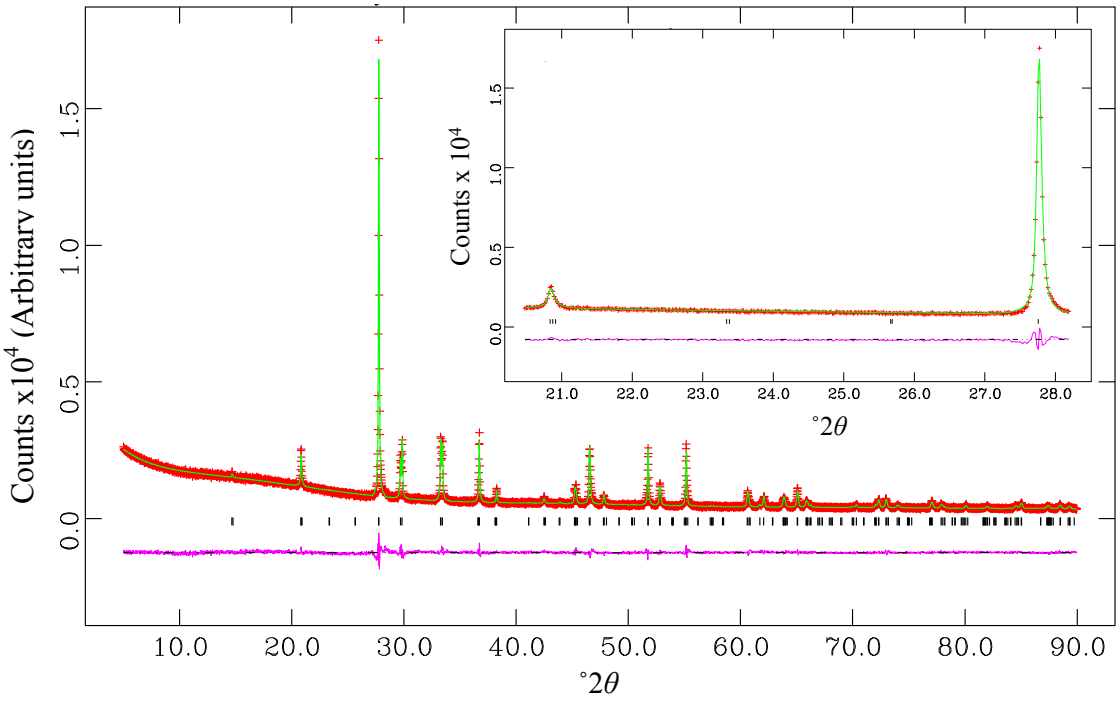

The final fit of $Co_{0.25}Fe_{0.75}Sb_{1.70}Pb_{0.30}O_4$ obtained from the Rietveld refinement of XRPD data in *Pbam*. The (+) observed (|) calculated and (|) difference profiles are as indicated whilst the tick marks (|) represent the nuclear structure of $Co_{0.25}Fe_{0.75}Sb_{1.70}Pb_{0.30}O_4$. Inset shows the fit of the region 20.5-28.5 °2*θ*.

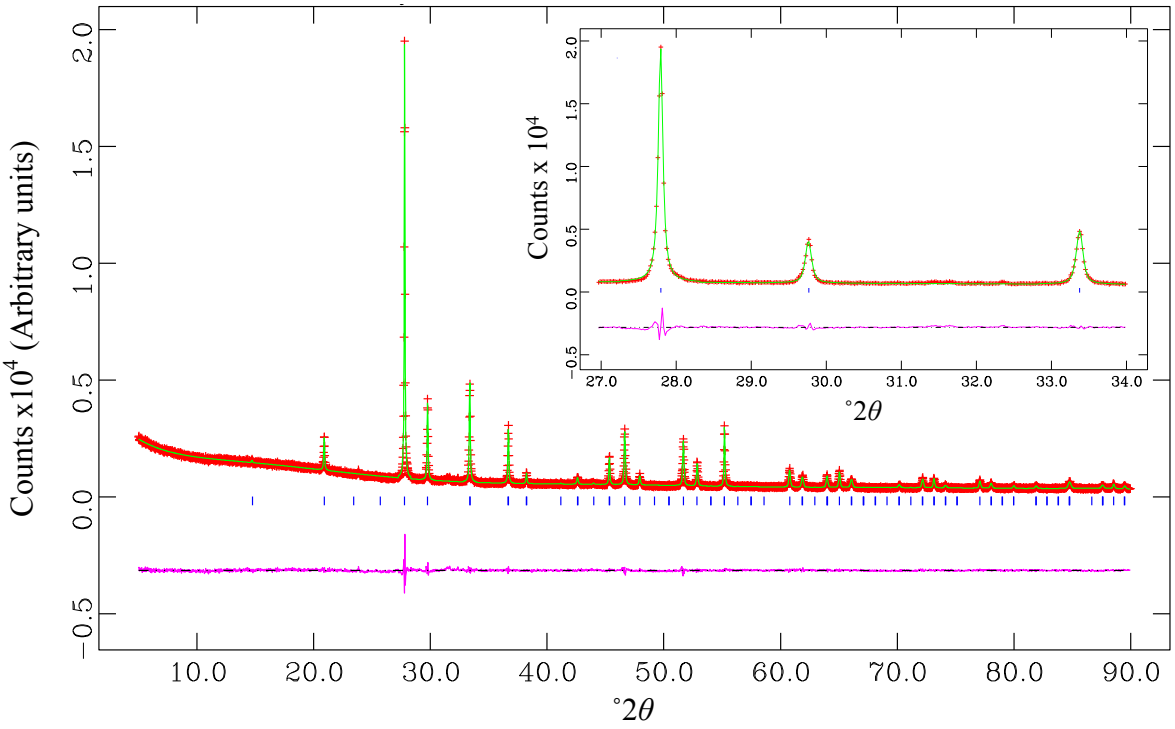

The final fit of $Co_{0.25}Fe_{0.75}Sb_{1.60}Pb_{0.40}O_4$ obtained from the Rietveld refinement of XRPD data in $P4_2/mbc$. The (+) observed (|) calculated and (|) difference profiles are as indicated whilst the tick marks (|) represent the nuclear structure of $Co_{0.25}Fe_{0.75}Sb_{1.60}Pb_{0.40}O_4$. Inset shows the fit of the region 27-34 °2*θ*.

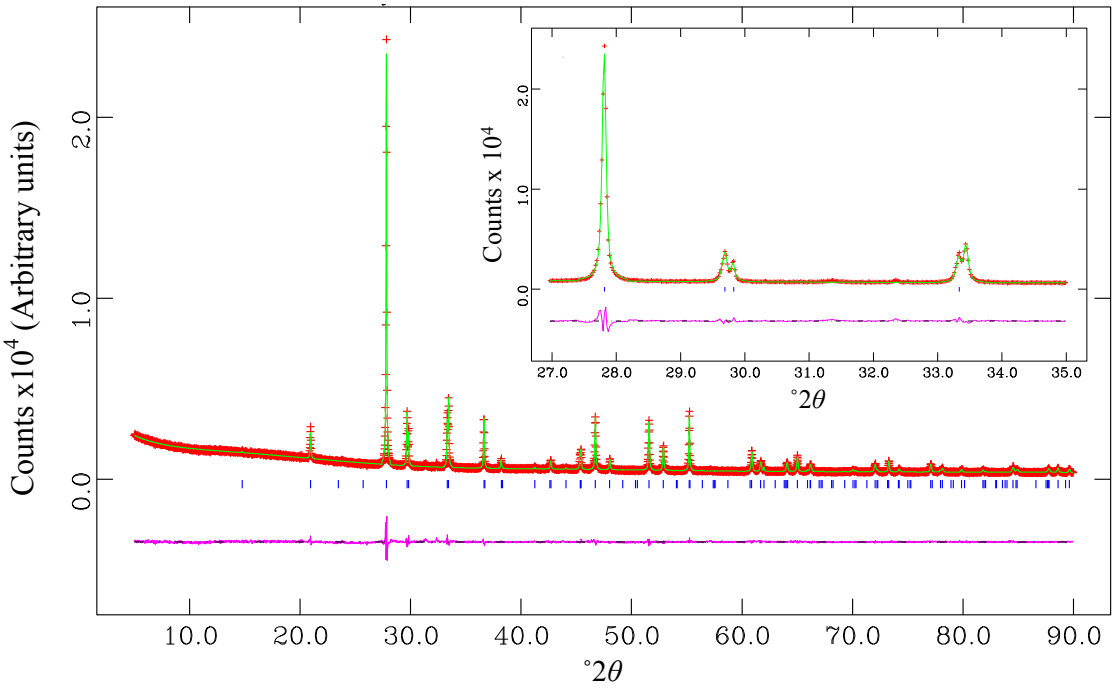

The final fit of $Co_{0.25}Fe_{0.75}Sb_{1.50}Pb_{0.50}O_4$ obtained from the Rietveld refinement of XRPD data in $P4_2/mbc$. The (+) observed (|) calculated and (|) difference profiles are as indicated whilst the tick marks (|) represent the nuclear structure of $Co_{0.25}Fe_{0.75}Sb_{1.50}Pb_{0.50}O_4$. Inset shows the fit of the region 27-35 °2θ.

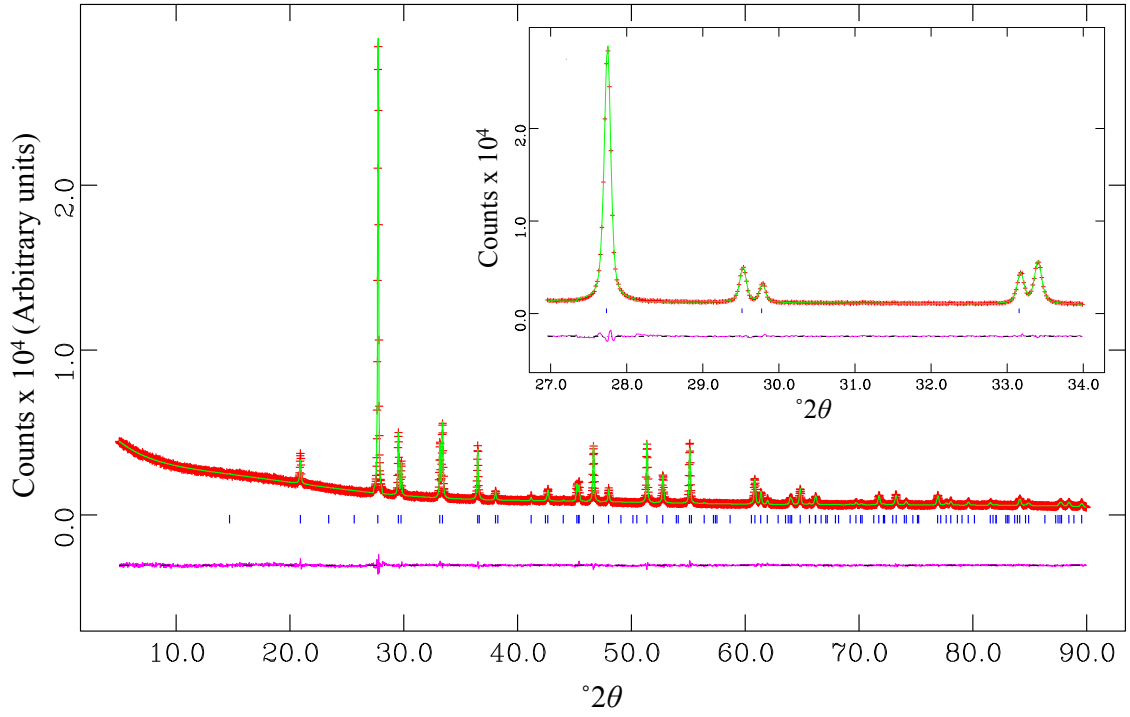

The final fit of $Co_{0.25}Fe_{0.75}Sb_{1.40}Pb_{0.60}O_4$ obtained from the Rietveld refinement of XRPD data in $P4_2/mbc$. The (+) observed (|) calculated and (|) difference profiles are as indicated whilst the tick marks (|) represent the nuclear structure of $Co_{0.25}Fe_{0.75}Sb_{1.40}Pb_{0.60}O_4$. Inset shows the fit of the region 27-34°2θ.

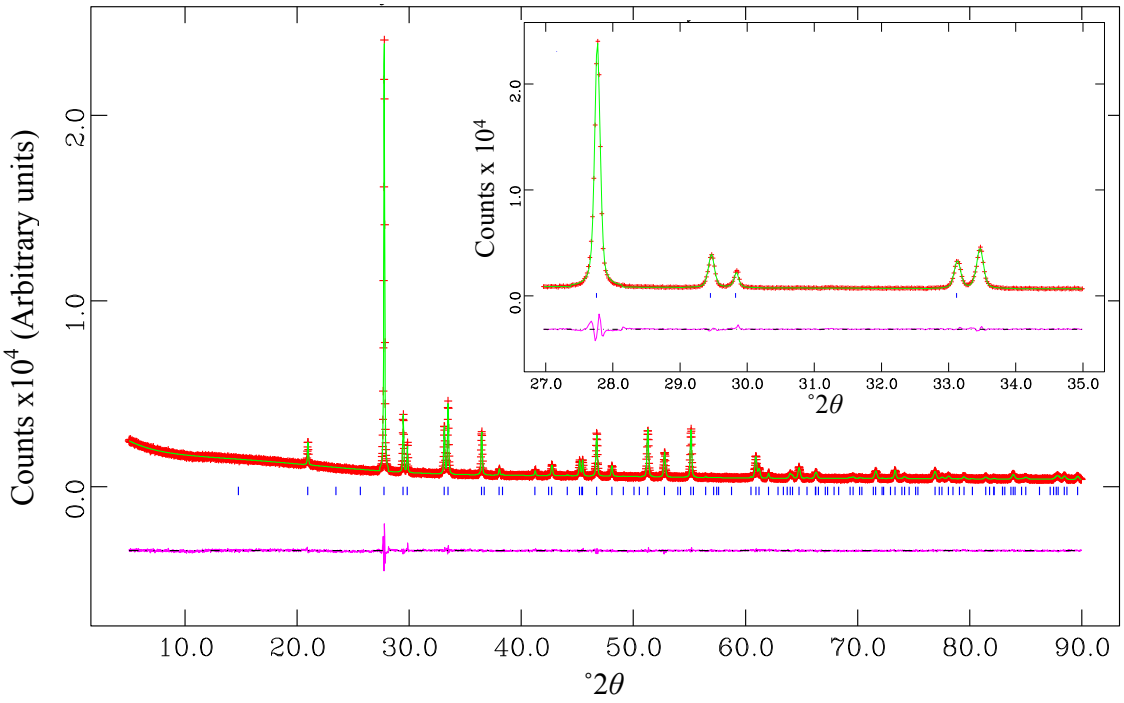

The final fit of $Co_{0.25}Fe_{0.75}Sb_{1.25}Pb_{0.75}O_4$ obtained from the Rietveld refinement of XRPD data in $P4_2/mbc$. The (+) observed (|) calculated and (|) difference profiles are as indicated whilst the tick marks (|) represent the nuclear structure of $Co_{0.25}Fe_{0.75}Sb_{1.75}Pb_{0.25}O_4$. Inset shows the fit of the region 27-35 °2θ.

The final fits of the $Co_{0.50}Fe_{0.50}Sb_{2-x}Pb_2O_4$ compounds based on XRPD data refinements.

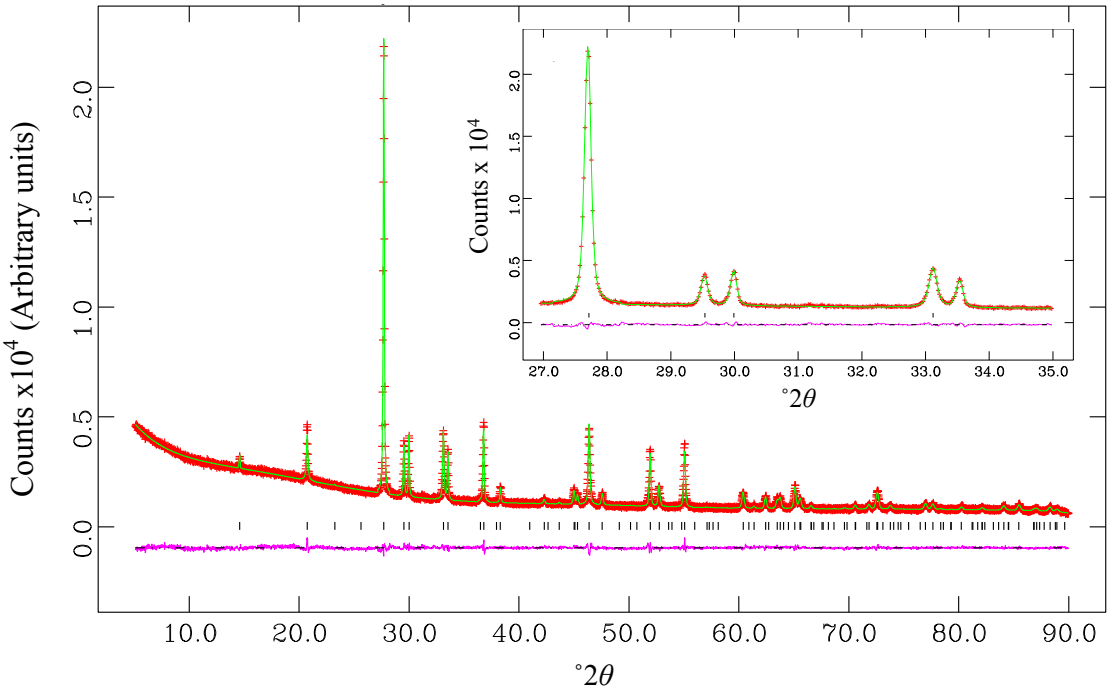

The final fit of $Co_{0.50}Fe_{0.50}Sb_{1.90}Pb_{0.10}O_4$ obtained from the Rietveld refinement of XRPD data in $P4_2/mbc$. The (+) observed (|) calculated and (|) difference profiles are as indicated whilst the tick marks (|) represent the nuclear structure of $Co_{0.50}Fe_{0.50}Sb_{1.90}Pb_{0.10}O_4$. Inset shows the fit of the region 27-35 ˚2θ.

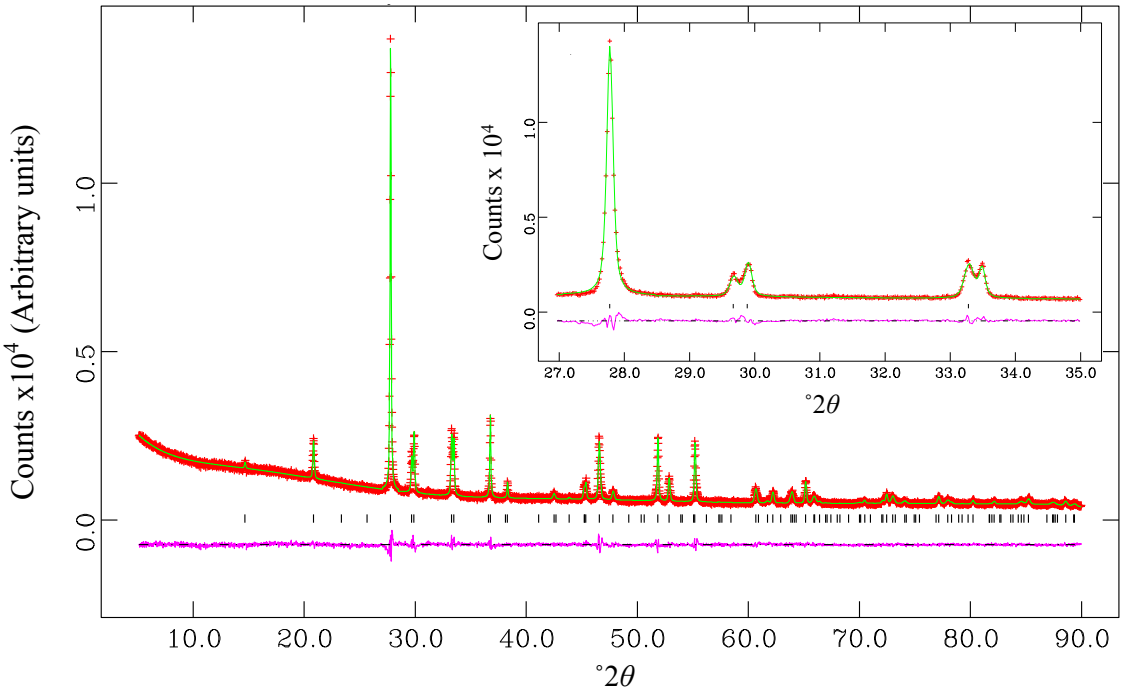

The final fit of $Co_{0.50}Fe_{0.50}Sb_{1.80}Pb_{0.20}O_4$ obtained from the Rietveld refinement of XRPD data in $P4_2/mbc$. The (+) observed (|) calculated and (|) difference profiles are as indicated whilst the tick marks (|) represent the nuclear structure of $Co_{0.50}Fe_{0.50}Sb_{1.80}Pb_{0.20}O_4$. Inset shows the fit of the region 27-35 ˚2θ.

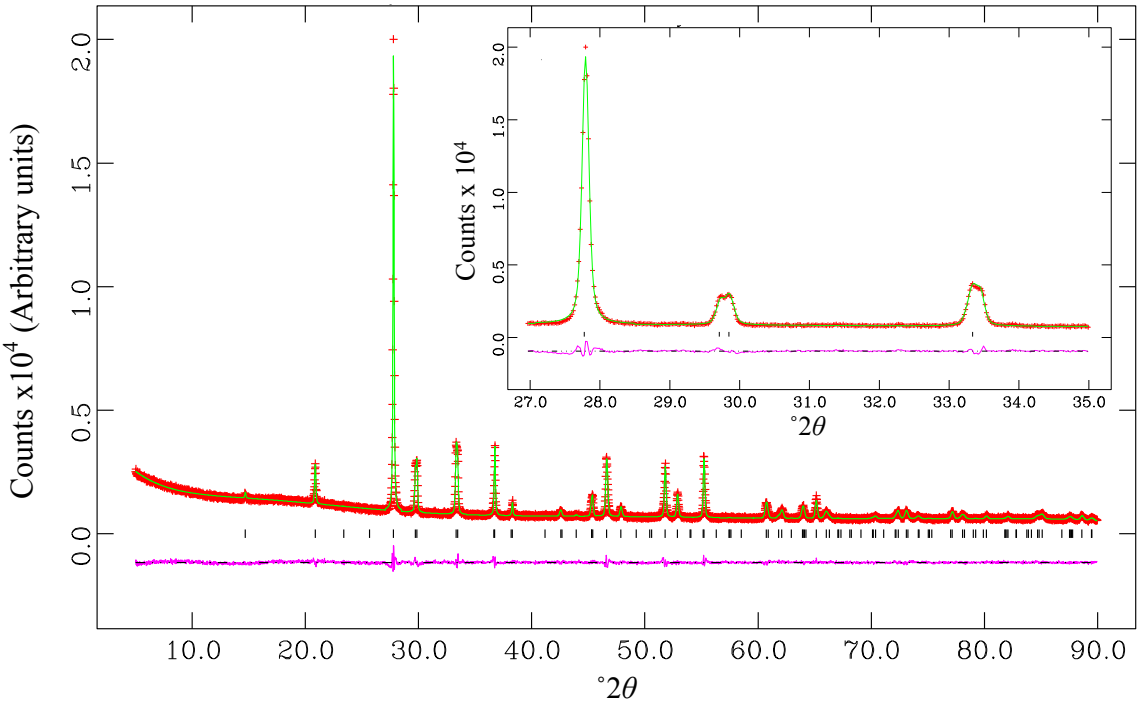

The final fit of $Co_{0.50}Fe_{0.50}Sb_{1.75}Pb_{0.25}O_4$ obtained from the Rietveld refinement of XRPD data in $P4_2/mbc$. The (+) observed (|) calculated and (|) difference profiles are as indicated whilst the tick marks (|) represent the nuclear structure of $Co_{0.50}Fe_{0.50}Sb_{1.75}Pb_{0.25}O_4$. Inset shows the fit of the region 27-35 °2θ.

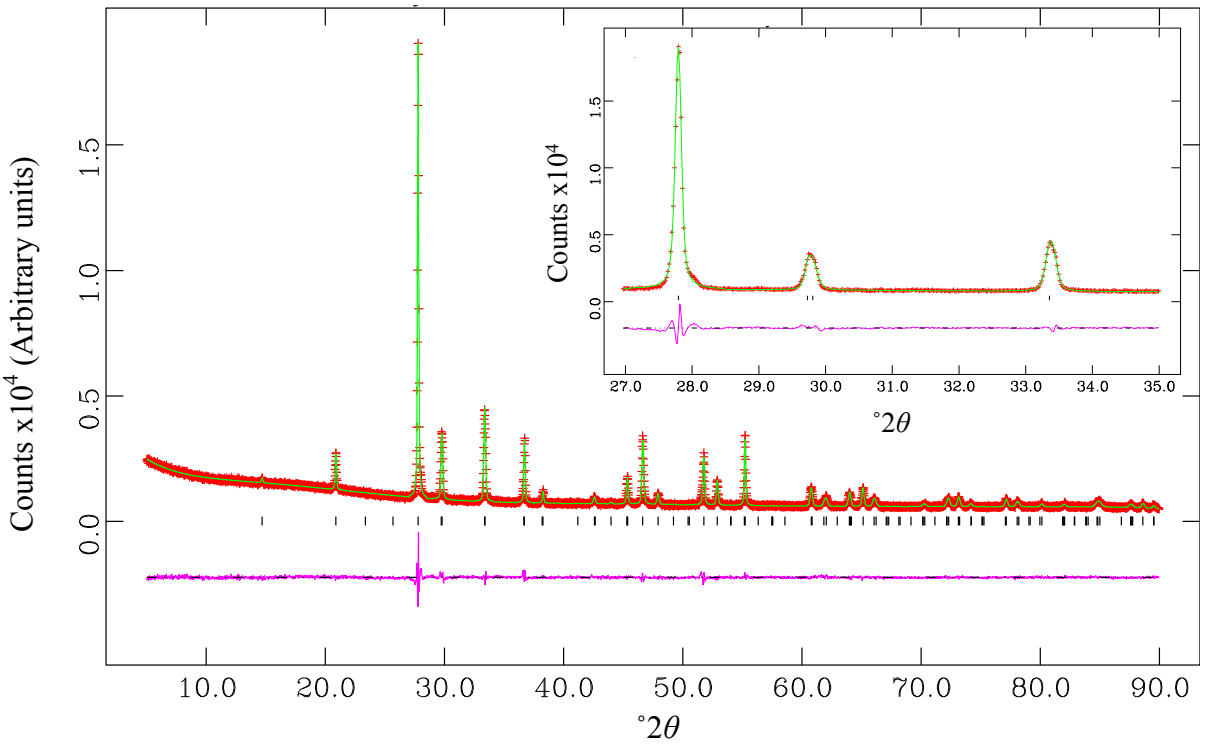

The final fit of $Co_{0.50}Fe_{0.50}Sb_{1.70}Pb_{0.30}O_4$ obtained from the Rietveld refinement of XRPD data in $P4_2/mbc$. The (+) observed (|) calculated and (|) difference profiles are as indicated whilst the tick marks (|) represent the nuclear structure of $Co_{0.50}Fe_{0.50}Sb_{1.70}Pb_{0.30}O_4$. Inset shows the fit of the region 27-35 °2θ.

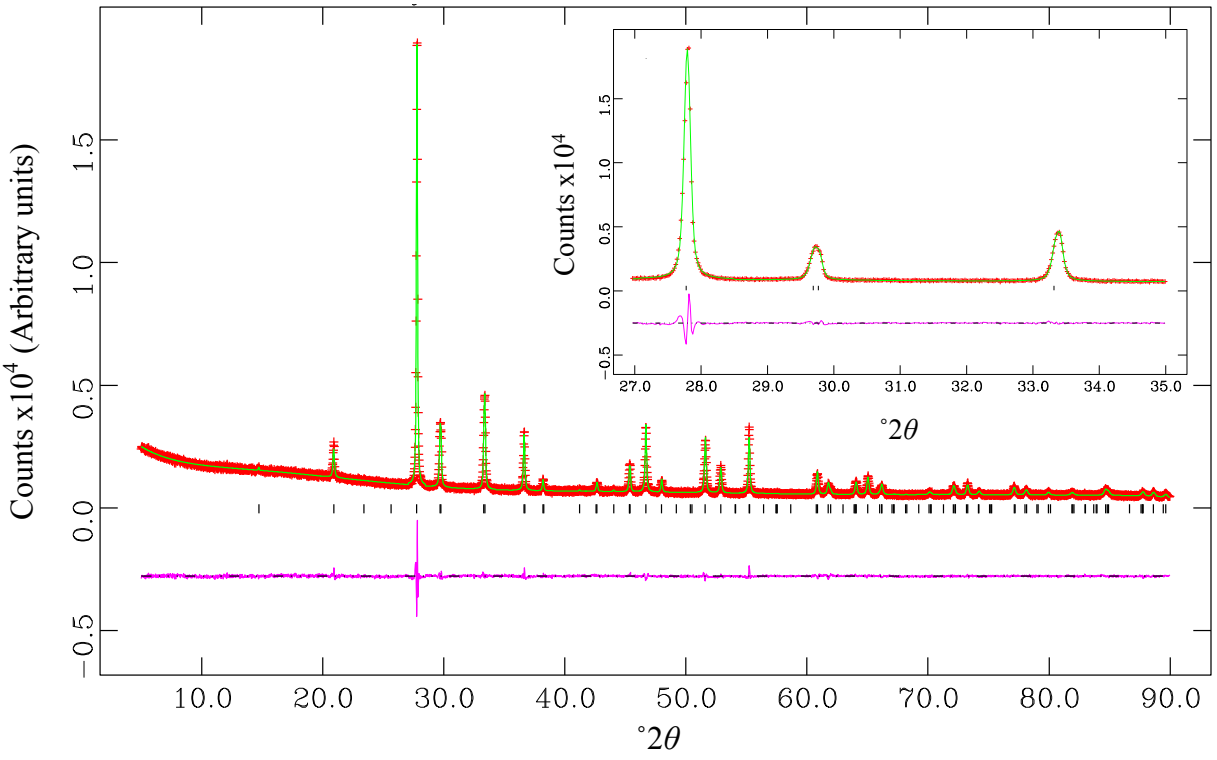

The final fit of $Co_{0.50}Fe_{0.50}Sb_{1.60}Pb_{0.40}O_4$ obtained from the Rietveld refinement of XRPD data in $P4_2/mbc$. The (+) observed (|) calculated and (|) difference profiles are as indicated whilst the tick marks (|) represent the nuclear structure of $Co_{0.50}Fe_{0.50}Sb_{1.60}Pb_{0.40}O_4$. Inset shows the fit of the region 27-35 °2θ.

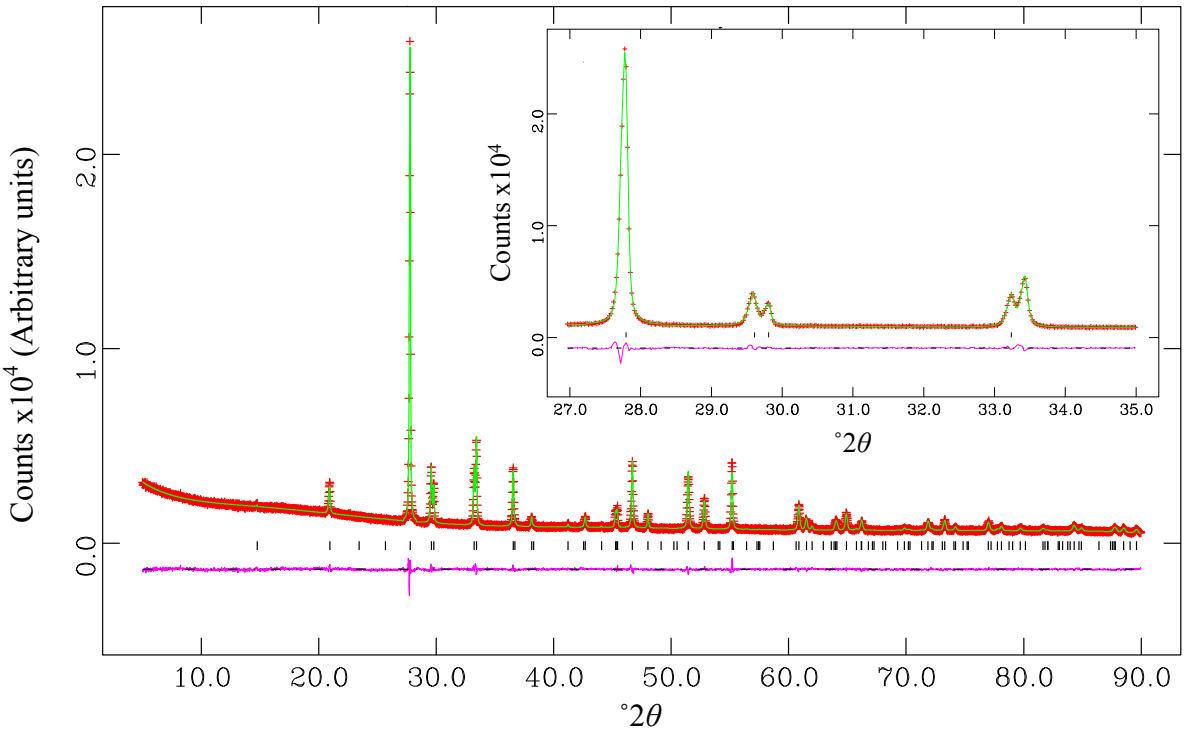

The final fit of $Co_{0.50}Fe_{0.50}Sb_{1.50}Pb_{0.50}O_4$ obtained from the Rietveld refinement of XRPD data in $P4_2/mbc$. The (+) observed (|) calculated and (|) difference profiles are as indicated whilst the tick marks (|) represent the nuclear structure of $Co_{0.50}Fe_{0.50}Sb_{1.50}Pb_{0.50}O_4$. Inset shows the fit of the region 27-35 °2θ.

The final fits of the $Co_{0.75}Fe_{0.25}Sb_{2-x}Pb_xO_4$ compounds based on XRPD data refinements.

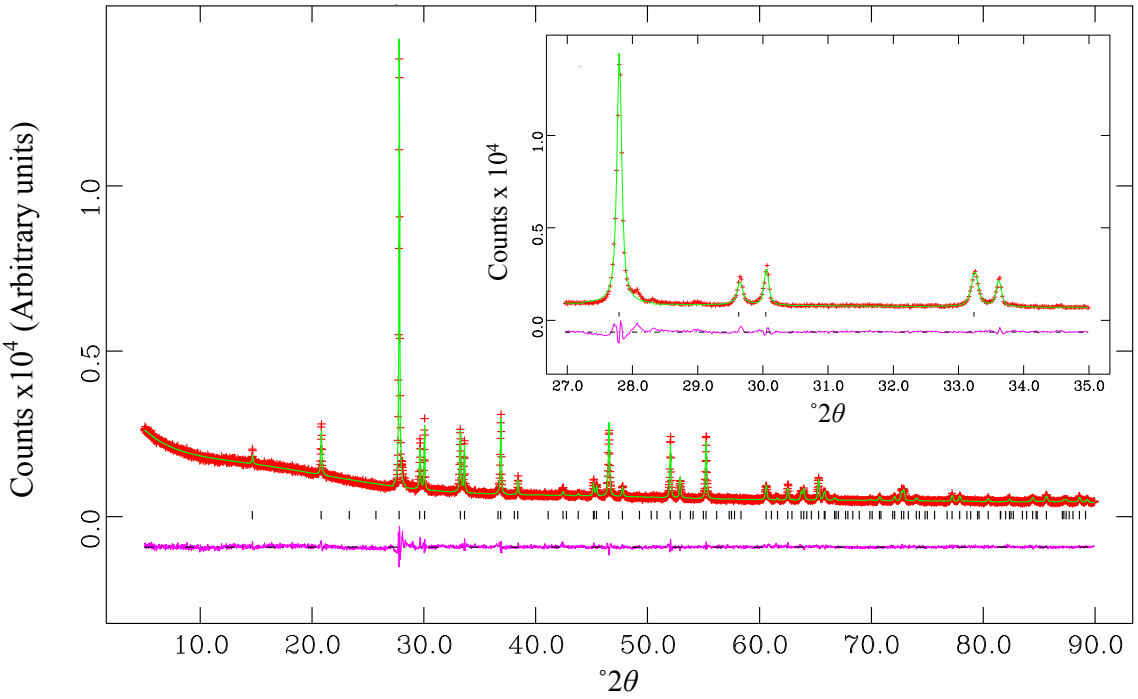

The final fit of $Co_{0.75}Fe_{0.25}Sb_{1.90}Pb_{0.10}O_4$ obtained from the Rietveld refinement of XRPD data in $P4_2/mbc$. The (+) observed (|) calculated and (|) difference profiles are as indicated whilst the tick marks (|) represent the nuclear structure of $Co_{0.75}Fe_{0.25}Sb_{1.90}Pb_{0.10}O_4$. Inset shows the fit of the region 27-35 °2θ.

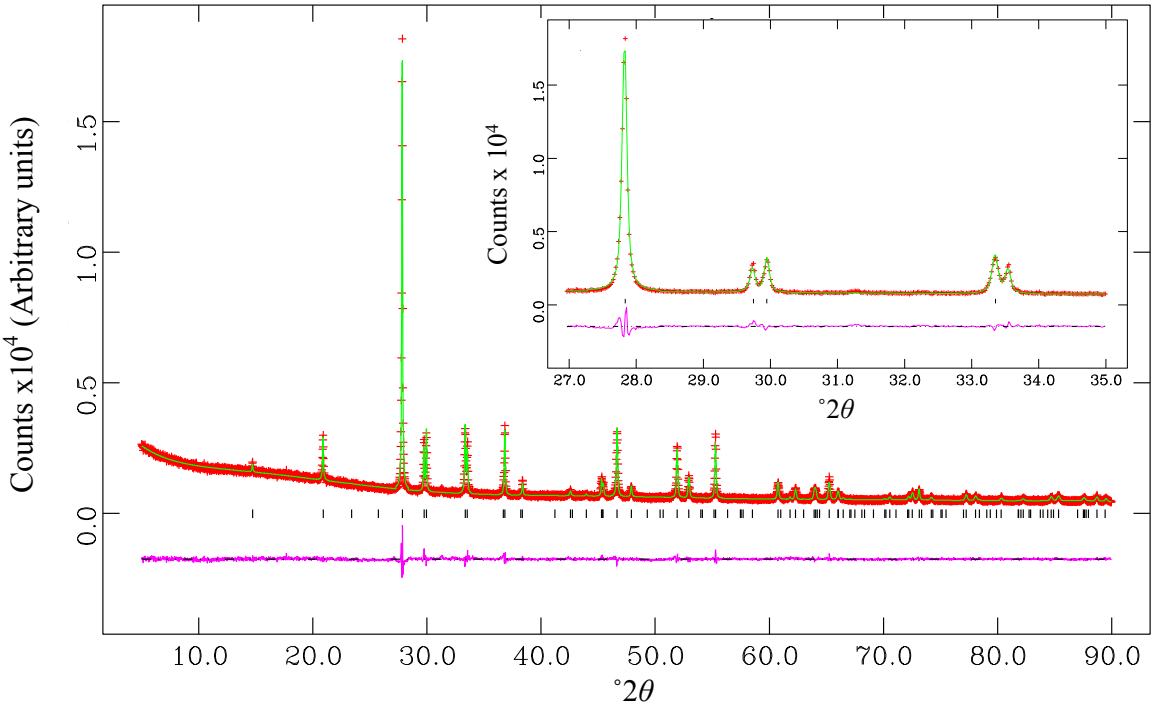

The final fit of $Co_{0.75}Fe_{0.25}Sb_{1.80}Pb_{0.20}O_4$ obtained from the Rietveld refinement of XRPD data in $P4_2/mbc$. The (+) observed (|) calculated and (|) difference profiles are as indicated whilst the tick marks (|) represent the nuclear structure of $Co_{0.75}Fe_{0.25}Sb_{1.80}Pb_{0.20}O_4$. Inset shows the fit of the region 27-35 °2θ.

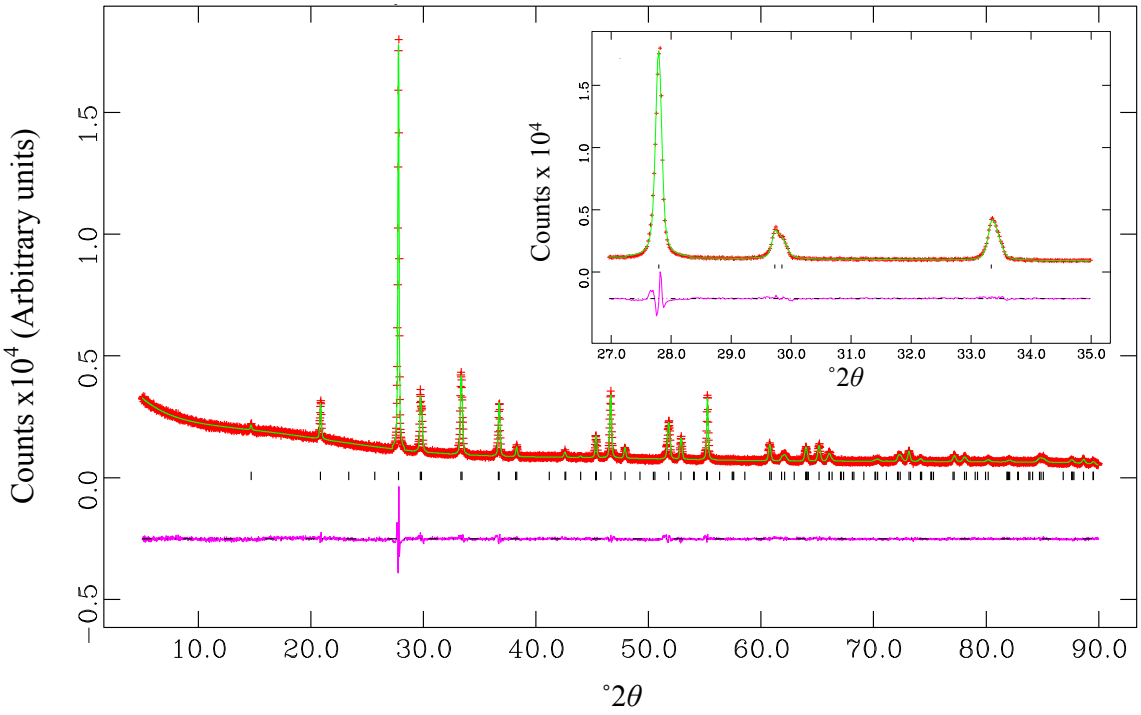

The final fit of $Co_{0.75}Fe_{0.25}Sb_{1.75}Pb_{0.25}O_4$ obtained from the Rietveld refinement of XRPD data in $P4_2/mbc$. The (+) observed (|) calculated and (|) difference profiles are as indicated whilst the tick marks (|) represent the nuclear structure of $Co_{0.75}Fe_{0.25}Sb_{1.75}Pb_{0.25}O_4$. Inset shows the fit of the region 27-35°2θ.

Appendix 3.2: 300 K NPD refinements of the $Co_{1-x}Fe_xSb_{2-y}Pb_yO_4$ phases

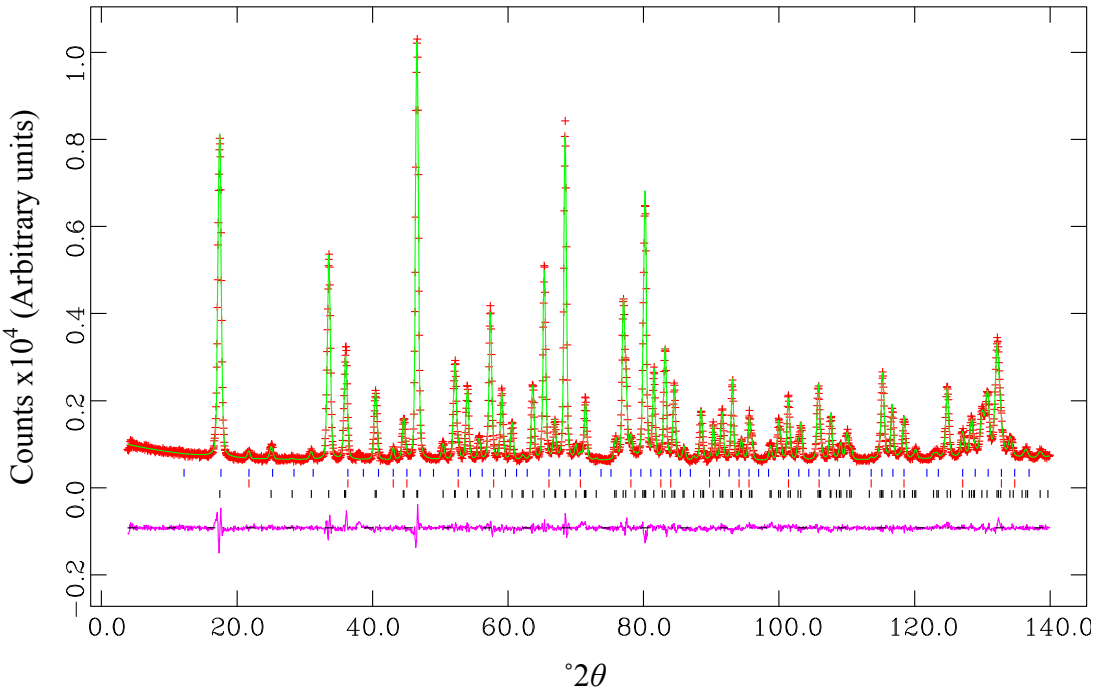

The final refinement of $Co_{0.25}Fe_{0.75}Sb_{1.50}Pb_{0.50}O_4$ in $P4_2/mbc$ at 300 K; the (+) observed (|) calculated and (|) difference profiles are as indicated whilst the tick marks represent the $Co_{0.25}Fe_{0.75}Sb_{1.50}Pb_{0.50}O_4$ nuclear (|), Fe_3O_4 nuclear (|), and Fe_3O_4 magnetic (|) structures.

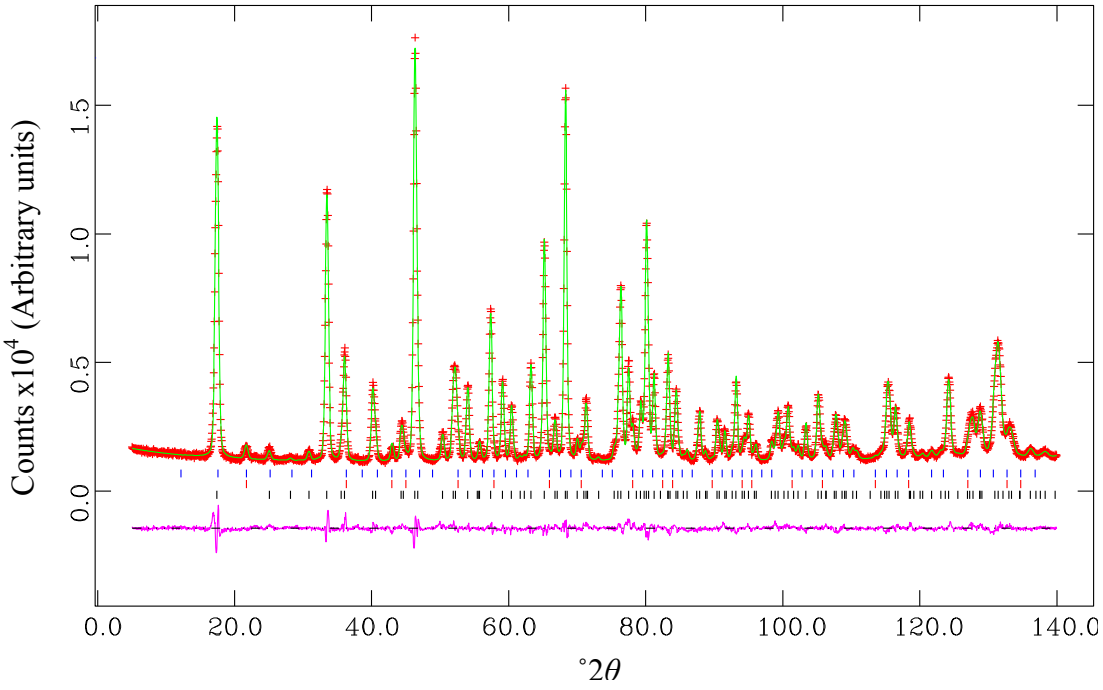

The final refinement of $Co_{0.25}Fe_{0.75}Sb_{1.25}Pb_{0.75}O_4$ in $P4_2/mbc$ at 300 K; the (+) observed (|) calculated and (|) difference profiles are as indicated whilst the tick marks represent the $Co_{0.25}Fe_{0.75}Sb_{1.25}Pb_{0.75}O_4$ nuclear (|), Fe_3O_4 nuclear (|), and Fe_3O_4 magnetic (|) structures.

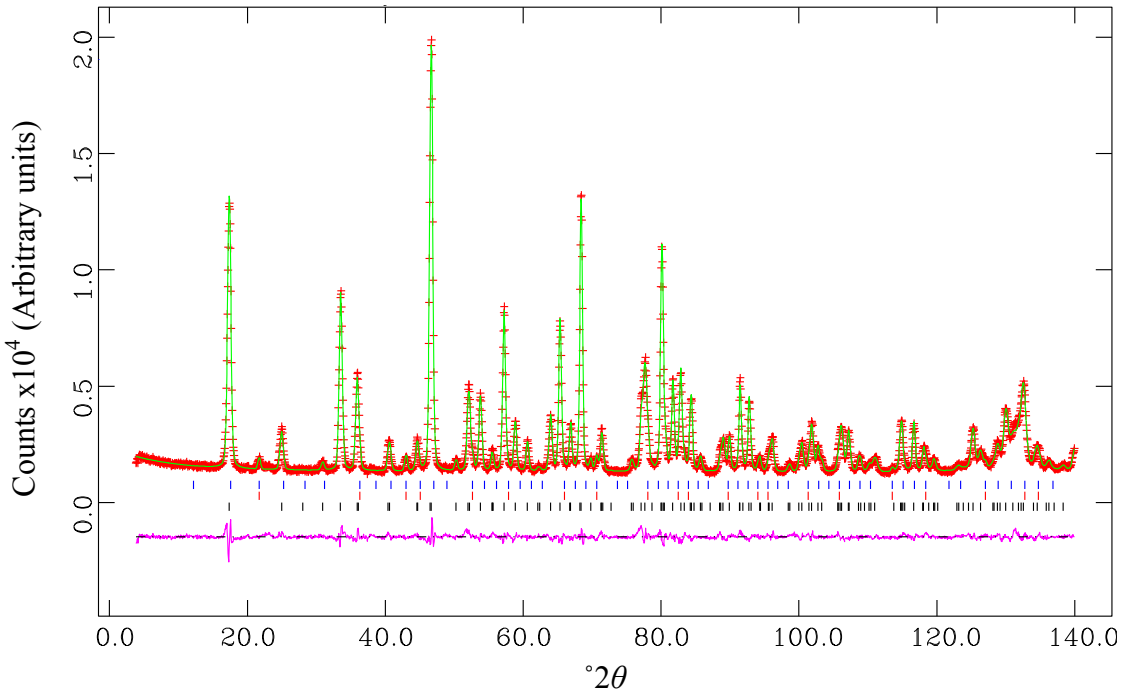

The final refinement of $Co_{0.50}Fe_{0.50}Sb_{1.75}Pb_{0.25}O_4$ in $P4_2/mbc$ at 300 K; the (+) observed, (|) calculated and (|) difference profiles are as indicated whilst the tick marks represent the $Co_{0.50}Fe_{0.50}Sb_{1.75}Pb_{0.25}O_4$ nuclear (|), Fe_3O_4 nuclear (|), and Fe_3O_4 magnetic (|) structures.

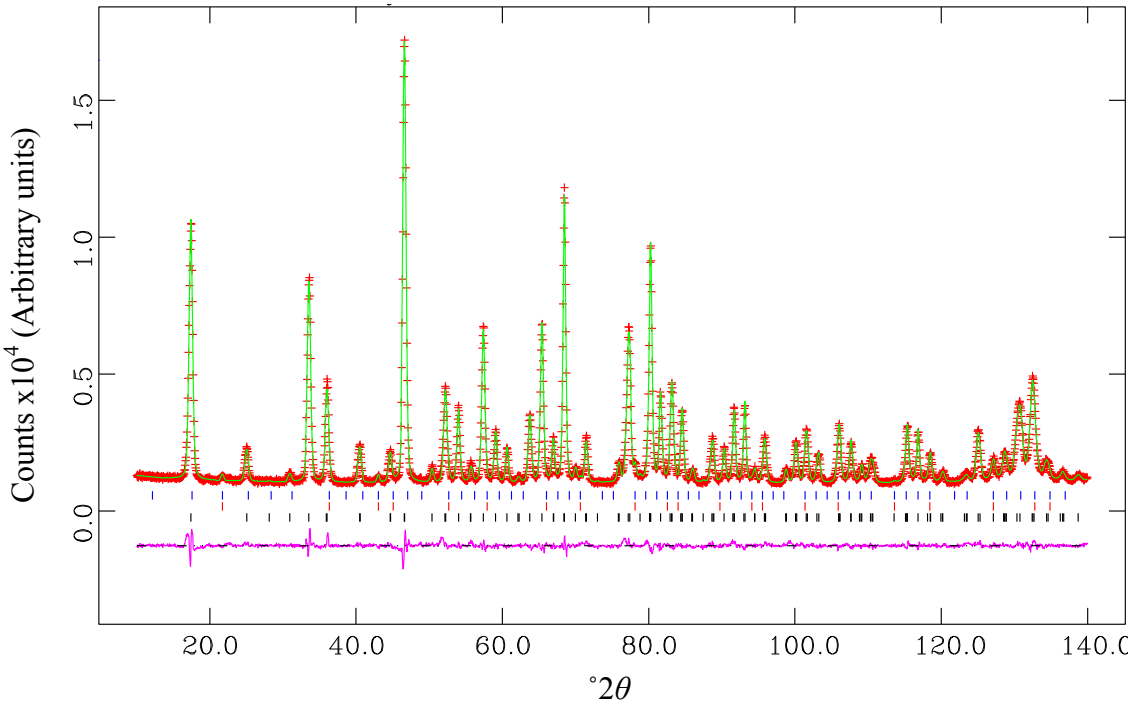

The final refinement of $Co_{0.50}Fe_{0.50}Sb_{1.60}Pb_{0.40}O_4$ in $P4_2/mbc$ at 300 K; the (+) observed, (|) calculated and (|) difference profiles are as indicated whilst the tick marks represent the $Co_{0.50}Fe_{0.50}Sb_{1.60}Pb_{0.40}O_4$ nuclear (|), Fe_3O_4 nuclear (|), and Fe_3O_4 magnetic (|) structures.

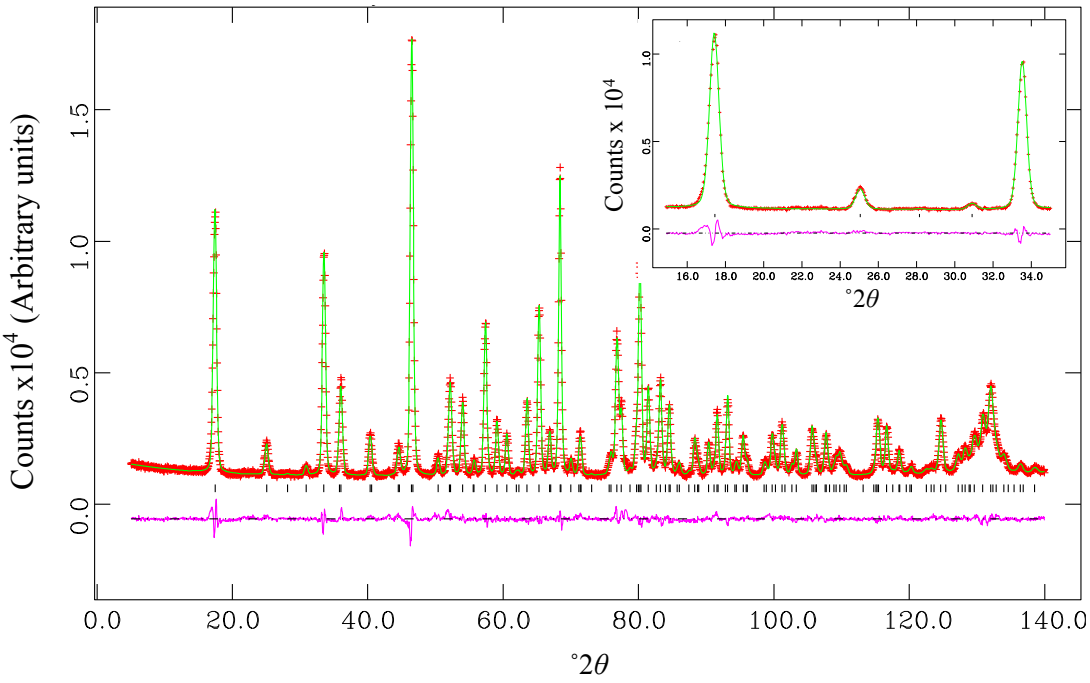

The final refinement of $Co_{0.50}Fe_{0.50}Sb_{1.50}Pb_{0.50}O_4$ in $P4_2/mbc$ at 300 K; the (+) observed, (|) calculated and (|) difference profiles are as indicated whilst the tick marks represent the $Co_{0.50}Fe_{0.50}Sb_{1.50}Pb_{0.50}O_4$ nuclear (|), Fe_3O_4 nuclear (|), and Fe_3O_4 magnetic (|) structures. The inset shows the region 15-35 °2θ note the absence of any Fe_3O_4 magnetic peak at around 21 °2θ.

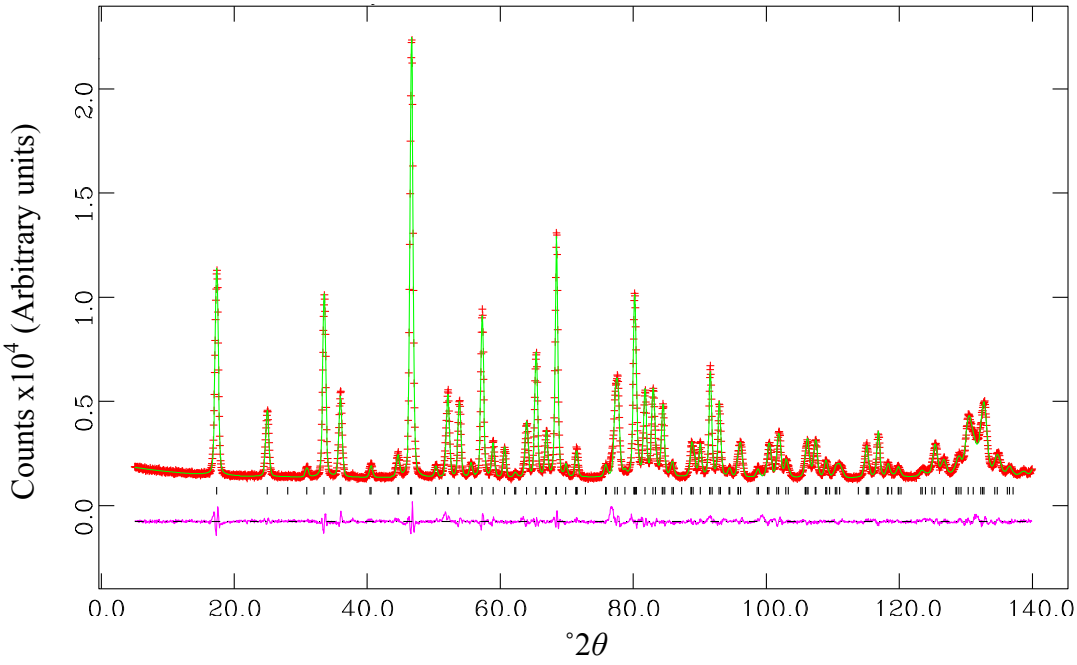

The final refinement of $Co_{0.75}Fe_{0.25}Sb_{1.75}Pb_{0.25}O_4$ in $P4_2/mbc$ at 300 K; the (+) observed, (|) calculated and (|) difference profiles are as indicated whilst the tick marks represent the $Co_{0.75}Fe_{0.25}Sb_{1.75}Pb_{0.25}O_4$ nuclear structure.

Appendix 3.3: 1.5 K NPD refinement of the $Co_{1-x}Fe_xSb_{2-y}Pb_yO_4$ phases

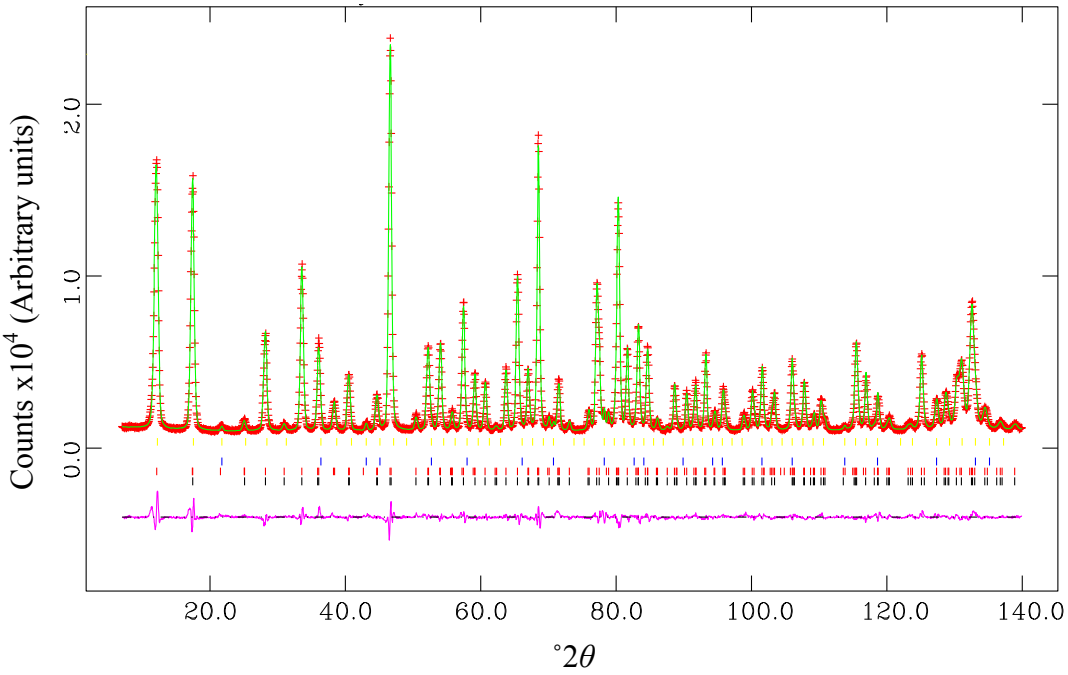

The final refinement of $Co_{0.25}Fe_{0.75}Sb_{1.50}Pb_{0.50}O_4$ in *P*4$_2$/*mbc* at 1.5 K; the (+) observed, (|) calculated and (|) difference profiles are as indicated whilst the tick marks represent the $Co_{0.25}Fe_{0.75}Sb_{1.50}Pb_{0.50}O_4$ nuclear (|), $Co_{0.25}Fe_{0.75}Sb_{1.50}Pb_{0.50}O_4$ magnetic (|), Fe_3O_4 nuclear (|), and Fe_3O_4 magnetic (|) structures.

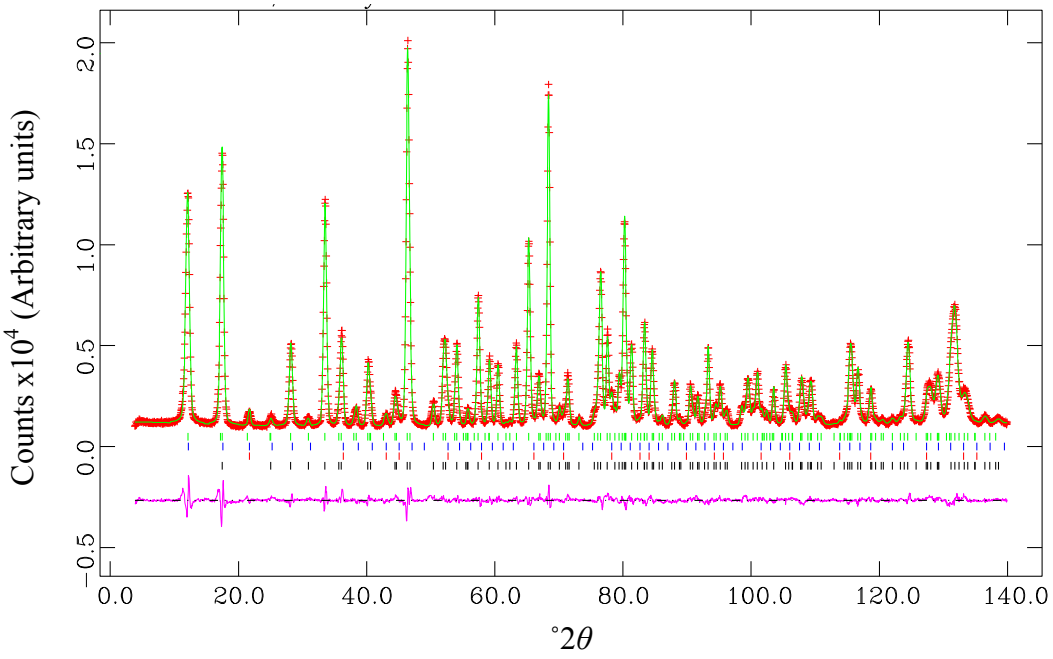

The final refinement of $Co_{0.25}Fe_{0.75}Sb_{1.25}Pb_{0.75}O_4$ in *P*4$_2$/*mbc* at 1.5 K; the (+) observed, (|) calculated and (|) difference profiles are as indicated whilst the tick marks represent the $Co_{0.25}Fe_{0.75}Sb_{1.25}Pb_{0.75}O_4$ nuclear (|), Fe_3O_4 nuclear (|), Fe_3O_4 magnetic (|), and $Co_{0.25}Fe_{0.75}Sb_{1.25}Pb_{0.75}O_4$ magnetic (|) structures.

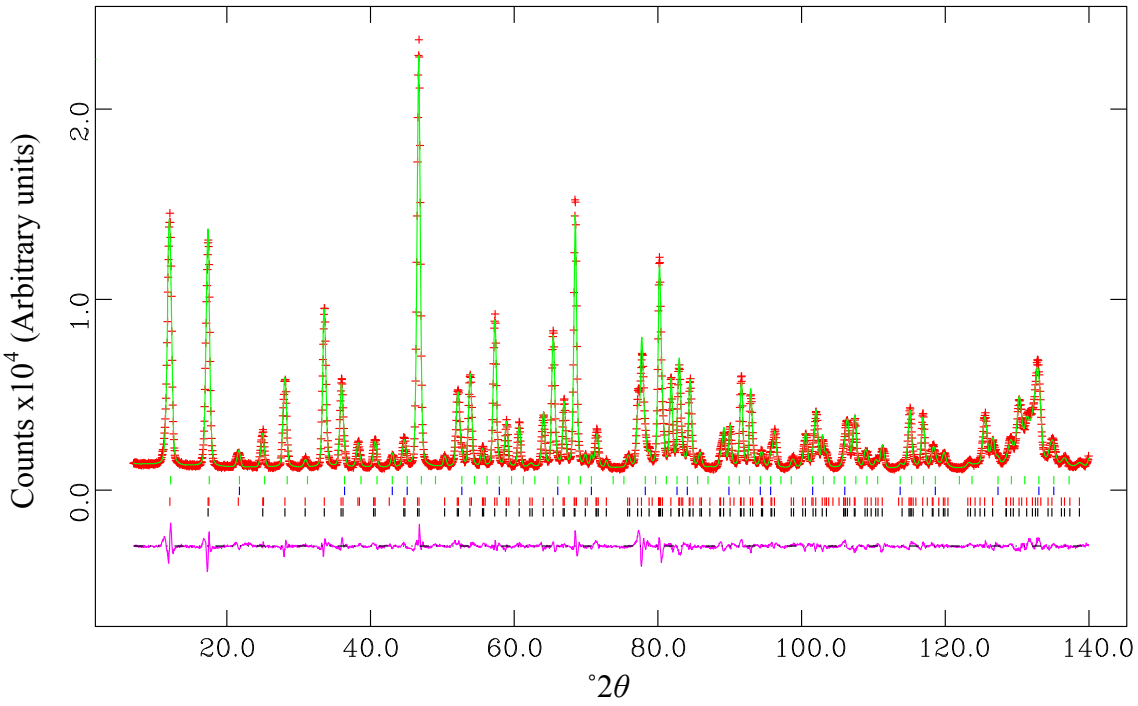

The final refinement of $Co_{0.50}Fe_{0.50}Sb_{1.75}Pb_{0.25}O_4$ in $P4_2/mbc$ at 1.5 K; the (+) observed (|) calculated and (|) difference profiles are as indicated whilst the tick marks represent the $Co_{0.50}Fe_{0.50}Sb_{1.75}Pb_{0.25}O_4$ nuclear (|), $Co_{0.50}Fe_{0.50}Sb_{1.75}Pb_{0.25}O_4$ magnetic (|), Fe_3O_4 nuclear (|), and Fe_3O_4 magnetic (|) structures.

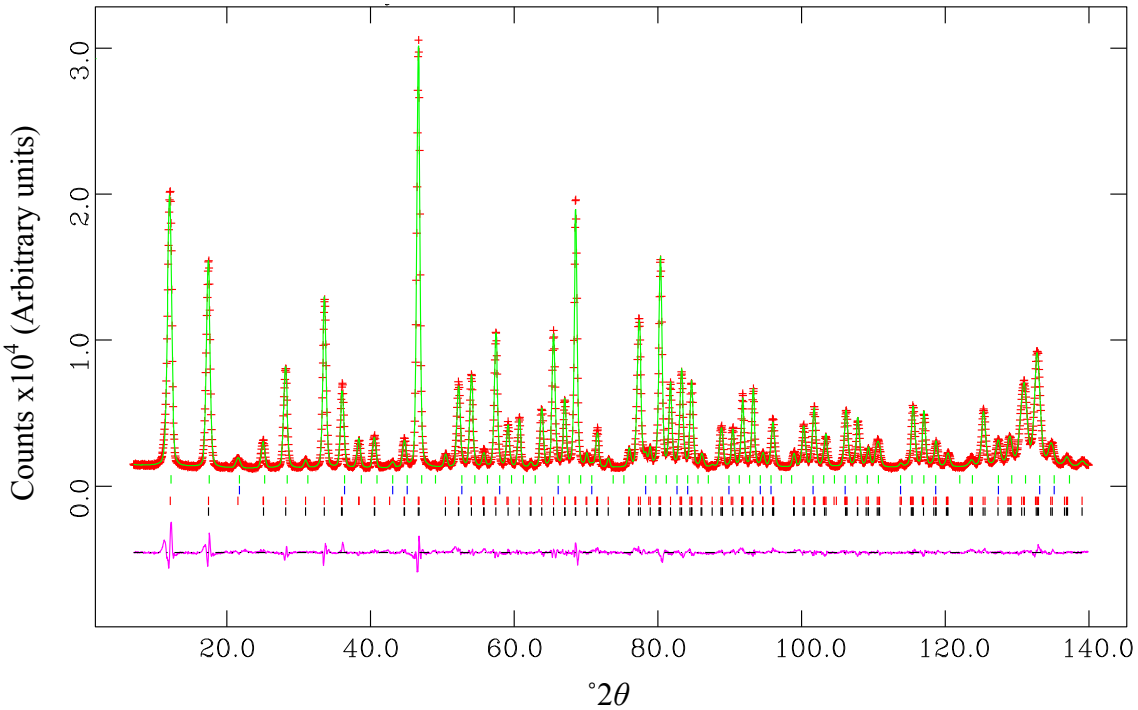

The final refinement of $Co_{0.50}Fe_{0.50}Sb_{1.60}Pb_{0.40}O_4$ in $P4_2/mbc$ at 1.5 K; the (+) observed (|) calculated and (|) difference profiles are as indicated whilst the tick marks represent the $Co_{0.50}Fe_{0.50}Sb_{1.60}Pb_{0.40}O_4$ nuclear (|), $Co_{0.50}Fe_{0.50}Sb_{1.60}Pb_{0.40}O_4$ magnetic (|), Fe_3O_4 nuclear (|), and Fe_3O_4 magnetic (|) structures.

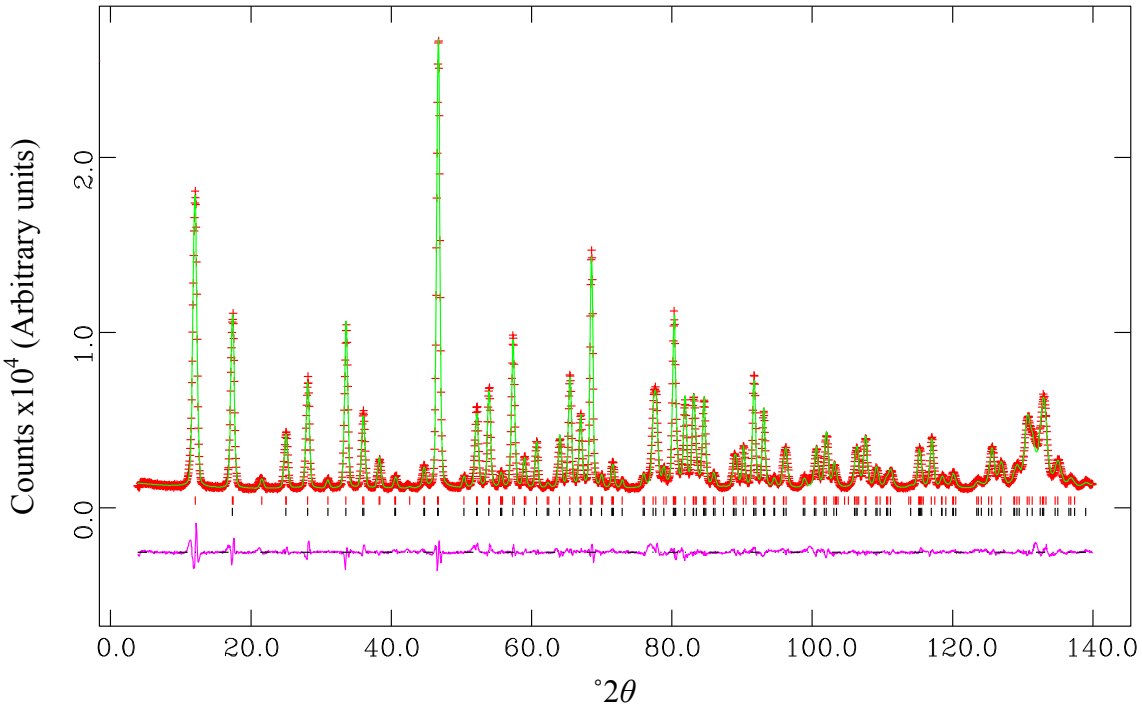

The final refinement of $Co_{0.75}Fe_{0.25}Sb_{1.75}Pb_{0.25}O_4$ in $P4_2/mbc$ at 1.5 K; the (+) observed (|) calculated and (|) difference profiles are as indicated whilst the tick marks represent the $Co_{0.75}Fe_{0.25}Sb_{1.75}Pb_{0.25}O_4$ nuclear (|), and $Co_{0.75}Fe_{0.25}Sb_{1.75}Pb_{0.25}O_4$ magnetic (|) structures.

Appendix 3.4: Magnetic susceptibility data for the $Co_{0.25}Fe_{0.75}Sb_{2-x}Pb_xO_4$ phases where x = 0.10, 0.25, 0.30, 0.50, 0.60 and 0.75

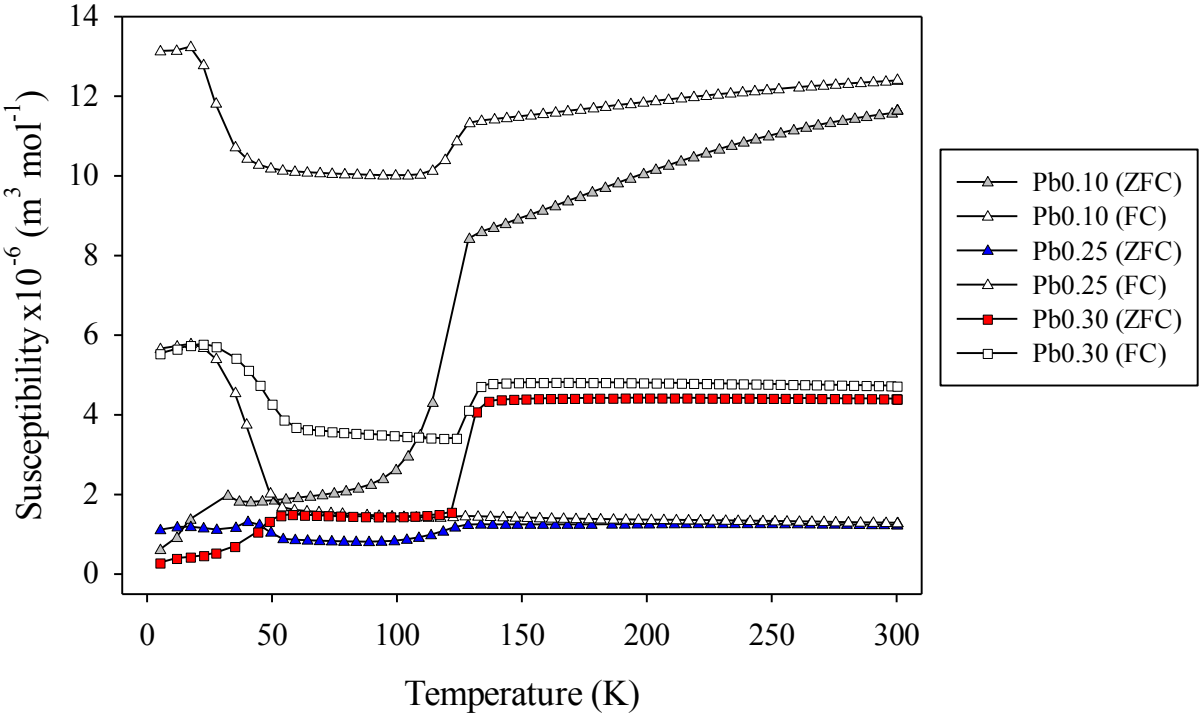

Susceptibility plots for the $Co_{0.25}Fe_{0.75}Sb_{2-x}Pb_xO_4$ phases (where x = 0.10, 0.25 and 0.30). Measurements were taken under ZFC/FC conditions with an applied field of 100 Oe.

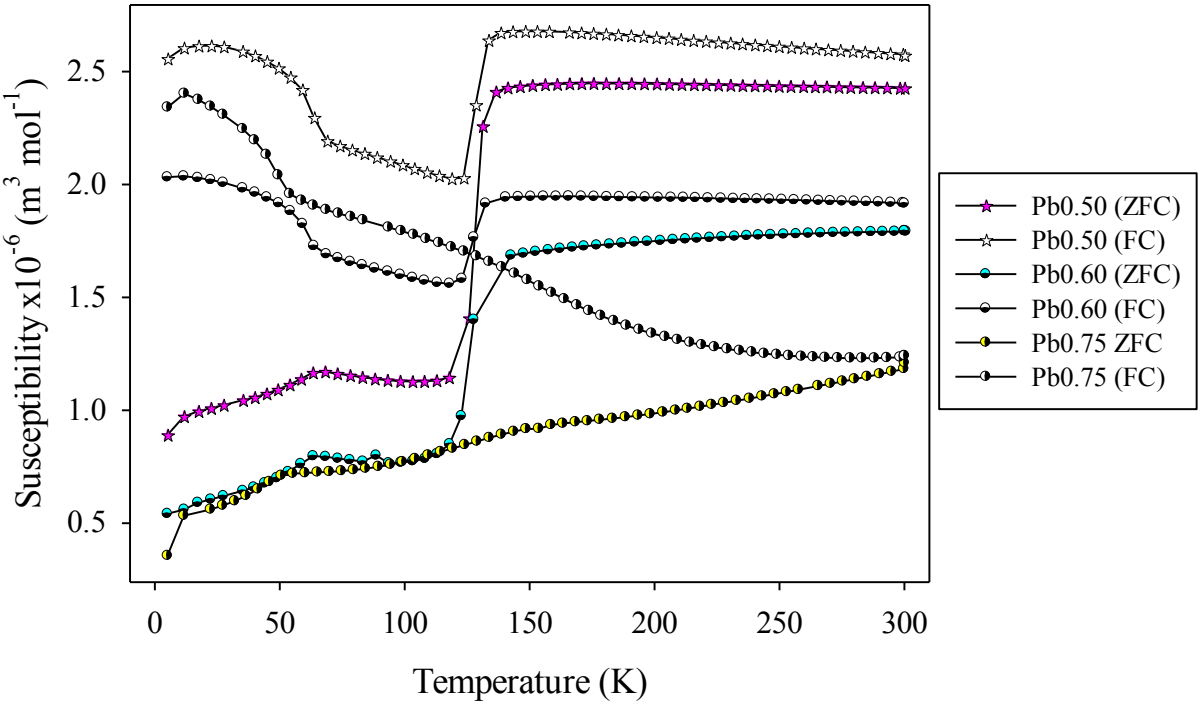

Susceptibility plots for the $Co_{0.25}Fe_{0.75}Sb_{2-x}Pb_xO_4$ phases (where x = 0.50, 0.60 and 0.75). Measurements were taken under ZFC/FC conditions with an applied field of 100 Oe.

List of publications resulting from this thesis

1. **$LiSbO_2$: Synthesis, Structure, Stability and Lithium-Ion Conductivity**

   B. P. de Laune, R. D. Bayliss and C. Greaves

   Inorg. Chem. **50** (2011) 7880.

2. **Structural and magnetic characterisation of $CoSb_2O_4$, and the substitution of Pb^{2+} for Sb^{3+}**

   B. P. de Laune and C. Greaves

   J. Solid State Chem. **187** (2012) 225.

3. **Magnetic interactions in ferrous antimonite, $FeSb_2O_4$ and some derivatives**

   R. D. Bayliss, F. J. Berry, B. P. de Laune, C. Greaves, Ö. Helgason, J. F. Marco, M. F. Thomas, L. Vergara, and M. J. Whitaker

   J. Phys.: Condens. Matter. **24** (2012) 276001